THE MISALIGNMENT OF OCULAR COMPONENTS AND OCULAR MONOCHROMATIC ABERRATIONS

by

Chengwu Cui

A thesis

presented to the University of Waterloo

in fulfillment of the

thesis requirement for the degree of

Doctor of Philosophy

in

Vision Science

Waterloo, Ontario, Canada, 1998

© Chengwu Cui 1998

National Library of Canada
Acquisitions and Bibliographic Services
395 Wellington Street
Ottawa ON K1A 0N4
Canada

Bibliothèque nationale du Canada
Acquisitions et services bibliographiques
395, rue Wellington
Ottawa ON K1A 0N4
Canada

Your file Votre référence

Our file Notre référence

The author has granted a non-exclusive licence allowing the National Library of Canada to reproduce, loan, distribute or sell copies of this thesis in microform, paper or electronic formats.

The author retains ownership of the copyright in this thesis. Neither the thesis nor substantial extracts from it may be printed or otherwise reproduced without the author's permission.

L'auteur a accordé une licence non exclusive permettant à la Bibliothèque nationale du Canada de reproduire, prêter, distribuer ou vendre des copies de cette thèse sous la forme de microfiche/film, de reproduction sur papier ou sur format électronique.

L'auteur conserve la propriété du droit d'auteur qui protège cette thèse. Ni la thèse ni des extraits substantiels de celle-ci ne doivent être imprimés ou autrement reproduits sans son autorisation.

0-612-30599-6

Canada

The University of Waterloo requires the signatures of all persons using or photocopying this thesis. Please sign below, and give address and date.

ABSTRACT

In this thesis, a theoretical method was developed to calculate the tilt and decentration of the crystalline lens from various possible reference axes in the human eye based on the misalignments of Purkinje images. The derivation was based on the Gullstrand-Emsley eye model utilizing the equivalent mirror theorem in the paraxial region.

A Purkinje image photographing system was developed to measure various misalignment parameters in the left eyes of twenty-one subjects. These factors included: 1) angle alphas defined both by aligning Purkinje image I and IV and by aligning Purkinje image I and III , 2) lens tilt and decentration with respect to the aligned Purkinje image I and IV, the pupillary axis and the line of sight, 3) the decentration of the pupil from the aligned Purkinje image I and IV. The measurement results explain the inconsistent results of current angle alpha measurements when compared to the traditional accepted value. Human eye lens tilt and decentration were measured for the first time. The pupil centration measurement revealed a special reference—the coaxially sighted corneal reflex axis - to represent the traditionally defined visual axis. A general trend of the misalignment of the 21 eyes measured was found.

An automated two-dimensional semi-Maxwellian view ocular aberration measurement system was developed for the first time. An effective and flexible wavefront aberration reconstruction procedure was also developed to reconstruct wavefront aberration from measured ray aberration data. Pilot measurement of four eyes under natural pupil condition, with the center of the natural pupil as the reference, proved the effectiveness of both the system and the wavefront reconstruction method.

Using the coaxially sighted cornea reflex as the reference, wavefront aberrations of the left eyes of twenty-one emmetropic subjects were reconstructed from the measured ray aberration data. These data were also converted to wavefront aberrations using the

geometrical center of the pupil as the reference. The average of the wavefront aberration of the twenty-one eyes measured showed mainly primary symmetrical aberrations.

Finally, the symmetrical component and the asymmetrical component of the mean squared wavefront aberration of each eye were calculated and used to correlate with each misalignment parameter measured. There is no significant correlation between either aberration component and the misalignment of the ocular structures in the twenty-one eyes studied.

Acknowledgments

Indeed, my thanks are long overdue to so many people during these many years of study. To write all of them down, it would not be proportional to the size of the scientific contribution presented in this thesis. Yet without mentioning some of them, this thesis is incomplete in the pursuit of truth. Without such extra help, it would simply be unimaginable for me to carry this long.

I specifically would like to thank my co-supervisor Dr. J. Hovis. Jeff got me started and then helped put the last stitch to my robe. All these years, besides his valuable scientific guidance, he showed me the virtue of a great teacher who would spend hours and hours correcting my Chinese English. The patience and thoroughness that I learned from Jeff would certainly benefit the rest of my life, not only as a researcher but also as a human being. I am forever thankful to Dr. V. Lakshminarayanan. Vengu's critical role as my co-supervisor demanded not only authoritative knowledge in the field but also a great deal of integrity, fairness, and even chivalry. I thank Dr. J. Flanagan, my co-supervisor, for his great courage and faith in graduate student education. I also would like to thank Dr. M.W.C. Campbell for many efforts she made in her valuable critiques of my work and for her financial support through her grants from the Natural Science and Engineering Research Council of Canada. I thank my committee member, Dr. Bobier for his evaluation of my work and for letting me using his lab equipment. I am indebted to Dr. Sivak, my committee member, for his evaluation of my work and for his encouragement during my study.

I have benefited a great deal from Mr. Robin Jones in the machine shop in the mechanical aspects of instrumentation and I thank him for much help in building my setups. I also thank Mr. Andy Lankin, Manfred Rieck, Andrew Nowinski for their technical support.

To Dr. W. Adrain, Dr. W. N. Charman, Dr. T. Cullen, Dr. H. Howland, Dr. G. Woo, Dr. R. Chou, I thank them for answering my many extra questions that I had as a

graduate student. I would like to thank the University of Waterloo for having professors like Dr. J. Brandon, Dr. C. A. Pearson and Dr. G. Strong.

I also feel grateful for much extra help from Ms. Sharon Dahmer, Ms. Agnes Kolic. I thank all the graduate students for helps in many aspects.

I thank all my subjects. I thank Dr. J. C. Barry for providing the information regarding the specification of a special photoflash unit from Germany.

To Fei Yuan, Jing Wang, Xiaowen Liu, Dr. Desmond Cheng, Dr. Geck Hong, Dr. Zengshe Liu, I thank them for support. I also thank my colleagues in GretagMacbeth for emotional support, especially Harold Van Aken.

I am also indebted to Burton Empey, the then president of GSA for his emotional support in a difficult time of my study.

I thank Austin Roorda, the then fellow graduate student, the now famous Dr. A. Roorda for so many things that I benefited from. I owe Dr. M. Andison, for her unforgettable emotional support in such an unforgettable way.

Dedication

To my family

To Tim and Tim

Table of Contents

CHAPTER 1 GENERAL INTRODUCTION 1

1.1 EYE MODEL AND DEFINITIONS 2

1.2 REVIEW OF THE CHARACTERISTICS OF DEFECTS OF THE TYPICAL HUMAN EYE 6

1.2.1 Defects of the optical components of the eye 7

1.2.2 Misalignment of the optical components of the eye 9

1.3 OPTICAL FUNCTIONAL DEFECTS OF THE HUMAN EYE 13

1.3.1 The monochromatic ideal optical system and the standard description of monochromatic wavefront aberration 13

1.3.2 The partition of total wavefront aberration into the symmetrical and asymmetrical components 15

1.3.3 Objective methods of wavefront aberration measurement 16

1.3.4 Subjective methods of wavefront aberration measurement 18

1.4 POSSIBLE CORRELATION BETWEEN THE OPTICAL STRUCTURAL DEFECTS OF THE HUMAN EYE AND THE OPTICAL FUNCTIONAL DEFECTS OF THE HUMAN EYE 24

1.4.1 General characteristics of aberrations measured in the human eyes 24

1.4.2 Correlation of asymmetric aberrations and the misalignment of various components of the eye 26

1.5 RESEARCH OBJECTIVES 27

CHAPTER 2 THEORETICAL MODELS FOR MEASURING THE TILT AND DECENTRATION OF THE CRYSTALLINE LENS *IN VIVO* 28

2.1 INTRODUCTION 29

2.2 DERIVATION OF THE EQUIVALENT MIRRORS OF THE TILTED AND DECENTERED OCULAR SURFACES 29

2.3 CALCULATION OF LENS TILT AND DECENTRATION FROM PURKINJE IMAGE DISPLACEMENTS 34

2.3.1 Derivation of lens tilt and decentration from Purkinje image displacements *34*

2.3.2 Verification of the calculation of lens tilt and decentration from Purkinje image displacements by raytracing *36*

2.3.3 Solution of lens tilt and decentration from the derived equations *37*

2.4 CALCULATION OF LENS TILT AND DENCENTRATION FROM THE ANGLES FOR ALIGNING TWO OF THE THREE PURKINJE IMAGES 40

2.5 DISCUSSION 42

2.6 SUMMARY 43

CHAPTER 3 A SEMI-MAXWELLIAN VIEW WAVEFRONT ABERRATION MEASUREMENT SYSTEM 44

3.1 INTRODUCTION 45

3.2 THEORY 45

3.2.1 The semi-Maxwellian view aberration measurement system *45*

3.2.2 Wavefront reconstruction from ray aberration data *49*

3.2.3 The choice of a reference axis *63*

3.3 METHODS 64

3.3.1 Design of the measurement system *64*

3.3.2 Alignment of the system *69*

3.3.3 Analysis of system errors *69*

3.4 PROCEDURES 73

3.4.1 Pupil location sampling scheme *73*

3.4.2 Procedures *73*

3.4.3 Subjects of the preliminary test *75*

3.5 RESULTS AND ANALYSIS 75

3.5.1 Direct diagrams from the measured ray aberration data *75*

3.5.2 Wavefront aberration reconstruction from ray aberration data *76*

3.6 DISCUSSION 82

3.6.1 Repeatability and error analysis *82*

3.6.2 Measured wavefront aberrations compared to other measurements *92*

3.6.3 Effectiveness of the measurement system and the data processing procedure *94*

3.7 CONCLUSIONS 95

CHAPTER 4 MEASUREMENT OF WAVEFRONT ABERRATION OF THE EYE USING THE COAXIALLY SIGHTED CORNEAL REFLEX **96**

4.1 INTRODUCTION 97

4.2 THE COAXIALLY SIGHTED CORNEAL REFLEX AS THE REFERENCE IN ABERRATION MEASUREMENT 97

4.3 EFFECT ON THE WAVEFRONT ABERRATION MEASURED WITH THE CHANGE OF THE REFERENCE AXIS 100

4.3.1 The Independence of the wavefront aberration measured with the shift of the reference axis *100*

4.3.2 The calculation of the root mean square (RMS) wavefront aberration needs to consider the real position of the pupil *101*

4.3.3 Transformation of the reconstructed wavefront aberration with the shift of the reference axis from the coaxially sighted cornea reflex to the geometrical center of the pupil *102*

4.4 METHODS 105

4.4.1 Apparatus *105*

4.4.2 Subjects *105*

4.4.3 Measurement procedure *106*

4.4.4 Repeatability tests *106*

4.5 RESULTS AND ANALYSIS 106

4.5.1. Diagram from the measured ray aberration data *108*

4.5.2 Wavefront aberrations reconstructed from ray aberration data *109*

4.6 REPEATABILITY AND EXAMINATION OF THE FIT 120

4.6.1 Vernier acuity *120*

4.6.2 Measurement repeatability *120*

4.6.3 The difference of 6th order and 8th order Taylor polynomials versus the two latest measurements *122*

4.6.4 Comparison of Zernike polynomial fit and Taylor polynomial fit *124*

4.6.5 Cases low r-squared value fit *126*

4.7 COMPARISON OF ABERRATION MEASURED ALONG CSCR AND ABERRATION MEASURED WITH ALONG THE GEOMETRICAL CENTER OF THE PUPIL 127

4.8 AVERAGE WAVEFRONT ABERRATION OF 20 SUBJECTS 129

4.9 CONCLUSIONS 133

CHAPTER 5 MEASUREMENT OF THE MISALIGNMENTS OF OCULAR COMPONENTS *IN VIVO* **134**

5.1 INTRODUCTION 135

5.2 CHOICE OF A REFERENCE AXIS 135

5.3 APPARATUS 136

5.3.1 Use of photoflash light as Purkinje image source *136*

5.3.2 Hardware *136*

5.3.3 Software *138*

5.3.4 System alignment *138*

5.4 PROCEDURES 139

5.4.1 Measurement with respect to the CSCR *140*

5.4.2 Measurement along aligned PI and PIV *140*

5.4.3 Measurement along PI and PIII *141*

5.5 RESULTS AND DATA ANALYSIS 141

5.5.1 Lens tilt and decentration *144*

5.5.2 Pupil decentration *148*

5.5.3 Angle alpha *150*

5.5.4 Derivation of lens tilt and decentration with respect to the line of sight and the pupillary axis *152*

5.6 DISCUSSION 159

5.6.1 Precision and repeatability *159*

5.6.2 Comparison with other measurements *163*

5.6.3 The average values of the eyes measured *168*

5.7 CONCLUSIONS 171

CHAPTER 6 OCULAR MONOCHROMATIC ABERRATIONS AND THE MISALIGNMENTS OF OCULAR COMPONENTS 172

6.1 INTRODUCTION 173

6.2 POSSIBLE CORRELATION BETWEEN THE ASYMMETRICAL COMPONENT OF THE OVERALL WAVEFRONT ABERRATION AND THE MISALIGNMENTS OF OCULAR COMPONENTS 173

6.2.1 Calculation of the asymmetrical components of wavefront aberrations measured .. *173*

6.2.2 Correlation of angle alpha and the asymmetrical component of the mean squared wavefront aberration *178*

6.2.3 Correlation of lens tilt and decentration and the asymmetrical components of MS wavefront aberration *180*

6.2.4 Correlation of pupil decentration and the asymmetrical components of MS wavefront aberration *182*

6.2.5 Correlation of the misalignment of ocular components with the symmetrical component of MS wavefront aberration *183*

6.3 CONCLUSIONS 183

CHAPTER 7 CONCLUSIONS AND FUTURE DIRECTIONS 184

7.0 INTRODUCTION 185

7.1 MISALIGNMENT FEATURES IN THE HUMAN EYES 185

7.1.1 Angle alpha *189*

7.1.2 Pupil centration *189*

7.1.3 Crystalline lens tilt and decentration *190*

7.2 WAVEFRONT ABERRATION MEASUREMENT 191

7.2.1 A semi-Maxwellian view wavefront aberration measurement system *191*

7.2.2 Measuring wavefront aberration along the CSCR *192*

7.3 CORRELATION BETWEEN THE MISALIGNMENTS OF VARIOUS OPTICAL COMPONENTS OF THE EYE 193

APPENDIX I A PRELIMINARY MEASUREMENT OF ANGLE ALPHA 195

A1.1 INTRODUCTION 196

A1.2 APPARATUS AND METHODS 199

A1.3 RESULTS 203

A1.4 DISCUSSION 208

A1.6 CONCLUSIONS 211

APPENDIX II CALCULATION OF THE DISPLACEMENT OF PURKINJE IMAGES DUE TO LENS TILT AND DECENTRATION 213

APPENDIX III VERIFICAITON OF THE WAVEFRONT FIT PROGRAM 220

APPENDIX IV WAVEFRONT RECONSTRUCTION FROM RAY ABERRATION DATA TO A 6^{TH} ORDER TAYLOR POLYNOMIAL 224

APPENDIX V C PROGRAMS WRITTEN FOR THE OPERATION OF THE 2-DIMENSIONAL SEMI-MAXWELLIAN VIEW WAVEFRONT ABERRATION MEASUREMENT SYSTEM 226

APPENDIX VI ALIGNMENT OF THE WAVEFRONT ABERRATION MEASUREMENT SYSTEM 245

A6.1 BASIC PREPARATION 246

A6.2 ALIGNMENT OF THE MAXWELLIAN VIEW CHANNEL 246

A6.3 ALIGNMENT OF THE NORMAL VIEW CHANNEL 247

A6.4 ALIGNMENT OF THE CAMERA MOUNT 248

A6.5 ALIGNMENT OF THE CAMERA BEAM SPLITTER (BS2) 249

A6.6 ALIGNMENT OF THE CAMERA BEAM SPLITTER (BS2) AND THE CAMERA MOUNT. 249

APPENDIX VII A MODEL EYE 252

APPENIDX VIII ERRORS INDUCED BY LENS ABERRATIONS-EXAMINED BY RAYTRACING THROUGH THE MAXWELLIAN VIEW LENS 256

A8.1 CALCULATION OF THE ABERRATION INDUCED BY THE ACHROMATIC LENS WHEN THE MAXWELLIAN VIEW PINHOLE IS OFF-AXIS(AT 5MM). 257

A8.2 CALCULATION OF THE ABERRATED RAYS THAT PASS BY EACH OF THE FOUR MAXWELLIAN VIEW TARGET TIPS. 259

APPENDIX VIIII DIAGRAMS OF THE LEFT EYES OF THE 21 SUBJECTS MEASURED AS DESCRIBED IN CHAPTER 4 262

APPENDIX X WAVEFRONT RECONSTRUCTION FROM RAY ABERRATION DATA TO A 6^{TH} ORDER ZERNIKE POLYNOMIAL 268

APPENDIX XI THE USE OF A TELECENTRIC STOP 271

APPENDIX XII QBASIC™ PROGRAM FOR THE CALCULATION OF MEAN SQUARED WAVEFRONT ABERRATIONS 273

BIBLIOGRAPHY 281

List of Tables

Table 1.1 Parameters Of The G-E Schematic Eye 3

Table 3.1 The 6th Order Taylor Polynomial And The R-Squared Values Of The Wavefront Aberrations Reconstruction 81

Table 3.2 The Standard Deviations And Maximums Of The Alignment Errors Of Subject AR For Three Pupil Sampling Locations 85

Table 3.3 Sensitivity Of The Measured Wavefront Aberration Change Due To Small Sampling Location Change 87

Table 4.1 New Coefficients Of All The Terms Of The 6th Order Taylor Polynomials After Shifting The Reference Axis From (0,0) To (ΔX, ΔY) 103-104

Table 4.2 The 95% Confidence Intervals Of All The Coefficients Of The Reconstructed Taylor Polynomials To The 4th Order 132

Table 5.1 Horizontal (H) And Vertical (V) Components Of Lens Tilt And Decentration Of The Left Eyes Of 21 Subjects Along The Aligned PI & PIV And The CSCR, Respectively 145

Table 5.2 Horizontal (H) And Vertical (V) Components Of Pupil Decentration Of 21 Subjects Measured Along The Aligned PI And PIV And The CSCR, Respectively 148

Table 5.3 Horizontal (H) And Vertical (V) Components Of Angle Alpha Values Of The Left Eyes Of 21 Subjects Measured By Aligning PI & PIV And PI &PIII, Respectively 150

Table 5.4 The Horizontal (H) And Vertical (V) Components Of Lens Tilt And Decentration With Respect To The Line Of Sight 154

Table 5.5 Horizontal (H) And Vertical (V) Components Of Lens Tilt And Decentration Of 21 Subjects From The Pupillary 157

Table 5.6 Horizontal (H) And Vertical (V) Components Of Lens Tilt And Decentration Of Subjects AR And JH Measured Two Times, Respectively 159

Table 5.7 The Differences Of Pupil Size And Pupil Decentrations Measured Two Different Times Of Subject JH 161

Table 5.8 Horizontal (H) And Vertical (V) Components Of Angle Alpha Values Of The Left Eyes Of Subjects AR And JH Measured Two Times By Aligning PI & PIV And PI &PIII, Respectively 162

Table 5.9 Angle Alphas Of The Left Eyes Of Subjects AR And DC Measured By Aligning PI And PIV Of Two Different Measurements 166

Table 5.10 Misalignment Of Ocular Components In An Average Emmetropic Human Eye Based On The 21 Eyes Measured With Respect To The Aligned PI And PIV 168

Table 5.11 The Average Lens Tilt And Decentration With Respect The Line Of Sight And The Pupillary Axis, Respectively 170

Table 6.1 Mean Squared Wavefront Aberrations Of The Left Eyes Of 21 Subjects And Their Symmetrical And Asymmetrical Components 174

Table 6.2 Mean Squared Wavefront Aberrations Of The Left Eyes Of 21 Subjects And Their Symmetrical And Asymmetrical Components Calculated Assuming The Pupil Is Centered At CSCR 177

Table A1.1 Measured Angle Alpha Values Of 11 Subjects 205

Table A1.2 Results Of Repeatability Measurements 207

Table A7.1. Parameter of the model eye used in this thesis 253

Table A7.2 Parameters of the model eye for the calculation of lens tilt and calculation 255

List of Illustrations

Fig.1.1 The Relaxed G-E Eye Model And Parameters. 3

Fig.1.2 Various Reference Axes In The Revised G-E Eye Model. 5

Fig.1.3 Situation When Purkinje Images I, III And IV Could Not Be All Aligned At The Same Time...10

Fig.1.4 A Diffraction Limited Optical System.. 14

Fig.1.5 3-Dimensional Plots Of Wavefront Aberrations.. 16

Fig.1.6 The Relationship Between The Transverse Ray Aberration And The Wavefront Aberration. 20

Fig.1.7 Principle Of Scheiner's Disc 22

Fig. 2.1 Definition Of Equivalent Mirror..... 30

Fig. 2.2 Coordinates System Setup For Derivation With The Gullstrand-Emsley Eye Model..... 32

Fig. 2.3 Calculation Of The Displacement Of PIII From Purkinje Image I.. 35

Fig. 2.4 Comparison Of The Purkinje Image Displacements Calculated With The Derived Equations And That Calculated With CODE V™ 38-39

Fig. 2.5 Calculation Of The Angle (T_{13}) Between The Optical Axis Of The Cornea And The Line Along Which The Object And The PI And PIII Can Be Aligned..... 41

Fig. 3.1 Principle Of The Maxwellian View System. 46

Fig. 3.2 Transverse Ray Aberration Expressed In The Object Space.. 48

Fig. 3.3 The Contour Plot And 3-D Surface Plot Of Simulated Wavefront Aberration Both Primary Spherical Aberration And Comatic Aberrations.. 57

Fig. 3.4 The Contour Plot And 3-D Surface Plots Of The Recovered Wavefront. 58

Fig. 3.5 3-Dimeniosnal Residual Plots Of Wavefront Aberration Reconstruction With Simulated Data..59

Fig. 3.6 The Contour Plot And 3-D Surface Plots Of The Recovered Wavefront With Noise..... 61

Fig. 3.7 3-Dimeniosnal Residual Plot Of Simulated Wavefront Aberration Reconstruction With Simulated Measurement Noise..... 62

Fig. 3.8 Two Dimensional Maxwellian View Wavefront Aberration Measurement System 66

Fig. 3.9 Target Configuration..... 67

Fig. 3.10 Effect Of The Maxwellian View Lens Aberration On Ocular Aberration Measurement..... 71-72

Fig. 3.11 Pupil Sampling Locations of A 6 mm Diameter Pupil.....74

Fig. 3.12 Diagrams From The Measured Ray Aberration Data Or The Target Misalignments In Object Space. 77

Fig. 3.13 Contour Plots And 3-Dimensional Plots Of Wavefront Aberrations Measured. 78-80

Fig. 3.14 Ray Aberrations Data Of AR's Left Eye Measured Three Times.....83

Fig. 3.15 Ray Aberrations Of Three Sampling Locations Of Subject AR's Left Eye.....86

Fig. 3.16 Pupil Centration Errors Of Subject LO During The Aberration Measurement. 88

Fig. 3.17 Wavefront Difference Reconstructed From The Difference Of Ray Aberrations Data Of AR's First And Second Measurements.. 90

Fig. 3.18 Wavefront Difference Reconstructed From The Difference Of Ray Aberrations Data Of AR's Second And Third Measurements.....90

Fig. 3.19 Wavefront Difference Reconstructed From The Difference Of Ray Aberrations Data Of Two Measurements Of AG.....91

Fig. 3.20 Taylor Coefficients Of 4 Subjects Measured Compared To That Of 55 Eyes Measured With The Howland And Howland Method. 93

Fig. 4.1 Definition Of The Coaxially Sighted Corneal Reflex. 98

Fig. 4.2 Picture Of The Pupil Saved During The Measurement Of The Left Eye Of Subject JH.....107

Fig. 4.3 The Combined Spot Diagram Of 21 Eyes Measured 108

Fig. 4.4 Contour Plots And 3-Dimensional Plots Of Wavefront Aberrations Measured Of The Left Eyes Of The 21 Emmetropic Subjects 110-118

Fig. 4.5 Taylor Coefficients Distribution Of The Left Eyes Of 21 Subjects Measured.....119

Fig. 4.6 Ray Aberration Data Of Subject JH's Left Eye From 3 Measurements. 121

Fig. 4.7 Difference Of 6^{th} And 8^{th} Order Fits Compared To Difference Of Two Measurements Of Subject JH. 123

Fig. 4.8 Ray Aberration Data Of JHL2econstructed To The 6th Order Taylor Polynomial.....125

Fig. 4.9 Ray Aberration Data Of JHL2 Reconstructed To The Zernike Polynomial To The 6^{th} Order.. ..125

Fig. 4.10 Raw Ray Aberration Data Plot Against Sampling Locations Of Subject LR's Left Eye. 126

Fig. 4.11 Decentration Of The Geometrical Center Of The Pupil From The CSCR. 128

Fig. 4.12 Wavefront Aberration Of Subject AG Using The Geometrical Center Of The Pupil As The Reference After Converted From Wavefront Aberration Measured Using The CSCR As The Reference 129

Fig. 4.13 Wavefront Aberration (Aberration Only) Of Subject DC Using The Geometrical Center Of The Pupil As The Reference After Converted From Wavefront Aberration Measured Using The CSCR As The Reference. 130

Fig.4.14 Wavefront Aberration To The 6th Order Taylor Polynomial Reconstructed From The Averaged Ray Aberration Data Of The Left Eyes Of The 20 Subjects Measured. 130

Fig. 4.15 Wavefront Aberration To The 4th Order Taylor Polynomial Reconstructed From The Averaged Ray Aberration Data Of The Left Eyes Of The 20 Subjects Measured 131

Fig. 4.16 Wavefront Aberration (6th Order Taylor Polynomials) Using The Geometrical Center Of The Pupil As The Reference Which Was Derived From Wavefront Aberration Measured Using The CSCR As The Reference. 133

Fig. 5.1 A Purkinje Image Photographic System For Measuring Ocular Component Misalignments 137

Fig. 5.2 Flow Chart Illustrating Target Adjustment to Achieve Purkinje Image Alignment..... 141

Fig. 5.3 A Picture Of The Pupil With Purkinje Images Along The CSCR Of The Left Eye Of Subject AG..... 142

Fig. 5.4 A Picture Of The Left Eye Of Subject AG With Aligned PI And PIV 143

Fig. 5.5 A Picture The Left Eye Of Subject AG With Aligned PI And PIII 144

Fig. 5.6 Lens Tilt Of 21 Subjects From PI & PIV And The CSCR, Respectively 146

Fig. 5.7 Lens Decentration Of 21 Subjects From The Aligned PI&PIV And The CSCR, Respectively..... 147

Fig. 5.8 Pupil Decentration Of 21 Subjects Measured With Respect To The Aligned PI&PIV And The CSCR, Respectively 149

Fig. 5.9 Angle Alphas Of The Left Eyes Of 21 Subjects Measured By Aligning PI & PIV And By Aligning PI &PIII, Respectively 151

Fig. 5.10 Relationship Between Lens Decentration With Respect To The Aligned PI&PIV And Lens Decentration With Respect To The Line Of Sight..... 153

Fig. 5.11 Lens Tilts With Respect To The Line Of Sight Of The 21 Eyes Measured. 155

Fig. 5.12 Lens Decentration With Respect To The Line Of Sight Of The 21 Eyes Measured..... 155

Fig. 5.13 Relationship Between Lens Decentration With Respect To The Pupillary Axis.. 156

Fig. 5.14 Lens Tilts With Respect To The Pupillary Axis Of The 21 Eyes Measured. 158

Fig. 5.15 Lens Decentrations With Respect To The Pupillary Axis Of The 21 Eyes Measured. 158

Fig. 5.16 Misalignment Of Ocular Components In An Average Human Eye In The Horizontal Meridian..... 169

Fig. 5.17 Misalignment Of Ocular Components In An Average Human Eye In The Vertical Meridian..... 170

Fig. 6.1 Correlation Between The Mean Squared Asymmetrical Components Of Wavefront Aberrations And The Angle Alphas Measured By Aligning PI And PIV 175

Fig. 6.2 Correlation Between The Mean Squared Asymmetrical Components Of Wavefront Aberrations And The Angle Alphas Measured By Aligning PI And PIV 178

Fig. 6.3 Correlation Between The Mean Squared Asymmetrical Components Of Wavefront Aberrations And The Angle Alphas Measured By Aligning PI And PIV 179

Fig. 6.4 Correlation Of The Asymmetrical Component Of The Mean Squared Wavefront Aberration Of The Left Eyes Of 21 Subjects And Lens Tilt With Respect To The Line Of Sight..... 180

Fig. 6.5 Correlation Of The Asymmetrical Component Of The Mean Squared Wavefront Aberration Of The Left Eyes Of 21 Subjects And Lens Decentration With Respect To The Line Of Sight..... 181

Fig. 6.6 Correlation Of The Asymmetrical Component Of The Mean Squared Wavefront Aberrations Of The Left Eyes Of The 21 Subjects And Pupil Decentration With Respect To The Approximate Optical Axis Of The Eye. 182

Fig. 7.1a-c Modified G-E Eye Model..... 185-188

Fig. A1.1 A Diagram Of The Setup For Measuring The Horizontal Component Of Angle Alpha. 200

Fig. A1.2 Horizontally Aligned Purkinje Images Of The Left Eyes Of Subject LZ. 203

Fig. A1.3 Vertically Aligned Purkinje Images Of The Left Eyes Of Subject LZ. 204

Fig. A1.4 Scatter Plot Of The Measured Angle Alphas Of 11 Subjects. 206

Fig. A1.5 The Correlationship Between The Angle Alpha Values Of The Right Eye And The Left Eye Of The 11 Subjects Measured 207

Fig. A1.6 A Situation When PI, PIII And PIV Could Not Be Aligned At The Same Time 210

Fig. A1.7 A Situation When PI, PIII And PIV Could Not Be Aligned At The Same Time 211

Fig. A5.1 General Structure Of The Program Used In This Thesis 227

Fig. A5.2 Flow Chart Of Aberration Measurement 244

Fig. A6.1 A Diagram Of Beam Shift Through The Beam Splitter 250

Fig. A7.1 The model eye and its dimensions 254

Fig. A9.1 Measured Diagrams Of The Left Eyes Of 21 Subjects 263-267

Fig. A11.1 A Telecentric Stop In A Camera Lens 271

Publications Related to the Thesis

1. Reducing Aberration at the Fovea by Defocus, Ophthalmic & Visual Optics/Noninvasive Assessment of the Visual System. 1993 Technical Digest Series Volumes. Feb. 1993, p.164-167.

2. Psychophysical Measurement of the Optical Quality of Varifocal Contact Lenses, Ophthalmic & Visual Optics/Noninvasive Assessment of the Visual System. 1993 Technical Digest Series Volumes. Feb. 1993, p. 12-15.

3. The Measurement of Angle Alpha. (To be submitted)

4. Theoretical Models for Measuring the Tilt and Decentration of the Crystalline Lens in Vivo. (To be submitted)

5. A semi-Maxwellian view wavefront aberration measurement system. (In preparation)

6. Measurement of wavefront aberration of the human eye along the coaxially sighted corneal reflex. (In Preparation)

7. Measurement of the misalignment of the optical components of the human eye in vivo. (In preparation).

8. Investigation of the correlation of the misalignments of the optical components of the human eye and asymmetrical ocular monochromatic aberrations.(In preparation)

9. Choice of a reference axis in the human eye of both theoretical and clinical practical significance.(In preparation)

Declaration

This dissertation is an account of work mainly carried out at the School of Optometry, University of Waterloo, between January 1992 and November 1995. Between September 1996 and present, I have been employed by the Macbeth Division of Kollmorgen Instruments in New York and continued the analysis and writing of the dissertation on a part-time basis.

I have received substantially amount of technical support from Mr. Robin Jones of the machine shop; some editorial comments and technical critiques from Dr. Campbell; many inspiring discussions with Dr. Austin Roorda, then fellow graduate student; and lately many useful suggestions from Dr. Vengu Lakshminarayanan. Dr. Hovis greatly helped the final experiments by screening most of my subjects for clinical safety reason.

I am the main designer and builder of all the apparatus. I performed all the experimental measurements. I am the author of all the programs attached in this dissertation. All data analyses are my own work and I am the only author of all the chapters in this dissertation.

I am the sole discoverer of all the scientific findings presented in this dissertation and related publications.

Chapter 1

General Introduction

Over a century ago, Helmholtz as quoted by Charman (1991), pointed out, '*The eye has every possible defect that can be found in an optical instrument and even some which are peculiar to itself; but they are so counteracted that the inexactness of the image which results from their presence very little exceeds, under ordinary conditions of illumination, the limits which are set to the delicacy of sensation by the dimensions of the real cones.*'

Today, this summary of the optical system of the human eye is as valid as when it was first drawn. Since then much work has been done on the source and nature of these defects. However, there are still gaps in our understanding.

These defects of the eye can be described in two ways. One is structural. The other is functional. The structural description compares the optical construction of the eye to a well designed optical instrument in terms of the surfaces, media and alignment of various ocular components. A functional description investigates the impact of these defects on retinal image quality. One can derive functional defects from structural defects.

This thesis will investigate certain aspects of the structural defects of the eye. These investigations include the measurement of angle alpha, the misalignment of the crystalline lens, and the misalignment of the pupil. The total wavefront aberration of the eye will also be measured. The possible correlation between the misalignment of the eye and the asymmetric and asymmetric components of the wavefront aberration of the eye will be investigated.

1.1 Eye model and definitions

In the study of the misalignment of the crystalline lens, the relaxed Gullstrand-Emsley (G-E) schematic eye will serve as the basis to derive the amount of lens tilt and decentration from the misalignment of Purkinje images. Accommodation will not be

considered. The G-E eye model is shown in Fig. 1.1 and its parameters are tabulated in Table 1.1.

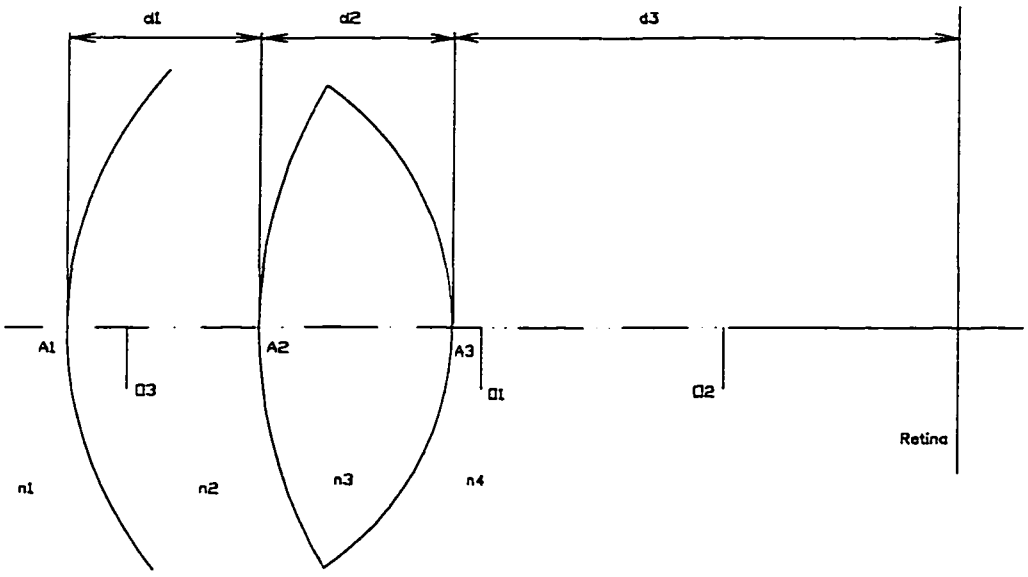


Fig 1.1 The relaxed G-E eye model and parameters.

Table 1.1 Parameters of the G-E schematic eye.

Parameter	Value
n1	1
n2	1.3333
n3	1.4160
n4	1.3333
d1	3.6 mm
d2	3.6 mm
d3	16.69 mm
r1(A1O1)	7.8 mm
r2(A2O2)	10.0 mm
r3(A3O3)	-6.0 mm

The G-E eye model is clearly inadequate to describe the misalignment of the eye system. First, there is no pupil defined in the G-E model. Pupil decentration is an

important factor both in the study of ocular optical components misalignments and in the study of wavefront aberration of the eye. A pupil will therefore be added in front of the crystalline lens in the eye model in this thesis.

Second, the G-E eye model is an aligned system with a defined optical axis. In the real human eye, there may not exist a true optical axis. Even when an approximate optical axis can be defined (Tscherning, 1924), the fovea is generally not coaxial with such an optical axis. As a consequence, the visual axis will not coincide with the approximate optical axis of the eye. This thesis will study the misalignment characteristics of the crystalline lens and the pupil.

In this thesis, the total wavefront aberration will be studied. The total wavefront aberration can result from surface defects, misalignment of the ocular optical system and irregular refractive index distribution. The G-E eye model will only be used for misalignment study. This thesis only deals with the possible contribution of the misalignment of ocular optical components to ocular monochromatic aberrations.

Given the chaotic situation in the definitions of various reference axes in the eye (Martin, 1942), there is a need to define these axes and related parameters that will be used in this thesis.

1) Optical axis: the axis along which all the Purkinje images including Purkinje image I (PI), Purkinje image II (PII), Purkinje image III (PIII), and Purkinje image IV (PIV) can be aligned. For practical reasons and to conform with the G-E eye model, PII will be ignored in this thesis.
2) Approximate optical axis: the axis along which all the Purkinje images can be roughly aligned. It can be defined by roughly aligning all Purkinje images, by aligning only PI and PIV, or by aligning only PI and PIII.
3) Visual axis: the axis that goes through both the fixation point and the first nodal point.

4) Line of sight: the line joining the fixation point and the geometrical center of the pupil.

5) Pupillary axis: the axis going through the center of the pupil and perpendicular to the anterior surface of the cornea.

6) Coaxially sighted corneal reflex axis (CSCR): the axis goes through the fixation point and the center of curvature of the front surface of the cornea (Pande and Hillman, 1993).

7) PI and PIV aligned axis(P1P4) : the axis along which PI and PIV can be aligned. It can be considered as the approximate optical axis of the eye.

8) PI and PIII aligned axis (P1P3): the axis along which PI and PIII can be aligned. It can be considered as the approximate optical axis of the eye.

9) Angle alpha: the angle between the visual axis and the optical axis or the approximate optical axis of the eye.

These axes are shown in Fig. 1.2.

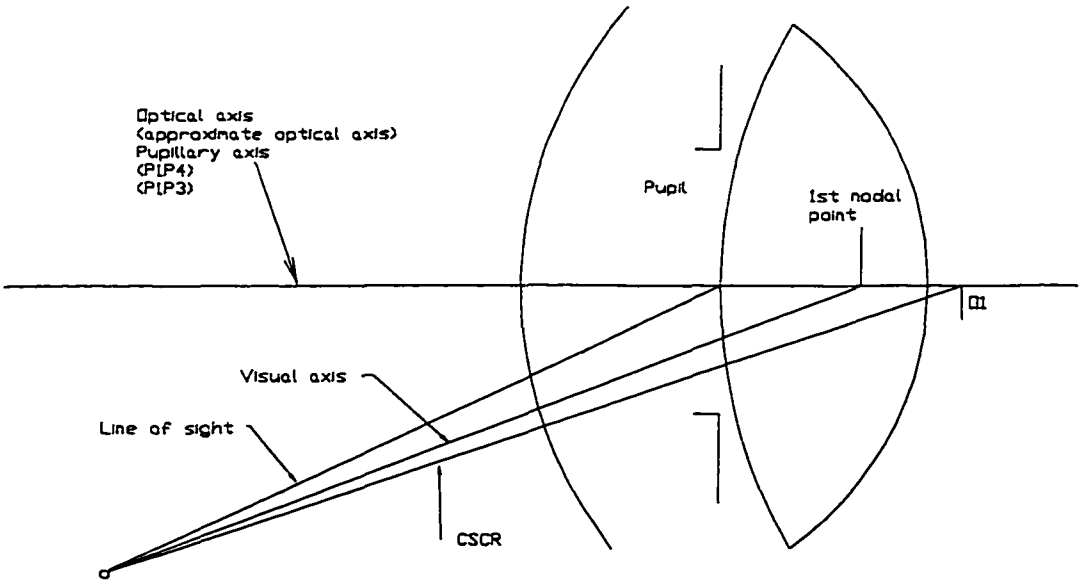


Fig 1.2 Various reference axes in the revised G-E eye model.

1.2 Review of the characteristics of defects of the typical human eye

The first optical component of the human eye is the cornea which consists of several structural layers. An average cornea is an aspherical surface with a center thinner than the periphery (Martola and Baum, 1968; Hitzenberger et. al. 1994). The average shape of the cornea is ellipsoidal with great variations between individuals (Keily et. al. 1982; Guillon, 1982; Howland et. al. 1994). Because of the large refractive index change from air to the cornea, the cornea contributes about two thirds of the total power of the eye (Charman, 1991). On top of the cornea, there always is a thin layer of tears which is about 5 microns thick (Charman, 1991). Because the refractive index change from the tear film to the cornea is small and the tear film is thin, it is not considered in the modeling.

Behind the cornea is the anterior chamber which contains aqueous humour. The aqueous humour is a reasonably uniform optical medium. So is the vitreous body which fills the space between the crystalline lens and the retina.

The iris defines the posterior border of the anterior chamber. This structure forms the optical stop of the eye--the pupil. The pupil controls the retinal illuminance and depth of focus by varying its size. The pupil plays an important role in the overall optical performance of the eye (Charman et. al. 1978; van Meeteren and Dunnewold, 1983; Walsh, 1988; Wilson et. al. 1992; Marcos et. al. 1994).

Immediately behind the iris is the crystalline lens of the eye. The lens has a layered structure and has a gradient-index property (Nakao et. al. 1969). The overlap of lens fiber cells also produces lens sutures which are seemingly harmful to the optical performance of the lens (Kuszak et. al. 1984; Kuszak et. al. 1991). The lens is kept in the lens capsule which is suspended by the zonular fibers controlled by the ciliary muscle. The purpose of the lens is to vary the focusing power of the eye. This is accomplished by the changing tension of the zonule due to the contraction and relaxation of the ciliary muscle. Consequently, the lens may have various aspherical shapes in different states of accommodation (Parker, 1972; Brown 1973). Its power contribution to the total power of the eye is less than that of the cornea and presumably its aberration contribution to the

overall aberration of the eye would also be less in scale, especially in the unaccommodated eye.

The retina is the image receiving plane of the eye. It is curved to be roughly concentric about the center of the pupil. This feature corrects for field curvature (Charman, 1983). The most important position on the retina is the fovea. The fovea has the highest density of cone photoreceptors which provide the highest resolution of the visual system. One unsolved issue about the fovea and the general structure of the eye is the fact that the fovea does not lie on the optical axis of the eye as might be expected. Rather, it is located about 1.5 mm to the temporal side to the symmetrical or approximately symmetrical axis of the optical axis of the eye (Emsley, 1952). This displacement of the fovea results in a visual axis which forms an angle with the approximate optical axis of the eye--the angle alpha (Tscherning, 1924; Martin, 1942; Emsley, 1952; Dunne and Barnes, 1989; Effert et. al. 1992).

1.2.1 Defects of the optical components of the eye

Not surprisingly, each component of a normal human eye has its optical defects from a modern optical engineering perspective. Due to its large contribution to the total refractive power of the eye, the cornea, particularly the front surface, presumably plays a more effective role in the overall optical performance of the eye. Corneal topographic measurements can be made to examine the front surface of the cornea. The most fundamental and widely adopted principle lies in the fact that the distortion of a reflective image bears the topographic information of the reflecting surface. A number of manufacturers have built videokeratographic systems based on this principle. Other principles include interferometry and rasterstereography. Interferometry utilizes the wave property of light to generate interference fringes from the light wave reflected by the cornea and the light reflected by a reference surface. Rasterstereography measures corneal topographic data by projecting a calibrated grid image onto a corneal film stained with fluorescein (Warnicki et. al. 1992).

The optical defects of the front surface of the cornea in terms of asymmetry can be seen from typical cornea topographic maps. The apex of the cornea is usually skewed

away from the center of the cornea in a seemingly random direction and a rotationally symmetrical cornea becomes something unusual (Mandel and Helen, 1969; Tomlinson and Schwartz, 1979; Edmund, 1987a; Dingeldein and Klyce, 1989). The normal topographical map of the cornea usually shows a large amount of irregularities. Also, the tear film on the cornea varies considerably at the wavelength level during the blink period as a result of evaporation (Guillon, 1982; Josephson, 1983).

The irregularity of the cornea will jeopardize the definition of its apex (Mandell and Helen, 1969; Tomlinson and Schwartz, 1979; Edmund, 1987) and its optical axis which needs to be used to evaluate the total alignment of the ocular optical system.

The back surface of the cornea has been shown to have a toric surface (Royston et. al. 1990). Due to the small refractive index change from the cornea to the aqueous, the back surface of the cornea plays a less significant role in eye power (contributes about –6 diopters to the total power of the eye) and is therefore sometimes ignored in eye modeling. Such kind of simplification is usually also due to another important reason-- the practical difficulty in obtaining the proper information for the evaluation of the optics of the back surface of the cornea.

Strictly speaking, the pupil has a rough edge and is not always perfectly circular. For some people, the eyelid may clearly cut the upper portion of the pupil off and the eye lash could function analogous to an optical grating. Although interesting, these factors are often ignored due to their negligible effect on the optical performance of the eye. The more important issues are pupil size and pupil centration (Charman et. al. 1978a; van Meeteren and Dunnewold, 1983; Walsh, 1988; Wilson et. al. 1992; Marcos et. al. 1994). These parameters vary with illumination intensity, accommodation, age, drugs and emotion (Janisse, 1973).

Every crystalline lens surface and shell has its asphericity and inherent irregularity (Parker, 1972; Brown, 1973). The fiber layers forming the lens have been known to have a strong scattering effect which will downgrade the performance of the eye (Simpson, 1953).

The lens sutures can also be regarded as another defect of the crystalline lens because they tend to produce stronger light scattering and produce irregular aberrations (Kuszak et. al. 1984; Kuszak et. al. 1991).

1.2.2 Misalignment of the optical components of the eye

1) Lens tilt and decentration

As shown in Fig.1.3, PI, PIII and PIV cannot usually be all aligned with the source at the same time as reported by Tscherning (1924). This situation indicates that the crystalline lens is misaligned with the cornea and there does not exist a true optical axis of the eye. This phenomenon and the existence of angle alpha were first reported by Tscherning (1924). Tscherning also reported a lens tilt of about 5°, but he considered the lens tilt with respect to the line of sight. Therefore, his value of lens tilt was directly related to the value of angle alpha. Given the two-element eye model used, cornea and lens misalignment can be best expressed with respect to the cornea.

To the best of my knowledge, no systematic measurement of lens tilt and decentration in the normal human eye *in vivo* has been reported. There are reports on various methods in the study of intraocular implant (IOL) in aphakic eyes. Lakshminarayanan et. al. (1986) measured the IOL implants tilt in cadaver eyes by anatomic method. Jacobs et. al. (1983) measured IOL tilt with high speed cinematography. Philips et. al. (1988) developed a method to measure the intraocular lens decentration and tilt in pseudophakic eyes *in vivo* which can be

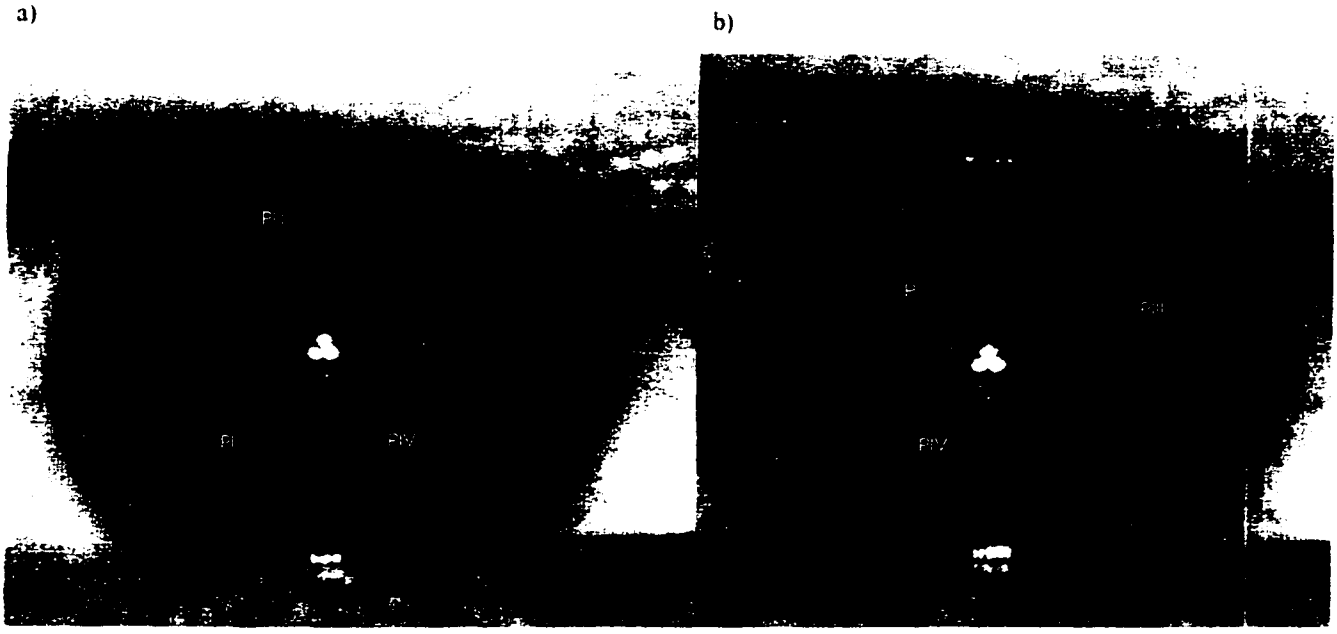


Fig. 1.3 A situation when Purkinje images I, III and IV could not be all aligned at the same time. The light source consisted of three small light bulbs mounted in the shape of an erect triangle. The light source was set coaxial with the video camera system. More details about the system can be found in Appendix I. Purkinje images are triangular shaped bright points. As shown in the photographs, the brightest and erect triangle is PI; the inverted and sharp small triangle was PIV; the erect but blurry triangle was PIII. In (a), PI and PIII are aligned horizontally while PIV is misaligned with them; in (b), PI and PIV are aligned horizontally while PIII is misaligned with them.

modified to measure lens tilt and decentration of the crystalline lens in the real human eye. The front surface of the IOL provides a superb specular reflection. Therefore it is much easier to observe all three Purkinje images. On the other hand, PIII is extremely difficult to view in phakic eyes.

2) *Pupil decentration*

The pupil may not be centered around either the optical axis or the approximate optical axis of eye. Furthermore, the decentration of the pupil will vary with the variation of pupil size (Janisse, 1973; Charman, et. al. 1978; van Meeteren and Dunnewold, 1983; Walsh, 1988; Wilson et. al. 1992; Marcos et. al. 1994). In certain cases, decentration could actually be helpful in reducing the off-axis aberration of the eye at the fovea given the existence of angle alpha (Bing and Campbell, 1994; Bullock et. al. 1995).

One of the problems in investigating pupil decentration the choice of a proper reference axis. Walsh (1988) chose the opening edge of the iris while Wilson et. al. (1992) chose the achromatic axis as the reference. Studies of the transverse chromatic aberration (TCA) of the eye have devoted much effort in trying to define the centration of the pupil with respect to the achromatic axis (Simonet and Campbell, 1990; Thibos et. al. 1990). Because the amount of TCA is directly related to the decentration of pupil with respect to the achromatic axis, pupil centration is well defined in these studies. Earlier results showed that the achromatic axis was generally in the nasal side of the geometrical center of the pupil (Simonet and Campbell, 1990; Thibos et. al. 1990). It would be of interest to investigate how the pupil is centered with the optical axis or the approximate optical axis of the eye.

Another compounding factor is the Stiles-Crawford effect of the first kind. The Stiles-Crawford effect apodizes the pupil of the eye. The peak of the Stiles-Crawford function is usually not at the geometrical center of the pupil (Enoch and Lakshminarayanan , 1991).

3) Angle alpha

Theoretically, the existence of angle alpha will affect the optical performance of the eye at the fovea (Bing and Campbell, 1994; Walsh and Charman, 1992). There have also been reports proposing that angle alpha may help the visual axis by avoiding the lens sutures which are harmful to the imaging performance of the lens (Kuszak et. al. 1991;

Bullock et. al. 1995). On the other hand, the measurement of angle alpha has only recently been repeated with values that are smaller than the values that quoted of Tscherning's measurement in ocular optics textbooks (Effert et. al. 1992). My investigation in Appendix I gives results more consistent with the recent results. Technical details of the measurement are elaborated in Appendix I.

One of the problems in measuring angle alpha is the location of the optical axis of the eye. If a true optical axis does not exist in the tested eye, an approximation would be necessary. Tscherning used an axis along which he could roughly align all three Purkinje images while Effert et. al. (1992) used only PI and PIV largely due to the difficulty of observing PIII. Is it the difference between the two experiments due to the difference in definition? Aligning Purkinje images I and IV is much easier and therefore potentially more useful in clinical applications (Effert et. al. 1992). It would therefore be of interest to know the inherent difference between the definitions.

4) Visual axis

Defining angle alpha also involves the theoretical dilemma of defining the visual axis. Because it is difficult to experimentally access the classically defined visual axis. Bennett and Rabbetts (1984) have defined the visual axis to be the line joining the fixation point and the geometrical center of the pupil. As stated in Section 2, this definition is flawed by the fact the effective center of the pupil may not be the geometrical center of the pupil because of the Stiles-Crawford apodization. However the error produced by using the effective geometric center of the pupil in calculating angle alpha can be shown to be negligible. In critical applications like modern refractive surgeries, the procedure would need to define an appropriate reference axis to work on (Uozato and Guyton, 1987; Pande and Hillman,1993; Colliac et. al. 1994). It is therefore important and necessary to review these definitions and verify the practical accessibility of these axes.

1.3 Optical functional defects of the human eye

The task of the optical system of the eyes of any creature is to image interested objects onto their photoreceptors with such a quality that will satisfy the need of the visual neural system. In the case of mankind, the image quality requirement of such an optical system is less than most modern man-made optical systems of similar use such as photographic cameras (usually of much larger optical apertures).

If the human eye is considered as an optical instrument, it suffers from diffraction, intraocular scattering, chromatic aberrations and monochromatic aberrations (Charman, 1983). When the pupil size is small (2-3 mm), diffraction is the main limiting factor. Intraocular scattering has been studied separately (Charman, 1991). Chromatic aberrations have been well understood due to its relative small inter-subject variation (Wald and Griffin, 1947; Bedford and Wyszecki, 1957; Charman and Jenning, 1976; Howarth and Bradley, 1986; Simonet and Campbell, 1990; Thibos et. al. 1990; Thibos et. al. 1991; Bradley, 1992). This thesis specifically investigates the overall monochromatic wavefront aberration of the eye. The overall wavefront aberration of the eye can be expressed as Taylor or Zernike polynomials which can relate to traditional Seidel aberration terms such as spherical aberration, coma, astigmatism, field curvature and distortion.

1.3.1 The monochromatic ideal optical system and the standard description of monochromatic wavefront aberration

A point on an extended object radiates optical radiation in terms of uniform spherical wavefronts at the same speed in all directions in an isotropic homogeneous medium. An ideal optical system is a device that can converge all the wavefronts concentrically at another point in another isotropic homogeneous medium. For an extended object, the spatial relationship is invariant.

The above definition is only of theoretical significance. The practical ideal optical system is an optical system that can accomplish the above for all wavefronts that pass through it. A diffraction limited optical system for a point source is shown as in Fig. 1.4.

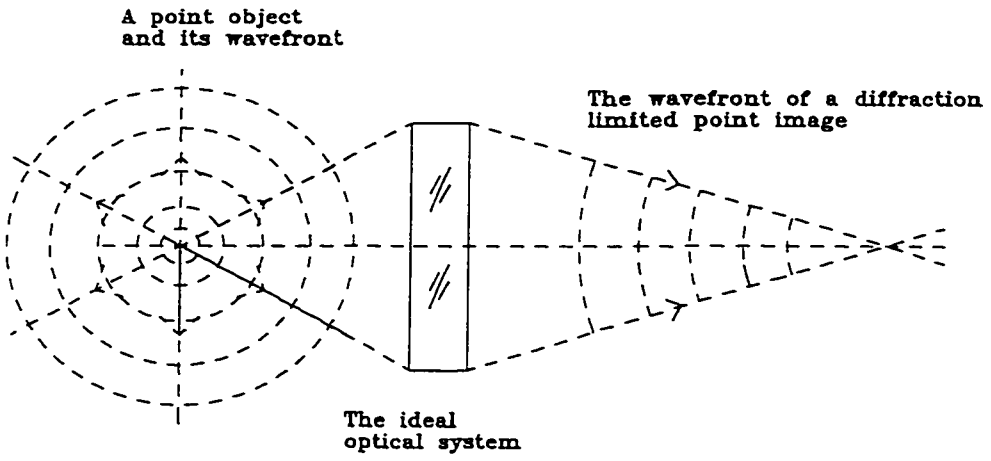


Fig. 1.4 A diffraction limited optical system. Perfect spherical wavefronts of the point object pass through the optical system and then converge to form a diffraction limited image.

In the real world, the optical system will first truncate the wavefront due to a limited aperture dimension. For an aberration-free system, the limiting aperture will produce diffraction limited image quality. Second, there will always be optical scattering in any realistic system. Third, there may exist optical aberration. In the case of the human eye, the final image quality may be a combination of diffraction effect, scattering and aberrations. The contribution of each factor to the final image quality depends on pupil size. In this thesis, only the monochromatic optical aberrations will considered.

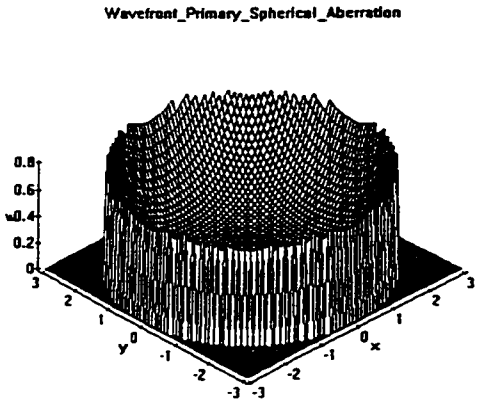
For an aberrated optical system, the concentric wavefront given in Fig. 1.4 will be distorted from a perfect spherical shape. The aberrated wavefront can be mathematically expressed and used to completely describe the aberration of the system. Once the wavefront aberration and the pupil size is known, the retinal image quality related to aberrations and diffraction can be deduced by calculating the point spread function.

1.3.2 The partition of total wavefront aberration into the symmetrical and asymmetrical components

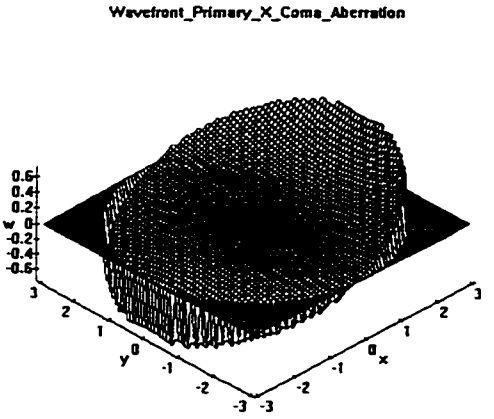
Be it ray aberration or wavefront aberration, the total amount of aberration can always be partitioned into two components: symmetrical and asymmetrical components. The symmetrical component will have a symmetrical blurring effect on the image and its effect can be reduced by choosing the proper imaging receiving plane. The asymmetrical component will have an asymmetrical blurring effect on the image and its effect cannot be reduced by varying the image receiving plane in the refracted ray bundle in the eye (Cui et. al. 1993). Fig. 1.5(a)-(c) shows the wavefront aberrations of a symmetrical wavefront aberration (primary spherical), an asymmetrical wavefront aberration (primary coma) and the combined aberration.

Experimentally measuring the wavefront aberration W(x,y) is therefore the key in evaluating the optical monochromatic performance of an optical system. There are a number of methods to determine the wavefront aberration of an optical system . In the case of human eye, these methods can be divided into two main categories -- objective methods and the subjective methods (Charman, 1991).

a) $w = 0.01(x^2 + y^2)^2$



b) $w = 0.03(x^2 + y^2)x - 0.02x$



c) $w = 0.03(x^2 + y^2)x - 0.02x + 0.01(x^2 + y^2)^2$

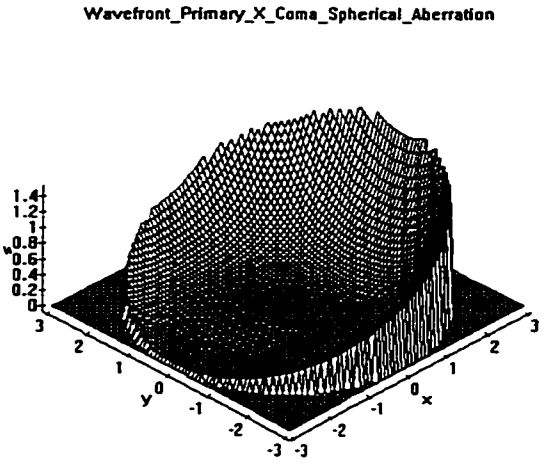


Fig. 1.5 3-dimensional plots of wavefront aberrations. a) symmetrical aberration (primary spherical); b) asymmetrical aberration (primary x coma); c) mixed aberration (primary x coma and primary spherical); x is in mm; y is in mm; w is in microns.

1.3.3 Objective methods of wavefront aberration measurement

To objectively measure wavefront aberrations, many ingenious methods have been developed. They include the ophthalmoscopic method (see Charman, 1991 for review); the Foucault knife edge method (Berny and Slansky, 1969); modification of

Howland's method (Walsh et. al. 1984; Atchison et. al. 1995); the Hartmann-Shack sensor method (Liang et. al. 1994).

The common advantages of these objective methods are that they do not involve a subject's response by their objective nature and it takes less time to collect necessary data. However, these objective methods all evaluate the retinal reflected image from outside of the eye, be it a point image or a certain pattern. Because light has to be delivered onto the retina of the eye and then imaged out of the eye, all non-invasive objective measurements have to deal with the contribution of both passes. If both passes contribute equally to the final result, the measurement is usually referred to as a double pass measurement. By this definition, the ophthalmoscopic method is the only true double pass measurement and it was proven to be flawed in theory (Roorda and Campbell, 1994; Artal et. al. 1995; Roorda, 1996). The rest of the objective methods all involve arranging the measurement system so that the contribution of one pass can be ignored.

Methods of ignoring the contribution of the first pass include the modified ophthalmoscopic method, the Foucault knife edge method and the Hartmann-Shack sensor method. Flaws of projection optics, multiple reflections and scattering of the retina by different distinct layers at different depths would all contribute to a less than ideal first pass image. The error induced by a less than ideal image after the single pass for the modified ophthalmoscopic method and the Foucault knife edge method will contribute to the final measured results. This type of error was reported to have a negligible effect on the Hartmann-Shack sensor method (Liang et. al. 1991). However, the Hartmann-Shack method is equivalent to imaging a projected bright spot on the retina to the lenslet focal plane through a pupil aperture array which is defined by the aperture of each lenslet

element. Aberrations within the lenslet aperture and the Stiles-Crawford effect will produce significant differences in the images formed by the lenslets. The variation of the shape and size of the images formed by the lenslets will contribute to calculation errors. The differences of images formed by lenslets between subjects are indeed strikingly obvious (Liang, 1991).

Methods of ignoring the contribution of the second pass are represented by various objective versions of Howland and Howland aberroscopes. The first pass produces an aberration distorted grid on the retina while the second pass images the grid image out of the eye. The distorted grid will be further distorted during the second pass. Error also occur in matching corresponding grid details on the original object grid and the blurred images.

Other common disadvantages of objective methods for measuring ocular aberration are the technical difficulties involved in system calibration and routine use. For most objective measurement systems, a large number of optical components are often used. The combined aberration effect may be significant to the measurement if not well-considered by reliable calibration procedures. Most objective measurement systems require great effort from the measurement operator to deal with weak light signals and laser speckles if laser is used.

1.3.4 Subjective methods of wavefront aberration measurement

On the other hand, the retina is a highly light sensitive detector array itself. The only problem is that the detected retinal image can only be interpreted by the visual neural system and expressed by the subject, which makes the measurement subjective in nature.

There have been a number of well thought out methods for the subjective evaluation of the ocular aberrations, starting as early as two centuries ago.

Subjective measurements that can be used to deduce wavefront aberrations can also be divided into two categories-- an overall evaluation method and a single ray tracing method. A typical example of the first category is a method involving a device named aberroscope (Tscherning, 1924; Howland and Howland, 1977). All the other measurements are transverse ray aberration measurements in principle. Regardless of the techniques, results of the most recent measurements have been presented in the form of wavefront aberrations based on the principle that wavefront aberration can be deduced from measured transverse ray aberration.

As shown in Fig. 1.6, the transverse ray aberration T $[\delta\xi(x,y),\delta\eta(x,y)]$ of a single ray entering at (x,y) in the pupil plane measured from the position of the principal ray on the retina can be related to *W(x,y)* which is the wavefront aberration, by

$$\delta\xi = -\frac{R}{n}\frac{\partial W}{\partial x} \tag{1.1}$$

and

$$\delta\eta = -\frac{R}{n}\frac{\partial W}{\partial y} \tag{1.2}$$

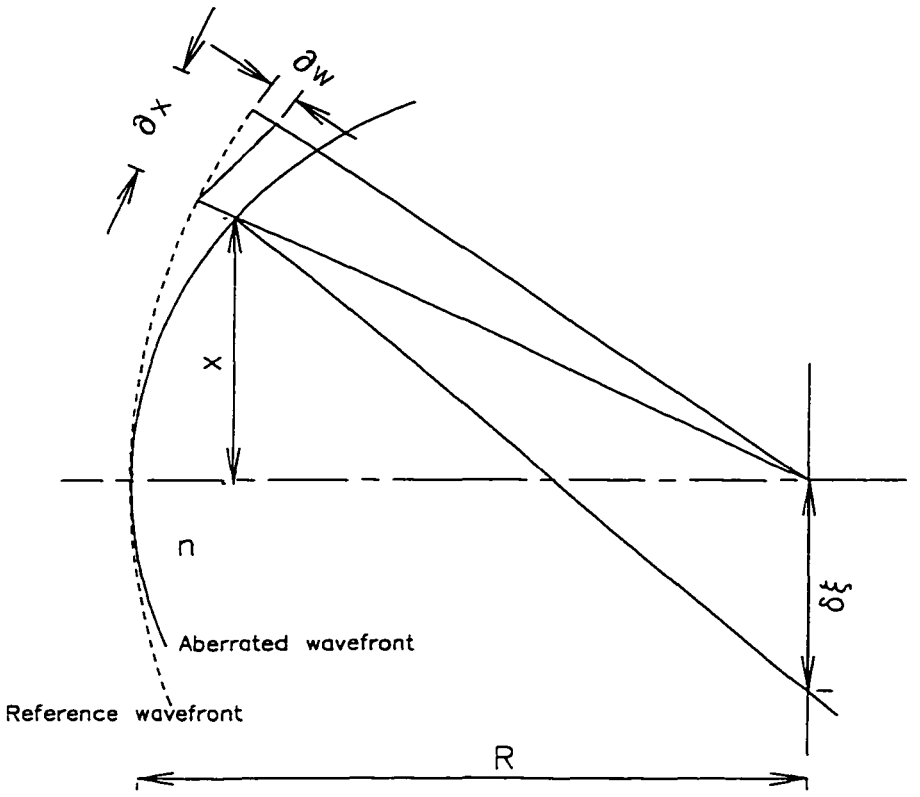


Fig. 1.6 The relationship between the transverse ray aberration and the wavefront aberration. n is the refractive index of the media; R is the secondary focal length of the eye.

For a specific pupil location, once $T\,[\delta\xi(x,y),\delta\eta(x,y)]$ is determined, $W(x,y)$ can be derived. In principle if W is a total differential, then,

$$dW = \frac{\partial W}{\partial x}dx + \frac{\partial W}{\partial y}dy \tag{1.3}$$

Therefore,

$$W(x,y) = \int [\frac{\partial W}{\partial x}dx + \frac{\partial W}{\partial y}dy] \tag{1.4}$$

The condition of the above integration is that $dW(x,y)$ has to be a total derivative (Welford, 1991). A straightforward method is to fit a wavefront polynomial function directly to the wavefront aberration derivatives, or transverse wavefront aberration (Cubalchini, 1979; Southwell, 1980).

Historically, the concept of transverse ray aberrations in the human eye originated from the concept of spherical aberration of the human eye. Spherical aberration was the first aberration discovered in the 13th century by Bacon (Freeman, 1990). Spherical aberration was the major concern until recently although Helmholtz pointed out about a century ago that the concept of spherical aberration does not exactly apply to the case of human due to the typical lack of symmetry (Charman, 1991).

Among the earlier subjective measurements, Young conducted the first recorded ocular spherical aberration measurement (Tscherning, 1924). A thread was pulled along his line of sight from one of his eyes to a considerable distance away. He viewed the thread through a plate of four slits closely placed to his eye. Due to different amount of spherical aberration at different states of accommodation, he therefore saw more than one thread. Using Young's principle, Volkmann used four pinholes to observe a pin at a number of distances (Tscherning, 1924). Ames and Proctor (1921) built the first sophisticated instrument to measure the spherical aberration along two meridians of the eye. These methods are more or less ray aberration measurements in principle. Ames and Proctor's setup is probably the first two-meridian ray aberration measurement device.

Of interest for this thesis are the full-meridian ray-wavefront aberration measurements that provide complete aberration information across the pupil plane. These measurements are all based on Scheiner's disc principle as shown in Fig. 1.7. The pinholes on a Scheiner's disc allows thin beams to enter the eye through different positions of the pupil plane. These beams usually consist of a detecting beam and a reference beam. The subject will see two separated spots . The displacement of the two beams on the retina is a measure of transverse ray aberration of the eye.

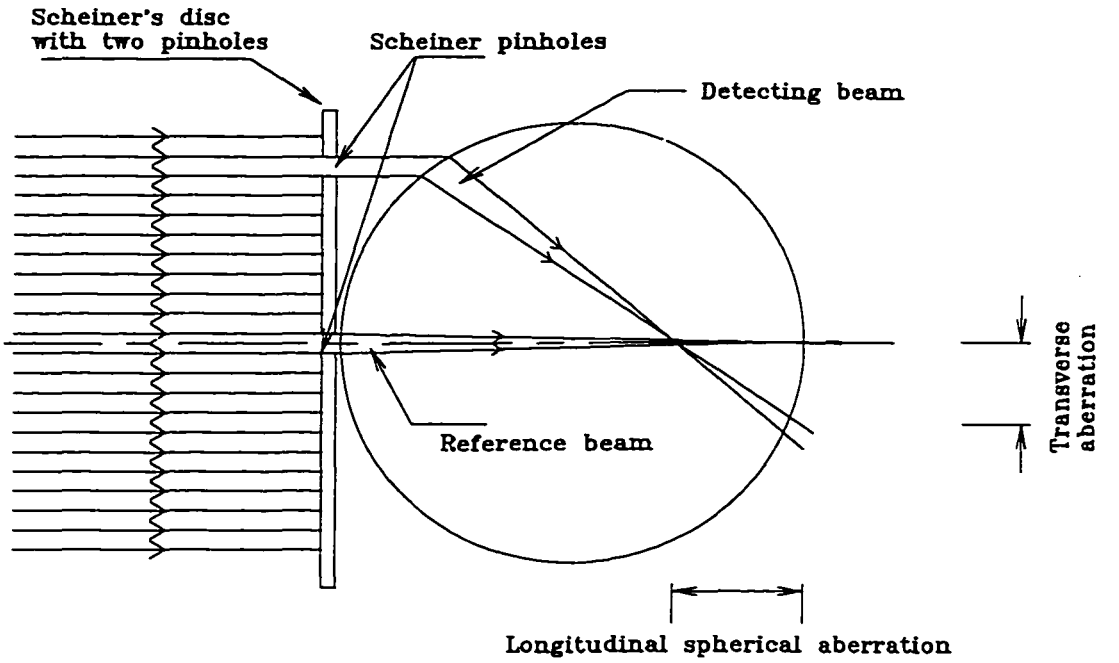


Fig. 1.7 Principle of Scheiner's disc. Rays of light entering the eye at different locations may intercept the retina at different positions. If a reference beam is fixed at the center of the optical system of the eye, another beam entering the eye through a different location can be called the detecting beam. The difference of the position of the detecting beam and the reference beam on the retina is a measure of transverse ray aberration. The distance of the interception of the detecting beam with the reference beam and the interception of the reference beam and the retina represents the longitudinal ray aberration.

In 1961, Smirnov (1961) published his wavefront aberration data from ray aberration measurements utilizing the polarization property of light to isolate a thin beam to scan the pupil plane. Smirnov measured the transverse aberrations of 10 subjects. Wavefront reconstruction was performed with the assistance of an electronic analogue circuit to yield the historical first set of two dimensional ocular wavefront aberration data.

Smirnov confirmed that the wavefront aberration of the human eye is asymmetrical in nature and showed that the aberration is negligibly small for a 2-3 mm pupil.

Webb et. al. (1992) also reported another ray-wavefront aberration measurement using a spatially resolved refractometer. Four eyes were measured to show the effectiveness of the method. With an automated system, the measurement could be finished within a few minutes according to Webb et. al.(1992), which is much faster compared to other subjective methods.

There are two main disadvantages to all subjective methods. One is the accountability of subjective results. In most subjective methods, the subject's task is reduced to the alignment of two misaligned vernier targets. Given the high performance of vernier acuity of the human visual system, if two targets are reasonably well presented to the subject, this disadvantage may well be tolerable.

The other disadvantage is that subjective measurement is time-consuming. This restricts the number of pupil sampling locations and also put stress on the subject which will affect subject's target alignment performance. Because of the longer time needed to accomplish the measurement, the subjective method of measuring aberration is not suitable to provide on-the-fly information of aberrations which may be constantly affected by tear film variation and accommodation fluctuations. Fortunately, the basic aberration of a particular eye does not seem to vary greatly for adult eyes over both the long term and the short term (Simirnov, 1961). Knowing the basic aberration of the eye is therefore enough for applications such as visual performance evaluation.

There are a number of advantages of the subjective methods in measuring aberration of the eye. The most significant advantage is that it is truly single pass in nature. The measured aberration will be the true aberration on the imaging receiving plane of the photoreceptors, compared to aberration measured by objective methods. Also, there is usually less of a technical requirement on the measurement system and the system is usually easier to operate.

Based on the examples given above, it is possible and necessary to develop a better method to try to maximally exploit the advantages of the old methods and systems and maximally overcome the disadvantages.

It seems that Smirnov's vernier task will provide the best subjective alignment. Webb et al's modern computerized automation control technology would be helpful in reducing measurement time and improve repeatability. To overcome the inferior image quality problem through a small pinhole for the detecting beam, the dual-Maxwellian view system adopted by Ivanoff in his one-dimensional ray aberration measurement can be used (Ivanoff, 1956). However, in Ivanoff's dual-Maxwellian view system, the reference beam could not control accommodation. Fortunately, the reference Maxwellian view channel can be substituted by a normal view to produce a semi-Maxwellian view system (Campbell, et. al. 1990).

An automated two dimensional semi-Maxwellian view aberration measurement will therefore be an improved subjective monochromatic wavefront aberration measurement system.

1.4 Possible correlation between the optical structural defects of the human eye and the optical functional defects of the human eye

Data of numerous aberration measurements tend to agree on many aspects of ocular aberration characteristics. On the other hand, a systematic study of the ocular components misalignments and other special features of the ocular asymmetry has not been reported.

1.4.1 General characteristics of aberrations measured in the human eyes

Aberration measurements of various methods have been able to confirm some characteristics of the aberration of the human eye. When the pupil size is around 2-3 mm

in diameter, fovea image quality is diffraction limited (Howland and Howland, 1977; Charman, 1991). Aberration of a typical human eye at the edge of a 4 mm pupil is about 1 Diopter (Charman, 1991). Aberration of the eye varies greatly between subjects (Smirnov, 1961; Howland and Howland, 1977; Walsh et. al. 1984). Comatic aberrations have been reported often to be the dominant aberration but the average of the wavefront aberrations of the sample of the population tends to be symmetrical (Smirnov, 1961; Howland and Howland, 1977; Walsh et. al. 1984; Charman, 1991). Aberrations in unaccommodated normal adult eyes are predominately positive (Koomen et. al. 1949; Ivanoff, 1956; Jenkin, 1963; Walsh et. al. 1984). Accommodation may vary both the symmetrical and asymmetrical components of the aberration of the eye (Tscherning, 1924; Koomen et. al. 1949; Ivanoff, 1956; Jenkin, 1963; Atchison et. al. 1995).

There are also issues that are not confirmed or unknown. The relative contributions of the cornea and the lens to the total aberration of the eye are not well understood. Directly related to this problem is the effect of accommodation on spherical aberration (EL Hage and Berny, 1973; Millodot and Sivak, 1979; Sivak, 1982). There have been mixed results in support of the old finding that accommodation changes spherical aberration from under-corrected to over-corrected spherical aberration (Tscherning, 1924; Atchison et. al. 1995). Another interesting but unconfirmed phenomenon is that the aberrations between the left and the right eyes of the same subject tend to be strikingly similar (Campbell et. al. 1990). Also, it is yet to be confirmed that the spherical aberrations in young eyes tend to be negative(Stine, 1930; Jenkins, 1963). Another unconfirmed issue is the contribution of the tear film to the aberration of the eye. Simirnov (1961) proposed that variations of the tear film can explain large variation in results between two different measurement sessions of the same eye.

1.4.2 Correlation of asymmetric aberrations and the misalignment of various optical components of the eye

Because the total wavefront aberration of the eye is at a micron level (Smirnov, 1961; Walsh et. al. 1985; Webb et. al. 1992) and corneal topographic data show corneal surface irregularities of a higher scale, it would be reasonable to speculate that a larger share of aberration may be contributed by the front surface of the cornea as suggested by Howland et. al. (1992, 1994). Unfortunately, it seems that the current corneal topography measurement systems are not accurate enough to quantify corneal aberration to a sufficient detail (Applegate and Howland, 1995).

On the other hand, it is possible and realistic to examine other factors that may possibly contribute to the total wavefront aberration of the eye such as pupil decentration, the value of angle alpha and crystalline lens tilt and decentration (Walsh and Charman 1992; Bing and Campbell, 1994). Lens tilt and decentration would affect the optical performance of the eye by introducing primarily asymmetrical aberrations (Ruben, 1963). There have been no known research in normal human eyes due to the difficulty involved both in measuring lens tilt and decentration and total aberration measurements.

Decentration of the pupil will also significantly affect the overall optical performance including chromatic aberration related performance (Simonet and Campbell, 1990; Ye et. al. 1992) and monochromatic aberration related performance of the eye (van Meeteren, 1983; Walsh, 1988). Because most full meridian aberration measurements use the geometrical center of the pupil as the reference point, it would be difficult to investigate how the amount of pupil decentration correlates with overall aberration of the eye unless another reference such as the optical axis of the eye is used.

Angle alpha will also introduce asymmetrical aberrations (Walsh and Charman, 1992; Bing and Campbell, 1994). The combination of a decentered pupil with other misaligned features may be able to compensate the effect of angle alpha. Angle alpha was related to oblique astigmatism with mixed successes (Lotmar and Lotmar, 1974; Dunne et.

al. 1993). Clearly, measurement of angle alpha and wavefront aberration of the eye will reveal the possible correlationship between them.

Measurements of these misalignment factors will not only help to resolve some of the structural mysteries of the eye, but also help to clarify the possible impact of these factors on the overall wavefront aberration.

1.5 Research objectives

In summary, some important questions regarding the optics of the human eye remain to be answered. Is the human eye an aligned optical system? If not, what are the general misalignment characteristics? What is the impact of a misaligned optical system on the definition of a common optical axis, angle alpha and various reference axes in the eye? What is the impact of the misalignments of various ocular components on the asymmetrical component of the overall monochromatic aberration in the eye? This thesis attempts to answer these questions systematically.

In Chapter 2 , theoretical methods for calculating lens tilt and decentration from Purkinje images misalignments are derived. In Chapter 3, the design and theoretical considerations of a new two-dimensional semi-Maxwellian view ocular wavefront aberration measurement system are presented. Measurement results on 4 subjects using the geometrical center of the pupil as the reference are given. System evaluation are also presented. Chapter 4 describes the experiments of wavefront measurements of the left eyes of 21 emmetropic subjects with the Coaxially Sighted Corneal Reflex (CSCR). Chapter 5 presents a Purkinje image photographic system and the final measurements of various misalignment factors of the same subjects as in Chapter 4. Chapter 6 investigates the possible correlation between the misalignment factors and the asymmetrical component of the wavefront aberration. Chapter 7 summarizes and discusses the results obtained in this thesis.

Chapter 2

Theoretical Models for Measuring the Tilt and Decentration of the Crystalline Lens *in vivo*

2.1 Introduction

As stated in Chapter 1, the true optical axis does not exist in most eyes. The lack of the true optical axis implies the cornea and the lens are misaligned. The implication of the misalignment between the cornea and the lens leads to the following questions. 1) What is the magnitude of the misalignment? 2) What is the functional significance? 3) Why does this misalignment exist? A general knowledge of the amount of the misalignment of the lens with the cornea will help to examine sources of the asymmetrical aberrations and will allow us to model the optics of the eye more accurately.

Each optical surface of the eye reflects a small portion of the incoming light and forms its corresponding catoptric image. These reflective images are named Purkinje images I, II, III, and IV corresponding to the anterior and posterior surface of the cornea and the anterior and posterior surface of the lens. When all the ocular surfaces are aligned, the Purkinje images can also be aligned along one direction. If the ocular surfaces are not aligned, the Purkinje images cannot be aligned at the same time.

Theoretically, a relationship can be found between the relative positions of the Purkinje images and the amount of lens tilt and decentration with respect to the cornea. In this Chapter, this relationship between the displacement of PIII and PIV from PI as a function of lens tilt and decentration was derived using the equivalent mirror theorem and the paraxial approximation based on the Emsley-Gullstrand eye model. In addition, an angular relationship was also derived.

2.2 Derivation of the equivalent mirrors of the tilted and decentered ocular surfaces

The relative positions of Purkinje images are functions of lens tilt and decentration. Calculation of these Purkinje image positions is complicated because each of these images are also affected by the optics in front of each reflective surface. However, each reflective surface and the optics in front of it can be treated as an equivalent mirror (Bennett and Rabbetts, 1984). Purkinje image displacements can be calculated based on these equivalent mirrors.

As shown in Fig. 2.1, for a one-surface cornea eye model, light from an object in front of the eye is refracted by the cornea and then reflected by the anterior surface of the lens and refracted again by the cornea to form PIII. The cornea and the anterior surface of the lens can be substituted by a single mirror which is the image of the anterior surface of the lens seen through the cornea. The property of a spherical mirror can be well defined by its apex and center of curvature. The calculation for an equivalent mirror then becomes the calculation of the images of the apex A_2 and center of curvature O_2 of the mirror through the optics in front of it, the images are A_2' and O_2', respectively.

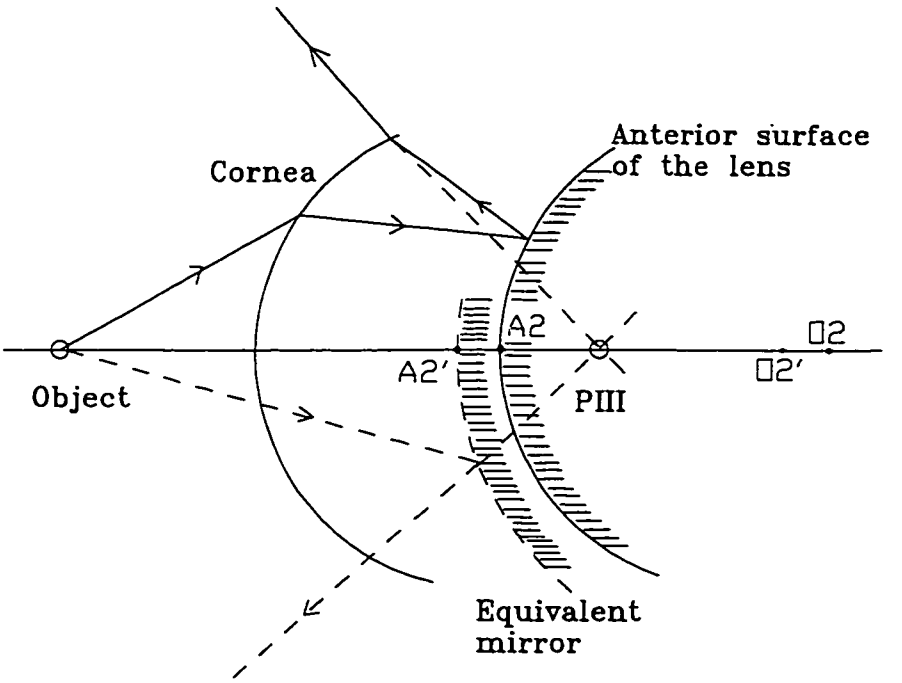


Fig. 2.1 Definition of equivalent mirror. In a three surface eye model, light from an object is refracted first by the cornea, reflected by the anterior surface of the lens and then refracted again by the cornea to form the PIII. This process is equivalent to a single mirror with a proper power at a appropriate position. This single mirror is called the equivalent mirror of the cornea and the anterior surface of the lens.

Purkinje image II is difficult to view because it is dim and obscured by Purkinje images I. Since our main interests are the two surfaces of the lens, therefore, the cornea will be treated as a single reflecting surface. The Gullstrand-Emsley model eye is therefore adopted in this derivation.

The setup of the coordinate system is important and is shown in Fig. 2.2. The apex of the cornea is the origin of the coordinate system. The abscissa is an optical axis of the cornea or an axis going through the center of curvature of the cornea. The optical axis of the cornea is therefore the reference axis. The lens is tilted by an angle θ and decentered by an amount y_0. A lens displacement to the temporal side of the eye or to the superior of the eye is positive. A lens tilt to the temporal side or to the superior is positive. Positive angles are measured clockwise in Fig. 2.2.

The center of rotation of the lens is set at the center of the equatorial plane, which is 1.219 mm from the apex (*A2*). In the coordinate system, defining the coordinates of the apexes and centers of curvature of the two surfaces of the lens is the first step in the derivation. For the anterior surface of the lens, the apex (A_2) is at, $[x_0 - \delta\cos\theta, y_0 + \delta\sin\theta]$, and the center of curvature (O_2) is at $[x_0 - (r_2 - \delta)\cos\theta, y_0 + (r_2 - \delta)\sin\theta]$. For the posterior surface of the lens, the apex (A_3) is at $[x_0 + (d_2 - \delta)\cos\theta, y_0 - (d_2 - \delta)\sin\theta]$, and the center of curvature(O_3) is at $[x_0 - (d_2 - \delta - r_3)\cos\theta, y_0 + (d_2 - \delta - r_3)\sin\theta]$.

The positions of the images of these four points through all the optics in front of it are then calculated by paraxial optics in the coordinate system. For the anterior surface of the lens, the image of the apex (A'_2) and the center of curvature (O'_2) through the cornea are, $[x'(A_2), y'(A_2)]$ and $[x'(O_2), y'(O_2)]$, respectively.

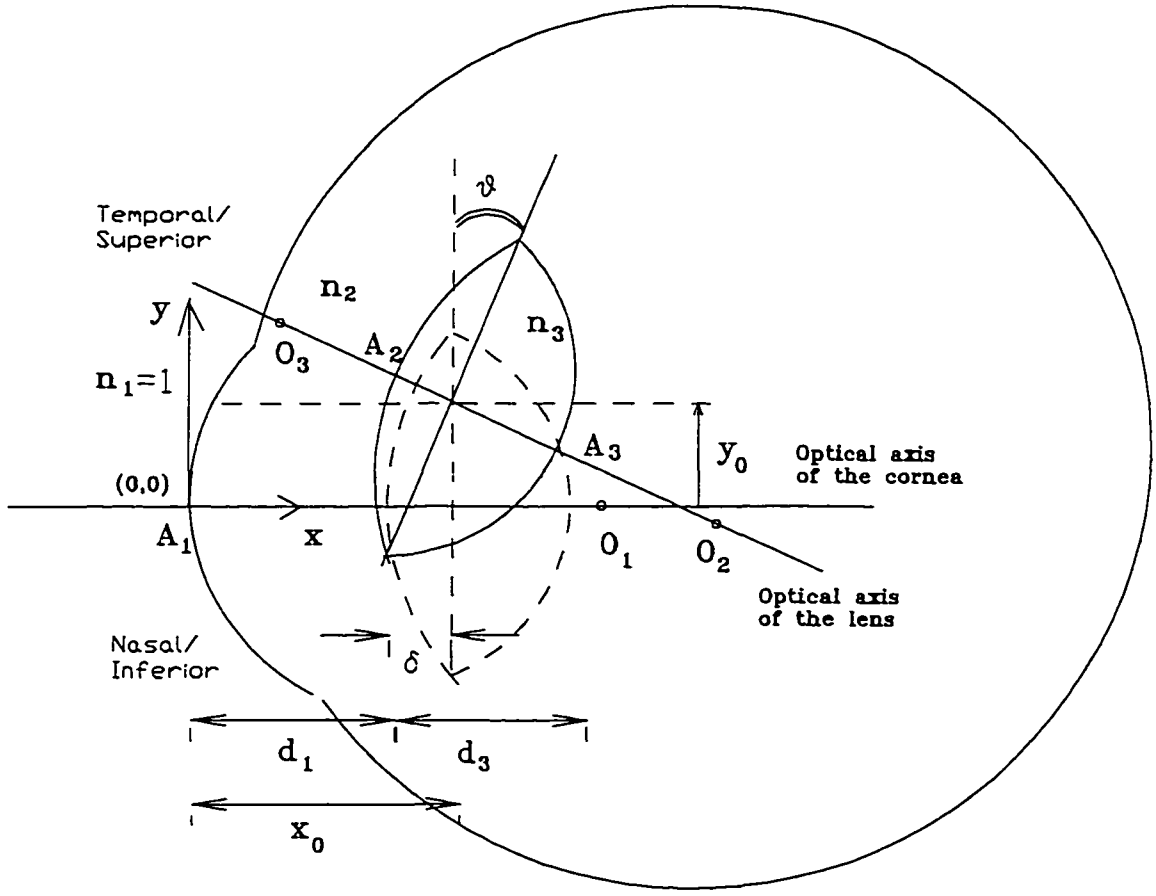


Fig. 2.2 Coordinates system setup for derivation with the Gullstrand-Emsley eye model. A_1, A_2 and A_3 are the apexes of the cornea, the anterior and posterior surfaces of the lens, respectively; O_1, O_2 and O_3 are the center of curvature of the cornea, the anterior and posterior surfaces of the lens, respectively; n_1, n_2 and n_3 are the refractive indices of air, the cornea and the lens, respectively; d_1 is the distance from A_1 to A_2; d_2 is the distance from A_2 to A_3; δ is the distance from A_2 to the pivot of the lens tilt, which is 1.219 for the Gullstrand-Emsley eye. x_0 is the distance from A_1 to the pivot of the lens tilt. The lens is tilted by θ and decentered by y_0 from the optical axis of the cornea.

Anterior surface of the lens

For apex (A_2), we have,

$$x'(A_2) = \frac{r_1}{\frac{n_2 r_1}{x_0 - \delta\cos\theta} + (1 - n_2)} \tag{2.1}$$

$$y'(A_2) = \frac{y_0 + \delta\sin\theta}{x_0 - \delta\cos\theta} * \frac{r_1}{\frac{n_2 r_1}{x_0 - \delta\cos\theta} + (1 - n_2)} * \frac{n_2}{n_1} \tag{2.2}$$

for the center of curvature (O_2),

$$x'(O_2) = \frac{r_1}{\frac{n_2 r_1}{x_0 + (r_2 - \delta)\cos\theta} + (1 - n_2)} \tag{2.3}$$

$$y'(O_2) = \frac{r_1}{\frac{n_2 r_1}{x_0 + (r_2 - \delta)\cos\theta} + (1 - n_2)} * \frac{y_0 - (r_2 - \delta)\sin\theta}{x_0 + (r_2 - \delta)\cos\theta} * \frac{n_2}{n_1} \tag{2.4}$$

Posterior surface of the lens

For the apex(A_3),

$$x'(A_3) = \frac{r_1}{\frac{n_2 r_1}{(x_0 - \delta\cos\theta) + \frac{r_2 n_2}{\frac{n_3 r_2}{d} + (n_2 - n_3)}\cos\theta} + (1 - n_2)} \tag{2.5}$$

$$y'(A_3) = \frac{r_1}{\frac{n_2 r_1}{(x_0 - \delta\cos\theta) + \frac{r_2 n_2}{\frac{n_3 r_2}{d} + (n_2 - n_3)}\cos\theta} + (1 - n_2)} * \frac{n_2}{n_1} * \frac{(y_0 + \delta\sin\theta) - \frac{r_2 n_2}{\frac{n_3 r_2}{d} + (n_2 - n_3)}\sin\theta}{(x_0 - \delta\cos\theta) + \frac{r_2 n_2}{\frac{n_3 r_2}{d} + (n_2 - n_3)}\cos\theta} \tag{2.6}$$

For the center of curvature(O_3),

$$x'(O_3) = \frac{r_1}{\frac{n_2 r_1}{(x_0 - \delta\cos\theta) + \frac{r_2 n_2}{\frac{n_3 r_2}{d - r_3} + (n_2 - n_3)}\cos\theta} + (1 - n_2)} \tag{2.7}$$

$$y'(O_3) = \frac{r_1}{\frac{n_2 r_1}{(x_0 - \delta\cos\theta) + \frac{r_2 n_2}{\frac{n_3 r_2}{d - r_3} + (n_2 - n_3)}\cos\theta} + (1 - n_2)} * \frac{n_2}{n_1} * \frac{(y_0 + \delta\sin\theta) - \frac{r_2 n_2}{\frac{n_3 r_2}{d - r_3} + (n_2 - n_3)}\sin\theta}{(x_0 - \delta\cos\theta) + \frac{r_2 n_2}{\frac{n_3 r_2}{d - r_3} + (n_2 - n_3)}\cos\theta} \tag{2.8}$$

With these four points expressed as functions of lens tilt and decentration, one can calculate the displacements of Purkinje images III and IV from I as functions of lens tilt and decentration. One can also calculate the angles between the optical axis of the cornea from aligning Purkinje image I with III and aligning Purkinje image I with IV as functions of lens tilt and decentration. Either of the two pairs of relationships will lead to the solution of lens tilt and decentration.

2.3 Calculation of lens tilt and decentration from Purkinje image displacements

2.3.1 Derivation of lens tilt and decentration from Purkinje image displacements

For the anterior surface of the lens, if the viewing system and the object is centered around the optical axis of the cornea, Purkinje image I will be on the optical axis of the cornea.

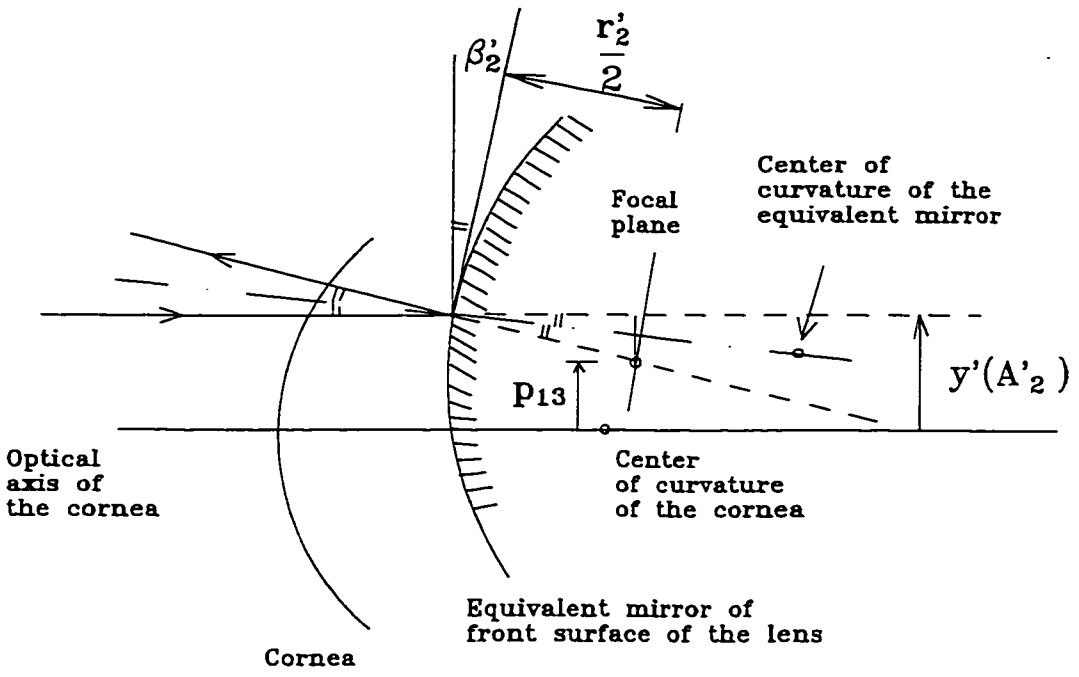


Fig.2.3 Calculation of the displacement of PIII from PI. The equivalent mirror of the anterior surface of the lens is tilted by β'_2 and decentered by y'(A'2). r'2 *is the radius of the equivalent mirror. PIII is displaced from the optical axis of the cornea by* p_{13}.

As shown in Fig. 2.3 given the apex and center of curvature of the equivalent mirror, the displacement of PIII from Purkinje image I (p_{13}) can be calculated by,

$$p_{13} = -r'_2 \sin\beta_2' + y'(A_2) \tag{2.9}$$

where ,

$$\beta_2' = a\tan\left[\frac{y'(A_2) - y'(O_2)}{x'(A_2) - x'(O_2)}\right] \tag{2.10}$$

which is the tilt of the equivalent mirror; and

$$r_2' = \sqrt{[x'(A_2) - x'(O_2)]^2 + [y'(A_2) - y'(O_2)]^2} \tag{2.11}$$

is the radius of curvature of the equivalent mirror as shown in Fig. 2.3.

Similarly, the displacement of Purkinje image IV from Purkinje image I (P_{14}) can be calculated by,

$$p_{14} = r'_3 \sin\beta_3' + y'(A_3) \tag{2.12}$$

where,

$$\beta_3' = a\tan[\frac{y'(A_3) - y'(O_3)}{x'(A_3) - x'(O_3)}] \tag{2.13}$$

which is the tilt of the equivalent mirror;

$$r_3' = \sqrt{[x'(A_3) - x'(O_3)]^2 + [y'(A_3) - y'(O_3)]^2} \tag{2.14}$$

which is the radius of curvature of the equivalent mirror.

Substitute the Gullstrand-Emsley eye model parameters (Bennett and Rabbetts, 1984) into Eq.(2.1)-(2.14) and using small angle approximation, we have,

$$p_{13} = 1.7726 y_0 - 0.2715\theta \tag{2.15}$$

$$p_{14} = 1.046 y_0 + 0.0629\theta \tag{2.16}$$

The calculations were performed using a Maple V™ symbolic calculation program (Appendix II).

2.3.2 Verification of the calculation of lens tilt and decentration from Purkinje images displacements by raytracing

The Gullstrand-Emsley eye model was also used to verify Eq. (2.15) and Eq. (2.16) by raytracing with raytracing software CODE V™. The results are shown in Fig.2.4. Fig. 2.4.a is PIII and PIV displacement with respect to PI vs. lens decentration only; Fig. 2.4.b is PIII and PIV

displacement with respect to PI vs. lens tilt only. The filled symbols are the raytraced results. The lines are theoretical calculations. Beyond about 10°, the paraxial regime breaks down and the two plots start to diverge. The expected range of lens tilt and displacement are expected to be within the paraxial region. Raytracing with combined lens tilt and decentration was also done to show the largest error is within 8.6% between the paraxial approximation and the raytracing for a tilt of 7° to the temporal side and decentration of 1 mm to the temporal side.

2.3.3 Solution of lens tilt and decentration from the derived equations

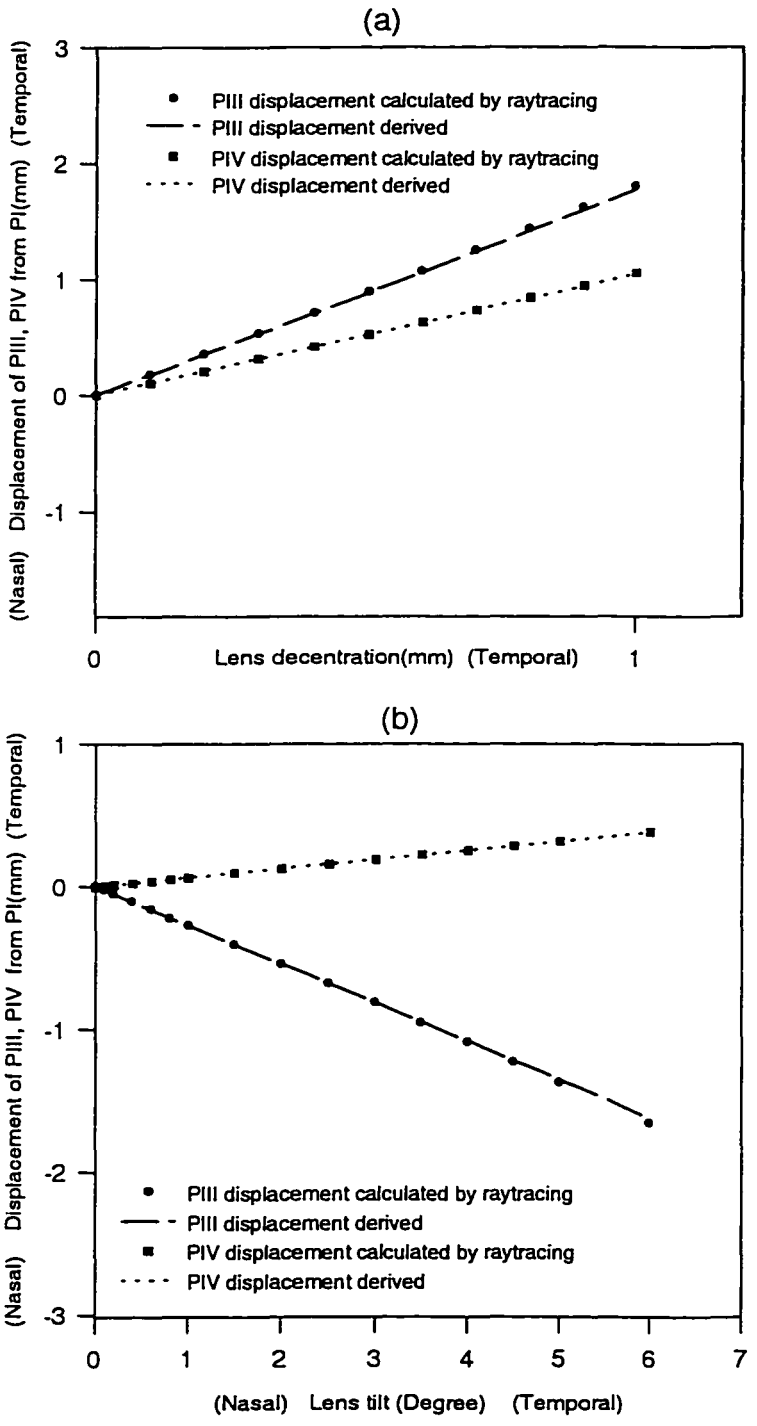
Combining Eq. (2.15) and Eq. (2.16) and solving for θ and y_0 results in,

$$\theta = -2.6449\, p_{13} + 4.4821\, p_{14} \tag{2.17}$$

$$y_0 = 0.1590\, p_{13} + 0.6865\, p_{14} \tag{2.18}$$

Given the validity of the Gullstrand-Emsley eye model and the measured Purkinje image displacement, the amount of lens tilt and decentration can be calculated reliably by using Eq.(2.17) and (2.18).

Fig. 2.4 Comparison of the Purkinje image displacements calculated with the derived equations and that calculated with CODE V™ . Fig. 2.4.a is the displacement of PIII and PIV from PI versus lens tilt only. Fig. 2.4.b is the displacement of PIII and PIV from PI versus lens decentration only. Filled circles represent displacements of PIII from PI calculated by raytracing; filled squares represent displacements of PIV from PI calculated by raytracing; the solid curve represents displacements of PIII from PI calculated using Eq.(2.15); the broken curve represents displacements of PIV from PI calculated using Eq.(2.16); N represents the nasal side; T represents the temporal side.


(a)
PIII displacement calculated by raytracing
PIII displacement derived
PIV displacement calculated by raytracing
PIV displacement derived
(Nasal) Displacement of PIII, PIV from PI(mm) (Temporal)
3
2
1
0
-1
0
Lens decentration(mm) (Temporal)
1
(b)
(Nasal) Displacement of PIII, PIV from PI(mm) (Temporal)
1
0
-1
-2
-3
PIII displacement calculated by raytracing
PIII displacement derived
PIV displacement calculated by raytracing
PIV displacement derived
0
1
2
3
4
5
6
7
(Nasal) Lens tilt (Degree) (Temporal)

2.4 Calculation of lens tilt and dencentration from the angles for aligning two of the three Purkinje images

Given the derived equivalent mirrors, it is also possible to derive a relationship between the Purkinje image displacements and lens tilt and decentration and a number of angles for aligning two of them at a time. These angle measurements can sometimes be simpler than Purkinje image displacement measurements. As shown in Fig. 2.5, for two mirrors, the two reflected images can be aligned with the object by the line joining the two centers of curvature. For the cornea and the equivalent mirror of the anterior surface of the lens, PI and PIII can be aligned along the line joining the center of curvature of the cornea and the center of curvature of the equivalent mirror of the anterior surface of the lens. The angle between this line and the optical axis of the cornea (t_{13}) which can be measured experimentally is,

$$t_{13} = a\tan[\frac{y'(O_2)}{x'(O_2) - r_1}] \tag{2.19}$$

where $y'(O_2)$ is the as shown in Fig. 2.5 and given by Eq.(2.4); $x'(O_2)$ is as shown in Fig. 2.5 and given by Eq.(2.3)

Similarly, for the angle between the optical axis of the cornea and the direction along which the object and Purkinje image I and IV can be aligned (t_{14}) which can be experimentally measured is,

$$t_{14} = a\tan[\frac{y'(O_3)}{x'(O_3) - r_1}] \tag{2.20}$$

where $y'(O_3)$ is given by Eq.(2.8); $x'(O_3)$ is given by Eq.(2.7).

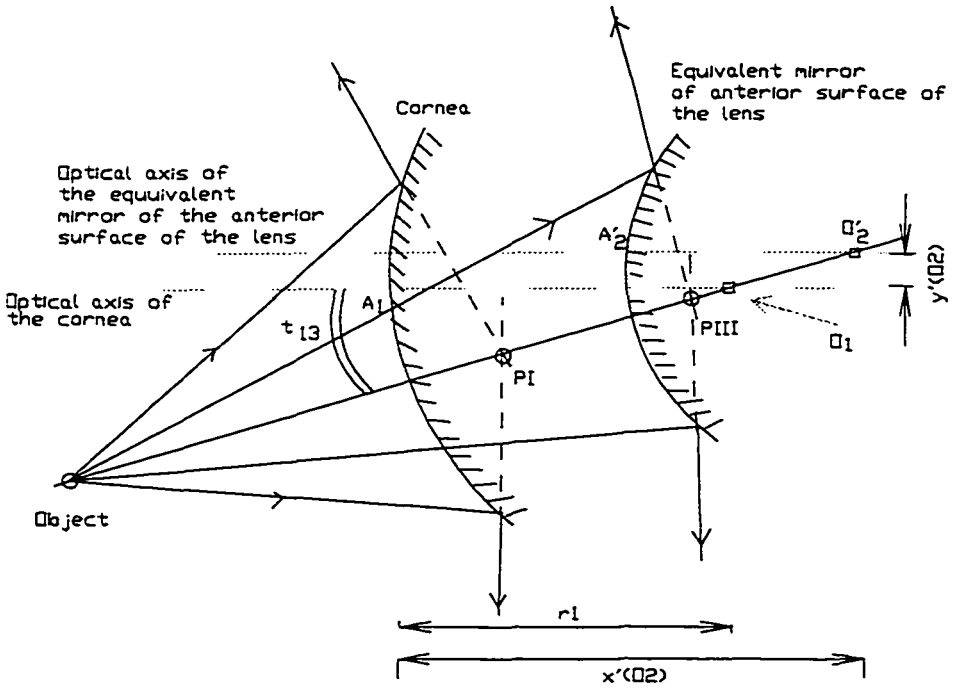


Fig. 2.5 Calculation of the angle (t_{13}) between the optical axis of the cornea and the line along which the object and the PI and PIII can be aligned. The line along which the object and the PI and PIII can be aligned is the line joining the centers of curvature of the cornea(O_1) and the equivalent mirror of the anterior surface of the lens(O'_2). A_1 is the apex of the cornea; A'_2 is the apex of the equivalent mirror of the anterior surface of the lens.

If we substitute the Gullstrand-Emsley eye model parameters into Eq.(2.19) and (2.20), with small angle approximation, we get,

$$t_{13} = 9.8836 y_0 - 1.514\theta \tag{2.21}$$

$$t_{14} = -8.8945 y_0 - 0.5349\theta \tag{2.22}$$

Combining Eq.(21) and (22) and solving for θ and y_0 results in,

$$\theta = -0.4743t_{13} - 0.5270t_{14} \tag{2.23}$$

$$y_0 = 0.02852t_{13} - 0.0807t_{14} \tag{2.24}$$

As with Eq.(2.17) and Eq.(2.18), assuming the validity of the Gullstrand-Emsley eye model, the amount of lens tilt and decentration can be calculated reliably by using Eq.(2.23) and (2.24) with the two angles t_{13} and t_{14}.

2.5 Discussion

The amount of lens tilt and decentration can be calculated from Eq.(2.17) and Eq.(2.18) by taking a picture of the Purkinje images after the optical axis of the cornea is located. This method is easy and straightforward. The problem with this method is the poor image quality of Purkinje image III and especially when it is defocused. The situation could be worsened when a telecentric stop has to be used to compensate for the image position error induced by defocus (Philips et. al. 1988; Smith, 1992). Photoflash light has to be used and some image enhancement may be needed when the measurement is conducted with CCD imaging system.

Also as shown, the amount of lens tilt and decentration can be calculated from Eq. (2.23) and Eq. (2.24). This method requires two steps. The first step is to measure the angle between the optical axis of the cornea and the line along which PI and PIII can be aligned. The camera can be focused on the image plane of PIII with PI defocused. Because PI is much brighter than PIII, a defocused PI is therefore brighter than a defocused PIII. The second step is to measure the angle between the optical axis of the cornea and the line along which PI and PIV can be aligned.

Sensitivity of measuring the amount of lens tilt and decentration is restricted by the resolution of Purkinje image displacement measurement and angle measurement in Purkinje image alignment. The Purkinje images displacement can be measured at pixel resolution (Appendix I). One pixel on the video screen corresponds to 0.03 mm on the pupil plane. This

converts to a resolution for measuring lens tilt of 0.2° and lens decentration of 0.02 mm. Purkinje image alignment measurements can give an angle resolution of 0.2° which corresponds to a measurement resolution of 0.2 ° for lens tilt and a measurement resolution of 0.02 mm for lens decentration.

The choice of which scheme is used depends on the available technology. In this thesis, the misalignment of Purkinje images will be measured and Eq.(2.23) and Eq.(2.24) will be used to calculate lens tilt and decentration.

In the real situation, the cornea has two surfaces. The validity of using the 3-surface G-E eye model in the derivation can be questioned. However, because the equivalent mirror theorem considers all the optics in front of the reflective surface and the reflective surface itself as an equivalent single element, and the single cornea surface in the G-E model represents the combined effect of the two surfaces, the 3-surface G-E model is valid in representing the real eye and the error induced is expected to be small.

2.6 Summary

Using a Gullstrand-Emsley model eye, the relationships between Purkinje image misalignment and the amount of lens tilt and decentration have been derived. The relationships between differences of the directions for aligning two of the three Purkinje images have also been derived. The relationships are linear under the small angle approximation. When the Purkinje image displacements or angle differences of the directions to align two of them are measured, the amount of lens tilt and decentration can be calculated by reversing the relationships.

Chapter 3

A Semi-Maxwellian View Wavefront Aberration Measurement System

3.1 Introduction

In essence, some ocular aberration measurements use isolated rays to scan the entrance pupil plane, either simultaneously or successively. Deviations of single rays are thereafter characterized as the ray aberrations of the eye. Most subjective methods use successive scan with which aberrations of the eye are sampled across the pupil plane successively. Results of various experiments to measure the overall aberrations of the human eye have confirmed the asymmetrical nature of the aberrations(Charman, 1991).

Aberration results can be expressed as wavefront aberration. Wavefront aberration has been the preferred method to describe the aberrations of the human eye rather than the traditional Seidel aberrations, which were derived to characterize traditional symmetrical optical systems consisting of mostly centered spherical surfaces.

This chapter describes the theory and design of a two-dimensional semi-Maxwellian view ray aberration measurement system. A method for deriving the wavefront aberration from the measured ray aberration is also given. A preliminary test of 4 subjects is also described.

3.2 Theory

3.2.1 The semi-Maxwellian view aberration measurement system

a)Maxwellian view as the scanning beam

Fig. 3.1 shows the schematic of the apparatus. Point source (*A*) is imaged onto the first principal plane (*P*) of the eye by a specific projection lens (*L*). The ray pencil constituted by the aperture (*U*) of the lens and the image (*A'*) of the point source on the pupil plane is refracted only once at the tip of the ray pencil. After the principal plane of the eye, the initial converging ray pencil will diverge and constitute another ray pencil from the image of the point source on the pupil plane to the retina (*R*). The subject will see the lens aperture uniformly filled with light. This specific view is named a Maxwellian view (Westheimer, 1966). Lens (*L*) is therefore called the Maxwellian view lens.

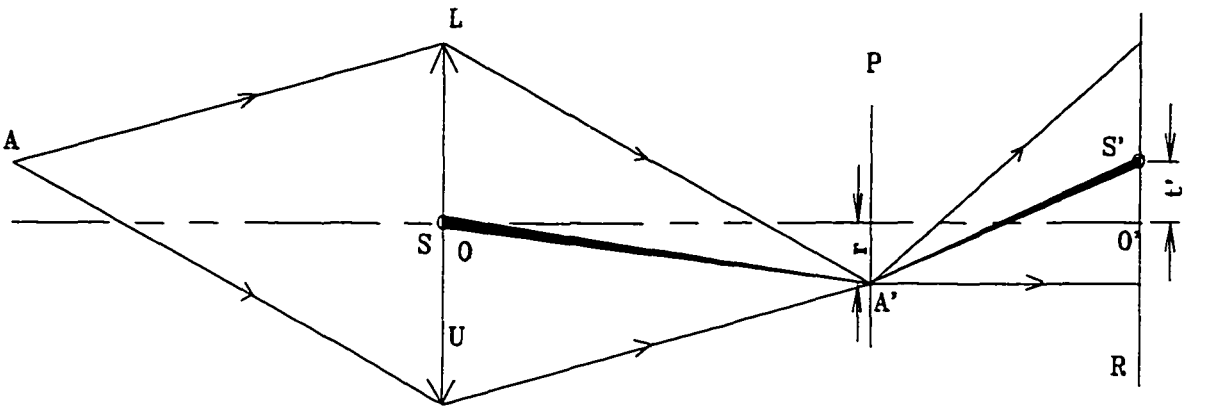


Fig. 3.1 Principle of the Maxwellian view system. A is the point source; P is the primary principal plane of the eye; L is the Maxwellian view lens; A' is the image of A at P; U is the aperture of L; R is the retina, O' is the reference point; S is the target; S' is the shadow of S; t' is the defined transverse ray aberration.

If an opaque object (*S*) stands in the path of the ray pencil, a shadow (*S'*) of the object will be produced in the Maxwellian view. The relative position of the shadow of the object on the retina is related to the position of the object in the lens *(L)* aperture. It is also related to the deviation of the outgoing ray pencil from the incoming ray pencil. If there is a reference point (*O'*) on the retina and the object blocks the principal ray of the Maxwellian view, the distance (*t'*) can be used to define the deviation of outgoing ray from the reference point (*O'*). For an ideal eye, no matter where the Maxwellian view point image falls on the principal plane, the shadow should fall at the same position on the retina. For a realistic aberrated human eye, the power of the eye across the principle plane is usually not the same and the shadow may not always fall at the same position. The deviation of the shadows from a single position is described as ray aberration *t'* and *t'* is a function of the location of (*A'*) on (*P*) that can be described by (*r*) .

b) A normal view target as the reference

When Ivanoff used the Maxwellian view system to measure aberrations of the human eye, he used one Maxwellian view channel as the reference beam and another Maxwellian view channel as the scanning beam (Ivanoff, 1956). This setup did not provide an adequate accommodative stimulus to control accommodation. Campbell et. al. (1991) used a normal view channel to provide a target to the subject both as accommodation control and as a reference target on the retina in a one dimensional setup. Such a system is called a semi-Maxwellian view system.

In reality, the entrance pupil plane is used instead of the imaginary principal plane. If the eye is clearly focused at a fixation target and if the head position is fixed, the image of the fixation target can be kept steady at one location on the retina as a reference point (O'). If a Maxwellian view is also provided to the eye at the same time, a shadow image (S') that is comparable to the normal view target will be present on the retina. If the normal view target and Maxwellian view target are imposed on each other at the center of the Maxwellian view lens (L) and if the Maxwellian view point source (A) is moved transversely, the Maxwellian view point image will also move on the pupil plane. Because the Maxwellian view lens is fixed, the Maxwellian view principal ray simulates single rays originating from the normal view target entering the eye through different pupil locations.

In other words, the Maxwellian view ray is used to depict single rays originating from the normal view target. Given the aberration in the eye, the normal view target is a blurred target on the retina. The position of the Maxwellian view target should always be in the range of the blur of the normal view target image. But this is not what the subject will always perceive in the real case. At the periphery of the pupil, the subject will usually see an image of the normal view target blurred to some extent depending on the focus and aberrations of the eye. To the subject, a clear Maxwellian view target shadow is usually outside the blurred portion of the normal view target image. There are two mechanisms that may produce this phenomenon. The first mechanism is the Stiles-Crawford effect, which is optical in nature. The second mechanism is neural in nature. Relatively weak signals will be ignored as noise in the visual neural processing system. In other

words, a point spread distribution can only be perceived partially and the weak periphery of the point spread distribution will be ignored.

c) Ray aberration data

Given a semi-Maxwellian view system, for a specific location on the pupil plane for the Maxwellian view point source, there will be a misalignment between the normal view target and the Maxwellian view target when the two targets are actually aligned. If the subject aligns the images of the two targets on his or her retina (align the two targets in his or her perception) by moving away the Maxwellian view target from the normal view target or the center of the Maxwellian view lens, the distance of the Maxwellian view target from the normal view target *t(r)* can be recorded. It represents the amount of ray aberration for the specific pupil location in the object space as shown in Fig. 3.2

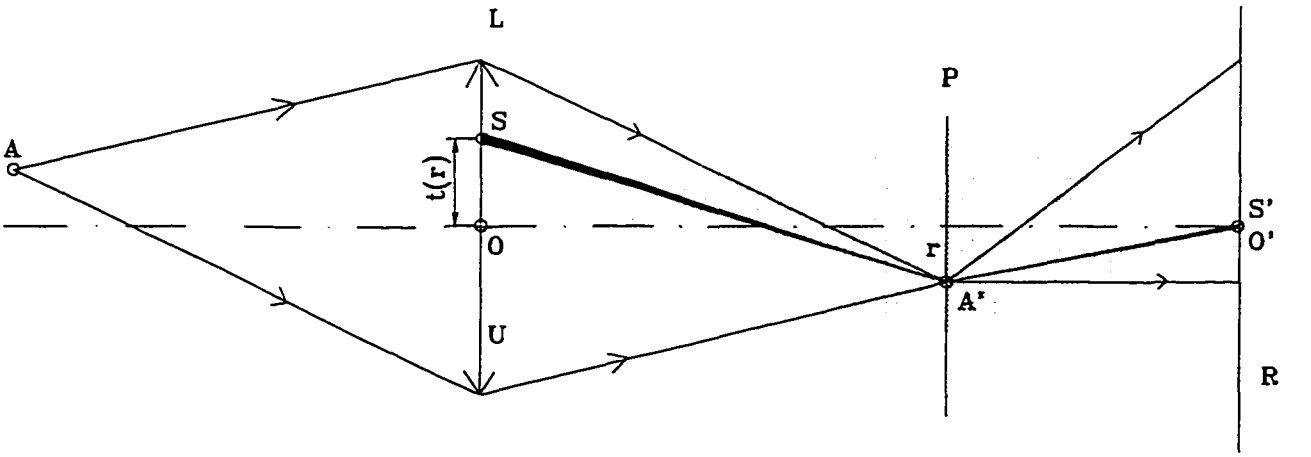


Fig.3.2 Transverse ray aberration expressed in the object space. Maxwellian view is depicted by single lines while the normal view represented by the shaded area. A is the point source; P is the entrance pupil plane of the eye; L is the Maxwellian view lens; A' is the image of A at P; U is the aperture of L; R is the retina; O is the normal view target; O' is the normal view image ; S is the Maxwellian view target; S' is the shadow of S which coincides with O'; t(r) is the transverse ray aberration measured in the object space.

If a series of pupil locations *r* are chosen as the Maxwellian view point image positions in a uniform way, a set of ray aberration data *t(r)* can be obtained. Such a set of ray aberration data can be used to specify the overall optical performance of the eye. One approach is to reconstruct the wavefront aberration from such a set of ray aberration data.

3.2.2 Wavefront reconstruction from ray aberration data

Considering only aberrations, the optical performance of the eye can be completely described by wavefront aberration. Wavefront aberration can be reconstructed from ray aberration data. There are two methods to obtain expressions for the classical optical wavefront reconstruction (Rimmer,1974; Southwell,1980). Here, an explicit solution by a least square estimator can be conveniently used (Cubalchini, 1979).

a) Principle of wavefront reconstruction

Wavefront aberration can be expressed on the pupil plane in terms of a polynomial of pupil coordinates. There are two sets of polynomials of specific interest to optical aberration theory. They are the Taylor polynomials and the Zernike polynomials. The Taylor polynomial is a simpler form and is directly related to Seidel aberration terms. The Zernike polynomial is orthogonal over a unit circle and it is directly related to the optimally balanced Seidel aberrations. It is also invariant in form with respect to axes of rotation about the origin. One other property of the Zernike polynomial is that its lower order terms correspond to simple shapes that can be compensated by a dynamic wavefront correction device such as deformable mirror, which is of considerable application potential. Despite the differences, the two polynomials of equivalent orders can be transformed to each other.

Because the goal of this research is to examine the general situation of aberrations in the human eye and also to attempt to correlate ocular component misalignments with ocular aberrations, the Taylor polynomial is used to represent the total amount of ocular wavefront aberration. The total wavefront aberration, which can be partitioned into a symmetrical and an asymmetrical component, can be expressed by,

$$W(x, y) = \sum_{i=1}^{I} a_i Z_i(x, y) \tag{3.1}$$

where, $W(x, y)$ is the wavefront aberration at the pupil plane; a_i is the coefficient of the i^{th} term, which corresponds to the coefficient vector $\hat{A}$; $Z_i(x, y)$ is the i^{th} term of Taylor or Zernike polynomials. Normally, i is from *1* to *I*. However, the first term is the piston term of the wavefront and is usually set to be zero. The physical meaning of this is the assumption that the origin has zero wavefront aberration.

The measurable data are transverse ray aberrations. In aberration theory (Welford, 1991), the x and y derivatives of the wavefront function $W(x, y)$ multiplied by -1.0 are transverse ray aberrations in x, y directions respectively. One has,

$$\delta\xi' = -\frac{1}{n}\frac{\partial W(x,y)}{\partial x} = -\frac{1}{n}\sum_{i=2}^{I} a_i \frac{\partial Z_i(x,y)}{\partial x} \tag{3.2}$$

$$\delta\eta' = -\frac{1}{n}\frac{\partial W(x,y)}{\partial y} = -\frac{1}{n}\sum_{i=2}^{I} a_i \frac{\partial Z_i(x,y)}{\partial y} \tag{3.3}$$

where $\delta\xi'$ and $\delta\eta'$ are x and y components of the transverse aberrations of the optical system in the image space, respectively; n is the refractive index of the media in the image space.

To convert the measured angle from the object space (whose refractive index is *1.0)* to the image space, the angles need to be divided by the refractive index n of the image space. Therefore, one has,

$$\frac{\delta\xi'}{n} = -\frac{1}{n}\sum_{i=2}^{I} a_i \frac{\partial Z_i(x,y)}{\partial x} \quad or \quad \delta\xi' = -\sum_{i=2}^{I} a_i \frac{\partial Z_i(x,y)}{\partial x} \tag{3.4}$$

$$\frac{\delta\eta'}{n} = -\frac{1}{n}\sum_{i=2}^{I} a_i \frac{\partial Z_i(x,y)}{\partial y} \quad or \quad \delta\eta' = -\sum_{i=2}^{I} a_i \frac{\partial Z_i(x,y)}{\partial y} \tag{3.5}$$

where $\delta\xi'$ and $\delta\eta'$ are the x and y components of the true transverse aberrations of the optical system in object space.

In the semi-Maxwellian view setup, transverse aberrations $P(x,y)_j$ and $Q(x,y)_j$ are measured for the j^{th} sampling location on the pupil plane in radians in object space along the x and y meridians, respectively. $j=1$ *to* J, with J representing the total number of sampling locations.

The essence of the wavefront reconstruction is to fit the derivatives of the wavefront function to the measured ray aberration values. One convenient approach is to use the least square estimator. The least square residual minimization functional ΔE is,

$$\Delta E = \sum_{j=1}^{J}\left[\left(P(x,y)_j + \sum_{i=2}^{I} a_i \frac{\partial Z_i(x,y)_j}{\partial x}\right)^2 + \left(Q(x,y)_j + \sum_{i=2}^{I} a_i \frac{\partial Z_i(x,y)_j}{\partial y}\right)^2\right] \tag{3.6}$$

By differentiating the above equation with respect to a_i, we obtain the k^{th} equation corresponding to the same value of i, ($k=2$ *to* I),

$$\sum_{j=1}^{J}\left[-P(x,y)_j \frac{\partial Z_k(x,y)_j}{\partial x} - Q(x,y)_j \frac{\partial Z_k(x,y)_j}{\partial y}\right]$$
$$= \sum_{i=2}^{I}\left[a_i \sum_{j=1}^{J}\left(\frac{\partial Z_k(x,y)_j}{\partial x}\frac{\partial Z_i(x,y)_j}{\partial x} + \frac{\partial Z_k(x,y)_j}{\partial y}\frac{\partial Z_i(x,y)_j}{\partial y}\right)\right] \tag{3.7}$$

Following Cubalchini (1979), the above equations set ($k=2$ *to* I) can be explicitly written as,

$$D\hat{P} = E\hat{A}$$

where, $\hat{P}$ is the measurement vector multiplied by -1.0,

$$\hat{P} = -\left[P(x,y)_1, P(x,y)_2, \ldots, P(x,y)_J, Q(x,y)_1, Q(x,y)_2, \ldots, Q(x,y)_J\right] \tag{3.8}$$

$$D = \begin{bmatrix} \frac{\partial Z_2(x,y)_1}{\partial x} & \frac{\partial Z_2(x,y)_2}{\partial x} & \cdots & \frac{\partial Z_2(x,y)_J}{\partial x} & \frac{\partial Z_2(x,y)_1}{\partial y} & \cdots & \frac{\partial Z_2(x,y)_J}{\partial y} \\ \frac{\partial Z_3(x,y)_1}{\partial x} & \frac{\partial Z_3(x,y)_2}{\partial x} & \cdots & \frac{\partial Z_3(x,y)_J}{\partial x} & \frac{\partial Z_3(x,y)_1}{\partial y} & \cdots & \frac{\partial Z_3(x,y)_J}{\partial y} \\ \vdots & \vdots & \vdots & \vdots & \vdots & \vdots & \vdots \\ \frac{\partial Z_I(x,y)_1}{\partial x} & \frac{\partial Z_I(x,y)_2}{\partial x} & \cdots & \frac{\partial Z_I(x,y)_J}{\partial x} & \frac{\partial Z_I(x,y)_1}{\partial y} & \cdots & \frac{\partial Z_I(x,y)_J}{\partial y} \end{bmatrix} \tag{3.9}$$

The dimensionality of the matrix depends on the terms of the wavefront function used and the number of sampling locations. For example, to use a 6^{th} order Taylor polynomial with a 49 points sampling locations on the pupil, the dimensionality will be 49x27.

And,

$$E = DD^T, \tag{3.10}$$

where $_T$ is the matrix transpose operator.

The coefficient vector is then,

$$\hat{A} = E^{-1}D\hat{P} = (DD^T)^{-1}D\hat{P}. \tag{3.11}$$

b)Methods of evaluation of the reconstruction

i) r-squared value

To test the fit, the Pearson correlation coefficient of the fit *pr* can be calculated directly by (Witte, 1989),

$$pr = \frac{J\sum_{j=1}^{J}[P(x,y)_j\delta\xi'(x,y)_j + Q(x,y)_j\delta\eta'(x,y)_j] - \sum_{j=1}^{J}P(x,y)_j\sum_{j=1}^{J}\delta\xi'(x,y)_j - \sum_{j=1}^{J}Q(x,y)_j\sum_{j=1}^{J}\delta\eta'(x,y)_j}{\sqrt{J\left[\sum_{j=1}^{J}[P(x,y)_j^2 + Q(x,y)_j]\right] - \left[\sum_{j=1}^{J}[P(x,y)_j + Q(x,y)_j]\right]^2}\sqrt{J\left[\sum_{j=1}^{J}[\delta\xi'(x,y)_j^2 + \delta\eta'(x,y)_j^2]\right] - \left[\sum_{j=1}^{J}[\delta\xi'(x,y)_j + \delta\eta'(x,y)_j]\right]^2}} \tag{3.12}$$

The pr value describes the wavefront derivatives or transverse aberration fit rather than the wavefront fit. The r-squared value can be obtained by squaring the *pr* value.

ii) Standard error of prediction of the ray aberrations

As a measure of the average amount by which known transverse aberrations values deviate from their predicted values, the standard error of prediction can also be calculated by (Witte, 1989),

$$\text{Standard error of prediction} = \sqrt{\frac{J\left[\sum_{j=1}^{J}[P(x,y)_j^2 + Q(x,y)_j^2]\right] - \left[\sum_{j=1}^{J}[P(x,y)_j + Q(x,y)_j]\right]^2}{J^2}}\sqrt{1-r^2} \tag{3.13}$$

iii) Transverse aberration residuals of the fit

Another method to test the fit would be to check the ray aberrations residual distribution of the fit. In this case, it would be,

$$F_{P(x,y)\,residual} = P(x,y) + \sum_{i=2}^{I} a_i \frac{\partial Z_i(x,y)}{\partial x} \tag{3.14}$$

and

$$F_{Q(x,y)\,residual} = Q(x,y) + \sum_{i=2}^{I} a_i \frac{\partial Z_i(x,y)}{\partial y}, \tag{3.15}$$

where $F_{P(x,y)\ residual}$ is the horizontal component of ray aberration residual after the fit, $F_{Q(x,y)\ residual}$ is the vertical component of ray aberration residual after the fit.

The two components can be plotted as a vector with respect to each corresponding sampling location on the pupil plane with the measured value expressed in the same manner. Such plots can be used to evaluate the residual of the fit.

iv) Propagation of variances

We can also apply linear theory to the estimator to calculate the variance of the estimated coefficients (Cubalchini, 1979). The covariance matrix (C_A) for the estimated coefficients is,

$$C_A = (DD^t)^{-1} DC_p D^T (DD^T)^{-1}, \tag{3.16}$$

where ,

$$C_A = \begin{pmatrix} \sigma^2_{a_2a_2} & \sigma^2_{a_2a_3} & \cdots & \sigma^2_{a_2a_I} \\ \sigma^2_{a_3a_2} & \sigma^2_{a_3a_3} & \cdots & \sigma^2_{a_3a_I} \\ \vdots & \vdots & \vdots & \vdots \\ \sigma^2_{a_Ia_2} & \sigma^2_{a_2a_2} & \cdots & \sigma^2_{a_Ia_I} \end{pmatrix} \tag{3.17}$$

and

$$C_p = \begin{pmatrix} \sigma^2_{P(x,y)_1 P(x,y)_1} & \sigma^2_{P(x,y)_1 P(x,y)_2} & \cdots & \sigma^2_{P(x,y)_1 Q(x,y)_J} \\ \sigma^2_{P(x,y)_2 P(x,y)_1} & \sigma^2_{P(x,y)_2 P(x,y)_2} & \cdots & \sigma^2_{P(x,y)_2 Q(x,y)_J} \\ \vdots & \vdots & \vdots & \vdots \\ \sigma^2_{Q(x,y)_J P(x,y)_1} & \sigma^2_{Q(x,y)_J P(x,y)_2} & \cdots & \sigma^2_{Q(x,y)_J Q(x,y)_J} \end{pmatrix} \tag{3.18}$$

where σ^2 represents variance. In the case of the semi-Maxwellian view ray aberrations measurement, the vernier acuity for various Maxwellian view beam positions across the pupil plane at the periphery of the pupil and at the center of the pupil can be expected to be similar. Equation 3.16 can be simplified as,

$$C_A = E^{-1}\sigma^2{}_p, \tag{3.19}$$

where σ_p is the typical foveal vernier acuity.

Therefore, C_A only varies with the Maxwellian view beam entering positions on the pupil plane (sampling locations) and the mode numbers of the fit. For a small number of sampling locations, and therefore for the estimation of a small number of modes, there may exist an optimal sampling configuration. It appears that this optimal configuration is not known. A square sampling scheme is used in this thesis to provide uniform sampling across the pupil plane.

v) Confidence level interval of the estimated coefficients

From the analysis of variance, the 95% confidence level interval of the estimated coefficients can be calculated to evaluate the significance of each term which can be related to Seidel aberrations. The 95% confidence level interval of the i^{th} estimated coefficient can then be calculated by,

$$\begin{aligned} Lower\ limit_{95\%}[i] &= a_i - 1.96 * \sigma_{a_i a_i} \\ Upper\ limit_{95\%}[i] &= a_i + 1.96 * \sigma_{a_i a_i} \end{aligned} \tag{3.20}$$

where $\sigma_{a_i a_i}$ can be calculated from Eq.(3.16).

vi) Test of the reconstruction algorithm by simulated data

There is always one effective way to test the performance of a data fit algorithm or program: that is to use a known relationship or equation to generate responses with a set of variables and then attempt to find the relationship or equation out of the simulated data. A good algorithm should be able to recover the exact original relationship or equation.

The best way to test the effect of numerical precision on wavefront reconstruction is to use simulated ray aberration data to recover the wavefront aberration equation that used in generating the simulated data.

A typical aberration situation in the human eye is a mix of symmetrical and asymmetrical aberrations.

Assume the wavefront aberration equation is,

$$w(x, y) = 0.1x^3 + 0.1xy^2 + 0.01x^4 + 0.02x^2y^2 + 0.01y^4 \qquad (3.21)$$

where $w(x,y)$ is the wavefront aberration at pupil location (x,y) in microns.

A contour plot and a 3-dimensional plot of this wavefront aberration is shown in Fig. 3.3.

A Mathcad™ program was used to generate ray aberration data from Eq. (3.21) for the pupil sampling locations that would be used in the experiment by (See Appendix III for detail). These generated ray aberration data were used to reconstruct the wavefront aberration with the Maple V™ wavefront reconstruction program (Appendix IV). The reconstructed wavefront is shown in Fig. 3.4.

a) Contour plot

b) 3-D plot

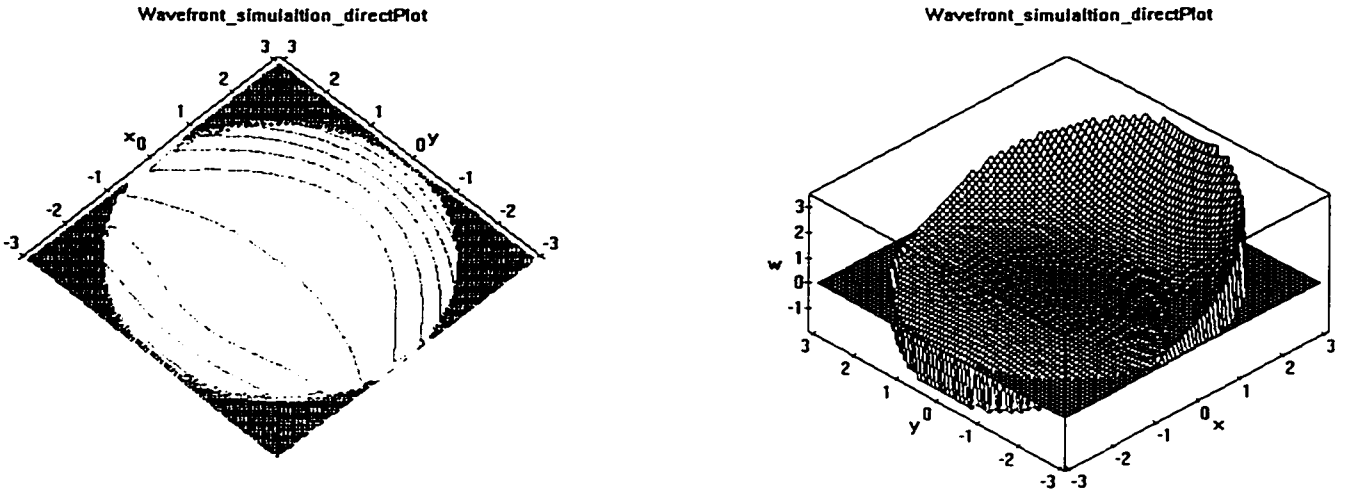


Fig. 3.3 The contour plot and 3-D surface plot of a simulated wavefront aberration of both primary spherical aberration and primary comatic aberration. The pupil is 6 mm in diameter; (a) is the contour plot; the contour interval is 1 wavelength; negative sign represents the nasal side of the eye in the horizontal meridian and the inferior of the eye in the vertical meridian; (b) is the boxed 3-dimensional wavefront plot; the wavefront aberration is in microns. For each plot, there is a caption as a short title of the plot.

a) Contour plot

b) 3-D plot

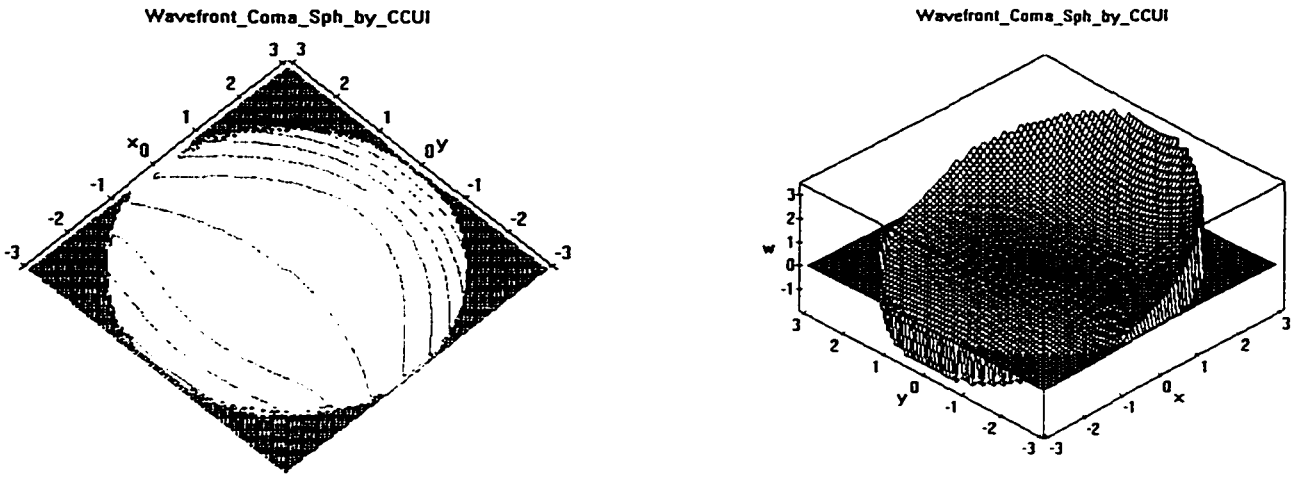


Fig. 3.4 The contour plot and 3-D surface plots of the recovered wavefront. (a) is the contour plot; the contour interval is 1 wavelength; the pupil diameter is 6 mm; negative sign represents the nasal side of the eye in the horizontal meridian and the inferior of the eye in the vertical meridian; (b) is the boxed 3-dimensional wavefront plot; the wavefront aberration is in microns.

The residuals were plotted in Fig. 3.5. Note that the Maple™ plot utility used automatically adjusted the scale range, which makes virtually zero residuals being plotted on a much smaller scale. The residual is indeed close to zero.

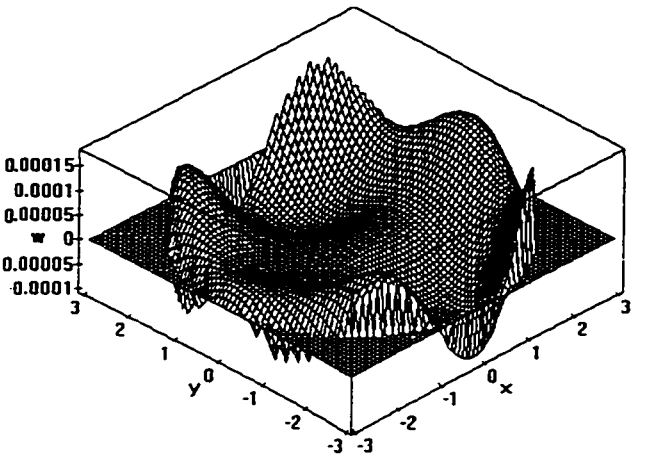


Fig.3.5 3-dimensional residual plots of wavefront aberration reconstruction with simulated data.

The reconstructed Taylor polynomials to the sixth order is,

$$
\begin{aligned}
W := {} & -.7090141100\,10^{-5}x^6 + .2355959693\,10^{-9}x^5 y - .00003954086660\,x^4 y^2 + .6170964704\,10^{-10}x^3 y^3 \\
& - .4686632600\,10^{-5}x^2 y^4 - .5485507603\,10^{-9}x y^5 - .6637030000\,10^{-5}y^6 - .3744356660\,10^{-5}x^5 \\
& + .3867000\,10^{-9}x^4 y + .00003170912481\,x^3 y^2 + .779000\,10^{-9}x^2 y^3 + .00003683098225\,x y^4 + .7000\,10^{-10}y^5 \\
& + 1.000832715x^4 - .7171552416\,10^{-8}x^3 y + 1.002541861x^2 y^2 + .1205797341\,10^{-7}x y^3 + 1.000969955y^4 \\
& + 1.000056646x^3 - .9511000\,10^{-8}x^2 y + .9997118447\,x y^2 + .6000\,10^{-9}y^3 - .0001223265490\,x^2 \\
& - .2901309523\,10^{-7}x y - .0004644447000\,y^2 - .00003945154609\,x + .118000\,10^{-7}y
\end{aligned}
\tag{3.22}
$$

The shaded terms correspond to the terms in Eq. (3.21). It can be seen that Eq.(3.22) and Eq.(3.21) are virtually the same. Again, it proves the superb reliability of the reconstruction theory and program. The 95% interval of the coefficients of the Taylor polynomials calculated with a misalignment error of 20 arc secs is,

$$confidence95 := \begin{bmatrix} -.02713974762 & .02713185732 \\ -.02713580129 & .02713580365 \\ -.009151235989 & .009126770679 \\ -.01292450536 & .01292449956 \\ -.009185447804 & .009092558864 \\ .09715573174 & .1028555975 \\ -.005791336441 & .005791334539 \\ .09417984899 & .1057625200 \\ -.002849932799 & .002849932919 \\ .009129140764 & .01088751354 \\ -.002264324803 & .002264323369 \\ .01688652610 & .02316431112 \\ -.002264322880 & .002264325292 \\ .009130513164 & .01088888594 \\ -.0002686659024 & .0002679170310 \\ -.0008560544190 & .0008560544964 \\ -.001402390763 & .001408732587 \\ -.001405561596 & .001405561752 \\ -.0008523713599 & .0008597375563 \\ -.0002682914597 & .0002682914737 \\ -.00008186884111 & .00008045081289 \\ -.0003178419701 & .0003178420173 \\ -.0006033649682 & .0005954567948 \\ -.0006886792552 & .0006886792676 \\ -.0005998795448 & .0005989422182 \\ -.0003178420482 & .0003178419384 \\ -.00008182353004 & .00008049612404 \end{bmatrix}$$

It shows that only the coefficients of the 6^{th}, 8^{th}, 10^{th}, 12^{th} and 14^{th} terms (shaded regions) are significant using 95% confidence level.

vi) Test of the reconstruction algorithm by simulated data with noise

Assuming the above simulated ray aberration data were measured and an extra measurement error was added on each sampling location, the above tests were rerun with random

errors added based on vernier test results given later in Section 3.6.1. The errors were set to be random between -30 and +30 arc secs with equal probability for each pupil sampling location.

The data with noise were then used in the same manner as above to reconstruct the wavefront aberration. Fig. 3.6 shows that with a 10 digit precision, a close to exact recovery is obtained with an R-squared value of 0.9929454695.

a) Contour plot

b) 3-D plot

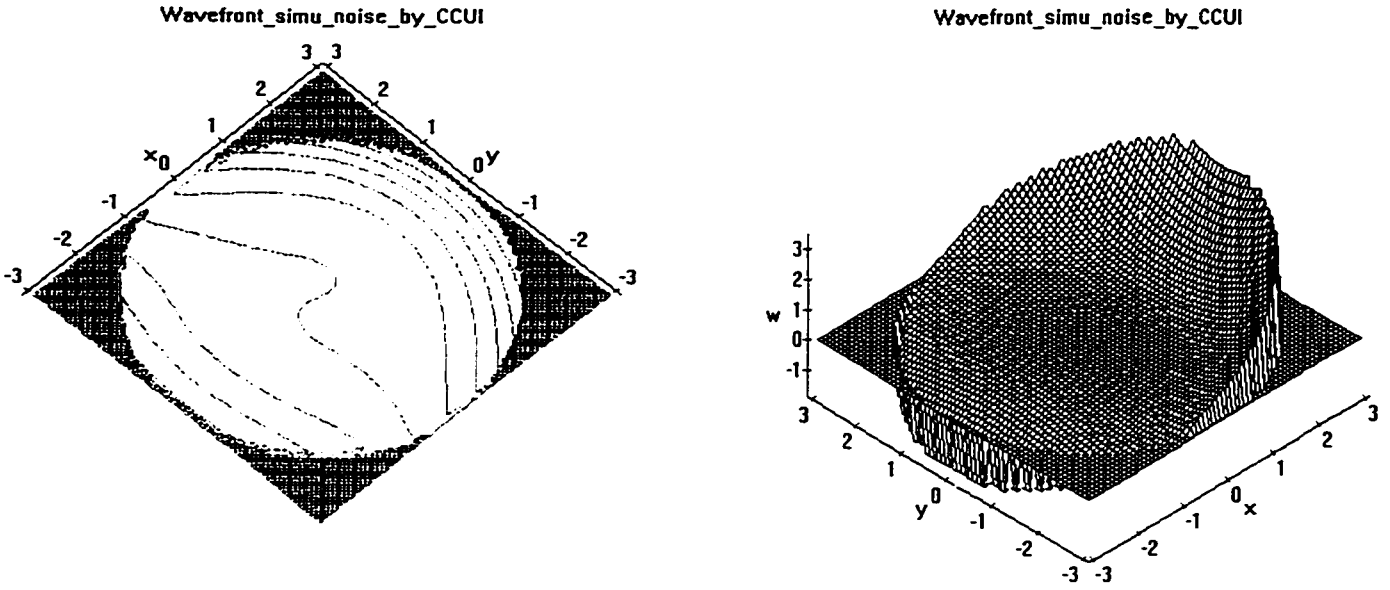


Fig. 3.6 The contour plot and 3-D surface plots of the recovered wavefront with noise. (a) is the contour plot; the contour interval is 1 wavelength; the pupil diameter is 6 mm; negative sign represents the nasal side of the eye in the horizontal meridian and the inferior of the eye in the vertical meridian; (b) is the boxed 3-dimensional wavefront plot; the wavefront aberration is in microns.

The residuals were plotted in Fig. 3.7. The residual indeed shows a random pattern.

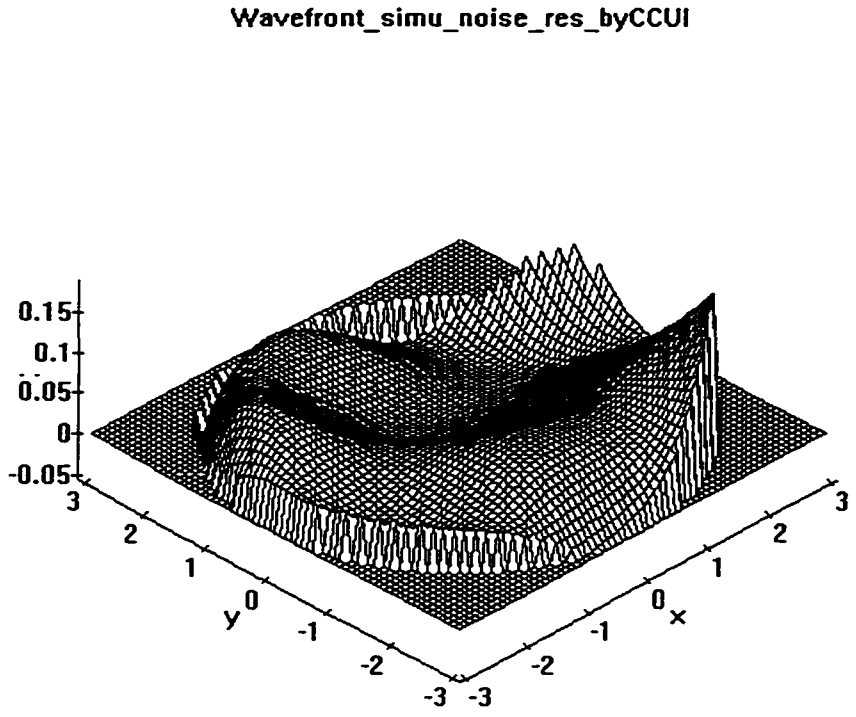


Fig.3.7 3-dimensional residual plot of simulated wavefront aberration reconstruction with simulated measurement noise.

The reconstructed Taylor polynomials to the sixth order is,

$$
\begin{aligned}
W = {} & .0001215758538\,x^6 + .001671510911\,x^5 y + .0005260336831\,x^4 y^2 + .001284161443\,x^3 y^3 \\
& + .0002805793122\,x^2 y^4 - .5225364295\,10^{-5}\,x y^5 + .9724730400\,10^{-5}\,y^6 + .0003130642379\,x^5 \\
& - .00001603007938\,x^4 y + .001213087077\,x^3 y^2 - .002643656105\,x^2 y^3 + .0003702246907\,x y^4 \\
& - .0004248041270\,y^5 + .007540659921\,x^4 - .01428961895\,x^3 y + .01531140679\,x^2 y^2 \\
& - .001965733210\,x y^3 + .008187144011\,y^4 + .09834848793\,x^3 + .008298833846\,x^2 y + .09996987016\,x y^2 \\
& + .008926545299\,y^3 + .01642234642\,x^2 + .007476290579\,x y + .01619424441\,y^2 - .01420418662\,x \\
& - .04682767574\,y
\end{aligned}
\tag{3.23}
$$

The corresponding terms in Eq.(3.23) and Eq.(3.21) are close. Again, it proves the robustness of theory and program against normal random measurement error.

3.2.3 The choice of a reference axis

To define aberrations in the eye, a valid reference axis or point must be defined. Such a reference must be repeatable and easy to access. It should also be of theoretical significance.

a) Geometrical center of the pupil

Most ocular aberration measurements reported used the geometrical center of the pupil as the reference axis. It is assumed that the geometrical center of the pupil defines the line of sight and probably represents the true image position at the fovea. Also it is easily accessible.

There are a few disadvantages to using the geometrical center of the pupil as the reference point: The geometrical center of the pupil may change with different pupil sizes (Walsh and Charman, 1988; Wilson et. al. 1992). It cannot be located with desired precision during clinical procedures (Pande and Hillman, 1993). Also, it may not coincide with the effective center of the pupil, which is defined by the peak of the Stiles-Crawford function for foveal vision (Applegate and Lakshminarayanan, 1993; Gorrand and Delori, 1994).

b) The coaxially sighted corneal reflex

The CSCR refers to the PI of a bright fixation point (source) under a specific condition. Under this condition the fixation source is positioned on the optical axis of the viewing system and the viewing system is positioned with respect to the eye so that the PI of the fixation point source is also on the optical axis of the viewing system. This optical axis of the viewing system essentially is the common optical axis of front surface of the cornea going through the fixation axis. This reference is often used in ophthalmic instrumentation such as some cornea topographic systems and some excimer laser photorefractive surgery systems (Uozato and Guyton, 1987; Applegate and Howland, 1995).

Because of the relative high intensity of PI and its close-to-the pupil-plane location, it is very easy and convenient to use. A theoretical exploration of its significance is given in Chapter 4.

3.3 Methods

3.3.1 Design of the measurement system

The system was mounted on a vibration damped Newport™ 1.2 m x 1.8 m x 0.1 m optical bread board. As shown in Fig. 3.8, white light from a *100 watt* Tungsten-Halogen light source PS1 passed through a 550nm interference filter MCF (bandwidth 10nm). The monochromatic light was then split into two different channels by beamsplitter BS1. For the sake of clarity, the following description is divided into separate sections according to the designated function of each portion of the system .

a) The Maxwellian view channel

Light from this channel of light was projected onto a 200 microns diameter pinhole (PH) which was mounted on an *x-y* translation stage MS12. Immediately in front of the pinhole was a piece of diffuse glass, DG1. An image of the illuminated pinhole was formed at the subject's pupil plane S through flat mirror M1, achromatic lens L4 and flat mirror M3. This channel of light could be blocked by a computer controlled shutter LS. The distance between pinhole PH and L4 was twice the focal length of L4 (*f=1 m*). And, the Maxwellian view point image was two focal lengths away from L4. Thus the magnification of the system is 1.0. A black cross target T1 was mounted onto an *x-y* computerized translation stage via a rigid U-shaped arm. The target was set as close as possible to the Maxwellian view lens L4.

b) The normal view channel

The other channel of light was delivered by a projection system onto diffuse glass DG2 to form a uniformly illuminated area. The projection system consisted of flat mirror M4, lens L1, flat mirror M5, flat mirror M6, lens L2, lens L3 and a neutral density light attenuating wedge NF. Another black cross target T2 was mounted directly onto diffuse glass DG2. A flat round mirror M2 of a diameter of *2 cm* supported by two thin and rigid steel wire legs was mounted in the center of Maxwellian view path. The position of target T2 was set at such a position that mirror M2 was the same distance away from target T1 and target T2, respectively. The brightness of the illuminated area on diffuse glass DG2 could be conveniently adjusted by rotating the neutral density light attenuating wedge NF.

c) Target design

Because aberrations of the eye were to be measured in terms of the separation of two physical targets, one in normal view and the other in Maxwellian view, the design of the targets had to consider various factors that affect vernier acuity. The targets should have optimal thickness, in order to provide the best vernier acuity allowed under the measurement conditions.

Fig. 3.9 is the schematic of the target. The dimensions of the target are 34' (20 mm) long and 1.4' (0.8 mm) thick. These dimensions are within the range reported by others (Westheimer and McKee, 1976) for optimal vernier performance.

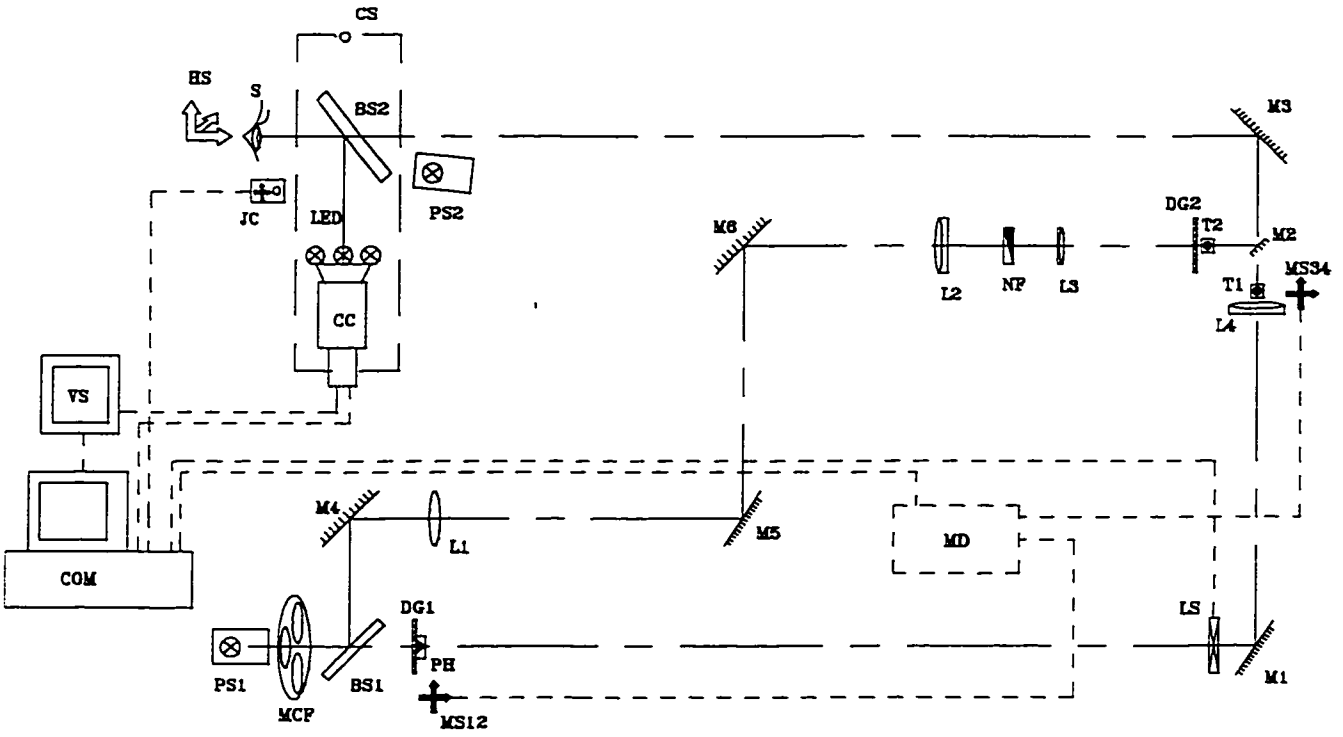


Fig. 3.8 Two dimensional Maxwellian view ocular wavefront aberration measurement system. PS denotes the light source; MCF is the color filter wheel; BS denotes beamsplitter; M denotes flat mirror; PH is the pinhole; MS denotes motorized optical stage; L denotes lens; MD is the motion control driver; LS is the light shutter; NF is the neutral density wheel wedge; DG denotes ground glass; T denotes cross target; CS is the center of rotation of the camera mount system; LED refers to the IR LEDs; CC is the video CCD camera; JC is the motion controlling joystick; S is the subject; HS is the head mount system; VS is the video screen and COM is the host computer; the solid lines represent the optical axis of the system; the dashed lines represent the controlling linkages.

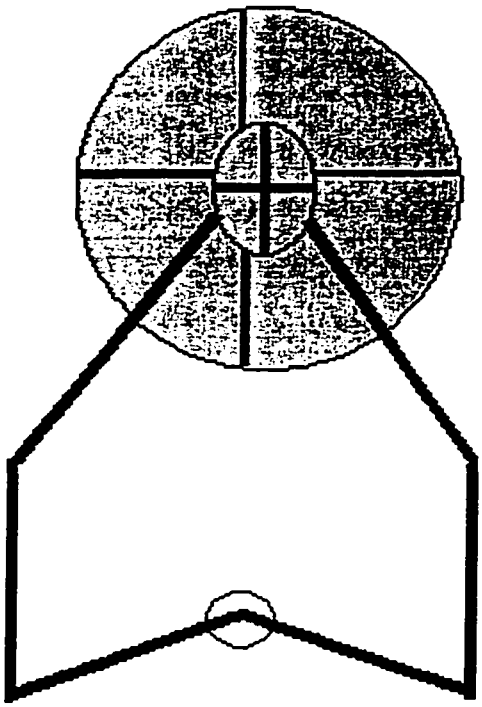


Fig. 3.9 Target configuration. The central ellipse was in the normal view and its size was defined by the edge of the normal view mirror. The central cross in the normal view was the normal view target. The peripheral circle was the Maxwellian view. The outer cross was the Maxwellian view target. The normal view mirror was supported by two steel wires which were mounted on the optical breadboard.

d) The pupil monitoring system

A Tungsten-Halogen source PS2 with an infrared-pass filter was used to illuminate the eye under test. A CCD Camera system CC was set up to capture pictures of the eye under test through beamsplitter BS2. The camera system consisted of a macro lens with a focal length of 150 mm and a Sony™ CCD module with a 512x484 pixel array. There were four IR LEDs mounted onto a ring concentrically mounted to the camera lens. The Camera system, CC, was mounted on a special stage CS that could be adjusted about x, y and z axes. The four IR LEDs

were set to represent the vertical and horizontal axes of the camera. They were not used as the reference in measurements that are described in this chapter.

e) Computer control system

i) Hardware

The host computer COM was a 486DX 33Hz PC with 8M RAM. The Maxwellian view pinhole and target T1 were positioned by four Newport™ Model 070875 DC servo modules equipped with BMCC™ actuators. This positioning system was controlled by the host computer via a Newport MotionMaster™ controller card plugged into the bus of the computer. The MotionMaster™ controller card was also connected to a joystick.

The CCD camera system was driven by a Coreco™ video digitizing board with a resolution of 1024 x 512 pixels installed in the host computer.

Maxwellian view shutter SH and the power supply of the pupil illumination source P2 were controlled by the computer via the parallel port by special wiring.

ii) Software

A basic flowchart is given in Appendix V. All the above intended functions and data acquisition were accomplished by a program written in C as attached in Appendix V.

The program could randomly move the Maxwellian view pinhole image to one of a set of pre-defined positions within the pupil of the eye. The subject could move the Maxwellian view target T1 to any position within its physical range via the joystick.

The subject could also trigger the program to store the final position of target T1 the moment at which an alignment or any other motion was accomplished.

f) Radiation safety

The combined effect of all the radiation sources were well below the corresponding ANSI standards. The evaluation was conservative. The estimated total infrared radiation to the front section of the eye was less than *1 mW/cm²* while the corresponding TLV limit was 10 *mW/cm²* (ACGIH, 1995). The total infrared radiation to retina was less than *1 mW/cm²* while the

corresponding TLV limit for laser sources was 13 mW/cm^2 (ACGIH, 1995; ANSI Z136.1, 1993). The Maxwellian view visible radiation hazard is 2 orders of magnitude below the corresponding TLV limit.

3.3.2 Alignment of the system

Alignment of the system was crucial and is described in detail in Appendix VI.

The subject was positioned with a stand-alone dental bite bar system. The bite bar was mounted on a 3-dimensional translation stage. The bite bar system was aligned with one column of mounting holes on the optical breadboard. Camera system CC was focused on Maxwellian view pinhole image. Thus, if the pupil of the test eye was in focus for the camera system CC, the Maxwellian view pinhole image was in the pupil plane.

3.3.3 Analysis of system errors

a) Aberrations in the Maxwellian view optical system

Optical aberrations of the Maxwellian view projection system would directly contribute to the ray aberrations measured in two different ways.

i) Error in Maxwellian view pinhole image positioning

Because the normal pupil size of the eye is less than 1 cm in diameter, the maximum practical deviation of the Maxwellian view pinhole from the optical axis of the Maxwellian view channel is less than 5 mm. Ray tracing via CODE V™ for the Maxwellian view lens for a pinhole position which is 5 mm off-axis resulted in a position error of 6 microns (equivalent to a 2 arc secs angle), which can be ignored.

To examine the precision of the Maxwellian view pinhole image positioning, a piece of graph paper with printed clear grid was placed at the pupil plane. A bright Maxwellian view pinhole image was then formed on the graph paper when the filter wheel was set to no-filter position. A list of pre-defined Maxwellian view pinhole positions was generated and a program

was used to drive the Maxwellian view pinhole positioning motors to these pre-defined positions. The video monitoring system could then pick up the actual positioning of the Maxwellian view pinhole image on the graph paper with a magnification of 18 times. A series of tests showed that positioning accuracy was as accurate as 0.03 mm.

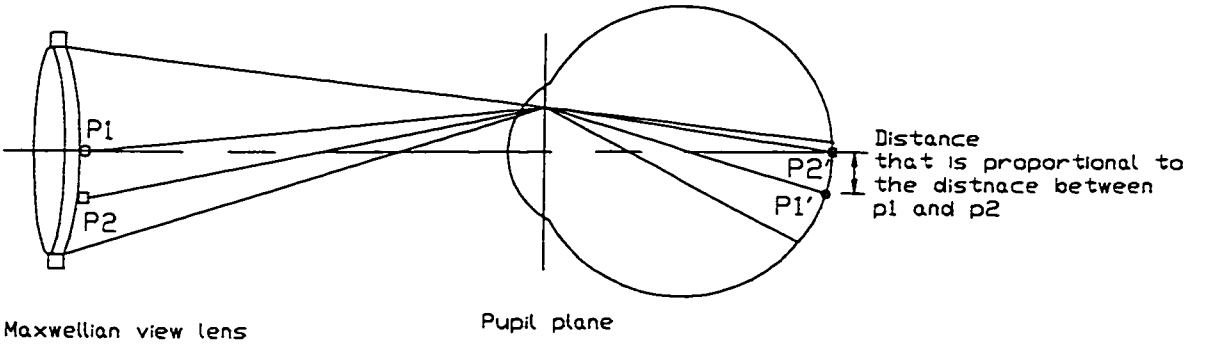
ii) Individual ray error in the Maxwellian view channel

When the centered Maxwellian view target seemed misaligned to the normal view target to the subject, the subject was to move the Maxwellian view target away from the center of the Maxwellian view lens to align the two targets. Aberrations of the individual ray that defines the position of the Maxwellian view target would therefore contribute to errors of the measured aberration value.

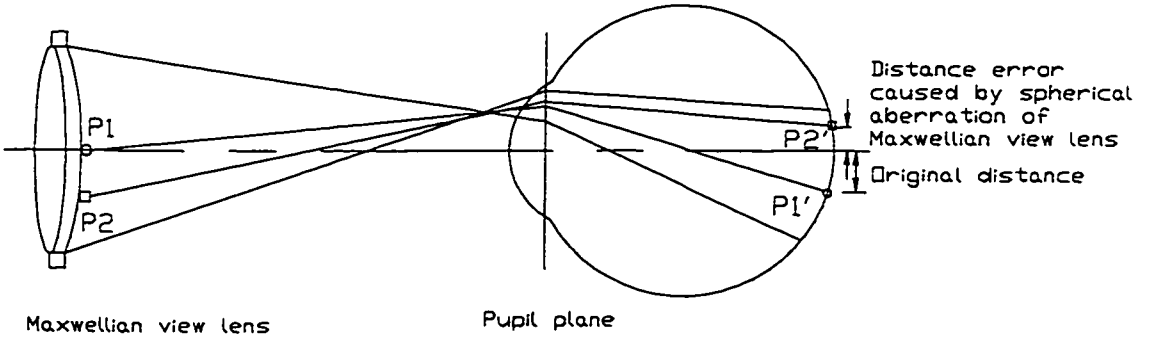
Figure 3.10 illustrates three cases of how aberrations of the Maxwellian lens can affect the measurement of ocular aberrations. The distance between *P1'* and *P2'* should be proportional to the distance between *P1* and *P2*. Only when the two distances are proportional, the distance between *P1* and *P2* can be used to represent the aberration in the eye. In Fig. 3.10 a), the Maxwellian view lens is aberration free. The distance between *P1'* and *P2'* will be the true aberration of the test eye. In Fig. 3.10 b), the Maxwellian view lens suffers from classical under-corrected spherical aberration. The distance between *P1'* and *P2'* will be the measured ray aberration of the eye under test. However, a portion of the ray aberration is caused by spherical aberration of the Maxwellian view lens. In Fig. 3.10 c), the Maxwellian view lens has comatic aberration. The distance between *P1'* and *P2'* will be the measured ray aberration. However, a portion of the ray aberration is induced by comatic aberration of the Maxwellian view lens. Raytracing of the Maxwellian view lens with CODE V™ for a 5 mm Maxwellian view pinhole image position with a Maxwellian view target deviation of 10 mm resulted in an error of 9 arc secs, a negligible quantity(See Appendix VIII).

Fig. 3.10 Effect of the Maxwellian view lens aberrations on the measurement of ocular aberrations. a) Maxwellian view lens has no aberrations, the ray aberration measured in the human eye is the true aberration. p1 is the target at the center of the Maxwellian view lens and it has a shadow image p1'; p2 is the target off the center of the Maxwellian view lens and has a shadow image p2'; the distance between p1 and p2 is proportional to the distance between p1' and p2', it can be used to measure the aberration of the eye; b)Maxwellian view lens has spherical aberration that will cause the difference in the distance between p1' and p2'; the measured aberration will also contain a systematic error caused by the spherical aberration of the Maxwellian view lens; c) Maxwellian view lens has comatic aberration that will cause the difference in the distance between p1' and p2'; the measured aberration will also contain a systematic error caused by the comatic aberration of the Maxwellian view lens.

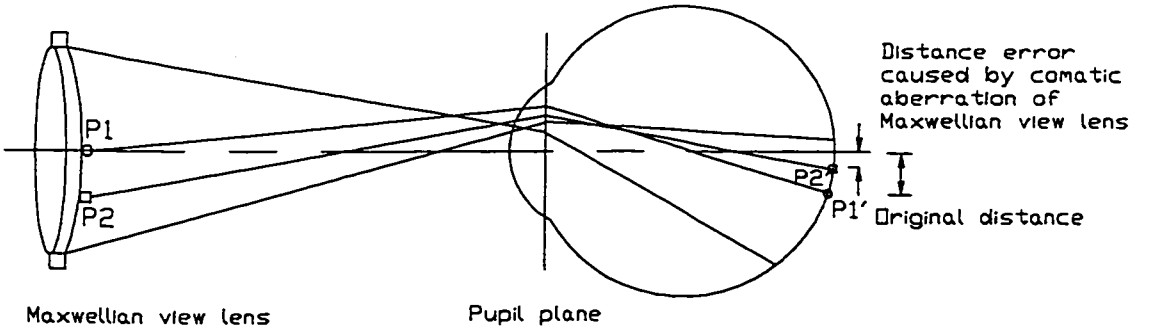
a) Maxwellian view lens with no aberration



b) Maxwellian view lens with spherical aberration



c) Maxwellianview lens with comatic aberration



b) Precision of the Maxwellian view target movement

The Maxwellian view target movement was directly related to the amount of ray aberration measured. The aberration measurement process required the subject to align two vernier targets, one in normal view and another in Maxwellian view by moving the Maxwellian view target. Human vernier acuity was reported at 5 arc secs level at best performance. Five arc secs subtended a distance of about 50 microns in the measurement system. The resolution of the motion system was about 1 micron, which easily satisfied this precision requirement.

c) Precision of the Maxwellian view pinhole movement

Positioning of the Maxwellian view pinhole directly affects the position of the Maxwellian view pinhole image on the pupil plane. A 1 micron precision for the positioning of pupil sampling location was more than sufficient.

3.4 Procedures

3.4.1 Pupil location sampling scheme

For all the measurements described in this thesis, 49 locations uniformly distributed on a 6 *mm* diameter pupil were pre-defined in the position storage file of the program. The sampling locations are shown in Fig. 3.11.

3.4.2 Procedures

Experiment preparation and procedures were as follows,

1) Pupil illumination, camera sensitivity range and camera offset were adjusted to obtain the best pupil picture. A reference box of the approximate size of the pupil was set via the program. The reference box contained a central cross that was centered on the video screen. A clear ruler was placed at the pupil plane and a focused picture was taken and saved for distance measurement calibration. 2) A piece of diffuse glass was placed directly in front of the Maxwellian view lens, and a Tungsten desk lamp was used to illuminate the diffuse glass uniformly. The subject was asked to adjust the light level of the original normal view channel to

match the brightness of the newly converted normal view field by adjusting the voltage output of the power supply to the Maxwellian view. 3) The subject was asked to carefully align the two normal view targets both with the controlling joystick. The subject was encouraged to make a few trials and inform the experimenter when a satisfactory alignment was obtained. The purpose of this procedure was to align the two targets in normal views to set the zero alignment positions of the two targets. 4) The Maxwellian view was restored by removing the diffuse glass away from the Maxwellian view lens and by removing the illumination source.

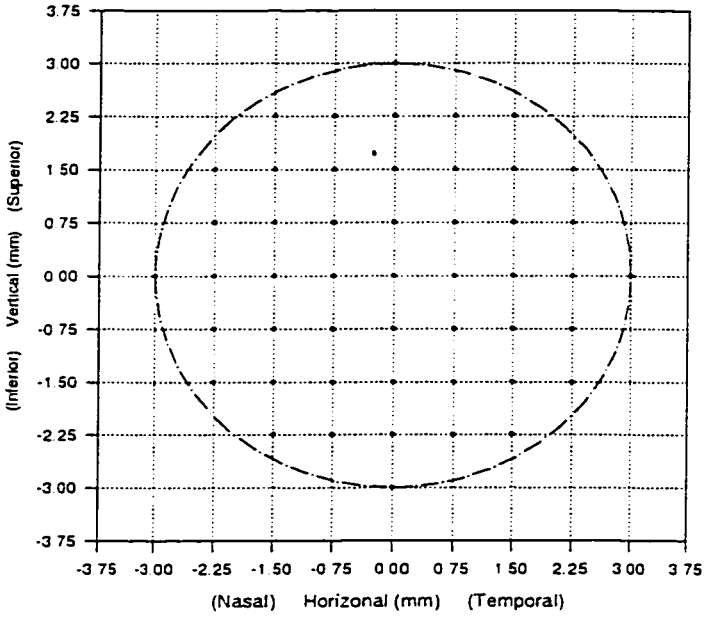


Fig. 3.11 Pupil sampling locations of a 6 mm diameter pupil. The dots represent the predefined sampling locations; these sampling locations are 0.75 mm apart both in the horizontal meridian and in the vertical meridian.

5) The pupil was aligned with the reference box on the video screen and two typical pictures of the pupil aligned with the reference box were saved for future analysis. 6) The aberration measurement was started and the subject was instructed to align the two targets when they seemed misaligned and press the button on the joystick when alignment was achieved. While the

subject was following the program and doing the alignment, the experimenter monitored the centration of the pupil with respect to the reference box on the video screen and restored the alignment whenever a misalignment was apparent. 7) When the subject finished alignments for all the pre-defined locations for the aberration measurement, two pictures of the eye were saved again and the program was terminated to save all the measured data.

3.4.3 Subjects of the preliminary test

To test the performance of the system and to examine the procedures intended, the left eyes of 4 volunteer subjects were tested. They were all males and were at an age between 25 to 35 years old. None of the subjects had any known pathology and all had uncorrected acuity better than 6/6.

3.5 Results and analysis

The left eye of subject AR was measured three times under the same conditions. The left eye of subject AG was measured two times. The left eyes of the rest of the subjects were measured one time. Each measurement took about 45 minutes. Subject AR was tested many times by using a one-dimensional version of the semi-Maxwellian view aberration system. The rest of the subjects had had no experience of this type of measurement prior to the test.

3.5.1 Direct diagrams from the measured ray aberration data

Because alignment of the pupil with the measurement system was maintained during the experiments, only some pupil pictures were saved for future analysis and reference. The program automatically placed the ray aberration data into a text file with the corresponding pupil sampling locations. The ray aberration data were directly used to generate a diagram to show the general aberration situation in the eye measured or to compare two different measurements.

Fig. 3.12 shows the diagrams of all measurements. These diagrams are plots of the raw data. Therefore, aberrations are represented by the Maxwellian vernier target misalignment from the normal view vernier target in millimeters in object space. In the horizontal meridian, the positive sign represents the Maxwellian view target moved to the temporal side of the subject; in the vertical meridian, the positive sign represents the Maxwellian view target moved to the superior. For subject AR, the three different measurements were all plotted on the same diagram with the same type of symbol. Similarly, for subject AG, the two different measurements were also all plotted on the same diagram with the same type of symbols. These diagrams generally confirmed the large between-subject variations found.

3.5.2 Wavefront aberration reconstruction from ray aberration data

The text file was called into the Maple V™ wavefront reconstruction program. The program performed wavefront reconstruction with a contour plot, a 3-dimensional wavefront plot, a 6th order Taylor polynomial, the r-squared value of the fit and the 95% confidence interval of the obtained Taylor coefficients. These calculations and graphs were accomplished in the Maple V™ program as listed in Appendix IV and could be done in about 15 minutes with a typical PC 486 machine (33Hz, 8M ram) when the experiments were performed. With a Cyrix® 686 P150+(16M ram) PC that is now used the above calculations and graphing takes less than 2 minutes.

The contour plots and 3-dimensional plots are given in Fig. 3.13.

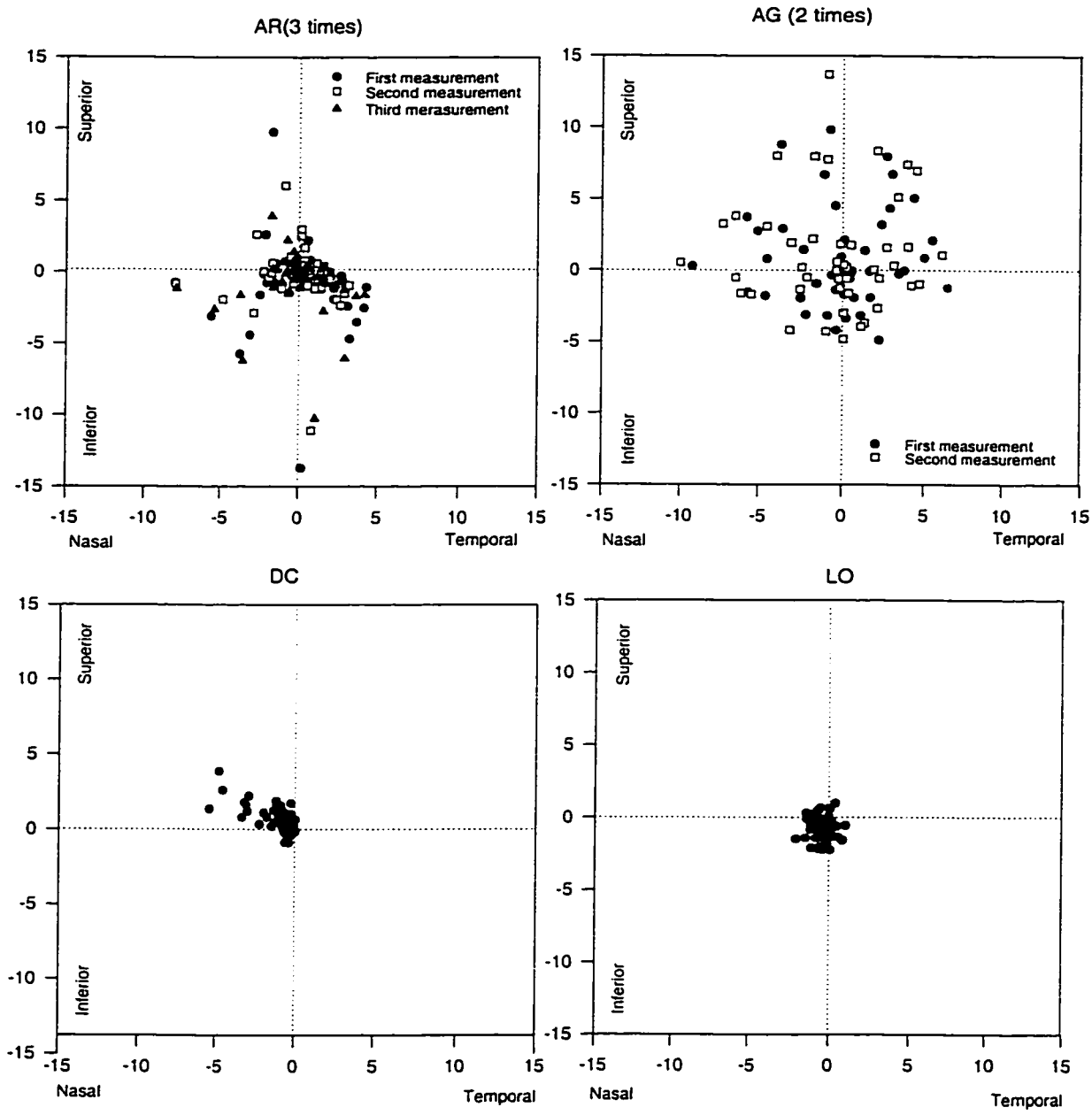
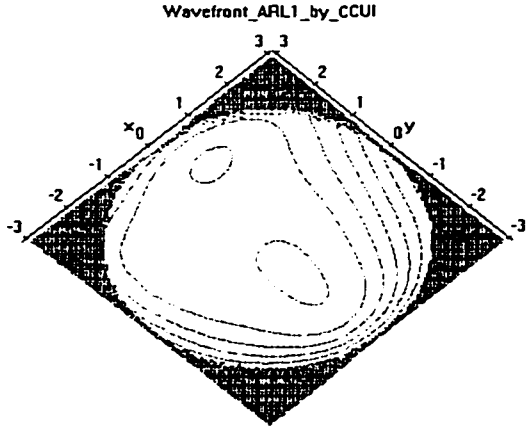
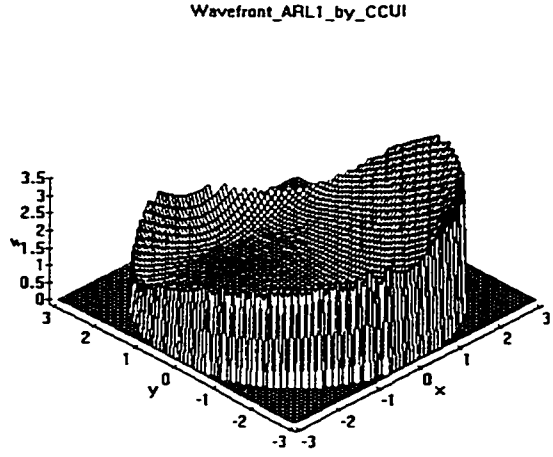
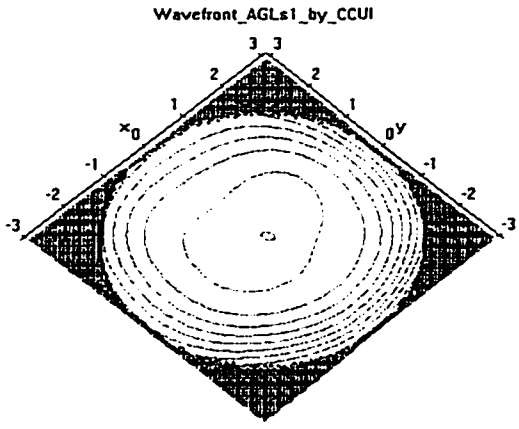
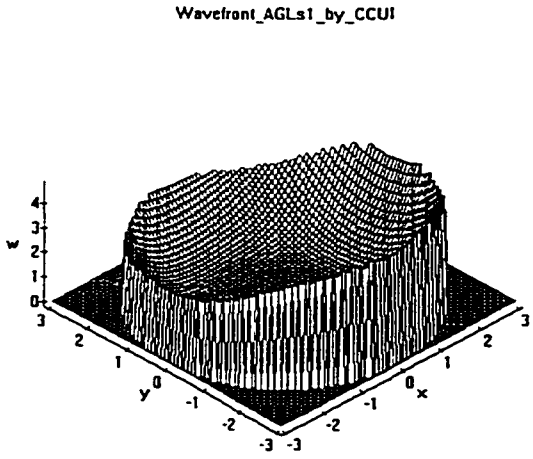
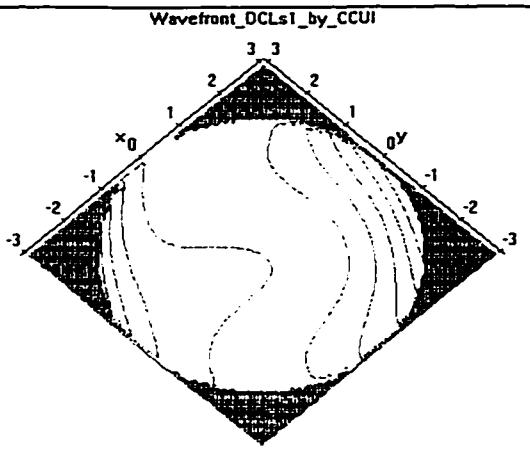
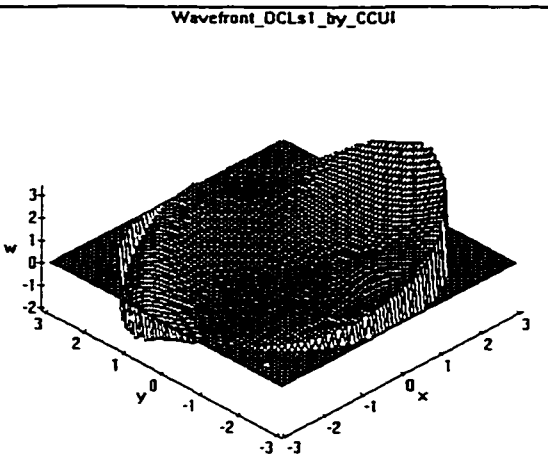
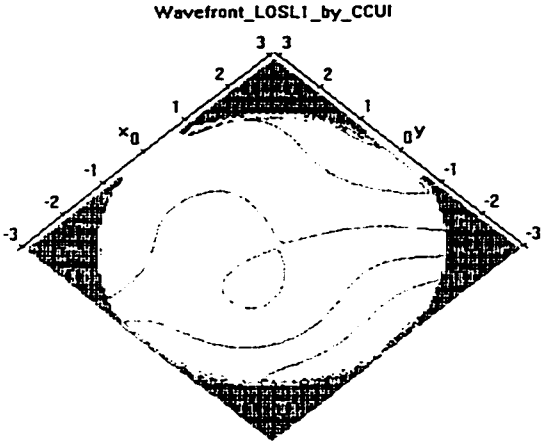
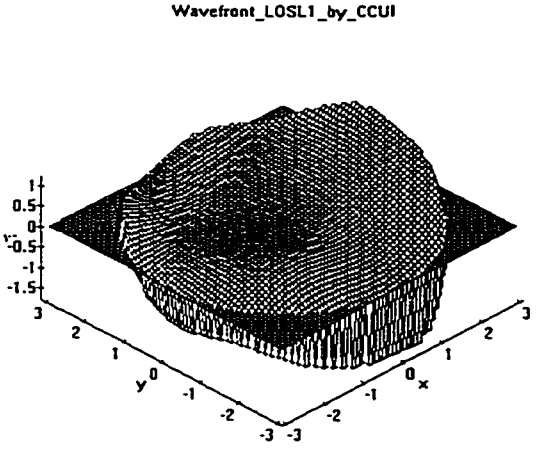


Fig. 3.12 Diagrams from the measured ray aberration data or the target misalignments in object space. The misalignment is in mm; the diagram of Subject AR consists of results of three different sessions plotted together; the diagram of Subject AG consists of results of two different sessions; the diagram of each other subjects consists of data of one measurement session.

Fig. 3.13 Contour plots and 3-dimensional plots of wavefront aberrations measured. For each subject, there is a contour plot and a 3-dimensional plot. The positive sign denotes the temporal side and the superior of the eye in defining the pupil sampling locations; the interval of the contour plots is one wavelength; the scale of the 3-dimensional plot is in microns. For the 3-dimensional plot, the wavefront deviation points into the eye.

	Contour plot	3-dimensional plot
AR		
AG		

DC	Wavefront_DCLs1_by_CCUI	Wavefront_DCLs1_by_CCUI
LO	Wavefront_LOSL1_by_CCUI	Wavefront_LOSL1_by_CCUI

The corresponding 6th order Taylor polynomials are tabulated in Table 3.1.The data for AR and AG is the first measurement.

Table. 3.1 The 6th order Taylor polynomial and the r-squared values of the wavefront aberration reconstruction. The r-squared value is in parenthesis under the subject's initial.

Subject (R-squared)	Taylor polynomials up to the 6th order
AR (0.9621)	$W = .001344617435\,x^6 + .0007700987419\,x^5y - .002324342202\,x^4y^2 + .007690704410\,x^3y^3 + .005931885431\,x^2y^4 + .004066850804\,xy^5 + .006120320706\,y^6 - .007874483327\,x^5 + .004446672563\,x^4y - .01233081207\,x^3y^2 + .003344725490\,x^2y^3 - .006596735060\,xy^4 - .0003248035300\,y^5 + .0003908381220\,x^4 - .009651703124\,x^3y + .02980304571\,x^2y^2 - .04449642723\,xy^3 - .03081157843\,y^4 + .07803886874\,x^3 - .1365644752\,x^2y + .03368460742\,xy^2 - .03719928470\,y^3 + .1849267620\,x^2 - .03278783106\,xy + .05150054550\,y^2 + .05180728689\,x + .1028420025\,y$
AG (0.9643)	$W = -.003950228345\,x^6 - .002727609181\,x^5y - .01057738413\,x^4y^2 - .009241331296\,x^3y^3 - .01039498165\,x^2y^4 - .008454351058\,xy^5 - .003924632055\,y^6 + .004283373588\,x^5 + .007887844457\,x^4y + .003067072356\,x^3y^2 - .003017682845\,x^2y^3 + .002830029168\,xy^4 - .001759609776\,y^5 + .09652363818\,x^4 + .03645221576\,x^3y + .1654208751\,x^2y^2 + .07969132125\,xy^3 + .09195563083\,y^4 - .02831638390\,x^3 - .08300733105\,x^2y - .03007610109\,xy^2 - .02916131445\,y^3 - .1725587675\,x^2 - .1040043490\,xy - .1018230610\,y^2 + .03553387042\,x + .01642284330\,y$
DC (0.9409)	$W = -.0003171061287\,x^6 + .002085355828\,x^5y - .002149894186\,x^4y^2 + .004823340630\,x^3y^3 - .004011865481\,x^2y^4 + .004953500906\,xy^5 - .0006821841003\,y^6 + .002322397649\,x^5 - .006912433644\,x^4y + .009739829757\,x^3y^2 - .008155398719\,x^2y^3 + .008469335770\,xy^4 + .0005874921872\,y^5 + .005524189061\,x^4 - .02966193491\,x^3y - .005421930252\,x^2y^2 - .05087812498\,xy^3 - .001912421677\,y^4 + .03315546617\,x^3 - .03357559510\,x^2y - .01804997181\,xy^2 - .03204137522\,y^3 + .08885006131\,x^2 + .1018938208\,xy + .1451378359\,y^2 + .1432752559\,x + .02177415745\,y$
LO (0.6589)	$W = .0009294316400\,x^6 + .005269018395\,x^5y + .004703605248\,x^4y^2 + .005545781648\,x^3y^3 - .0008831579439\,x^2y^4 + .005389364330\,xy^5 - .001194513608\,y^6 - .003509806597\,x^5 - .001890215989\,x^4y - .007414624647\,x^3y^2 - .006580429326\,x^2y^3 + .002040196659\,xy^4 - .005276110680\,y^5 - .01682172184\,x^4 - .06881942577\,x^3y - .006312921731\,x^2y^2 - .06393679051\,xy^3 + .01962731901\,y^4 + .06996439609\,x^3 + .05521149847\,x^2y - .001160634273\,xy^2 + .09009394624\,y^3 + .08474989125\,x^2 + .2310722190\,xy - .1577994516\,y^2 - .02326364996\,x - .03866141935\,y$

3.6 Discussion

Results from measurements of the 4 subjects demonstrated the effectiveness of the measurement system. The results confirmed the general irregular characteristics of monochromatic aberrations as found by other measurements (Smirnov, 1961; Howland and Howland, 1977). Those characteristics include large variations between individual subjects and the frequent dominance of asymmetrical aberrations.

3.6.1 Repeatability and error analysis

The subjects showed some variations in head-eye position during each session. Subject AR's position was stable for a few minutes but drifted gradually for a relatively longer period of time. Subject AG was very stable from the beginning to the end of a measurement session. Subject DC was stable but had a problem with the upper eye lid that always cut into the upper part of the pupil. Because the measurements were conducted with natural pupil condition, the pupils of all subjects showed large fluctuation during the measurements, which had no doubt contributed to the errors of positioning the Maxwellian view beam on the pupil plane.

a)Ray aberration data

Experimental data measured at two different times of the same eye of the same subject may be different. As shown in Fig. 3.14, the ray aberration data of subject AR's left eye from 3 different measurements were plotted with respect to the corresponding pupil sampling locations. In the plot, zero aberration is represented by the corresponding symbol imposed at the sampling location. The further away the symbol deviates from the sampling location, the larger the magnitude of the ray aberration. Their signs are from the raw measured data and are therefore opposite to the signs of the pupil coordinates.

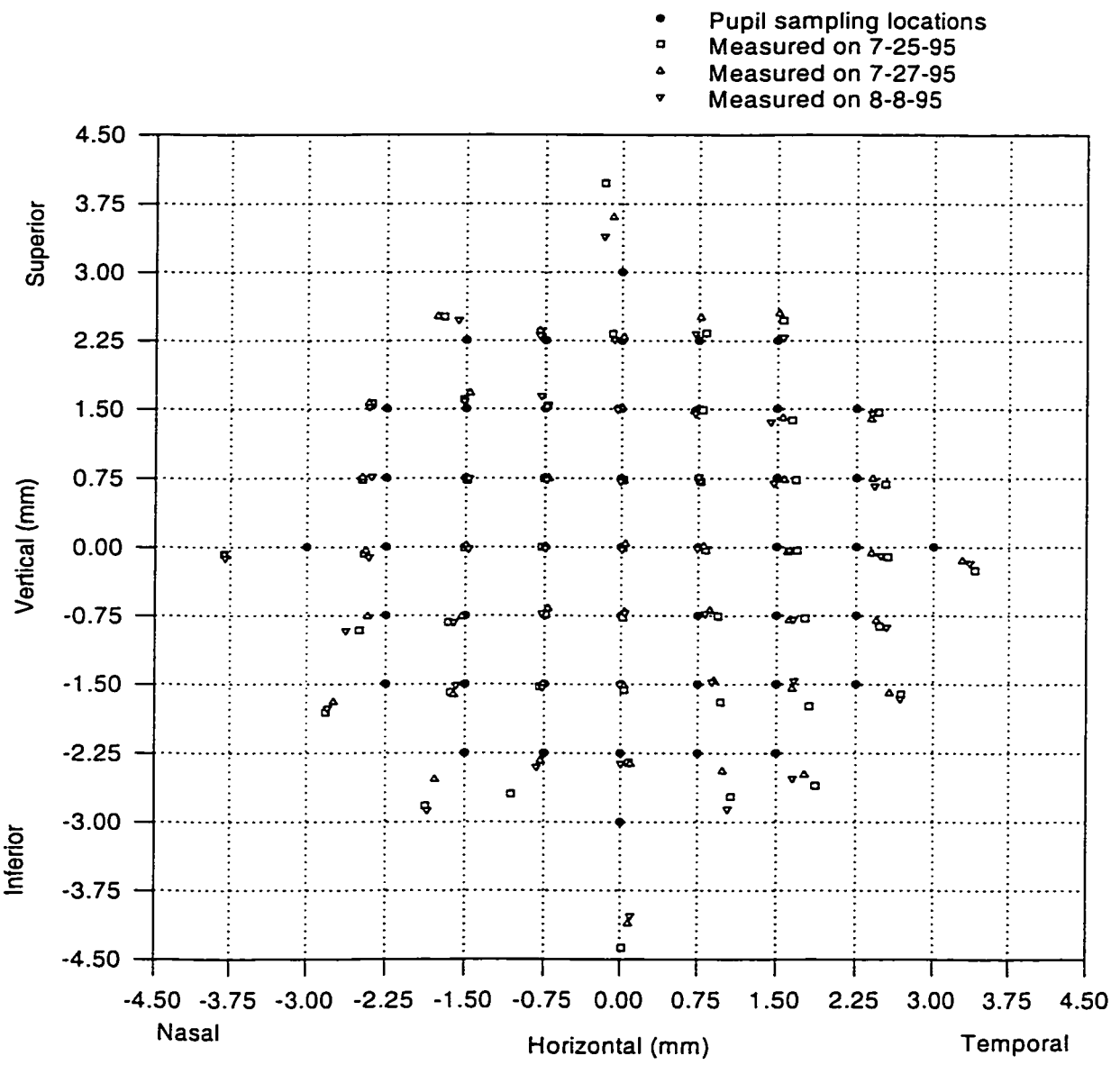


Fig. 3.14 Ray aberrations data of AR's left eye measured 3 times. The filled circles are the pupil sampling locations; the rest of the symbols represent the ray aberrations measured for three different times as indicated by the legend. Each symbol represents the corresponding ray aberration using the deviation of the symbol from the corresponding sampling location.

In this graph and the same type of graph after here, all the aberration values are scaled down to 10%. The difference in aberration measured from the same eye at two different times could be caused by three different factors: a) subject's vernier targets alignment errors; b) sampling location errors that were directly related to the experimenter's ability to center the pupil; and c) true aberration changes of the eye.

Considering vernier acuity error for this subject, the largest measured ray aberration difference happened at pupil location *(0,3.00)* between the first and the last measurement. There was a difference of *5.829* mm in measured target misalignments. Such an error corresponds to an angular value of *10* minutes of arc, which is *60* times worse than the typical vernier acuity. Therefore it was unlikely that the vernier alignment error was the major cause.

However, it can be shown that such an error could be introduced by a *0.48* mm pupil sampling location error that was possible given the method used in defining the geometrical center of the pupil. Pupil sampling location error could be caused either by the experimenter's failure to center the test eye with expected precision or by the true change of pupil center during the measurement. Because the measurements were under natural pupil conditions, large pupil size fluctuations were observed.

Also, a ray aberration difference of *5.829* mm in measured target misalignment corresponds to a difference of *2.098* microns in reconstructed wavefront aberration value. Since the lacrimal liquid film is about 5 microns thick and pupil location *(0,3.00)* is close to the upper eye lid, a tear film thickness change might also produce such a real aberration change (Smirnov, 1961).

Lastly, although the accommodation stimulus was strong, accommodation fluctuation could also cause large measurement errors.

b) Vernier alignment errors

To test the repeatability of the system in locating a specific sampling location, to test how well the experimenter can center the subject's pupil and to test the ability of the subject to align the two targets, a special test was designed for subject AR in a separate experiment. The pupil sampling location table was changed to a special table of only three sampling locations. They were position (0,0), (3,0) and (0, 1.5). Each of these three locations was repeated 20 times during the aberration measurement. The experiment was run as normal except that only three pupil sampling locations were repetitively used. The result is 20 alignments for each of the three sampling locations as shown in Fig. 3.15. Table 3.2 tabulates the standard deviations and maximums of both meridians of the three special pupil sampling locations.

Table 3.2 The standard deviations and maximums of the alignment errors of subject AR for three pupil sampling locations.

Pupil sampling	(0.0, 0.0)		(3.0, 0.0)		(0.0, 1.5)	
Location(mm)	Horizontal	Vertical	Horizontal	Vertical	Horizontal	Vertical
STDV(arcsec)	22	34	38	28	21	27
MAX(arcsec)	41	-124	-193	147	62	-67

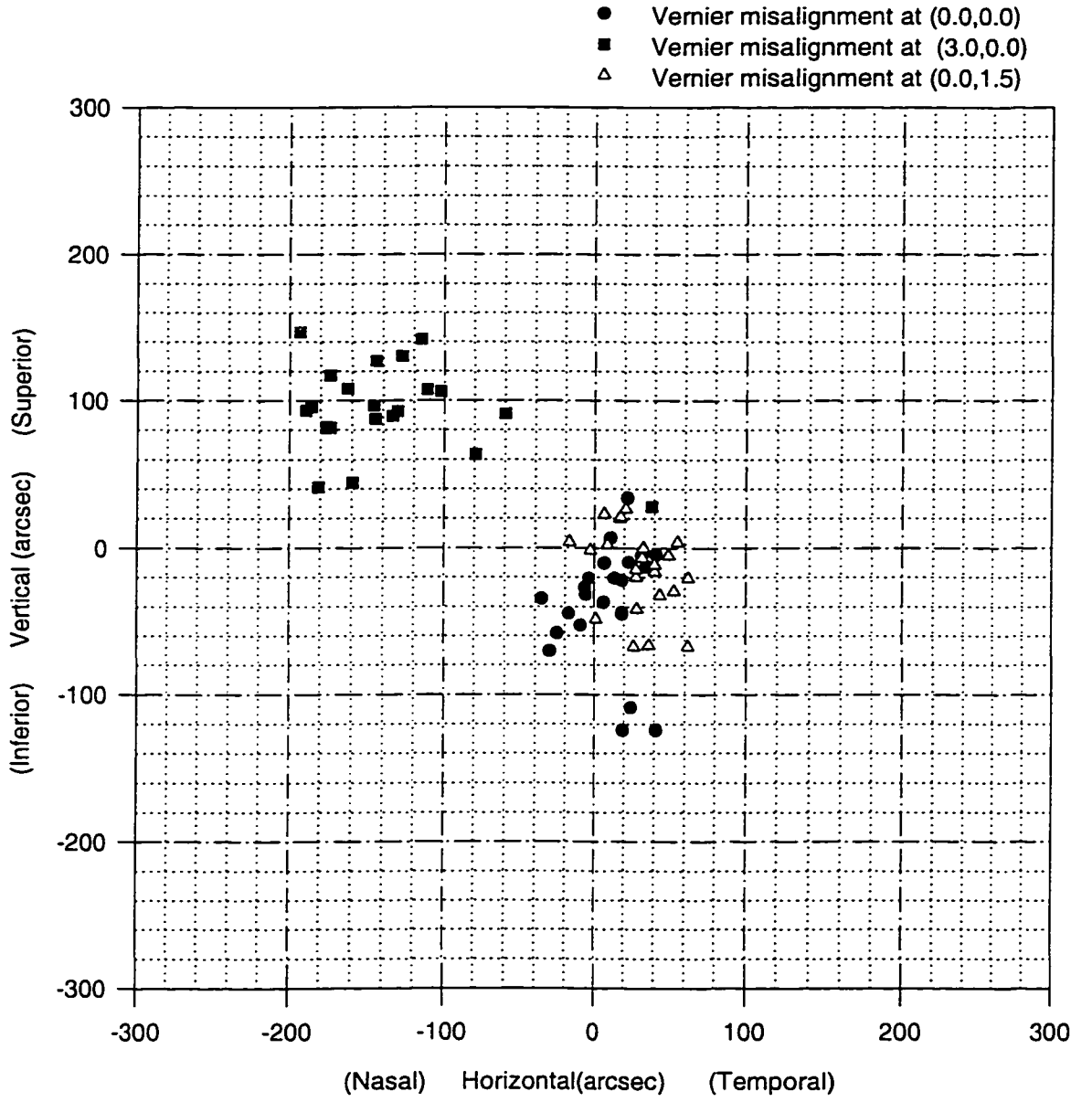


Fig. 3.15 Ray aberrations of three sampling locations of AR's left eye. Each sampling location was repeated for 20 times. The aberration data were plotted as three clusters of symbols. The filled circles represent aberrations measured at (0, 0); the filled squares represent aberrations measured at (3.0, 0); the open triangles represent aberrations measured at (0, 1.5).

c) Pupil alignment error

The sampling location error arose from two sources: eye movement and pupil decentration.

From Fig. 3.14, it is obvious that the aberration differences between two measurements for the same eye is proportional to the magnitude of ray aberration value. Therefore, at the edge of the pupil, small amount of sampling location error due to pupil location error could produce large wavefront aberration variations.

To examine this effect, the reconstructed wavefront Taylor polynomials function of AR's left eye for the third time was used to test the effect of eye movement. Along the horizontal meridian, 5 different sampling locations *0.1* mm apart were used to calculate the corresponding wavefront aberrations. Table 3.3. shows that a 0.1mm position error produces a large change of aberration.

Table 3.3 Sensitivity of the measured wavefront aberration change due to small sampling location change.

Sampling locations (x ,y) (mm)	(-2.8, 0)	(-2.9, 0)	(-3.0, 0)	(-3.1, 0)	(-3.2, 0)
W(x,y) (λ)	1.355	1.702	2.105	2.570	3.101

To determine the experimenter's alignment precision, a special experiment was done. Subject LO, who was observed to have a less stable pupil centration, was the subject. During the measurement of subject LO's left eye, the picture of the subject's pupil was saved each time when the subject finished the targets alignment and pressed the button on the joystick. The pupil decentration with the axis of the camera system was then measured and plotted as in Fig. 3.16.

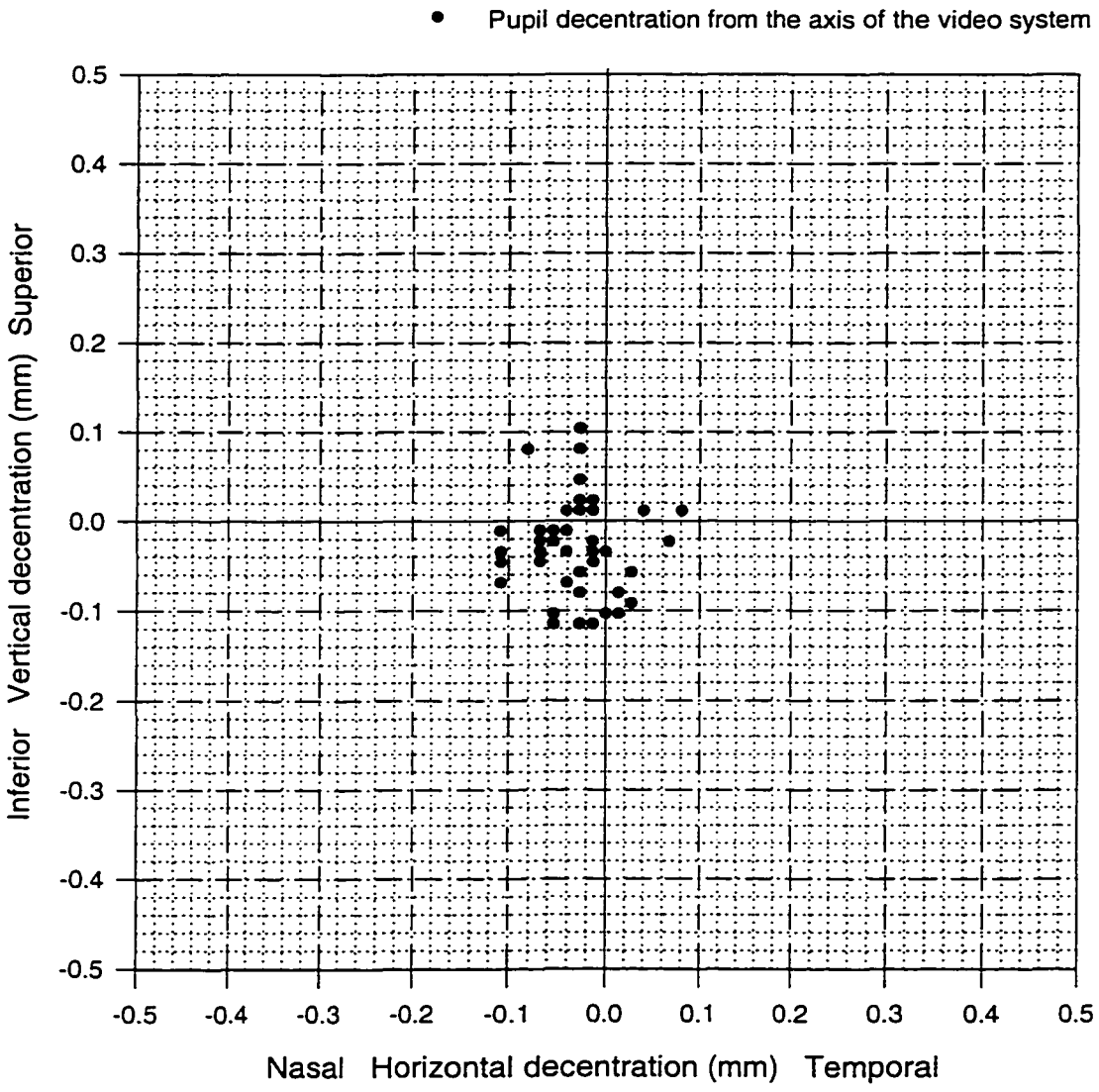


Fig. 3.16 Pupil centration errors of subject LO during the aberration measurement. The filled circles are the measured pupil centers with respect to the center reference of the video system, which is represented by point (256, 242) on the video screen.

The standard deviation of the pupil center shift is *0.05* mm both for the horizontal and the vertical dimensions. The maximum pupil shift is *0.1* mm both for the horizontal and vertical dimensions. The actual aberration difference of two measurement session for subject AR could be as large as 2.1 microns, which is equivalent to a 0.48mm pupil centration error. This result tends to prove that the large ray aberration difference between two measurements of subject AR might not come solely from a pupil centration error.

d) Wavefront reconstruction from the difference of ray aberration data measured in two different measurements

One of the ways to examine the fit is to calculate the difference in the measured ray aberration of two different times and reconstruct the wavefront difference from the differences of the measured ray aberration. If the difference is due to random experimental errors, the wavefront fit would be a bad fit indicated by a low R-squared value. If there is true aberration change of the eye between the two different measurements it should be possible to reconstruct the wavefront with an acceptable R-squared value.

Fig. 3.17 shows the wavefront difference plots (both the contour plot and the 3-d plot)reconstructed from the difference of ray aberration data of the first and the second measurements of subject AR. The r-squared value of the fit is *0.70*. The mean squared wavefront aberration change for a 6 mm pupil from the first measurement to the second measurement was *0.41* micron^2.

Fig. 3.18 shows the wavefront difference plots (both the contour plot and the 3-dimensional plot)reconstructed from the difference of ray aberration data of the second and the third measurements of subject AR. The r-squared value of the fit is *0.40*. The mean squared wavefront aberration change for a *6* mm pupil from the second measurement to the third measurement was *0.09* micron^2.

a) Contour plot

b) 3-dimensional plot

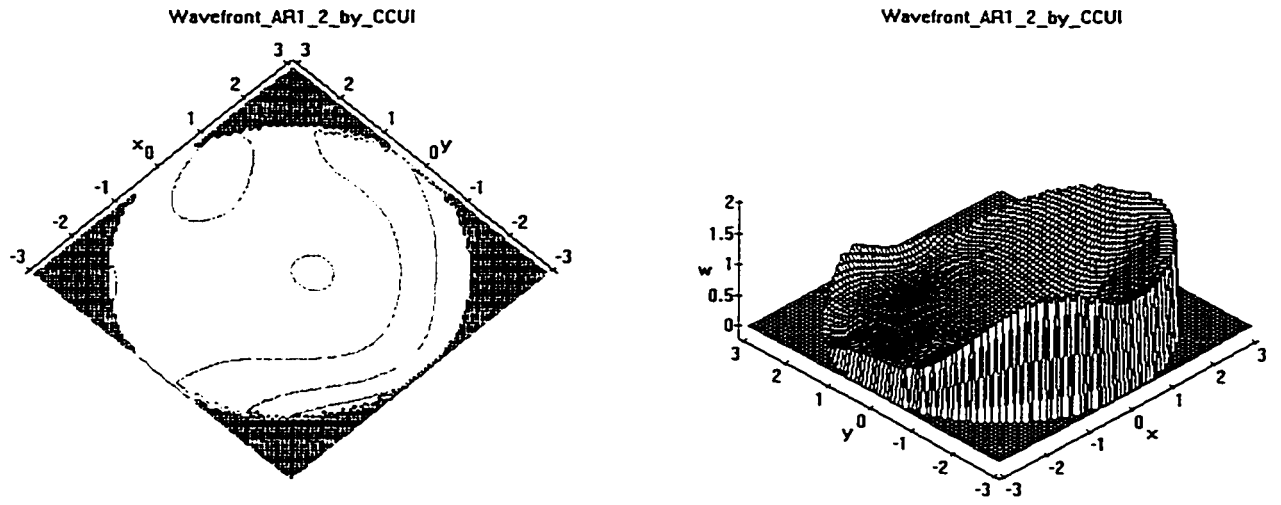


Fig. 3.17 Wavefront difference reconstructed from the difference of ray aberration data of AR's 1st and 2nd measurements. a) is the contour plot ; b) is the 3-dimensional plot. The contour interval in a) is 1 wavelength; in b), wavefront aberration is in microns.

a) Contour plot

b) 3-dimensional plot

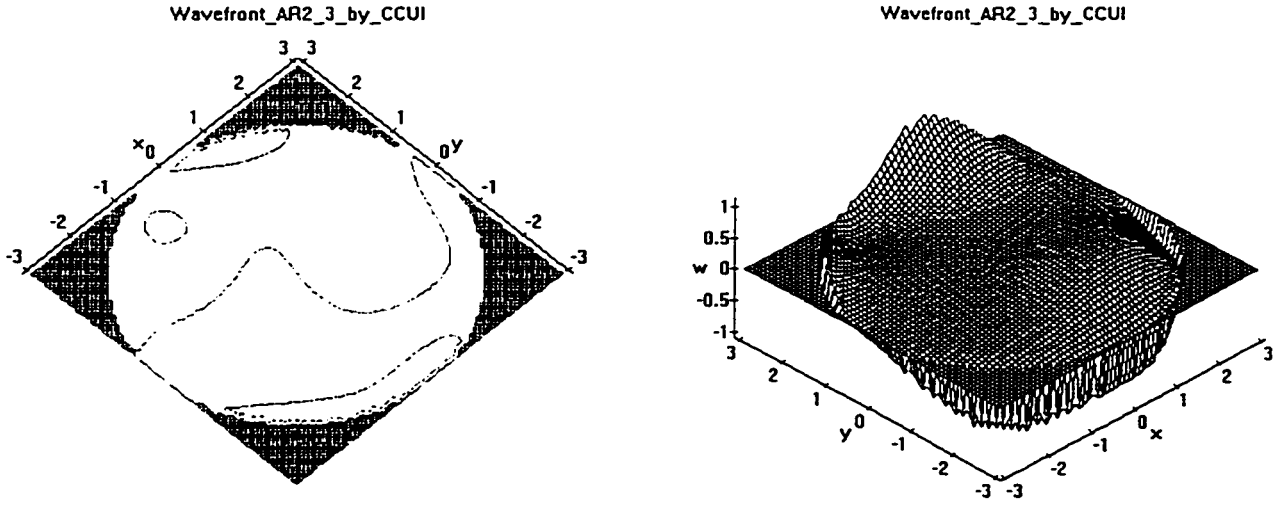
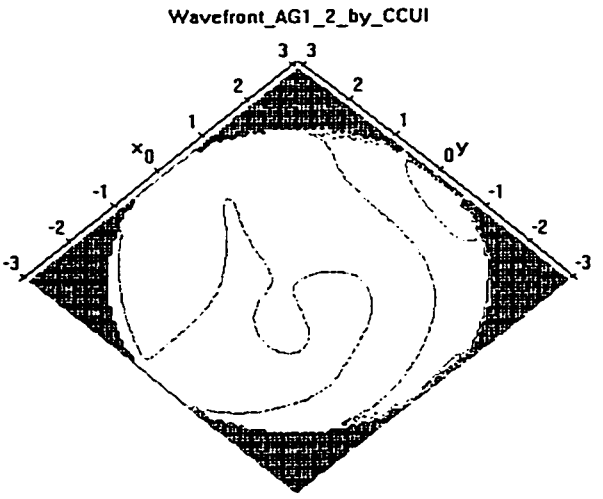


Fig. 3.18 Wavefront difference reconstructed from the difference of ray aberrations data of AR's second and third measurements.

Fig.3.17 shows significant aberration difference with an r-squared value as high as 0.7 between subject's first and second measurements. Fig. 3.18 shows a smaller scale difference with an r-squared value of 0.4 between the second and third measurements. On the other hand, wavefront aberration contour plots and the 3-D plots of all three measurements show very similar patterns. In other words, the differences are on a smaller scale compared to the total wavefront aberration. The difference shown between the second and third measurements was more likely due to random experimental errors such as sampling location error and subject's vernier alignment error. The difference between the first and second time was more likely due to a true aberration change.

Fig. 3.19 shows the wavefront difference plots reconstructed from the difference of the ray aberration data from the two sessions of subject AG. The r-squared value of the fit is 0.57.

a) Contour plot



b) 3-dimensional plot

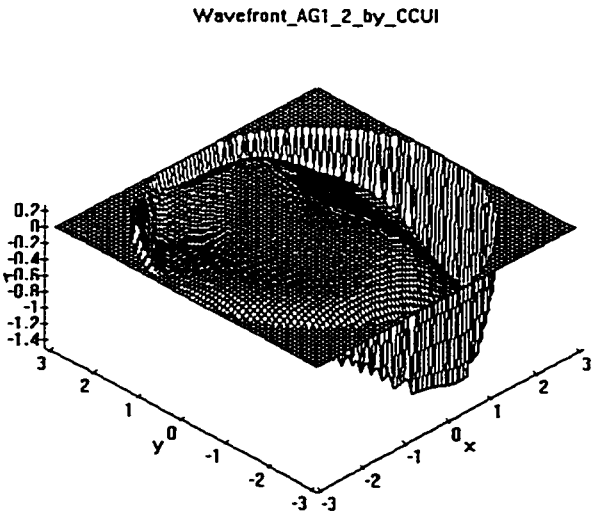


Fig. 3.19 Wavefront difference reconstructed from the difference of ray aberrations data of two measurements of AG.

Fig. 3.19 shows that the difference between the two different sessions of subject AG was similar in magnitude to that of subject AR but changed in a different direction. This suggests that the difference in the wavefront aberration measured in different sessions may show some intra-subject variability.

Overall, both subject AR and subject AG showed significant changes in their aberrations measured on repeated sessions. Measurement differences between two different sessions could be due to an actual change in aberration or measurement errors, or both. Actual aberration change could be a result of lacrimal film thickness change (Smirnov, 1961) and other structural change of the eye such as accommodation fluctuation of the lens, etc. Pupil centration errors probably contributed to a relatively larger portion of measurement errors, as elaborated in Section 3.6.1 c. Criteria shift in terms of what was aligned to the subject could also contribute to measurement errors. Although significant based on the r^2 value of the difference plots as given in Fig. 3.17-3.19, the overall qualities of the aberrations remained the same.

3.6.2 Measured wavefront aberrations compared to other measurements

Most of the previous wavefront aberration measurements produced very similar results although both the methods and subject populations were different. There are always dramatic between-subject variations of measured aberrations. However, the results of the group averages are similar. The majority of published wavefront reconstruction used 4^{th} order Taylor polynomials (Howland and Howland, 1977; Walsh et. al. 1984; Atchison, et. al. 1995). The coefficients of these 4^{th} order Taylor polynomials were usually represented by a single alphabetic letter in the alphabetic order from *A* to *O*. For

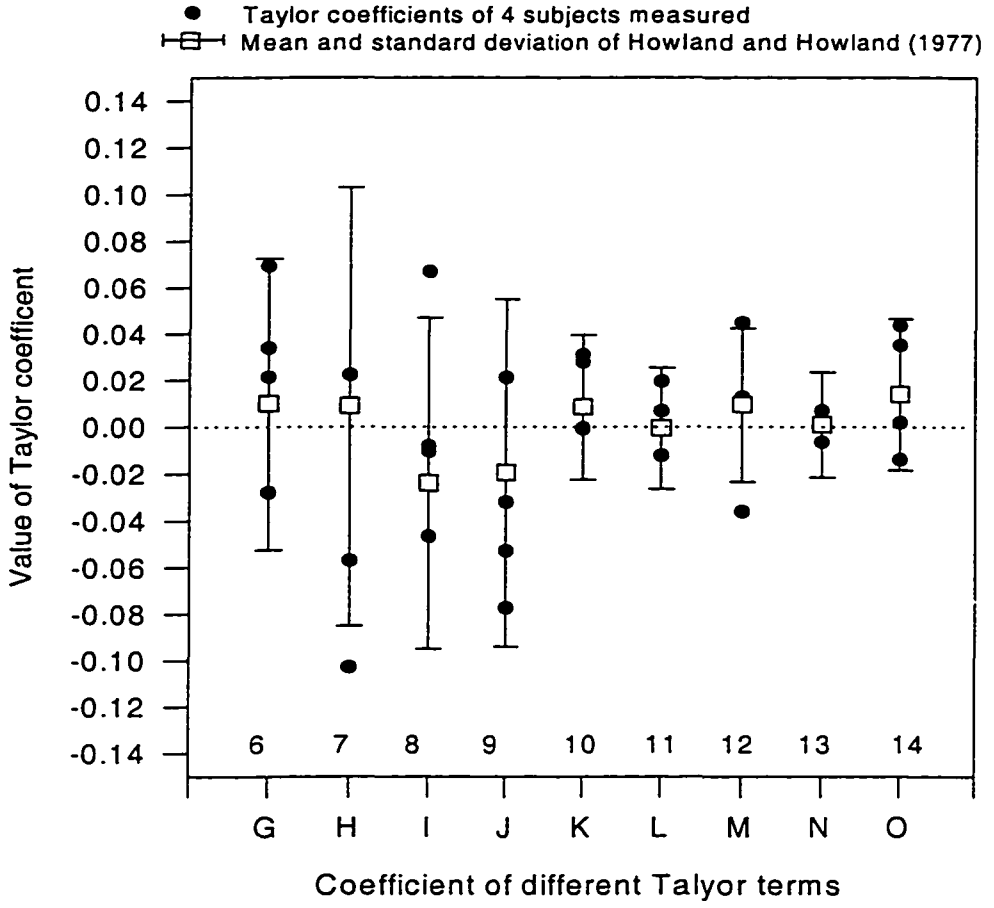


Fig. 3.20 Taylor coefficients of the 4 subjects measured compared to that of the 55 eyes measured with the Howland and Howland method. Taylor coefficients from G to O are labeled on the horizontal axis Term G to O corresponds to the 6^{th} to 14^{th} term in the Taylor polynomials, respectively. The filled circles represent data of this measurement; the open boxes represent the means of each coefficients of the Taylor polynomials of the 55 eyes measured by Howland and Howland (Howland and Howland, 1977); the error bar for each open boxes is the standard deviation of the coefficients of the55 eyes measured by Howland and Howland.

the purpose of comparison, wavefront aberrations were reconstructed with 4^{th} order Taylor polynomials from the measured ray aberration data of the 4 subjects. The obtained Taylor coefficients from G to O were plotted against the results of Howland and Howland (1977) in Fig. 3.20.

The coefficients of the 4 subjects falls within the range of the larger sample.

3.6.3 Effectiveness of the measurement system and the data processing procedure

While the general aberration situation of the human eye is roughly known, this new measurement system is intended to provide a more reliable subjective method to quantify the aberration in an individual eye under specific conditions.

a) Advantages to the measurement system

The system was ergonomically designed and effectively automated. The most significant advantages of this method over other subjective methods are,

i) settings are more precise due to hyperacuity;

ii) there is a better control of pupil sampling locations because of the precision in positioning of the Maxwellian system on the pupil;

iii) accommodation is better controlled by using a normal view channel as the reference channel;

iv) aberration can be measured with a natural pupil because there is an infrared pupil monitoring system;

v) it is less time consuming because of the automation;

vi) different reference axes can be used.

b) Advantage of data processing

The data processing procedure has been demonstrated to be effective and fast. It is automatic and takes only a few minutes from the measured raw data to plotting a 3-dimensional wavefront aberration graph and outputting a Taylor polynomial with the computer that operated the measurement system.

The computer program is also flexible for examining different aspects of the aberration characteristics of the eye. For example, the program can handle data of any set of pupil sampling locations, any orders of Taylor polynomials and any other polynomial forms such as the Zernike polynomials.

3.7 Conclusions

A two-dimensional Maxwellian view ocular wavefront aberration measurement system was designed and built. Preliminary measurements of 4 subjects have demonstrated the effectiveness of the system. These results agree with results from other ocular aberration measurements using different methods.

Chapter 4

Measurement of Wavefront Aberrations of the Eye Using the Coaxially Sighted Corneal Reflex

4.1 Introduction

In this chapter, the coaxially sighted corneal reflex axis and the implication of using this reference axis in measuring wavefront aberration are examined. Wavefront aberration measurements of the left eyes of 21 subjects are presented. For each subject, immediately after the aberration measurement, the measurement of the misalignment of various ocular components were also done and is described in Chapter 5.

4.2 The coaxially sighted corneal reflex as the reference in aberration measurement

If a point source is placed in front of the eye, the first Purkinje image of the source will be formed along the line that connects the point source and the center of curvature of the anterior surface of the cornea. For any position in front of the cornea, there will always exist such an axis. However, there will only be one such axis that also goes through the fixation point as shown in Fig. 4.1.

Given an on-line video camera system with the light source mounted coaxially with the optical axis of the camera and a reference center on the video screen to define the axis of the camera, this axis can be easily located by aligning the first Purkinje image of the source with the reference center on the video screen. This reference axis is essentially the optical axis of the cornea going through the fixation point.

In clinical visual optics, this axis has a unique significance and is often referred as the coaxially sighted corneal reflex (CSCR) (Uozato and Guyton, 1987; Pande and Hillman, 1993). This axis is often simply referred to as the cornea reflex (Applegate and Howland, 1995; Uozato and Guyton, 1987). Most videokeratographic systems and some refractive surgery alignment devices use this axis as the reference axis. The theoretical justification of using this axis as the reference axis has been argued both in corneal topography and in refractive surgery (Applegate and Howland, 1995; Uozato and Guyton,

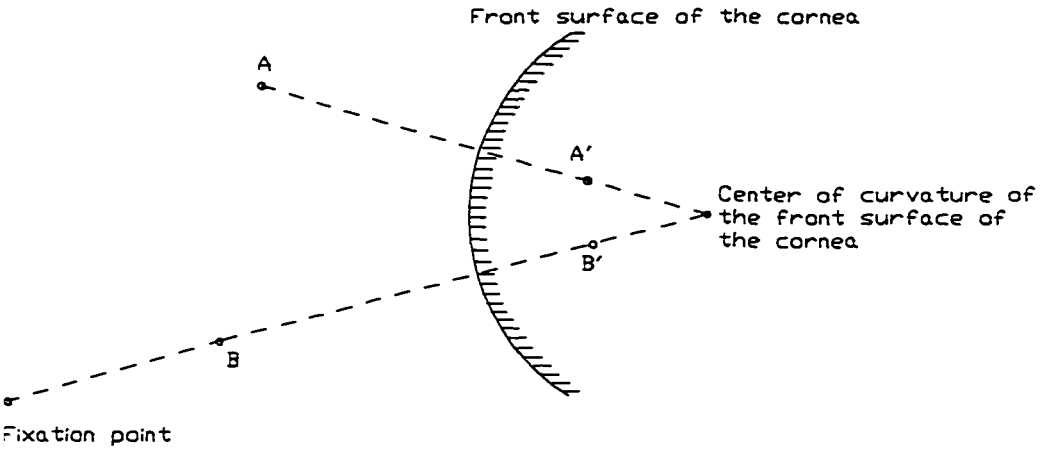


Fig.4.1 Definition of the coaxially sighted corneal reflex. A is point source at an arbitrary location in front the eye; A' is the first Purkinje image of A; B is a point source at a the line joining the fixation point and center of curvature of the front surface of the cornea; B' is the first Purkinje image of B; B' is also on the line joining the fixation point and the center of curvature of the front surface of the cornea.

1987). The CSCR is believed to be an inappropriate reference because it is away from the line of sight which is defined by the center of the entrance pupil (Applegate and Howland, 1995; Uozato and Guyton, 1987). Yet, in clinical applications, this axis remains as a widely used and effective reference axis. The reasons of the popularity of this axis are that it provides better precision, stability and repeatability than any other possible references such as the center of the entrance pupil. Another reason of popularity is that its alignment can be easily incorporated into most clinical instruments that include a viewing microscope.

Yet, the consequence of ignoring the strong argument from theoreticians is not evident in clinical practices, as might be expected. It appears that the discrepancy induced by the possible theoretical error is very likely to be either negligible or irrelevant.

From a theoretical point of view, the visual axis is the axis that connects the fixation point and the first nodal point in the object space. In the image space it is defined as the line connecting the secondary nodal point and the fovea. Interestingly, for the Gullstrand-Emsley eye model as shown in Fig. 1.1-1.2, the first nodal point is 0.74 mm in front of the center of curvature of the front surface of the cornea. The distance between the theoretical visual axis and the CSCR on the pupil plane is about 0.06 mm and can be safely regarded as insignificant. On the other hand, the distance between the theoretical visual axis and center of the pupil that defines the line of sight is about half a millimeter with the center of the pupil to the temporal side, assuming the pupil is centered with the optical axis of the eye. That is to say, from the theoretical point of view, the traditionally defined visual axis is very close to the axis defined by the coaxially sighted corneal reflex.

Interestingly, Applegate and Lakshminarayanan's (1993) normal data base of Stiles-Crawford functions measured from 53 eyes show a mean horizontal peak location of 0.51 mm nasal. Furthermore, photoreceptor alignment results of 20 eyes measured by Gorrand and Delori (1995) with a photoreceptor alignment reflectometer showed a mean horizontal peak location of 0.86 mm to the nasal side of the center of the pupil. Considering Stiles-Crawford apodization, these results are suggesting that the effective center of the pupil may be centered with the CSCR. It would ultimately justify the use of the coaxially sighted corneal reflex axis as the reference axis both in clinical procedures and in studies of the detailed structure of ocular optics.

For the intended aberration measurements, pictures of the pupil with the corneal reflex can be saved during the experiment and the relative position of the geometrical center of the pupil and the cornea reflex can always be conveniently measured and compared. Aberration data can also be converted to different reference axes.

Because of the precision of locating its position and its theoretical significance, the CSCR axis was chosen as the reference axis for the wavefront aberration

measurements in this thesis. However, the aberrations are expressed with respect to the geometrical center of the pupil for the convenience of calculating and comparing the total wavefront aberrations. The issue that needs to be addressed is how to transform the wavefront aberration expression with regard to reference shifts.

4.3 Effect on the wavefront aberration measured with the shift of the reference axis

4.3.1 The independence of the wavefront aberration measured on the choice of the reference axis

Given any point on the pupil plane in the semi-Maxwellian view aberration measurement system, the ray deviation will be independent of the choice of reference axis. As a consequence, the target blur shape and size on the retina are independent of the choice of different reference axis. The physical distance between the perceived center of the blur of the normal view target and each point of the blur is independent of the choice of the measurement reference axis.

What changes will be the mathematical expression of the aberration. For example, if the coaxial sighted cornea reflex is at (Δx, Δy) with the geometrical center of the pupil as the reference *(0, 0)*, the amount of aberration at *(0, 0)* when the coaxial sighted cornea reflex is used as the reference axis is essentially the same amount of aberration at (Δx, Δ *y*) when the geometrical center of the pupil is used as the reference.

If there is a reference axis shift, a simple coordinates transformation shift is needed. For the change of the reconstructed wavefront in mathematical expression, a transformation would be needed. Such a mathematical transformation can be accomplished. The relationships of the coefficients for each term of the wavefront aberration function will also be simply transformed.

4.3.2 The calculation of the root mean square (RMS) wavefront aberration needs to consider the real position of the pupil

The important point to remember is that for the evaluation of the optical performance of the eye, the real pupil position has to be used. If the CSCR is used as the reference axis in aberration measurement and if the real pupil is decentered from this reference, the calculation of the total amount of wavefront deviation will need to be done with a decentered pupil. On the other hand, if the geometrical center of the pupil is used as the reference, the calculation of the RMS wavefront aberration will need to be done with a centered pupil.

In reality, the CSCR is normally on the nasal side of the geometrical center of the pupil and therefore, a decentered pupil should be used if the RMS wavefront aberration is to be calculated. Alternatively, the wavefront aberration expression with the CSCR can be transformed mathematically into the wavefront aberration expression with the geometrical center of the pupil as the reference provided the distance between the two reference points is known.

It should be remembered as stated in Section 4.2.1 that the effective center of the pupil may actually be centered with the CSCR. This new line of rationale deserves to be re-examined and if proved, could change our traditional view of the aberration measurement of the eye. For this research, the calculation will be performed with the geometrical center of the pupil. However, it is not a compromise to tradition, because this study explores the aberration of the eye before the Stiles-Crawford effect takes effect. Since Stiles-Crawford apodization is not considered in this thesis, the use of the geometrical center of the pupil is justified.

4.3.3 Transformation of the reconstructed wavefront aberration with the shift of the reference axis from the CSCR to the geometrical center of the pupil

If the deviation of the geometrical center of the pupil from the CSCR is Δx in the horizontal meridian and Δy in the vertical meridian, and if the wavefront aberration reconstructed with the CSCR as the reference is,

$$W(x,y)=\sum_{i=1}^{I} a_i Z_i(x,y) \tag{4.1}$$

where $Z_i(x,y)$ is the i^{th} Taylor polynomial term with a_i as its coefficient.

The wavefront aberration expressed with the geometrical center of the pupil as the reference will be,

$$W(x,y)=\sum_{i=1}^{I} a_i Z_i(x+\Delta x, y+\Delta y) \tag{4.2}$$

Expanding Eq.(4.2) yields,

$$W(x,y)=\sum_{i=1}^{I} b_i(\Delta x,\Delta y) Z_i(x,y) \tag{4.3}$$

where $Z_i(x,y)$ is the i^{th} Taylor polynomial term with $b_i(\Delta x,\Delta y)$ as its coefficient. $b_i(\Delta x,\Delta y)$ is a function of Δx and Δy.

Table 4.1 shows $b_i(\Delta x,\Delta y)$ for the new coefficients of all the terms of Taylor polynomials up to 6^{th} order.

Table 4.1 New coefficients of all the terms of the 6th order Taylor polynomial after shifting the reference axis from (0,0) to (Δx, Δy).

Term of Polynomial	$b_i(\Delta x, \Delta y)$
Piston term	$a_{16}\Delta x^4\Delta y + a_{15}\Delta x^5 + a_{26}\Delta x\Delta y^5 + a_{20}\Delta y^5 + a_{21}\Delta x^6 + a_{27}\Delta y^6 + a_{19}\Delta x\Delta y^4 + a_7\Delta x^2\Delta y + a_8\Delta x\Delta y^2 + a_{11}\Delta x^3\Delta y + a_{18}\Delta x^2\Delta y^3 + a_{13}\Delta x\Delta y^3 + a_{12}\Delta x^2\Delta y^2 + a_{24}\Delta x^3\Delta y^3 + a_{22}\Delta x^5\Delta y + a_{17}\Delta x^3\Delta y^2 + a_{25}\Delta x^2\Delta y^4 + a_{23}\Delta x^4\Delta y^2 + a_4\Delta x\Delta y + a_1\Delta x + a_2\Delta y + a_3\Delta x^2 + a_5\Delta y^2 + a_6\Delta x^3 + a_9\Delta y^3 + a_{10}\Delta x^4 + a_{14}\Delta y^4$
x	$3a_6\Delta x^2 + a_{26}\Delta y^5 + 3a_{24}\Delta x^2\Delta y^3 + 2a_{25}\Delta x\Delta y^4 + a_{13}\Delta y^3 + 2a_3\Delta x + 5a_{15}\Delta x^4 + 4a_{16}\Delta x^3\Delta y + 3a_{11}\Delta x^2\Delta y + 2a_{18}\Delta x\Delta y^3 + a_4\Delta y + 5a_{22}\Delta x^4\Delta y + 6a_{21}\Delta x^5 + a_8\Delta y^2 + 4a_{10}\Delta x^3 + 2a_7\Delta x\Delta y + a_{19}\Delta y^4 + a_1 + 3a_{17}\Delta x^2\Delta y^2 + 2a_{12}\Delta x\Delta y^2 + 4a_{23}\Delta x^3\Delta y^2$
y	$5a_{26}\Delta x\Delta y^4 + 2a_{12}\Delta x^2\Delta y + a_{16}\Delta x^4 + 4a_{14}\Delta y^3 + 4a_9\Delta x\Delta y^3 + a_2 + 3a_{13}\Delta x\Delta y^2 + 2a_{17}\Delta x^3\Delta y + 5a_{20}\Delta y^4 + a_{22}\Delta x^5 + 3a_{18}\Delta x^2\Delta y^2 + 2a_5\Delta y + a_{11}\Delta x^3 + a_4\Delta x + 6a_{27}\Delta y^5 + 3a_{24}\Delta x^3\Delta y^2 + 3a_9\Delta y^2 + 4a_{25}\Delta x^2\Delta y^3 + a_7\Delta x^2 + 2a_{23}\Delta x^4\Delta y + 2\,a_8\Delta x\Delta y$
x^2	$3a_{11}\Delta x\Delta y + 15a_{21}\Delta x^4 + a_3 + 6a_{10}\Delta x^2 + 10a_{22}\Delta x^3\Delta y + 3a_{17}\Delta x\Delta y^2 + 3a_6\Delta x + a_7\Delta y + a_{25}\Delta y^4 + 3a_{24}\Delta x\Delta y^3 + 10a_{15}\Delta x^3 + a_{12}\Delta y^2 + a_{18}\Delta y^3 + 6a_{23}\Delta x^2\Delta y^2 + 6a_{16}\Delta x^2\Delta y$
xy	$6a_{18}\Delta x\Delta y^2 + 8a_{25}\Delta x\Delta y^3 + 5a_{22}\Delta x^4 + 2a_8\Delta y + 3a_{13}\Delta y^2 + 8a_{23}\Delta x^3\Delta y + 2a_7\Delta x + 3a_{11}\Delta x^2 + 6a_{17}\Delta x^2\Delta y + 4a_{12}\Delta x\Delta y + 5a_{26}\Delta y^4 + a_4 + 9a_{24}\Delta x^2\Delta y^2 + 4a_{16}\Delta x^3 + 4a_{19}\Delta y^3$
y^2	$6a_{25}\Delta x^2\Delta y^2 + 3a_{24}\Delta x^3\Delta y + 3a_{18}\Delta x^2\Delta y + 3a_9\Delta y + 10a_{20}\Delta y^3 + a_5 + 10a_{26}\Delta x\,\Delta y^3 + 6a_{19}\Delta x\Delta y^2 + a_{23}\Delta x^4 + a_{12}\Delta x^2 + 6a_{14}\Delta y^2 + 15a_{27}\Delta y^4 + a_8\Delta x + 3a_{13}\Delta x\,\Delta y + a_{17}\Delta x^3$
x^3	$10a_{22}\Delta x^2\Delta y + 20a_{21}\Delta x^3 + 4a_{16}\Delta x\Delta y + a_{11}\Delta y + a_6 + 4a_{23}\Delta x\Delta y^2 + 4a_{10}\Delta x + a_{24}\Delta y^3 + 10a_{15}\Delta x^2 + a_{17}\Delta y^2$
x^2y	$2a_{12}\Delta y + 3a_{11}\Delta x + 3a_{18}\Delta y^2 + a_7 + 12a_{23}\Delta x^2\Delta y + 6a_{16}\Delta x^2 + 10a_{22}\Delta x^3 + 6a_{17}\Delta x\Delta y + 4a_{25}\Delta y^3 + 9a_{24}\Delta x\,\Delta y^2$
xy^2	$3a_{13}\Delta y + 9a_{24}\Delta x^2\Delta y + 2a_{12}\Delta x + 10a_{26}\Delta y^3 + a_8 + 3a_{17}\Delta x^2 + 6a_{19}\Delta y^2 + 6a_{18}\Delta x\,\Delta y + 4\,a_{23}\,\Delta x^3 + 12\,a_{25}\,\Delta x\,\Delta y^2$

y^3	$10a_{20}\Delta y^2 + 4a_{25}\Delta x^2\Delta y + 20a_{27}\Delta y^3 + 4a_{19}\Delta x\Delta y + 10a_{26}\Delta x\Delta y^2 + a_{18}\Delta x^2 + a_9 + a_{24}\Delta x^3 + a_{13}\Delta x + 4a_{14}\Delta y$
x^4	$a_{16}\Delta y + a_{10} + 5a_{15}\Delta x + 5a_{22}\Delta x\Delta y + 15a_{21}\Delta x^2 + a_{23}\Delta y^2$
x^3y	$8a_{23}\Delta x\Delta y + a_{11} + 10a_{22}\Delta x^2 + 4a_{16}\Delta x + 3a_{24}\Delta y^2 + 2a_{17}\Delta y$
x^2y^2	$9a_{24}\Delta x\Delta y + 6a_{25}\Delta y^2 + 3a_{18}\Delta y + 3a_{17}\Delta x + a_{12} + 6a_{23}\Delta x^2$
xy^3	$3a_{24}\Delta x^2 + 4a_{19}\Delta y + 8a_{25}\Delta x\Delta y + a_{13} + 2a_{18}\Delta x + 10a_{26}\Delta y^2$
y^4	$5a_{26}\Delta x\Delta y + 5a_{20}\Delta y + a_{19}\Delta x + a_{25}\Delta x^2 + a_{14} + 15a_{27}\Delta y^2$
$x5$	$a_{15} + 6a_{21}\Delta x + a_{22}\Delta y$
x^4y	$2a_{23}\Delta y + a_{16} + 5a_{22}\Delta x$
x^3y^2	$a_{17} + 3a_{24}\Delta y + 4a_{23}\Delta x$
x^2y^3	$4a_{25}\Delta y + a_{18} + 3a_{24}\Delta x$
xy^4	$2a_{25}\Delta x + 5a_{26}\Delta y + a_{19}$
y^5	$a_{20} + a_{26}\Delta x + 6a_{27}\Delta y$
x^6	a_{21}
x^5y	a_{22}
x^4y^2	a_{23}
x^3y^3	a_{24}
x^2y^4	a_{25}
xy^5	a_{26}
y^6	a_{27}

4.4 Methods

4.4.1 Apparatus

The aberration measurement system is described in detail in Chapter 3. Here only the device to generate and locate the CSCR will be described.

Four infrared LEDs were mounted at the front end of the camera lens in such a way that two of them represented the horizontal meridian while the other two represented the vertical meridian of the camera system. These Purkinje images of the LEDs could be easily aligned with the reference cross on the video screen by the experimenter. The alignment precision was at pixel level which are 0.032mm x 0.025mm on the pupil plane. When the subject's eye moved during the experiment, the experimenter could easily realign the eye by moving the head position of the subjects via the special XYZ adjustable head mount.

4.4.2 Subjects

The monochromatic aberrations of the left eyes of 21 emmetropic or near emmetropic subjects were measured. The subjects were recruited from the University of Waterloo. Immediately after the aberration measurement, ocular components misalignment measurements of each eye were also performed (See Chapter 6). Subject selection included in the study met the following requirements.

i) age ranged from 17 to 35 years old;

ii) astigmatism error was no greater than 0.75D;

iii) no regular contact lens wear;

iv) no significant ocular pathology;

v) uncorrected visual acuity of at least 6/6 under normal room illumination condition and 6/10 under mescopic illumination condition.

vi) spherical error of from 0 to 0.75DS as assessed by an AR-1000 NIDEK™ autorefractor.

4.4.3 Measurement procedure

The measurement procedure was very similar to the procedure as described in Chapter 3. In Chapter 3, the subject was aligned with the measurement system by aligning the entrance pupil with the reference box of approximately equal size on the video screen. The difference in the measurements described here was that the experimenter kept the Purkinje image Is of the four IR LEDs that were centered with the camera lens aligned with the reference cross on the video screen.

The measurement procedure and subject's task for the experiment were explained to the subject. Informed consent was obtained from the subject. 1 drop of 2.5% Phenylephrine was instilled in the left eye and was dark adapted for 15 minutes before the measurement. Because Phenylephrine was applied, all the subjects had well-dilated pupils with the minimum diameter of 7mm.

4.4.4 Repeatability tests

Subject JH was tested additional two times nine months later under the same conditions to test both the long term and short term repeatability of the measurements.

4.5 Results and analysis

Typical pictures used for analysis are as shown in Fig. 4.2. The cross is centered at pixel (256, 242) and used as the reference of the video system. The four sharp and small PIs of the four IR LEDs were aligned with the reference cross. The large blurry bright spot in the right side of the pupil was the PI of the Tungsten-Halogen source filtered by an IR pass only filter to illuminate the pupil plane. The smaller image immediately to the left side was the PIV of the same source.

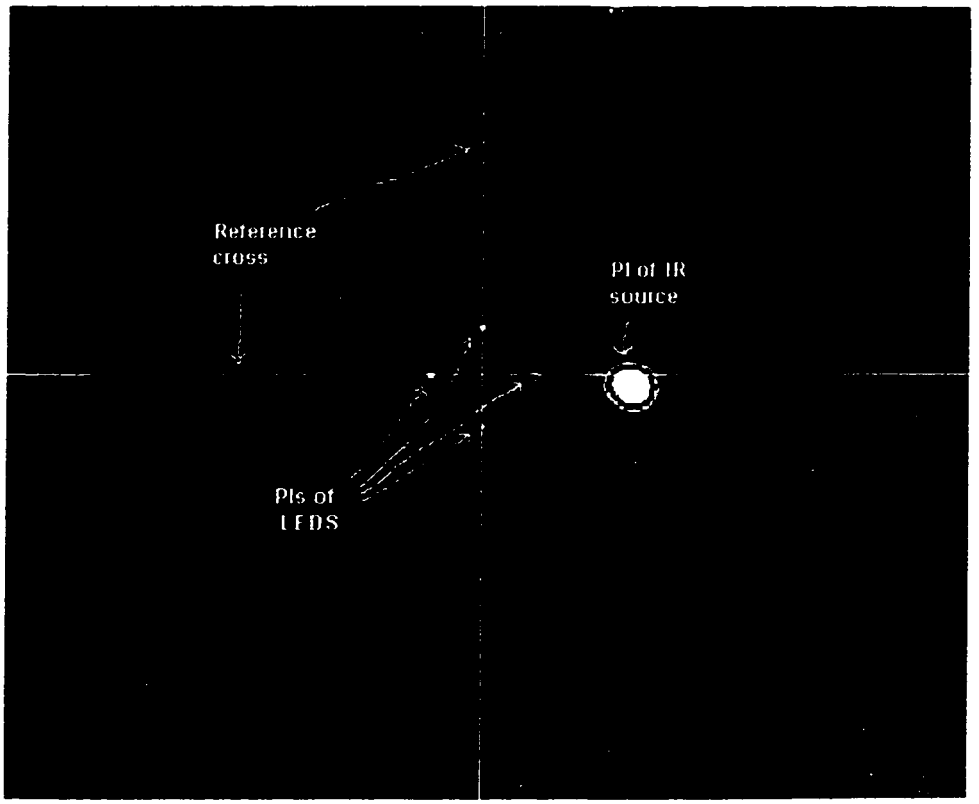


Fig. 4.2 Picture of the pupil saved during the measurement of the Left eye of subject JH. The central cross is the reference of the video system which is represented by pixel (256, 242). The four sharp and small PIs of the four IR LEDs were aligned with the reference cross. The large blurry bright spot in the right side of the pupil was the Purkinje image I of the Tungsten-Halogen source filtered by a IR-pass-only filter to illuminate the pupil plane. The smaller image immediately to the left side was the PIV of the same source.

4.5.1. Diagram of the measured ray aberration data

The measured ray aberration can be used to generate the diagram for each eye measured. The diagram can show the basic shape of the point spread of the eye measured before the Stiles-Crawford pupil apodization. The diagram of individual eye is given in Appendix VIIII.

Plotting the diagrams of all the eyes on the same plot can reveal the general population distribution of the aberration of the human eye. Fig. 4.3. shows the data of all 21 subjects.

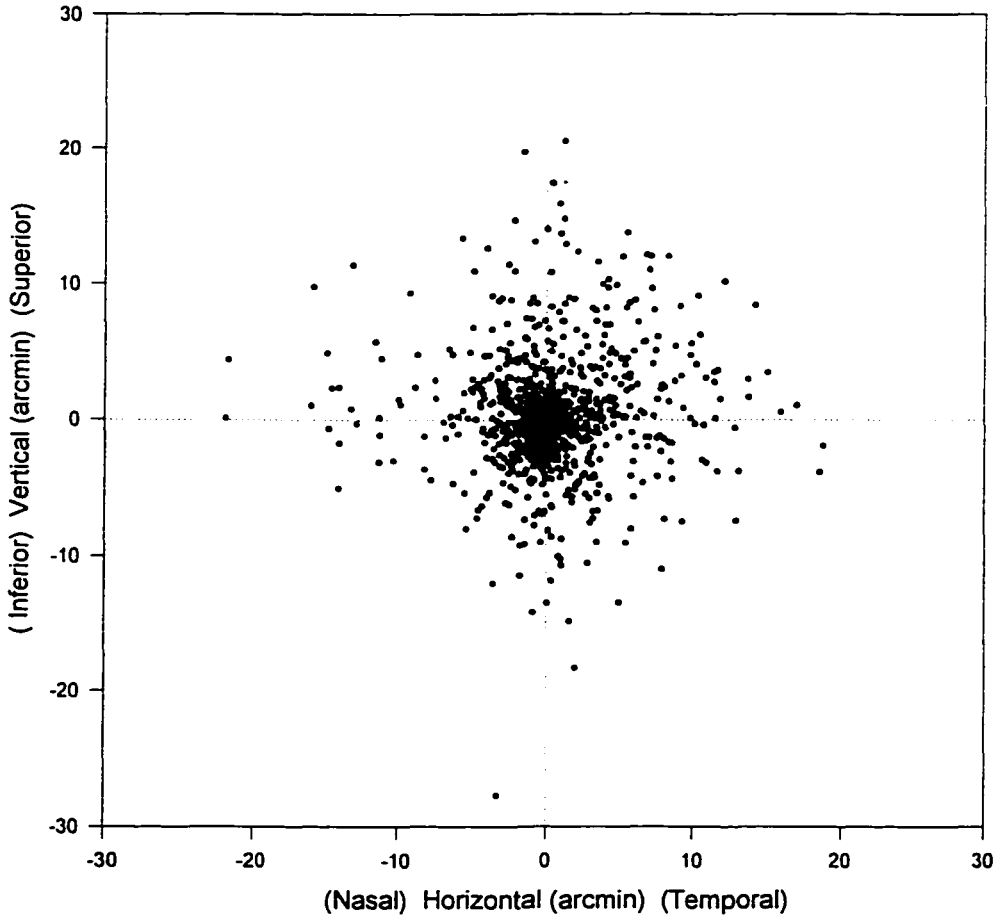


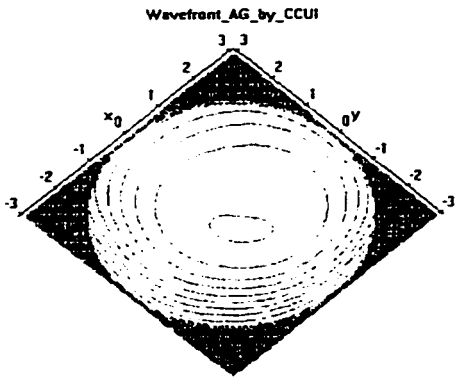
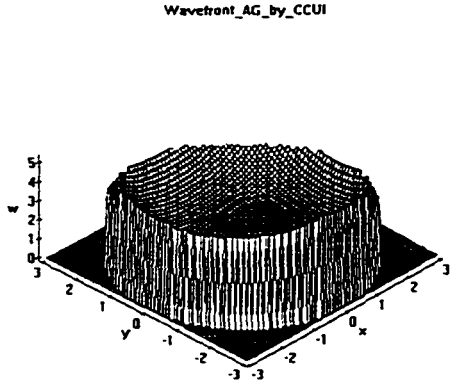
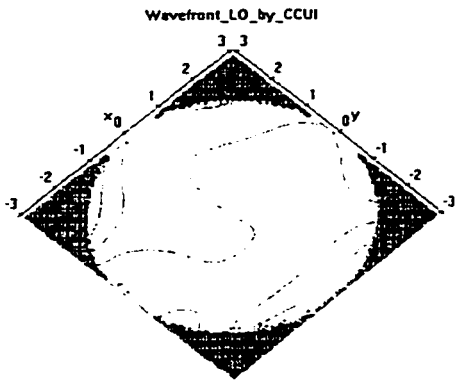
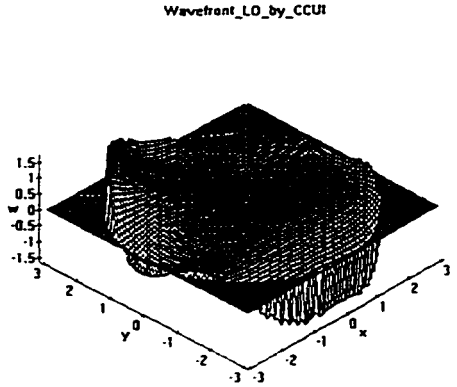
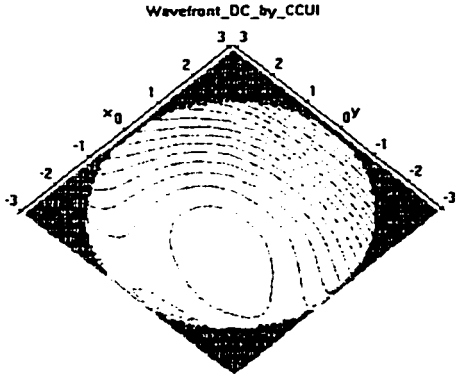
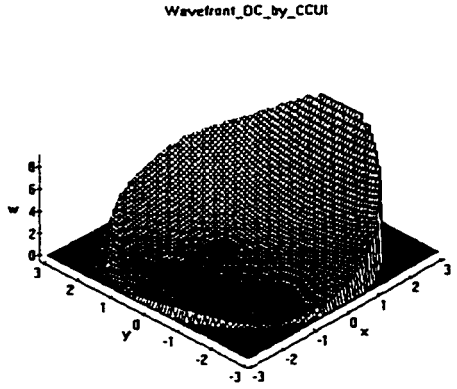
Fig. 4.3 The combined diagram of 21 eyes measured.

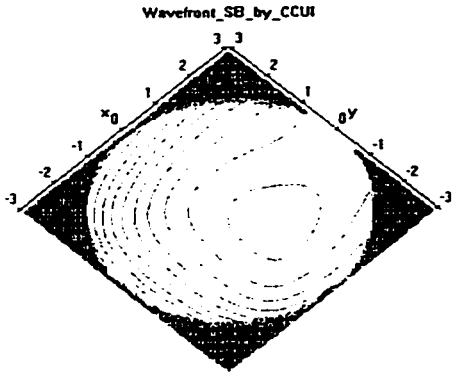
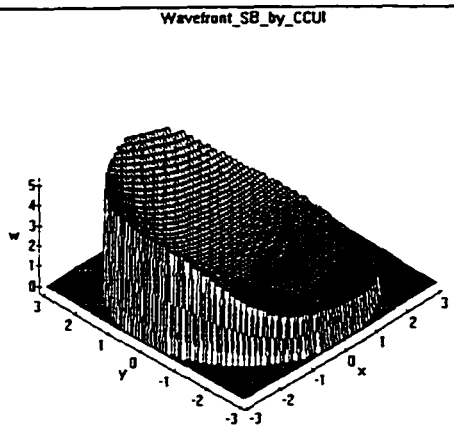
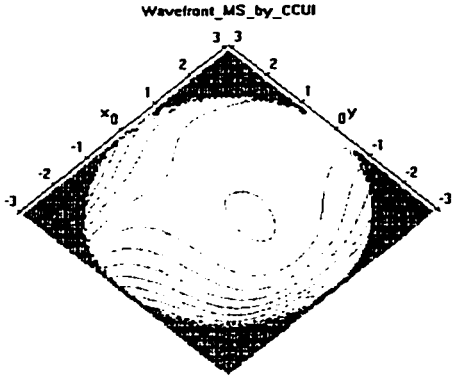
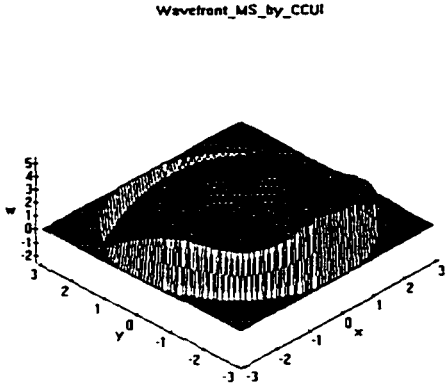
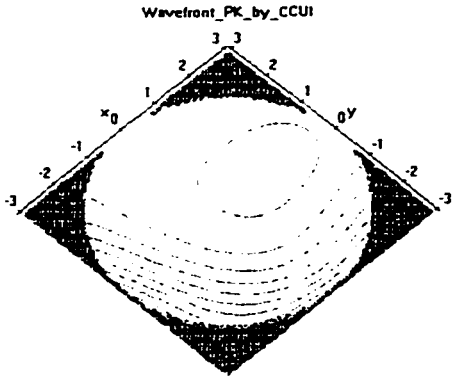
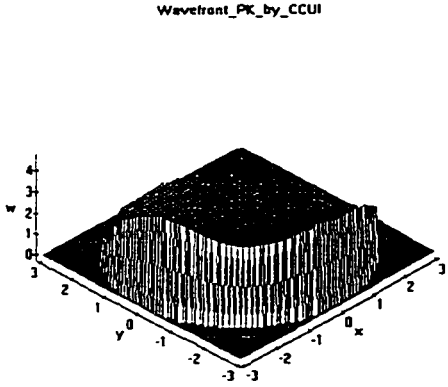
4.5.2 Wavefront aberrations reconstructed from ray aberration data

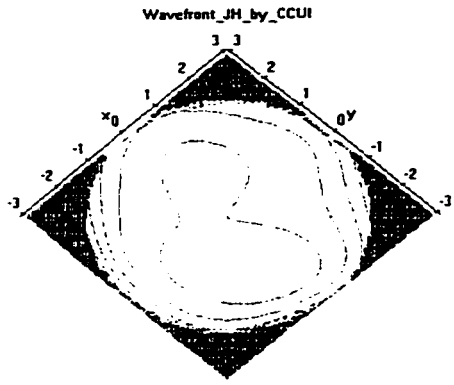
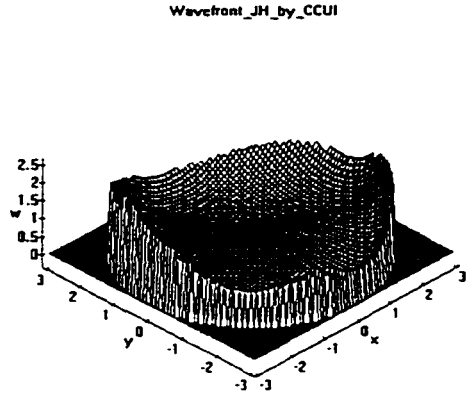
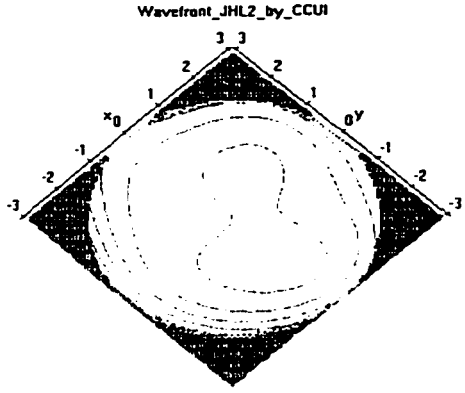
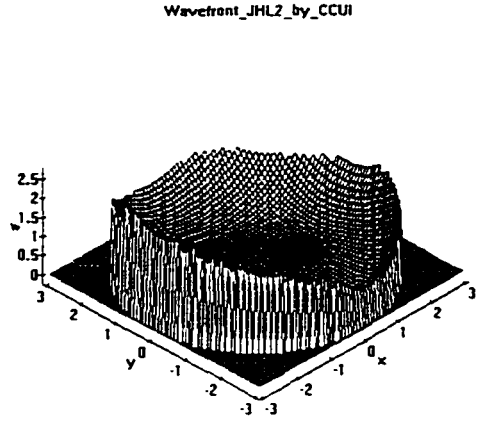
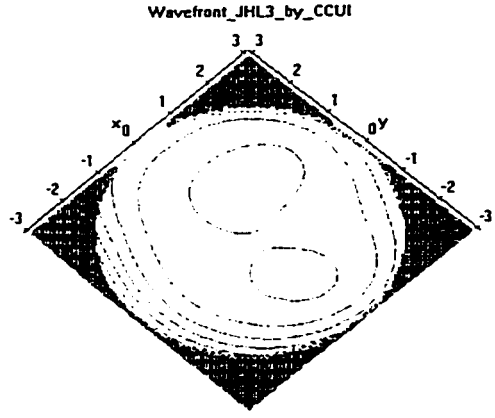
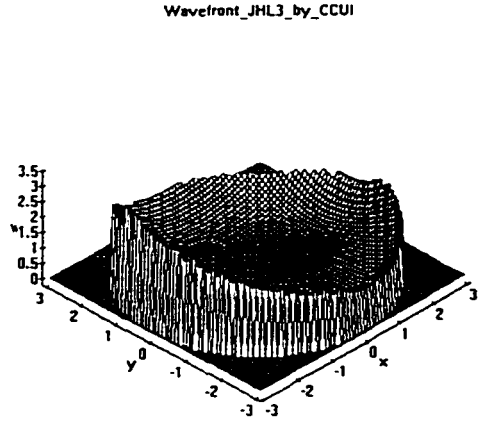
The ASCII format ray aberration data were processed by the Maple V™ wavefront reconstruction program (see Appendix IV). The program performed the wavefront reconstruction with the contour plot, the 3-dimensional wavefront plot, the 6th order Taylor polynomial, the r-squared value of the fit and 95% confidence interval of the obtained Taylor coefficients.

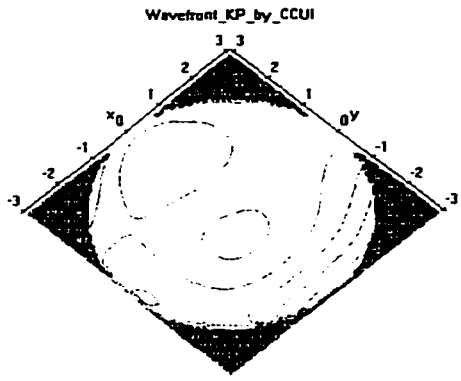
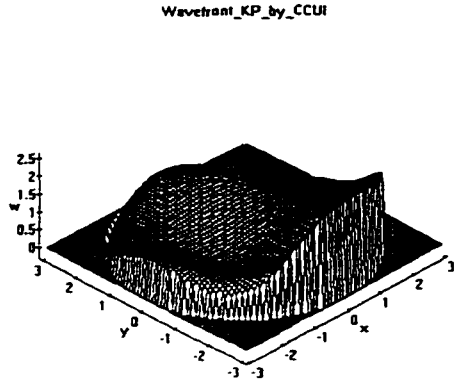
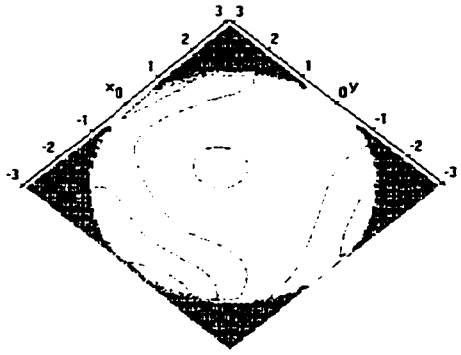
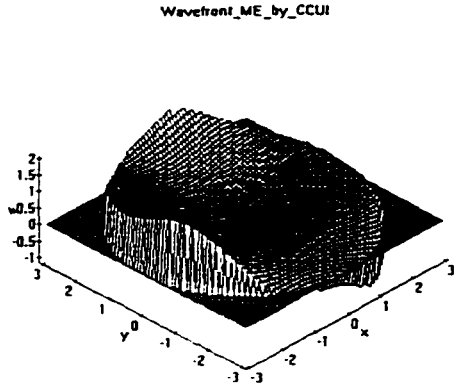
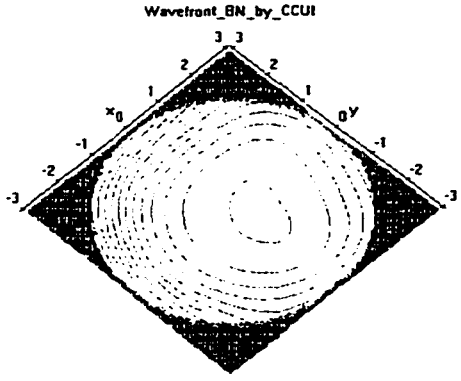
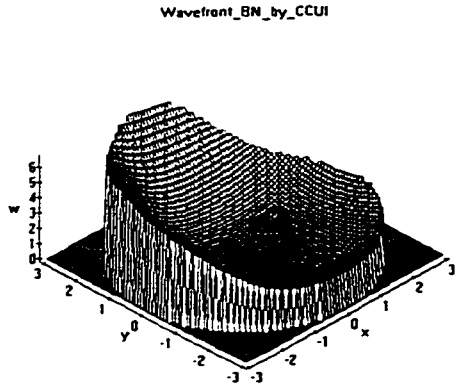
The contour plots and 3-dimensional plots are given in the Fig. 4.4. The contour lines are at 1 λ intervals. The 3-dimensional wavefront plot is in microns. In both types of plots, positive signs denote the temporal side of the eye in the horizontal meridian and the superior of the eye in the vertical meridian. Positive aberration implies the aberrated wavefront lies in front of the reference sphere.

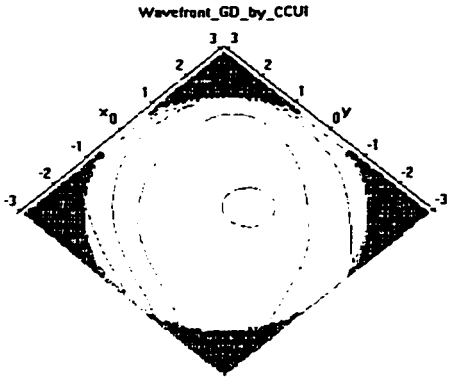
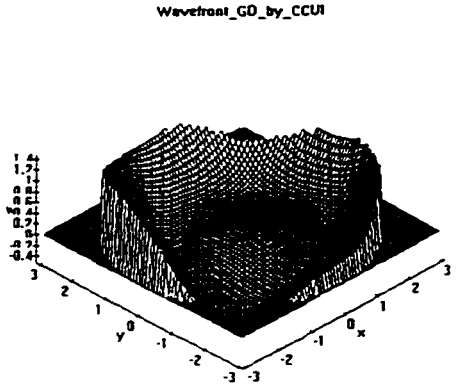
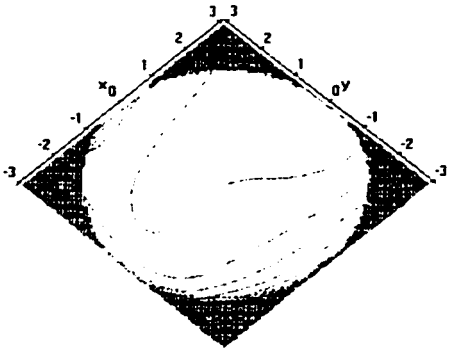
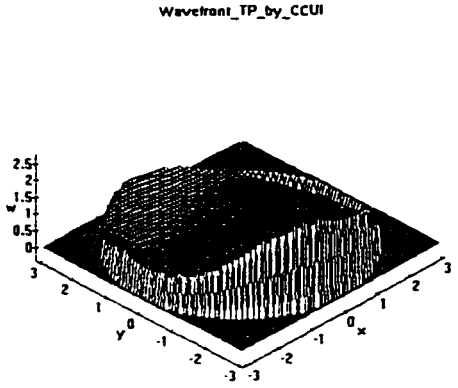
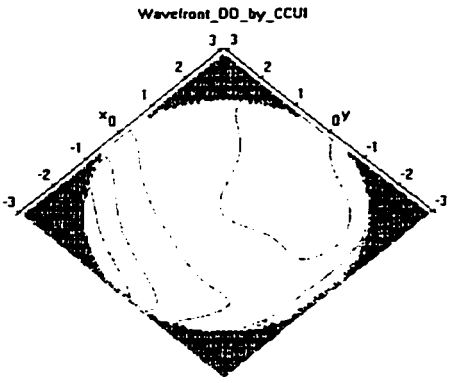
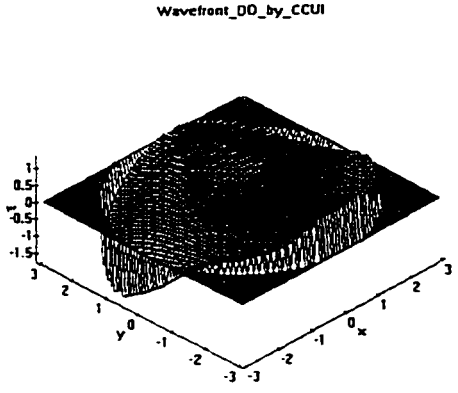
Fig. 4.4 Contour plots and 3-dimensional plots of wavefront aberrations measured of the left eyes of the 21 emmetropic subjects; the r-squared value of the fit is parenthesized under the initial of the subject

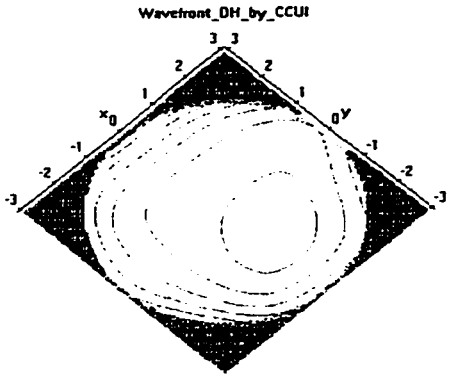
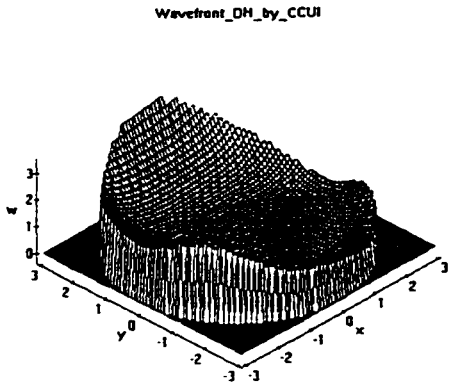
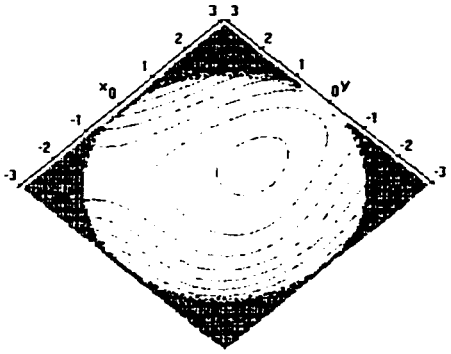
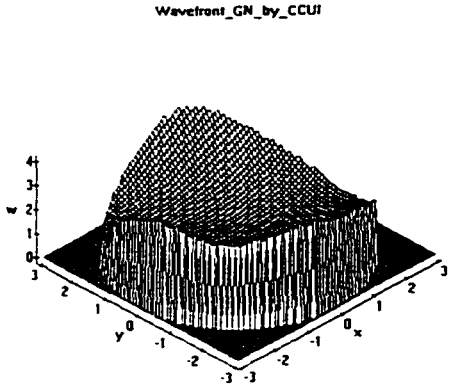
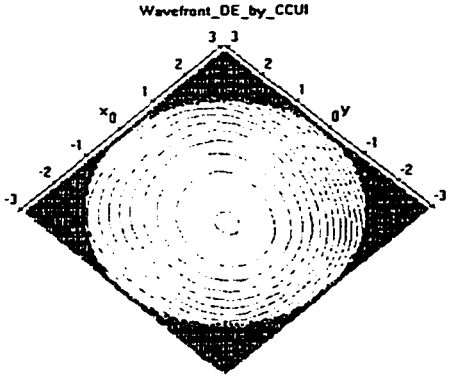
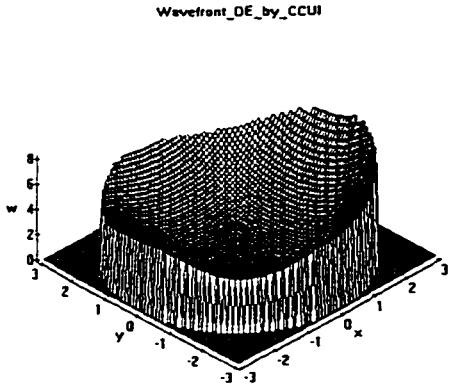
Subject (r-squared value)	Contour plot	3-dimensional plot
AG (0.97)		
LO (0.72)		
DC (0.98)		

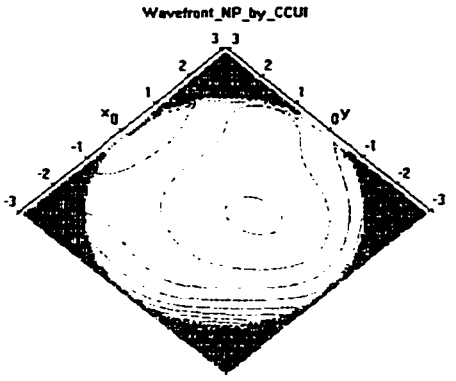
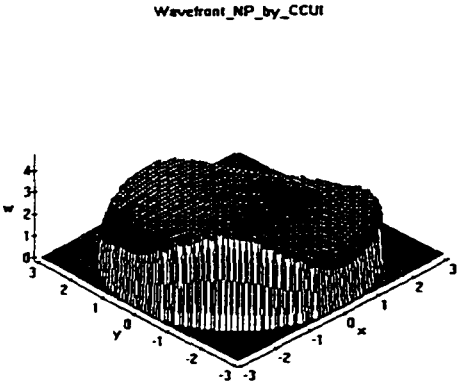
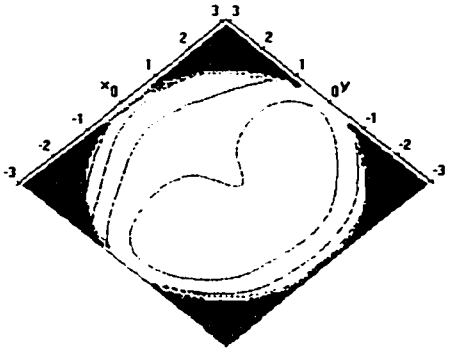
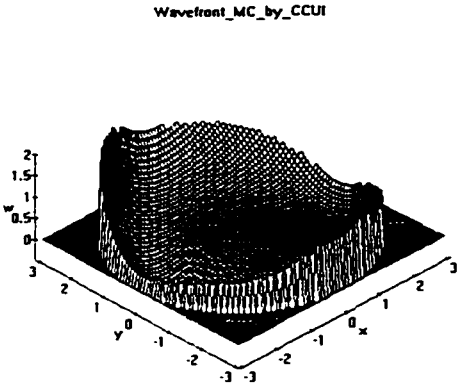
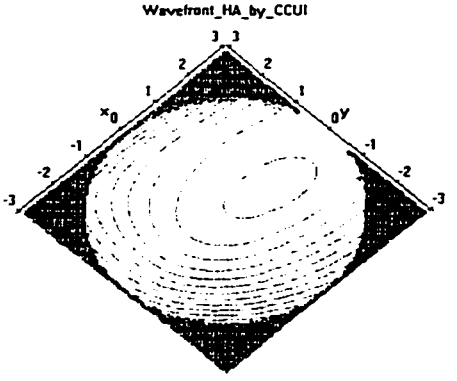
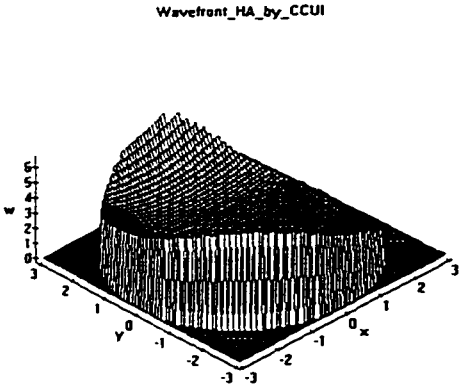
SB (0.96)		
MS (0.98)		
PK (0.96)		

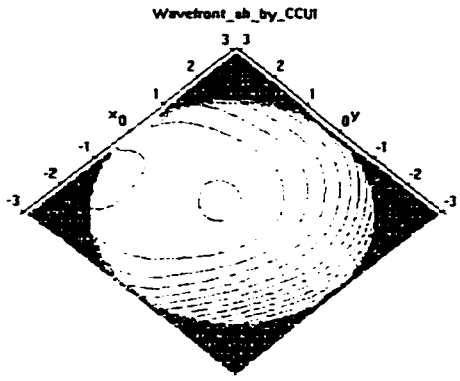
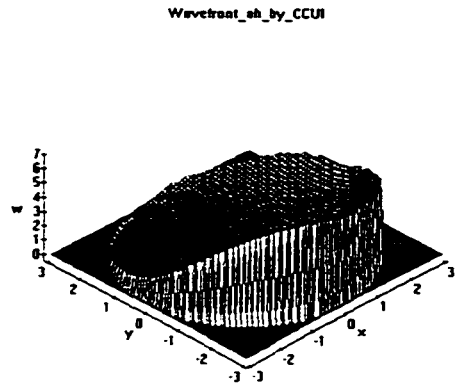
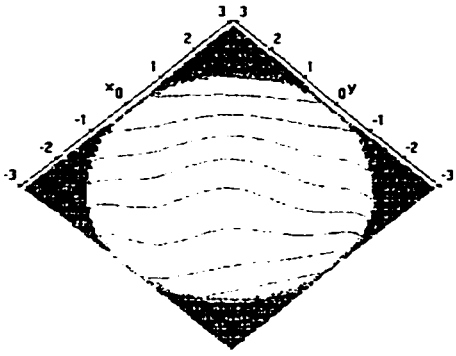
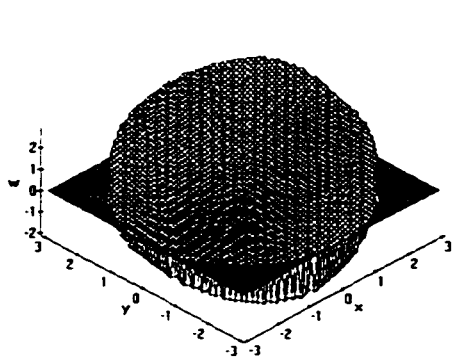
JH (1^{st}) (0.96)		
JH (2^{nd}) (0.96)		
JH (3^{rd}) (0.98)		

KP (0.92)		
ME (0.83)		
BN (0.97)		

GD (0.86)		
TP (0.93)		
DD (0.93)		

DH (0.93)		
GN (0.98)		
DE (0.98)		

NP (0.94)		
MC (0.92)		
HA (0.96)		

AH (0.77)	 Wavefront_ah_by_CCUI	 Wavefront_ah_by_CCUI
LR (0.31)	 Wavefront_LR_by_CCUI	 Wavefront_LR_by_CCUI

The distribution of the Taylor coefficients of the 21 subjects measured is plotted in Fig. 4.5. Each eye is represented by one type of symbol.

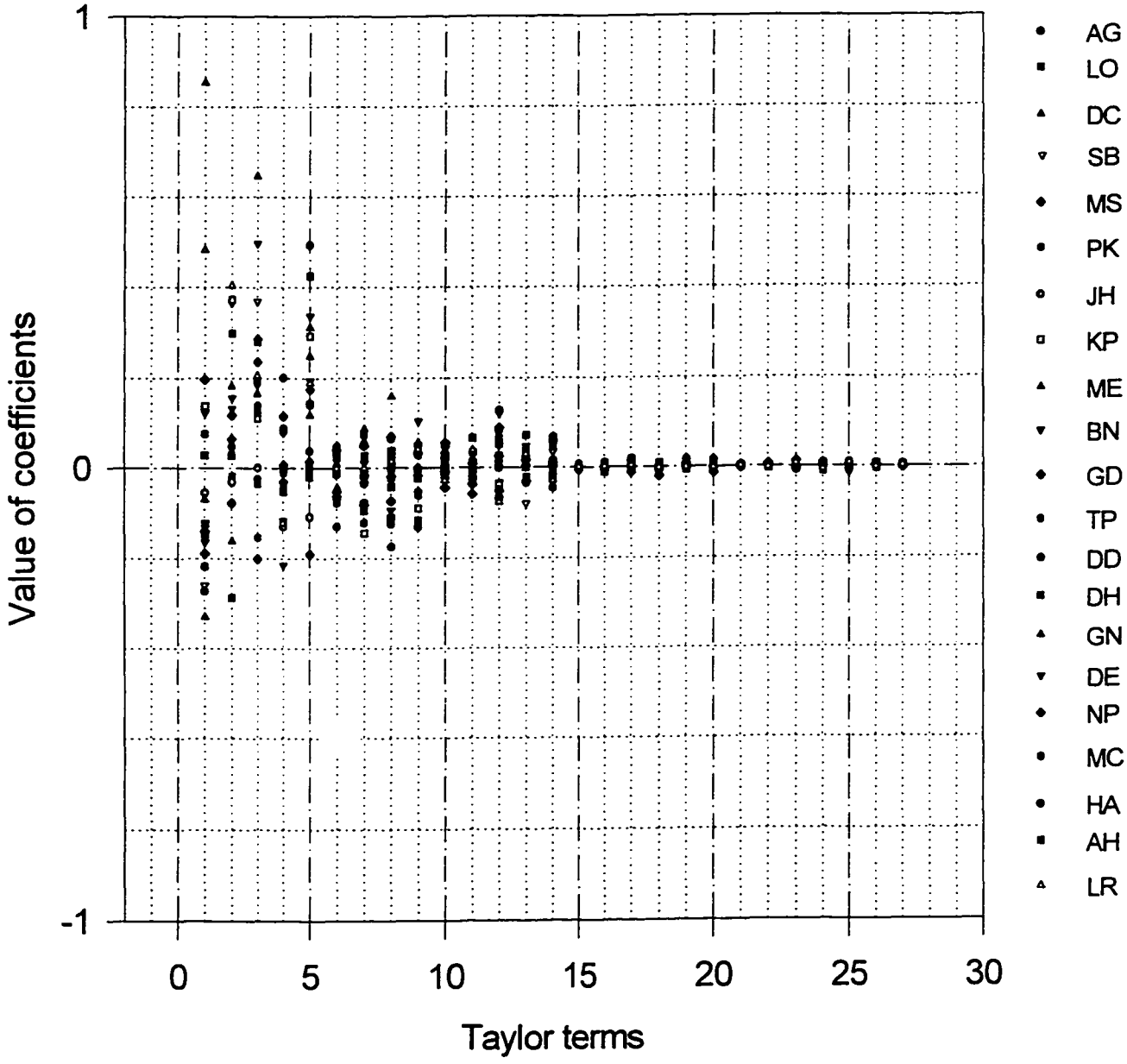


Fig. 4.5 Taylor coefficients distribution of the left eyes of 21 subjects measured. For each subject, the coefficients are represented by one type of symbol.

4.6 Repeatability and examination of the fit

During the first aberration measurement of subject JH, the (0,0) position was sampled extra 20 times to check the semi-Maxwellian view vernier acuity performance. JH's aberration was measured another two times about nine months later. The latter two measurements were one day apart.

4.6.1 Vernier acuity

The results of measuring sampling location (0,0) for 20 times show a standard deviation of 15 arc secs, which is better than AR's vernier acuity (28 arc secs). Recall AR's vernier acuity was measured with geometrical center of the pupil as the reference as given in Chapter 3. As a reference, the geometrical center of the pupil is harder to define and control. This could have contributed to the worse vernier acuity of subject AR.

4.6.2 Measurement repeatability

Fig. 4.6 represents a pupil plane with 49 filled circular dots representing the 49 pupil sampling locations. From each sampling location, a vector with a head of a filled solid square represents the ray aberration measured of JH's left eye at the first session(measured on 11-20-95, referred as JHL later). The magnitude of the vector is scaled down to 10% for the sake of clarity. As expected, the normal trend shows larger ray aberrations at the periphery of the pupil.

The two latter measurements of JH's left eye (measurement on 9-21-96 and referred to as JHL2, measurement on 9-22-96 and referred to as JHL3) were also plotted in a similar way without the line segment. They are represented as clear erect triangles and clear inverted triangles, respectively. The three measurements are generally close to each other and the last two measurements are closer to each other.

To examine the fit and compare the fit to the repeated measurements, the reconstructed wavefront from the second measurement were used to calculate ray aberration. The data were also plotted in Fig. 4.6 as erect filled solid triangles. It is clear that the erect solid triangle is almost always closer to the erect clear triangle (in most cases, the two symbols overlap). This implies that the reconstruction algorithm is sufficiently effective to resolve the difference of two measurements of the same eye.

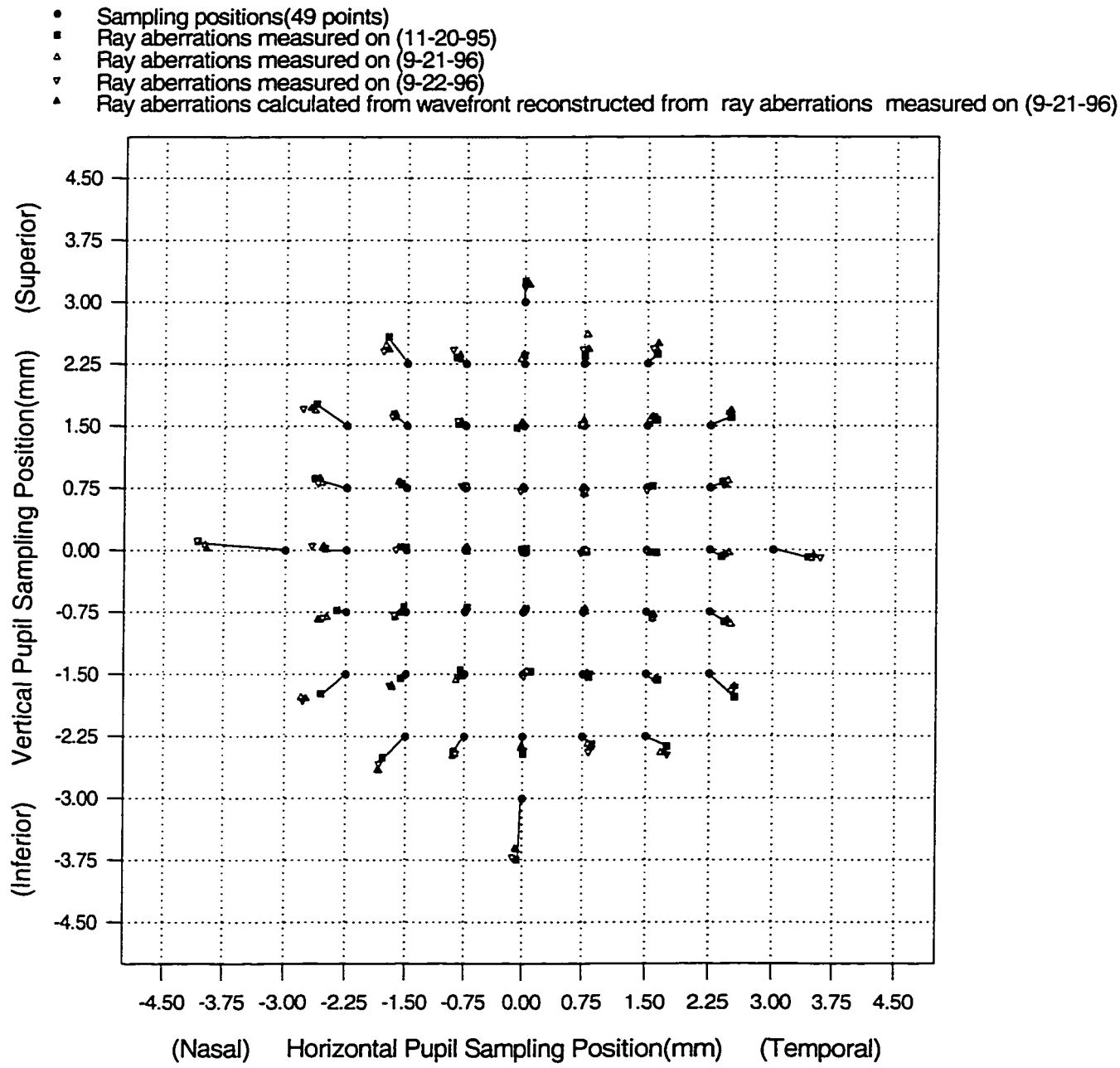


Fig. 4.6 Ray aberration data of subject JH's left eye of 3 measurements. A vector was also drawn from each sampling location to the corresponding ray aberration data of the first measurement. The filled erect triangles represent the ray aberrations calculated from the Taylor polynomial fit to the second measurement. The magnitude of the vector is scaled down to 10% for the sake of clarity.

The measurement difference between the three sessions of subject JH can also be seen by comparing the three pairs of wavefront aberration plots in Fig 4.4. As discussed in Section 3.6.1, the wavefront aberration difference between two sessions could result from true aberration change between the two measurement sessions, from measurement errors, or both. The small difference between JH's second and third measurements as shown in Fig. 4.7a was probably largely due to measurement errors. The relatively larger difference between the first and second measurement of JH would imply that there was an additional change in the aberration between the two measurements. This is not surprising given the fact that the second measurement was taken 10 months later after the first measurement. Such true aberration changes could be partly attributed to lacrimal film thickness changes as pointed by Smirnov (1961), and possible accommodative fluctuations during the measurement.

A comparison of Fig. 3.16 with Fig. 4.6 shows that the repeatability of JH's measurements was better than that of AR's measurements. The better repeatability of JH was partly due to the use of a more stable reference axis, which would result in smaller pupil sampling location errors. Subject JH also performed two-fold better in vernier acuity than subject AR, which would also contribute to a better measurement repeatability. Further, subject AR had aberrations of relatively larger magnitude which would result in larger absolute aberration measurement errors. Overall, it can be concluded that subject AR not only had larger measurement errors but also had larger true aberration changes between measurement sessions. For both subjects, the general shape of the measured wavefront remained the same for all repeated measurements.

4.6.3 The difference of 6th order and 8th order Taylor polynomial versus the two latest measurements

Using a polynomial with higher order to fit experimental data will usually produce a better fit. However, the polynomial order to use depends on the number of sampling locations, the precision of the measurement, and the accuracy of the measurement. For example, the number of terms in the polynomial cannot exceed the number of sampling locations. Also, a fit using a polynomial of an inappropriate high order may deceivingly pick up measurement noise as higher order aberrations.

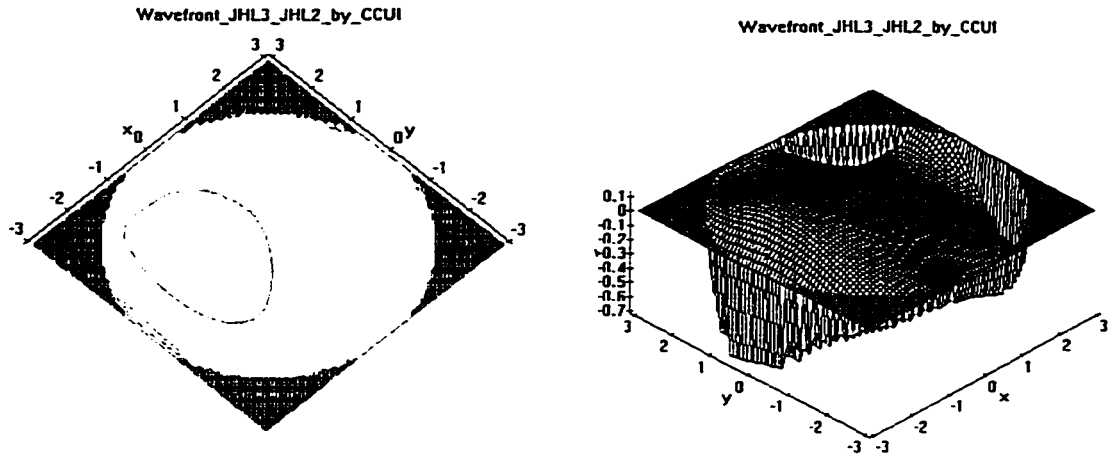


Fig. 4.7a Wavefront difference of JHL3 and JHL2. The left plot is the contour plot with the contour interval of 1λ; the right plot is the 3-dimensional wavefront aberration plot in microns with positive aberrations going into the eye; in the pupil coordinate system, positive denotes the temporal side in the horizontal meridian and the superior in the vertical meridian.

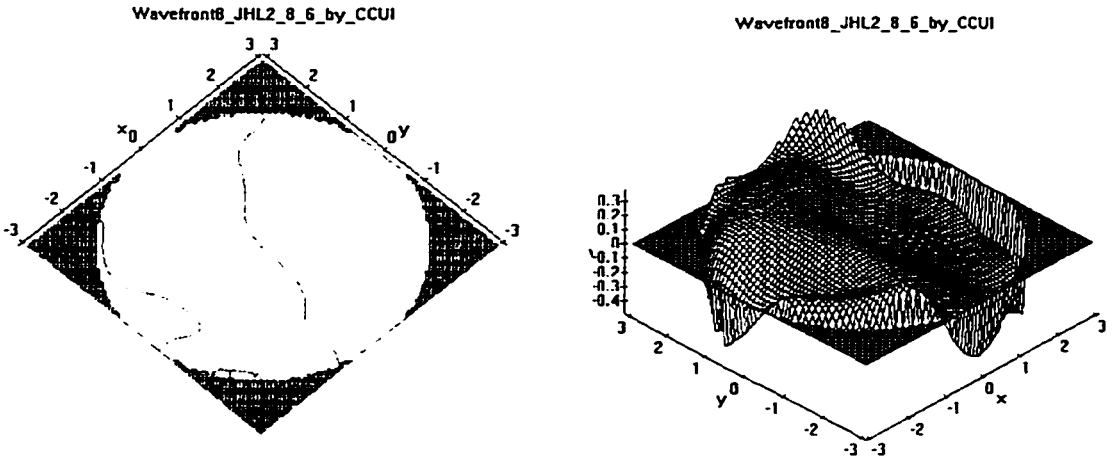


Fig. 4.7b Wavefront difference of JHL2 reconstructed to the 8th order Taylor polynomials and to the 6th order polynomials. The left plot is the contour plot with the contour interval of 1λ; the right plot is the 3-dimensional wavefront aberration plot in microns with positive aberrations going into the eye; in the pupil coordinate system, positive denotes the temporal side in the horizontal meridian and the superior in the vertical meridian.

From Fig. 4.6, it is already clear that the 6th order Taylor polynomial fit produces a satisfying fit to the measured data with respect to measurement repeatability. To further examine the issue, data of JHL2 were used to reconstruct wavefront up to the 8th order. Because there are already 43 terms in a Taylor polynomial to the 8th order, 8th order is the highest order possible to fit out of 49 data points.

Fig. 4.7a shows the wavefront difference of JHL2 and JHL3. Fig. 4.7b shows the wavefront difference of the 6^{th} order fit and 8^{th} order fit to JHL2. The wavefront difference between the 6^{th} order fit to JHL2 and the 8^{th} order fit to JHL2 is apparently smaller than the wavefront difference between JHL2 and JHL3.

On the other hand, the difference between JHL2 and JHL3 is comparable to the difference between the 6^{th} order and the 8^{th} order fit. In the worst scenario, assuming the difference between JHL2 and JHL3 was due to pure measurement errors, the measurement error was small.

4.6.4 Comparison of Zernike polynomial fit and Taylor polynomial fit

Because the human eye is neither a precisely centered optical system nor a system of elements of spherical surfaces, Zernike polynomials may not be advantageous to use, especially if the investigation was to study the total symmetrical and asymmetrical wavefront aberrations as intended in this study.

However, the orthogonal property of Zernike polynomials makes it a preferable polynomial for regression. In aberration measurements, the regression process is to fit the derivatives of the intended polynomials to the measured data. Since the derivative of Zernike polynomials is not necessarily orthogonal any more, the advantage to using Zernike polynomials may not exist. Nonetheless, it should produce comparable results when compared to Taylor polynomials with the method of least square regression adopted in this study.

Data of JHL2 were reconstructed to a 6^{th} Zernike polynomial using the same Maple V™ program as given in Appendix IV with corresponding terms switched to Zernike terms(see Appendix X). The result of a 6^{th} order Taylor polynomial fit is plotted in Fig. 4.8. The result of a 6^{th} Zernike polynomial fit is given in Fig. 4.9. The r-squared value is very close to the regression by the Taylor polynomial.

The contour plot shows consistent peripheral shapes and layers. The central region shows a normal unstable pattern due to the small and uniform aberration in the central

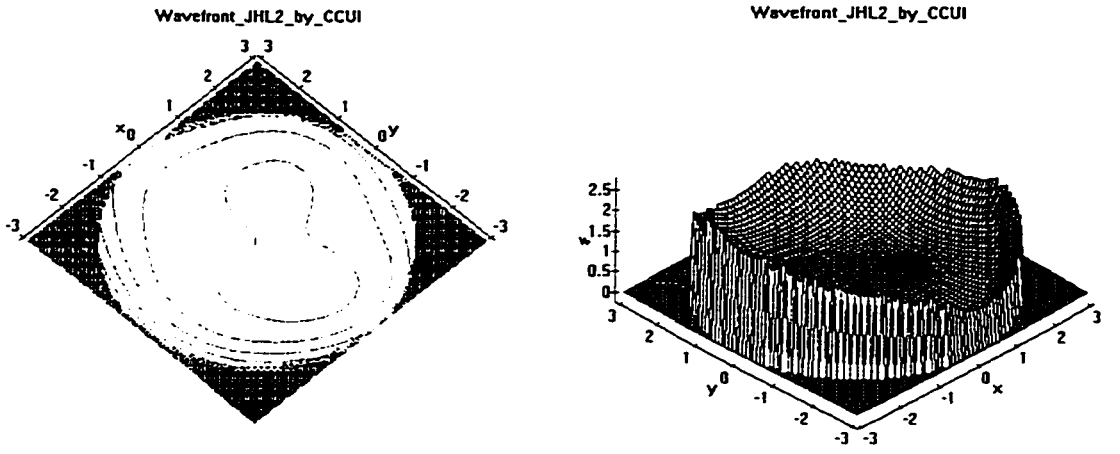


Fig. 4.8 Ray aberration data of JHL2 reconstructed to the 6th order Taylor polynomial. The left plot is the contour plot with the contour interval of 1λ; the right plot is the 3-dimensional wavefront aberration plot in microns with positive aberrations going into the eye; in the pupil coordinate system, positive denotes the temporal side in the horizontal meridian and the superior in the vertical meridian. The r-squared value of the fit is 0.96.

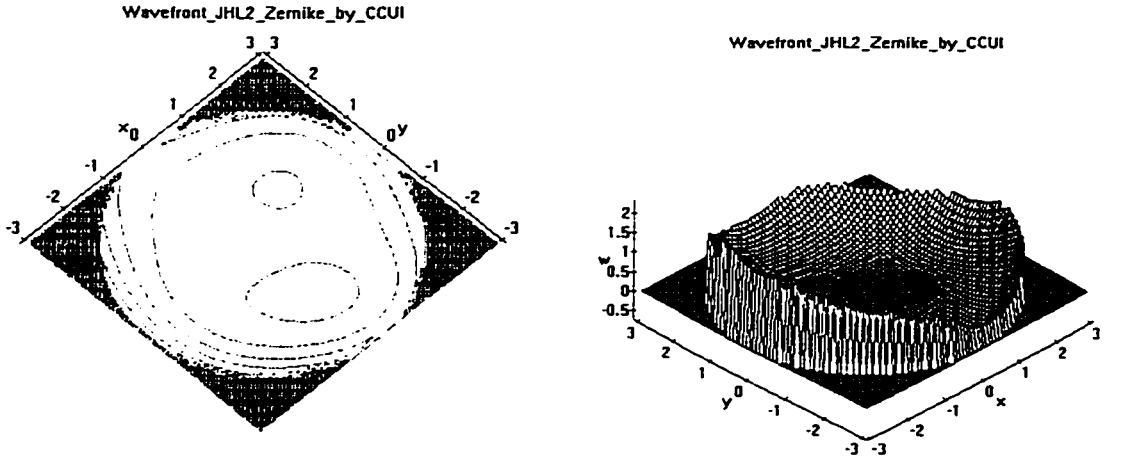


Fig. 4.9 Ray aberration data of JHL2 reconstructed to the Zernike polynomial to the 6th order. The r-squared value of the fit is 0.96.

zone. Again, contour lines are at 1 λ interval and the *w* axis in the 3-dimensional plot is in microns. The consistency of the two fits is more apparent when the 3-D plots on the right are compared.

4.6.5 Cases of low r-squared value fit

Fig. 4.4 includes the r-squared value for each the fit. The r-squared values for most subjects' fits are remarkably high. An exception is the case of subject LR. The r-squared value is as low as 0.31. Fig. 4.10 shows the raw ray aberration data plot. The distribution reveals a constant offset at all the sampling locations including the reference point.

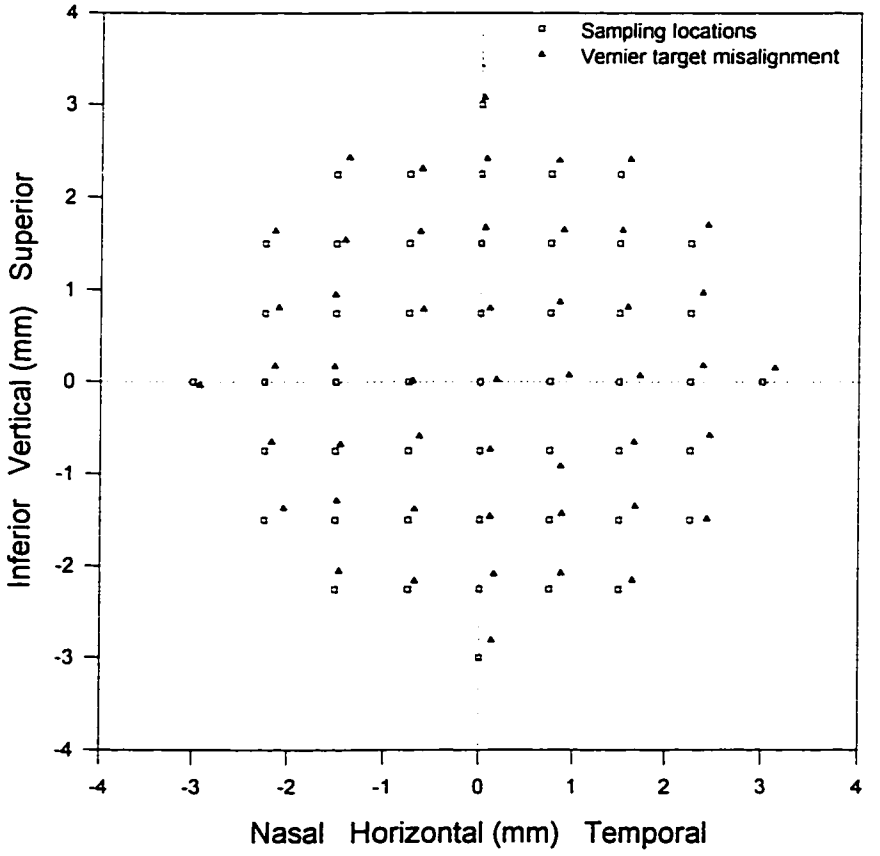


Fig. 4.10 Raw ray aberration data plot against sampling locations of subject LR's left eye. The convention of the plot is the same as that of Fig. 4.6.

In the operation of the measurement system, the computer program actually misaligned the two vernier targets after each alignment was made by the subject for a sampling location. The deliberate offset was 2 mm both for the horizontal and vertical meridians. It appears subject LR did not align the two vernier targets as instructed.

4.7 Comparison of aberration measured along CSCR and aberration measured with respect to the geometrical center of the pupil

The relationship between CSCR and the geometrical center of the pupil can be found by measuring the distance between them from the saved pictures. Fig. 4.11 shows the decentrations of the pupil center from the CSCR all the 21 subjects measured.

Although aberration measurements along the CSCR are potentially more accurate than measurements along the geometrical center of the pupil, it would be of interest to compare the difference of aberrations measured along the two different references for the same eye. The pilot measurements using the geometrical center of the pupil as the reference were conducted under natural pupil conditions.

Subjects AG and subject DC participated in both types of measurements. Fig. 4.12 shows the coordinate translated aberration plots of subject AG. For subject AG, his center of pupil is 0.38 mm to the temporal side of the CSCR and 0.19 mm to the inferior of the CSCR. It is obvious that Fig. 4.12 shows an aberration similar to aberration measured of the same eye using the geometrical center of the pupil as the reference as described in Chapter 3 (page 79).

Fig. 4.13 shows the coordinate translated aberration plots of subject DC. For subject DC, his center of pupil is 0.26 mm to the temporal side of the coaxially sighted cornea reflex and 0.60 mm to the inferior of the coaxially sighted cornea reflex. In DC's

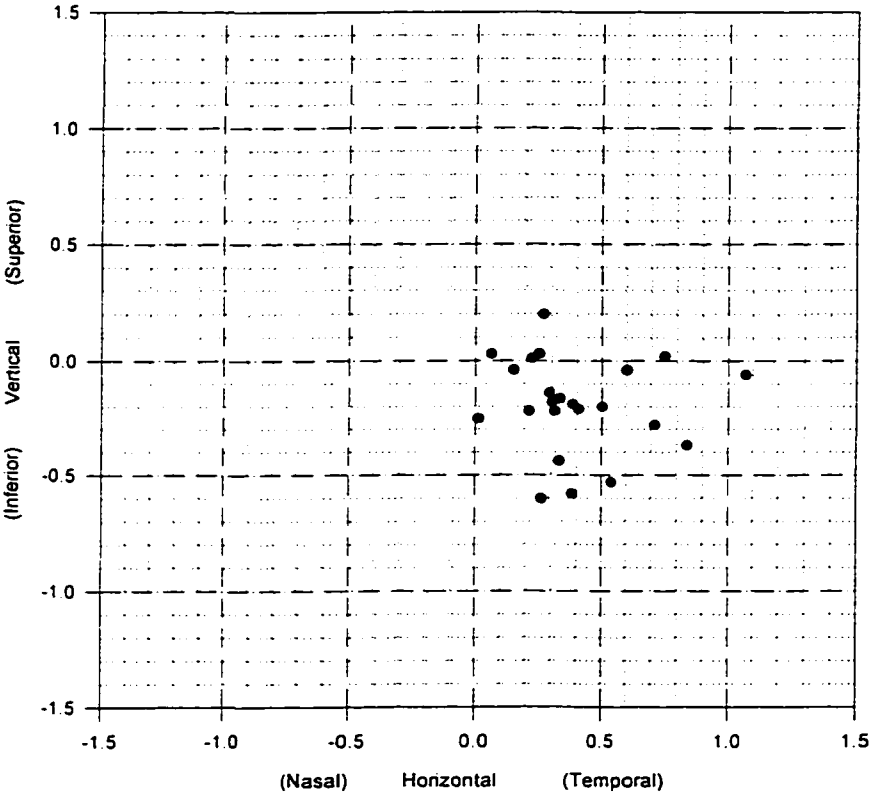


Fig. 4.11 Decentration of the geometrical center of the pupil from the CSCR. Each filled circle represents the position of the geometrical center of the pupil. The origin of the coordinates system is the position of CSCR.

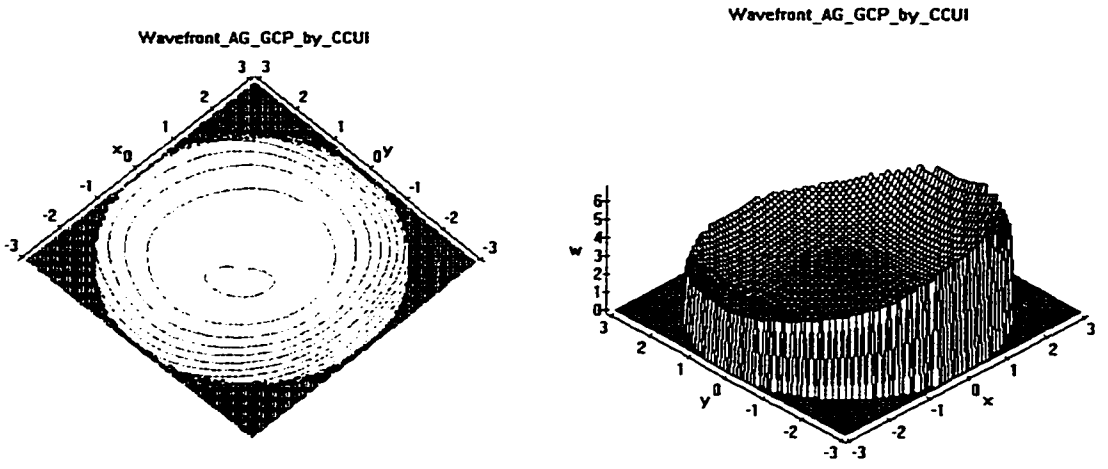


Fig. 4.12 Wavefront aberration of subject AG using the geometrical center of the pupil as the reference after converted from wavefront aberration measured using the coaxially sighted corneal reflex as the reference.

case, a plot of pure aberrations shows a more distinguishable relationship. Subject DC showed a natural pupil with substantial amount of overlapping between his upper eyelid and his upper portion of his pupil. This situation of eyelid overlapping would change the effective center of his pupil. It is also clear that Fig. 4.13 shows aberration similar to the aberration measured in the same eye using the geometrical center of the pupil as the reference as described in Chapter 3.

4.8 Average wavefront aberration of 20 subjects

The average ray aberration data were used to reconstruct wavefront aberration to show the general aberration situation in the human eye. Ray aberration data were averaged for 20 subjects (subject LR excluded). This averaged data set was used to reconstruct the wavefront aberration of a corresponding average eye to a 6th order Taylor polynomial. The result is as shown in Fig. 4.14. The r-squared value of the fit is as high as 0.996.

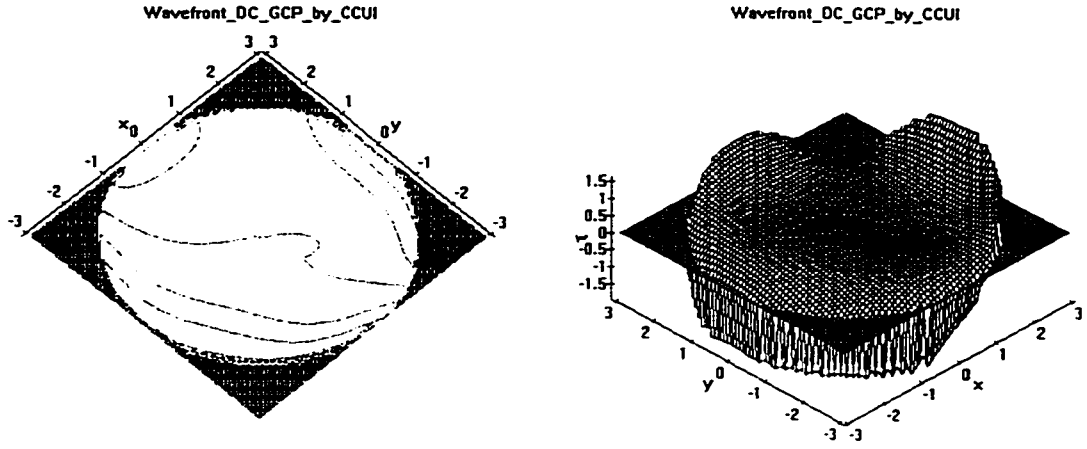


Fig. 4.13 Wavefront aberration (aberration only) of subject DC using the geometrical center of the pupil as the reference after converted from wavefront aberration measured using the CSCR as the reference. The left plot is the contour plot and the right plot is the 3-dimensional plot.

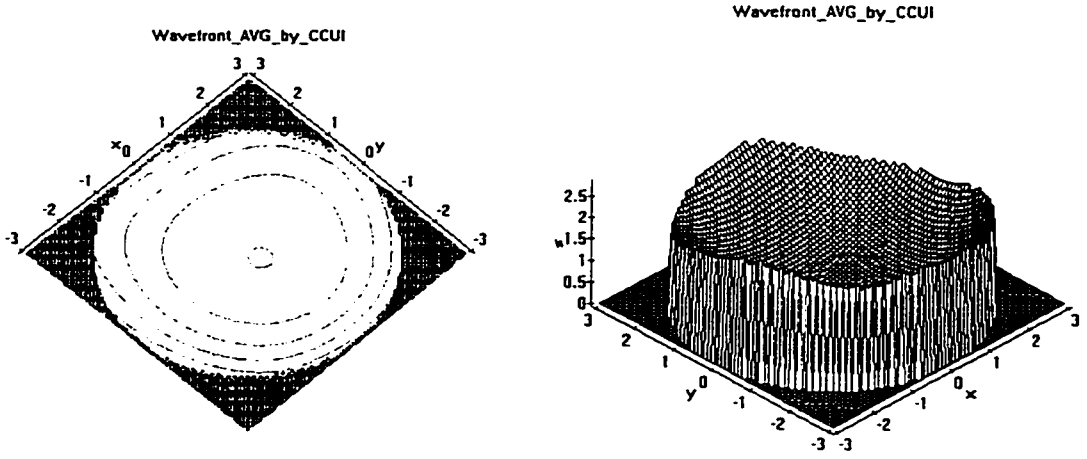


Fig.4.14 Wavefront aberration reconstructed to the 6th order Taylor polynomial from the averaged ray aberration data of the left eyes of the 20 subjects measured. The reference point is the CSCR. The left plot is the contour plot and the right plot is the 3-dimensional plot.

The total mean squared aberration (pure aberration) in this case is 0.18 μm^2 ; the asymmetrical component is 0.05 μm^2; the symmetrical component is 0.13 μm^2.

To develop a simpler aberration model, the average of the measured ray aberration data of the 20 subjects was fit to a 4th order Taylor polynomial. The wavefront is shown in Fig. 4.15.

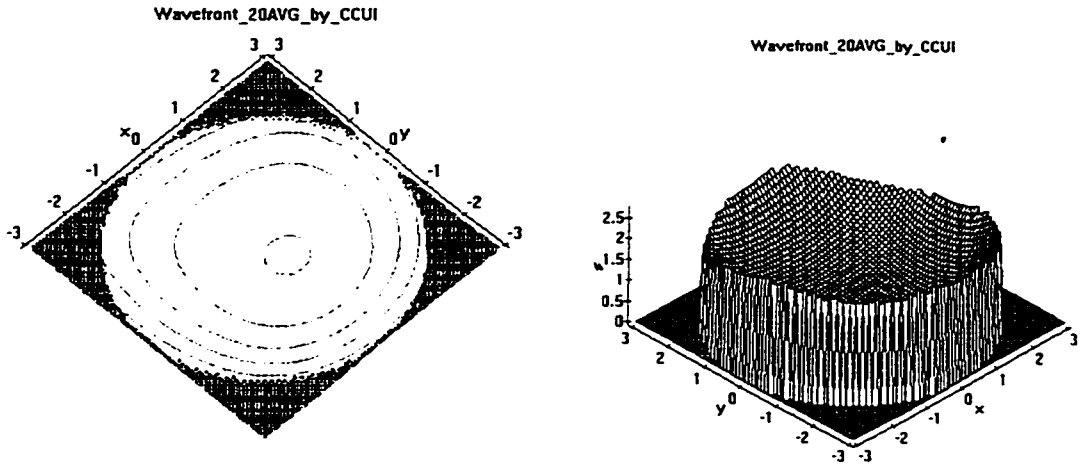


Fig. 4.15 Wavefront aberration reconstructed to the 4th order Taylor polynomial from the averaged ray aberration data of the left eyes of the 20 subjects measured. The reference point is the CSCR. The left plot is the contour plot and the right plot is the 3-dimensional plot.

The r-squared value of the fit is 0.996. This suggests that, for the "average" eye out of the population of 20 eyes measured, there is not much aberration higher than the 4^{th} order. Assuming a vernier alignment repeatability of 40 arc secs, the 95% confidence interval of all the Taylor polynomial coefficients is listed in Table 4.2. The terms that are significant are highlighted.

Table 4.2 The 95% confidence intervals of all the coefficients of the reconstructed 4th order Taylor polynomial.

Taylor term	Coefficients		95% confidence level	
			Lower limit	Upper limit
x	1(A)	-0.0585	-0.113	-0.004
y	2(B)	0.124	0.070	0.178
x^2	3(C)	0.148	0.130	0.166
xy	4(D)	0.000235	-0.026	0.026
y^2	5(E)	0.136	0.118	0.154
x^3	6(F)	-0.0133	-0.019	-0.008
x^2y	7(G)	-0.0416	-0.053	-0.030
xy^2	8(H)	0.00945	-0.002	0.210
y^3	9(I)	-0.0236	-0.029	-0.018
x^4	10(J)	0.0102	0.008	0.012
x^3y	11(K)	0.00981	-0.004	0.006
x^2y^2	12(L)	0.0101	0.004	0.016
xy^3	13(M)	0.00499	0.000	0.010
y4	14(N)	0.0134	0.012	0.015

If the above aberration is converted to the geometrical center of the pupil as the reference, the aberration plot is as shown in Fig. 4.16. The average reference shift is 0.403 mm to the temporal side and 0.195 mm to the inferior of the eye.

The total mean squared aberration (pure aberration) in this case is 0.25 μm^2 ; the asymmetrical component is 0.07 μm^2; the symmetrical component is 0.18 μm^2. The data here show that for an average eye, the aberration measured along the coaxially sighted

corneal reflex is actually smaller than the aberration of the same eye measured along the geometrical center of the pupil.

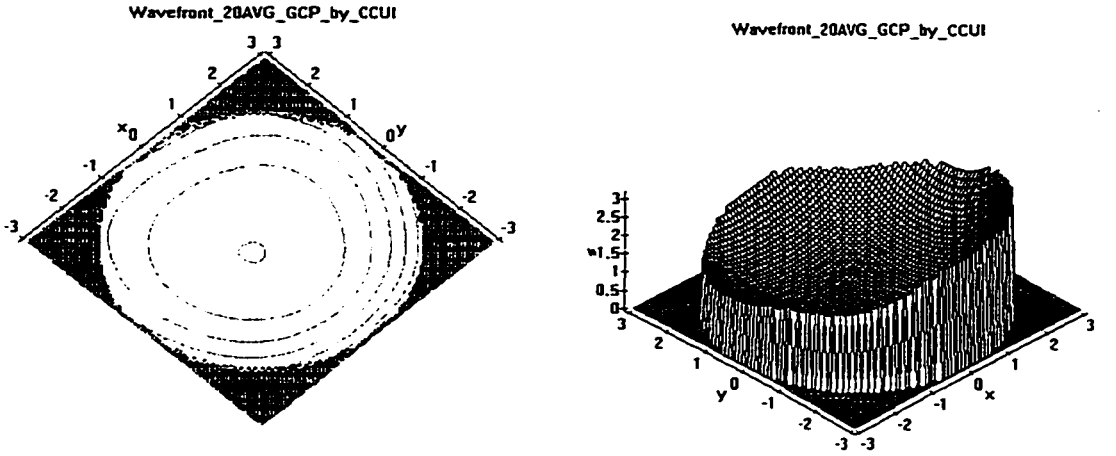


Fig. 4.16 Wavefront aberration (6th order Taylor polynomial) using the geometrical center of the pupil as the reference after converted from wavefront aberration measured using the coaxially sighted cornea reflex as the reference.

4.9 Conclusions

Monochromatic ray aberrations of the left eyes of 21 emmetropic subjects were measured using an automated semi-Maxwellian view measurement system. The coaxially sighted corneal reflex was used as the reference axis. This proved to be a more effective reference to study the wavefront aberration of the human eye than the geometrical center of the pupil. Pupil decentrations with respect to the coaxially sighted corneal reflex were also measured using saved pupil frames.

Relationships of the coefficients between using two different reference axes were derived. Aberrations measured using the coaxially sighted corneal reflex as the reference can be conveniently converted to aberrations using the geometrical center of the pupil as the reference. The average aberration of the 20 eyes measured shows mainly symmetrical aberrations.

Chapter 5

Measurement of the Misalignment of Ocular Components *in vivo*

5.1 Introduction

In this chapter, a special Purkinje image photographic system was devised and used to systematically measure the misalignments of the ocular components and identifying various reference axes. These measurements include crystalline lens tilt and decentration, pupil decentration, angle alpha and effect of the non-existence of an optical axis on the measurement of angle alpha. Relationships between these parameters are also discussed. These data can be used to build an appropriate eye model to demonstrate the general misalignment characteristics of the human eye.

5.2 Choice of a reference axis

There are three axes that can be possibly used as the reference for measuring the misalignments of the eye.

1) The line of sight

Problems in precisely locating the geometrical center of the pupil, controlling the real pupil center shift under different conditions and the non-centered Stiles-Crawford apodization will present difficulties in locating the line of sight.

2) The coaxially sighted corneal reflex (CSCR)

As defined in Chapter 1, this axis connects the fixation point and the center of curvature of the anterior surface of the cornea. It is easily accessible by a video camera with one or more than one light sources mounted coaxially with the axis of the camera. Its location at the pupil plane is Purkinje I of the light sources. It is also theoretically close to the traditionally defined visual axis or nodal axis.

3) PI and PIV aligned axis (P1P4)

From its definition, this axis is the common optical axis of the anterior surface of the cornea and the posterior surface of the lens. It is also the optical axis of the eye if the cornea and the lens are aligned. Because PIV is relatively easy to view, this axis can be

easily located with a video camera and a light source that is coaxial with the camera by aligning both Purkinje images I and IV with the axis of the camera represented by the center of the video screen.

5.3 Apparatus

5.3.1 Use of photoflash light as the Purkinje image light source

One of the formidable difficulties involved in examining the misalignments of ocular components by using the Purkinje images is the difficulty of observing PIII. The reasons for its poor visibility include (Bennett and Rabbetts, 1984),

a) The orange peel surface structure of the anterior surface of the lens;

b) It is formed at a plane that is deeper into the eye than the pupil plane where Purkinje I and IV are approximately focused;

c) It is of a larger magnification (about twice of that of PIV) while it is formed with about the same total amount of light flux as PIV.

The obvious solution to obtaining PIII of acceptable quality is to increase the brightness of the light source. The immediate problem that arises is the concern of the radiation safety to the subject. A compromise is to use a photoflash light source. Combined with a synchronized video frame grabbing system, it is possible to view PIII.

5.3.2 Hardware

As shown in Fig. 5.1, a Nikon™ 105 mm f/2.8 macro photographic lens with a built-in telecentric stop (Appendix XI) combined with a CCD module (512x512) was mounted on an optical bench and focused at the eye. A ring was tightly mounted to the front of the camera lens. On the ring, there were four holes uniformly drilled 90° apart for mounting the ends of fiber optical cables. The rings were precisely adjusted to have two

holes to represent the horizontal and vertical meridians of the camera lens, respectively. The other ends of the optical cables were inserted into the reflector chamber of a

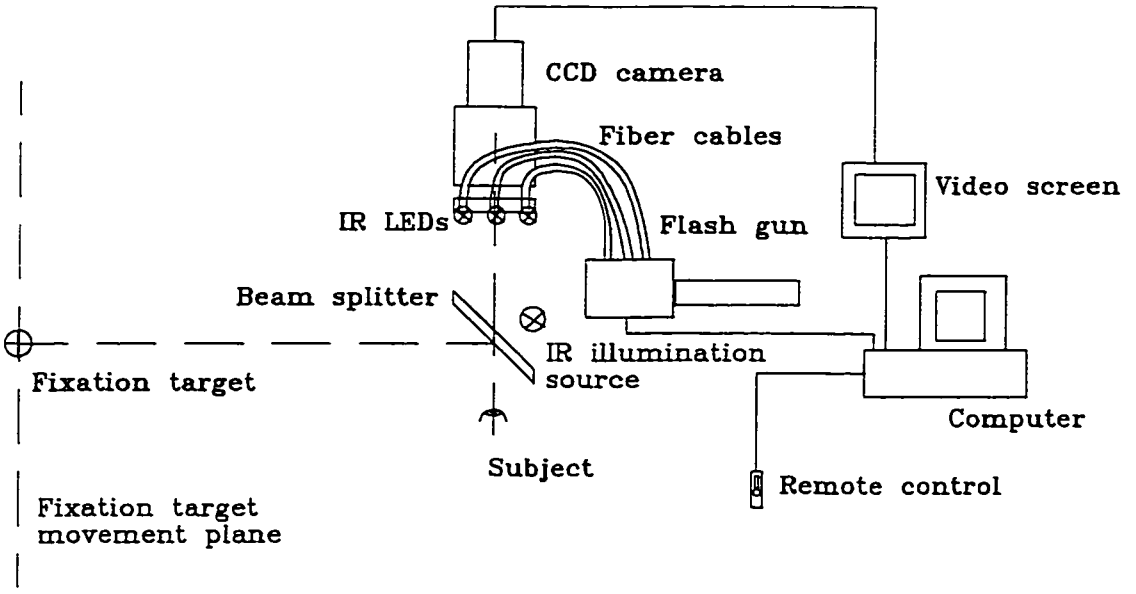


Fig. 5.1 A Purkinje image photographic system for measuring ocular component misalignments. The camera system consists of a macro photographic lens, a CCD module, a frame grabbing board and the host computer; the illuminations include the photographic photoflash gun, an IR LED array and a filtered Tungsten-Halogen source; the fixation target is on a split channel.

photographic photoflash gun (Metz™ 45). The photoflash gun was controlled by the host computer via the printer port and could be fired by a control button. During the actual measurement, only two fiber cables were used to represent the horizontal and vertical meridians of the camera system. On top of the photoflash cable ring, another ring was mounted. On this ring, four IR LEDs as used in Chapter 4 were uniformly mounted in a similar way as the optical cables were mounted.

A thin beam splitter was mounted immediately in front of the eye with a 45° angle to introduce another channel of view -- the view of a fixation target. This view of fixation could be adjusted to be coaxial with the optical axis of the camera lens system. In this view, a cross target with a magnetic base was mounted onto a vertical metal screen which was adjusted to be perpendicular to the optical axis of the camera lens system. The target was illuminated by a desk lamp. The magnetic target could be moved freely on the metal screen and the magnetic force tightly held the magnetic target position. A sheet of graph paper was mounted on the metal screen to record positions of the magnetic target.

The subject was positioned by a bite bar system which was mounted on a 3-dimensional adjustable stand.

To reduce UV hazard radiation, a piece of UV absorbing glass was used at the exit window of the photoflash gun. Considering the specific configuration, a conservative evaluation showed that the safe distance from the ends of the fiber bundles to the eye was 24 cm when the photoflash gun was used at its full power output. The actual distance used was 40cm and the actual photoflash light level used was ¼ its maximum output.

5.3.3 Software

Custom software (Appendix V) was written to,

a) display of the pupil plane in real time with a reference cross representing the axis of the camera in the background;

b) fire a single photoflash and grab a picture of the photoflash light illuminated pupil simultaneously;

c) save and retrieve pictures of the eye and measure distances of a pupil picture displayed on the video screen.

5.3.4 System alignment

The alignment procedures are as follows.

a) The critical step was to establish a reference laser beam to define the reference axis of the system. This beam line could be scanned accurately in the horizontal and vertical meridians separately. This step required a reliable adjustable laser tube mount, a solid tripod stand with fine adjustment screws. Two alignment conic pins of the same heights were mounted on the optical bench at sufficient distance along the path of the laser beam and the axis of the cornea. A He-Ne laser tube was placed behind the bite bar and was pointed toward the camera lens. The fine adjustment screws of the camera mount were adjusted until both tips of the pins intercepted the laser beam at the same location.

b) The camera with the smallest aperture size and attenuated by polarization plates was slid back and forth on the optical bench. The mounting screws of the camera mount were adjusted until the laser beam always stayed at the center of the video screen when slid back and forth.

c) The beam splitter was adjusted so that the reflected laser beam was of the same height as of that of the tips of the two conic pins on the optical bench no matter where it was examined between the beamsplitter and the magnetic target.

d) The position of the laser beam on the graph paper was marked as the zero reference position, or the point that was coaxial with the optical axis of the camera system.

5.4 Procedures

Measurement procedures were different depending on the reference axis used. One emmetropic subject was measured twice to test the apparatus and method. The left eyes of 21 emmetropic subjects were then measured after the monochromatic aberration experiment.

5.4.1 Measurement with respect to the CSCR

The subject was instructed to steadily fixate at the fixation target which was coaxial with the camera. Clearly focused PI of the IR LEDs were aligned with the central reference cross on the video screen and the alignment was maintained during the measurement.

The photoflash light was then fired and a picture of the pupil was grabbed and frozen on the video screen while the PI of the IR LEDs were aligned with the central cross on the video screen. The frozen picture was immediately examined and saved for later analysis.

5.4.2 Measurement along aligned PI and PIV

The subject was asked to fixate at the target. PIs of the LEDs were aligned with the reference cross on the video screen and the photoflash gun was fired with a picture of the pupil and Purkinje images grabbed. The quality of the images captured was visual evaluated. The target was moved horizontally to the nasal side of the subject by 17 cm (about 5°). The procedure is represented in Fig. 5.2. The amount of target adjustment step size generally followed a geometrical progression scheme.

After the horizontal alignment was achieved, the same adjustment was done to reach the vertical alignment. At the end, repeated adjustment was needed to reach both horizontal and vertical alignments. When the final alignment was reached, the pupil picture with the Purkinje images were saved. The position of the fixation target was also recorded relative to the origin of the fixation plane for the calculation of angle alpha.

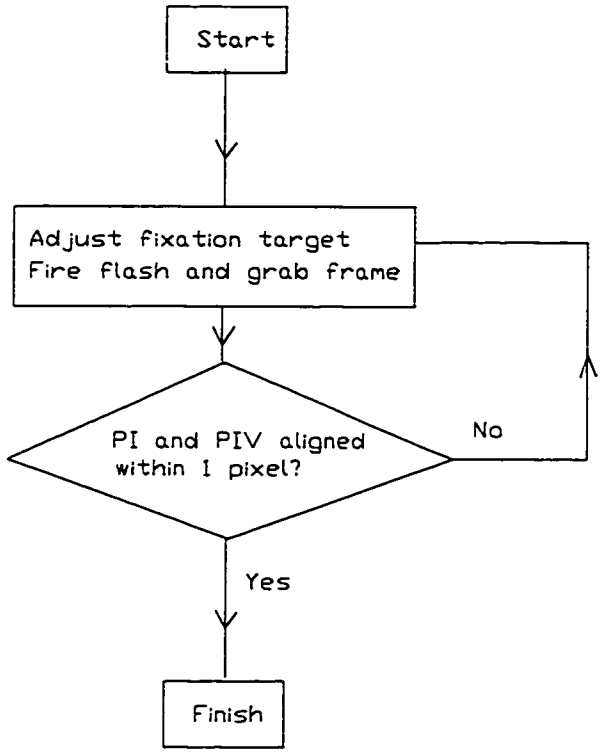


Fig. 5.2 Flow chart illustrating target adjustment to achieve Purkinje image alignment.

5.4.3 Measurement along PI and PIII

Similar to Section 5.4.2), the alignment of PI and PIII were also done for most subjects. Normally when PI and IV were aligned, PI and PIII were also close to alignment. The data can be most helpful in comparing angle alphas measured by aligning PI and PIV and angle alpha measured by roughly aligning all Purkinje images (Tscherning, 1924).

5.5 Results and data analysis

Pupil decentration, Purkinje image misalignment and fixation target deviation from the optical axis of the eye were measured from the saved frames. Fig. 5.3 shows an example of the saved pictures of the left eyes of subject AG along the CSCR. The cross inside the box represents the axis of the camera system. To the left of the pupil, the largest

inside the box represents the axis of the camera system. To the left of the pupil, the largest two Purkinje images were PIII of the ends of the two optical cables illuminated by the photographic photoflash light; in the middle, the two brightest images were PI; to the right, the two smallest images were Purkinje images IV. Along this axis, of all the 21 eyes tested, only 6 eyes showed all three Purkinje images clearly. The other eyes either showed only one of the two PIIIs or neither of them. The obvious reason would be that the PIIIs were out of the entrance pupil. There were some other factors that would also contribute to the disappearance of PIII. These factors include the reflection property of the anterior surface of the lens and the actual curvature of anterior surface of the lens.

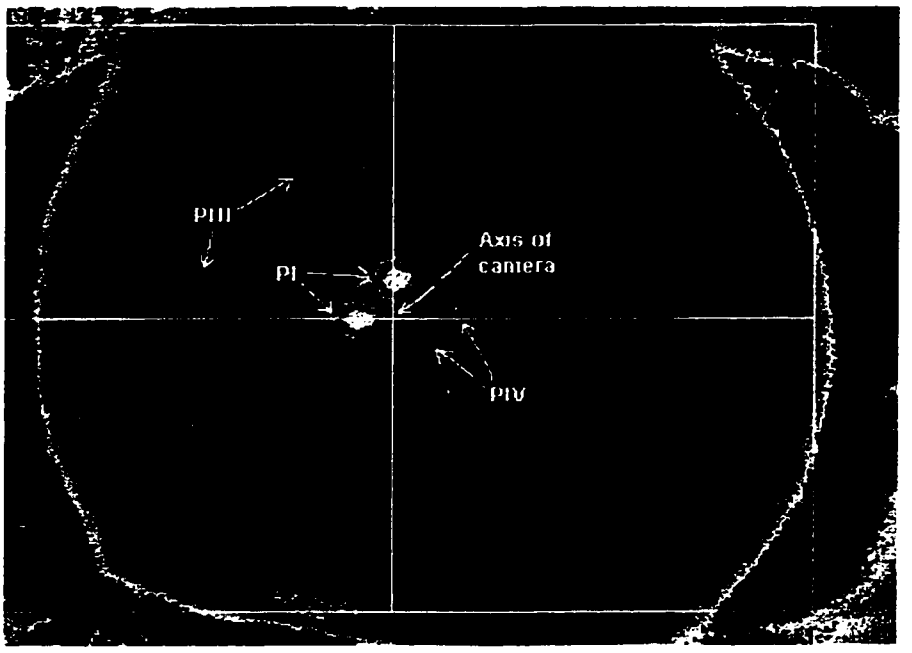


Fig. 5.3 A picture of the pupil with Purkinje images along the CSCR of the left eye of subject AG. The box with the cross is the centered at pixel (256, 242) representing the axis of the camera system; the ends of two optical fiber cables were flashed when the picture was grabbed; PIIIs are in the left upper quadrant of the pupil; PIs are aligned with the reference cross and are the brightest two spots in the picture; PIVs are to the right of the reference cross.

Fig. 5.4 shows the picture of the eye when PI and PIV were aligned at the same time for subject AG. When PI and PIV were aligned, PIII always tended to have a much improved image quality.

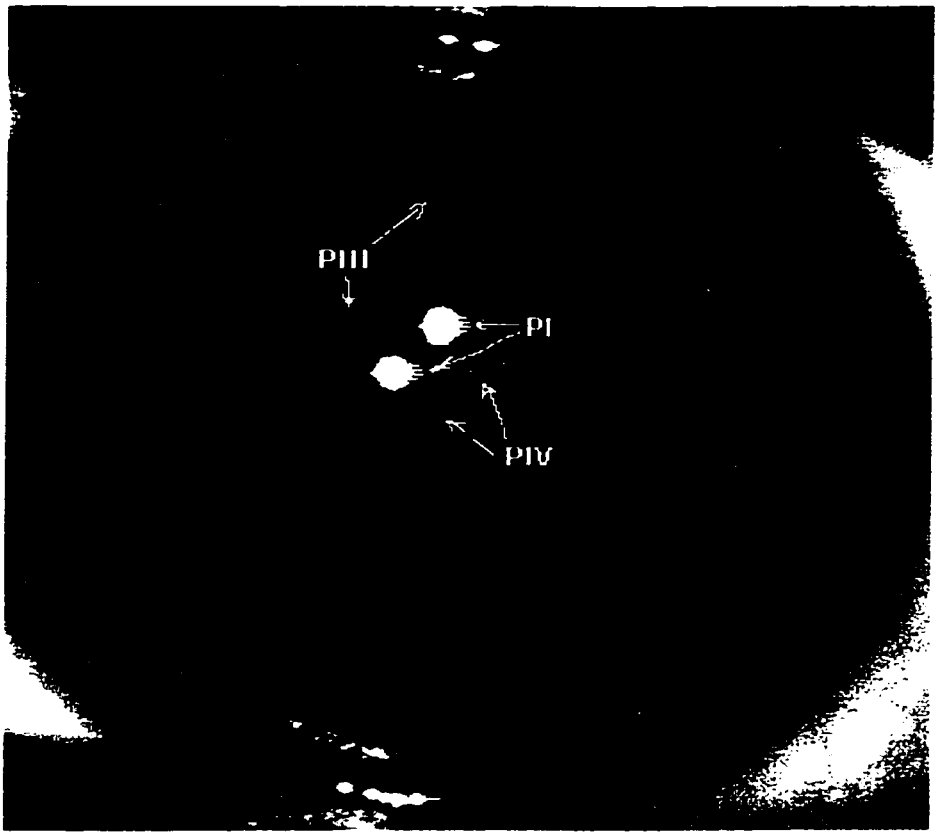


Fig. 5.4 A picture of the left eye of subject AG with aligned PI and PIV. The ends of two optical fiber cables were flashed when the picture was grabbed; PIIIs are in the left upper quadrant of the pupil; PIs are the brightest two spots in the center of the pupil; PIVs are to the right of PIs. PIII is misaligned upward.

Fig. 5.5 shows the picture of the eye when PI and PIII were aligned.

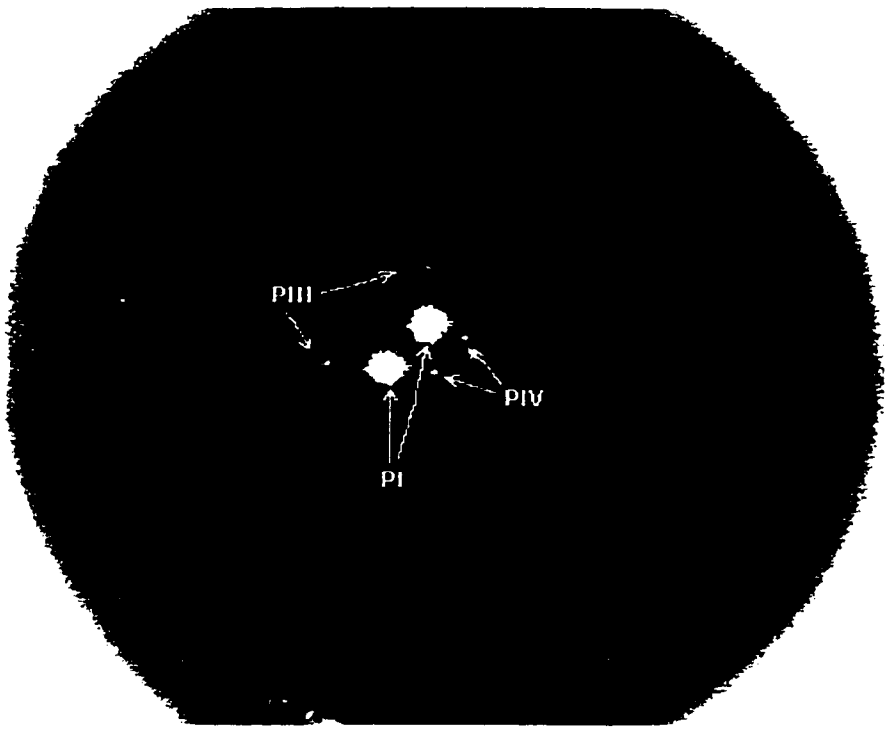


Fig. 5.5 A picture of the left eye of subject AG with aligned PI and PIII. PIV is misaligned to the upper right.

5.5.1 Lens tilt and decentration

From approximately 200 pictures similar to those shown in Fig. 5. 3 - 5.5, the magnitude of Purkinje image misalignments were measured and used to calculate lens tilt and decentration along the respective reference axes.

Table 5.1 shows the amount of lens tilt along the aligned PI and PIV and the CSCR. For both lens tilt and decentration, the temporal side and the superior of the eye represent positive directions. Only 6 subjects showed measurable PIII when measured along the CSCR. For some subjects, measurement data can only be obtained in one dimension.

Table 5.1 Horizontal (H) and vertical (V) components of lens tilt and decentration of the left eyes of 21 subjects along the aligned PI & PIV and the CSCR, respectively. The standard deviations, the group means and the 95% confidence intervals are also tabulated.

Subject	Tilt from the aligned PI&PIV (°)		Decentration from the aligned PI&PIV (mm)		Tilt from the CSCR (°)		Decentration from CSCR (mm)	
	H	V	H	V	H	V	H	V
AG	-0.56	-1.72	0.03	0.10	5.06	0.70	0.31	0.19
LO	1.22	-0.71	-0.07	0.04				
DC	1.75	-1.38	-0.11	0.08				
SB	0.95	-2.35	-0.06	0.14				
MS	1.11	-2.62	-0.07	0.16				
PK	1.01	-1.64	-0.06	0.10	7.26		0.05	
JH	0.48	-0.93	-0.03	0.06	5.48	-1.64	0.13	0.10
KP	2.17	-3.47	-0.13	0.21				
ME	0.05	-2.28	0.00	0.14		-3.14		0.52
BN	2.83	-2.30	-0.17	0.14		-3.14		0.52
GD	0.61	-0.90	-0.04	0.05	4.51	-0.01	0.22	0.23
TP	0.00	-1.19	0.00	0.07				
DD	0.29	-1.72	-0.02	0.10		-0.29		0.27
DH	0.50	-0.79	-0.03	0.05	4.86	-0.60	0.16	0.15
GN	1.69	-2.34	-0.10	0.14				
DE	1.06	-1.96	-0.06	0.12				
NP	2.12	-2.65	-0.13	0.16				
MC	0.03	-2.12	0.00	0.13	4.14	-1.40	0.24	0.00
HA	-1.00	-1.40	0.06	0.08	4.99	-1.33	0.16	0.05
AH	0.26	-2.65	-0.02	0.16				
LR	1.93	-2.91	-0.12	0.18				
AVG	0.88	-1.91	-0.05	0.12	5.19	-1.21	0.18	0.23
STDV	0.97	0.76	0.06	0.05	1.01	1.32	0.08	0.19
	95% Confidence intervals							
	0.440	0.347	0.026	0.021	0.933	1.017	0.078	0.144

Lens tilt values are also plotted in Fig. 5.6. Lens decentration values are plotted in Fig. 5.7.

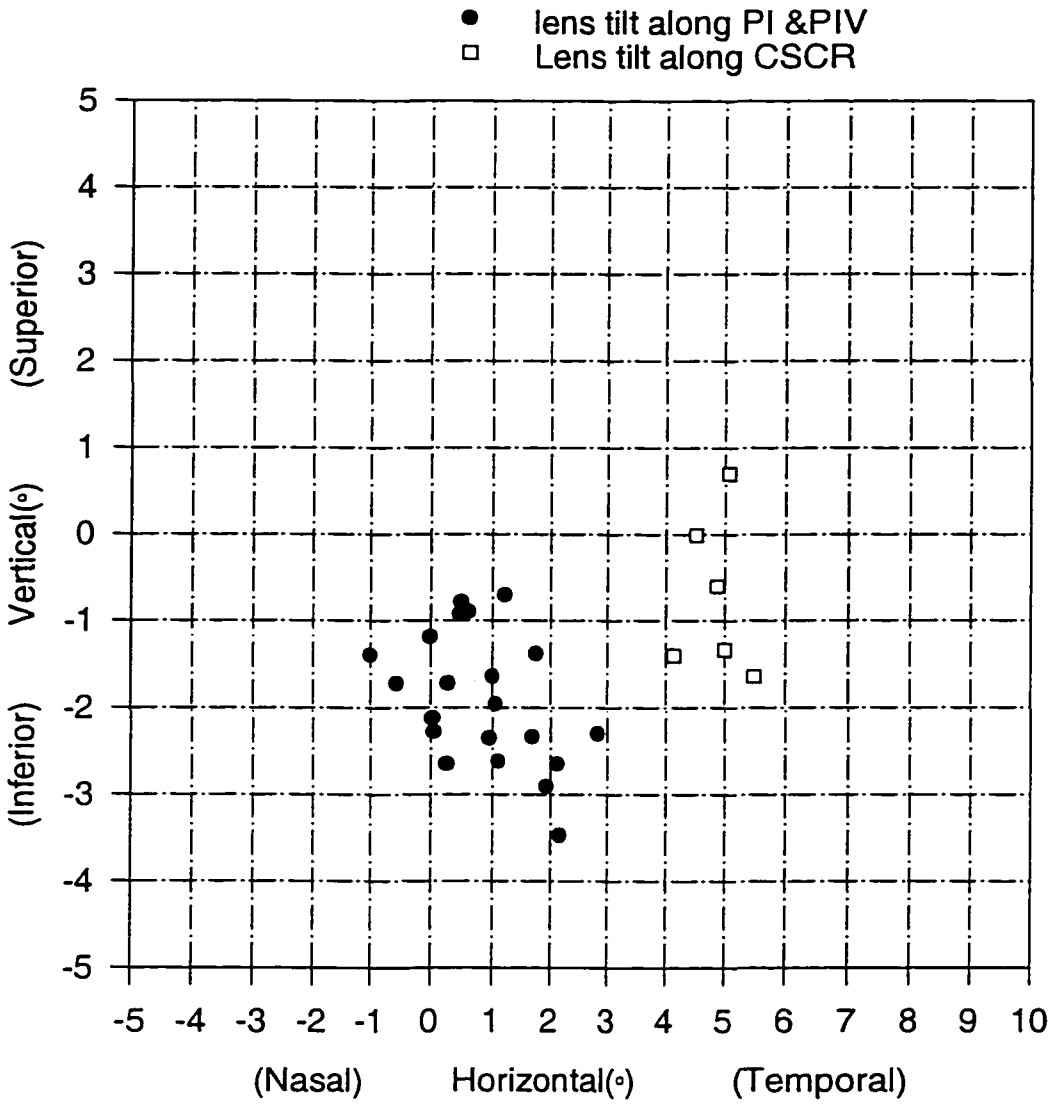


Fig. 5.6 Lens tilt of 21 subjects from PI & PIV and the CSCR, respectively. The filled circles represent the lens tilt from the PI & PIV; the open squares represent the lens tilt from the CSCR. Data of lens tilt from the CSCR are only available for 6 eyes.

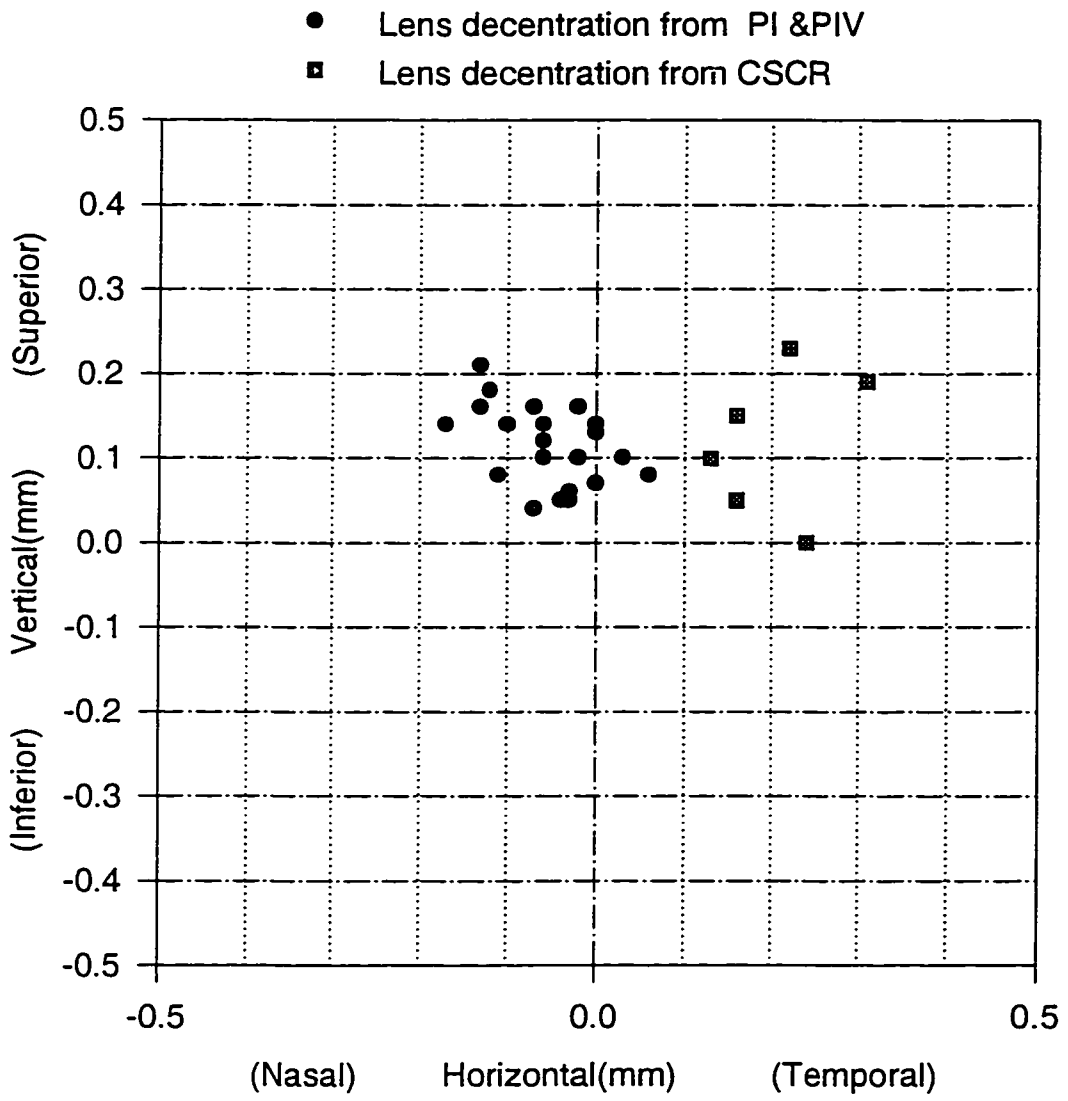


Fig. 5.7 Lens decentration of 21 subjects from the aligned PI&PIV and the CSCR, respectively. The filled circles represent the lens decentration from the PI & PIV; the open squares represent the lens decentration from the CSCR. Data of lens decentration from the CSCR are only available for 6 eyes.

5.5.2 Pupil decentration

From pictures similar to Fig. 5.3 to Fig. 5.5, the amount of pupil decentration for each picture was also measured with respect to each reference axis. Pupil decentrations from aligned PI and PIV and from the CSCR are tabulated in Table 5.2 and plotted in Fig.5.8 . Again, the temporal side and the superior of the eye are positive.

Table 5.2 Horizontal (H) and vertical (V) components of pupil decentration of 21 subjects measured along the aligned PI&PIV and the CSCR, respectively. The standard deviations, the group means and the confidence intervals are also tabulated.

Subject	Decentration from the aligned PI&PIV (mm)		Decentration from the CSCR (mm)	
	H	V	H	V
AG	-0.25	-0.21	0.64	-0.14
LO	-0.63	-0.80	0.55	-0.93
DC	-0.41	-0.39	0.65	-0.28
SB	-0.37	-0.05	0.63	0.14
MS	-0.31	-0.44	0.75	-0.25
PK	-0.39	-0.02	0.18	0.20
JH	-0.24	-0.51	0.50	-0.43
KP	-0.16	-0.20	0.44	0.24
ME	-0.21	-0.39	0.59	0.16
BN	-0.53	-0.70	0.41	-0.46
GD	-0.29	-0.24	0.35	0.02
TP	-0.11	-0.13	1.02	-0.12
DD	-0.61	-0.20	0.40	0.08
DH	-0.52	-0.36	0.38	-0.06
GN	-0.50	-0.19	0.09	0.09
DE	-0.39	-0.23	0.22	0.01
NP	-0.03	0.06	0.89	0.02
MC	-0.13	-0.30	0.29	-0.23
HA	-0.08	-0.15	0.40	-0.18
AH	-0.29	-0.15	0.29	-0.11
LR	-0.00	-0.30	0.33	-0.14
Mean	-0.31	-0.28	0.48	-0.11
STDV	0.19	0.21	0.23	0.27
	95% Confidence intervals			
	0.08	0.10	0.11	0.12

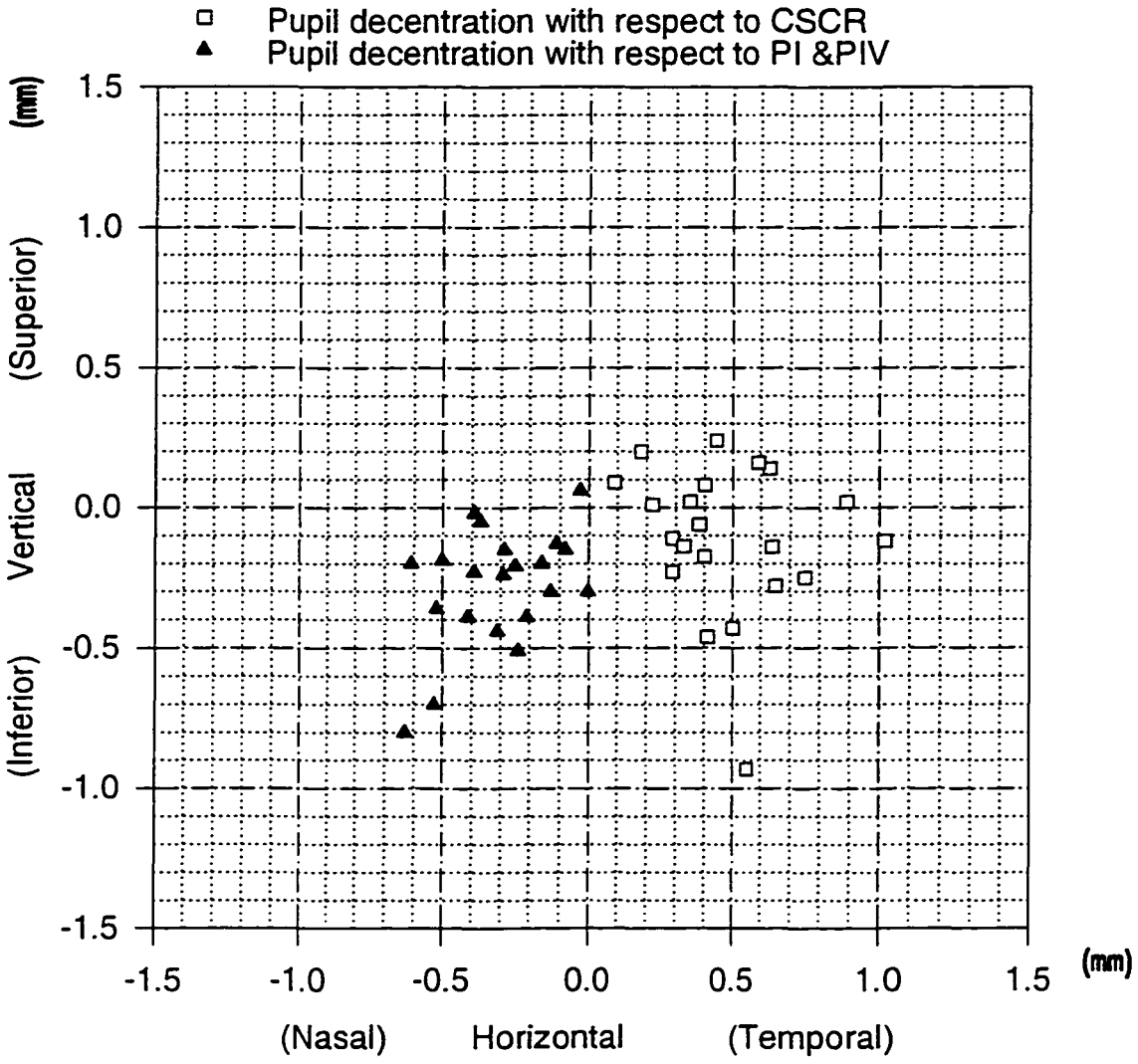


Fig. 5.8 Pupil decentration of 21 subjects measured with respect to the aligned PI&PIV and the CSCR, respectively. The filled triangles represent pupil decentration with respect to the aligned PI and PIV; the clear squares represent the pupil decentration with respect to the CSCR.

5.5.3 Angle alpha

Angle alpha was calculated from the deviation of the fixation target from the origin of the fixation plane. They are tabulated in Table 5.3 and plotted in Fig. 5.9. To conform with traditionally quoted angle alpha values (Bennett and Rabbetts, 1984), an angle alpha to the nasal side of the eye in the horizontal meridian and to the inferior of the eye in the vertical meridian is positive. The difference of angle alpha measured by aligning PI and PIV and by aligning PI and PIII were also examined. Subject LO's angle alpha value by PI and PIII was not available due to poor image quality of PIII.

Table 5.3 Horizontal (H) and vertical (V) components of angle alpha values of the left eyes of 21 subjects measured by aligning PI & PIV and PI &PIII, respectively.

Subject	Angle alpha (°) by PI & PIV		Angle alpha (°) by PI & PIII	
	H	V	H	V
AG	5.16	0.76	4.28	-1.86
LO	5.70	-1.14		
DC	4.26	-2.27	6.12	-4.10
SB	6.50	-1.37	7.91	-3.36
MS	4.56	0.17	5.64	-4.33
PK	4.38	0.14	5.92	-1.88
JH	4.21	-0.48	5.95	-2.91
KP	4.66	0.92	6.94	-2.66
ME	5.43	2.45	5.00	-2.22
BN	5.64	0.69	7.25	-2.09
GD	4.49	1.58	4.85	-1.30
TP	7.11	0.49	7.24	-3.25
DD	5.18	1.82	7.11	-4.21
DH	3.61	0.86	5.11	-1.35
GN	4.67	2.31	5.90	-1.75
DE	4.49	1.03	5.90	-1.46
NP	7.15	0.92	9.00	-1.46
MC	5.40	2.43	4.97	-3.55
HA	5.54	0.38	4.35	-2.49
AH	5.93	2.48	6.62	-1.86
LR	6.19	1.03	8.11	-3.67
Mean	5.25	0.72	6.21	-2.59
STDV	0.96	1.28	1.26	1.02
	95% Confidence intervals			
	0.44	0.58	0.61	0.48

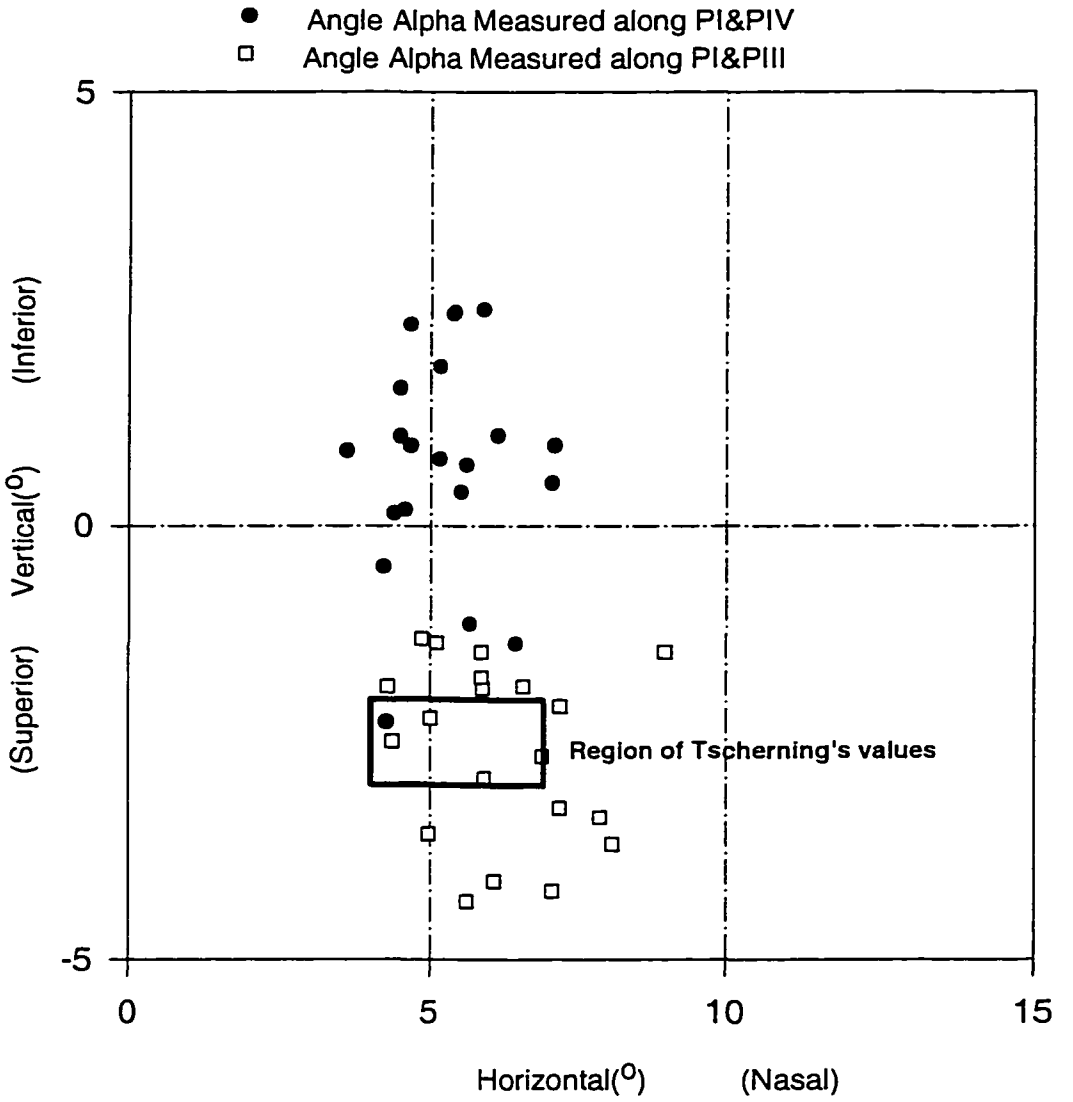


Fig. 5.9 Angle alphas of the left eyes of 21 subjects measured by aligning PI & PIV and by aligning PI &PIII, respectively. The filled circles represent the angle alphas measured by aligning PI and PIV (or angle deviation of the visual axis from the aligned PI and PIV); the clear squares represent angle alphas measured by aligning PI and PIII (or angle deviation of the visual axis from the aligned PI and PIII).

5.5.4 Derivation of lens tilt and decentration with respect to the line of sight and the pupillary axis

Measurement of lens tilt and decentration with respect to the aligned PI and PIV can reveal the general lens misalignment situation. Still, it would be desirable to calculate these values with respect to a reference that has been better understood and more often used in clinical applications or in traditional research. Given other parameters measured and an average eye model, lens tilt and decentration can be calculated with respect to the line of sight, pupillary axis, etc.

a) Lens tilt and decentration with respect to the line of sight

Lens tilt with respect to the line of sight can be easily derived. Given the Gullstrand-Emsley eye model, the angle between the aligned PI and PIV and the line of sight can be calculated from the pupil decentration from aligned PI and PIV and the distance from the center of curvature of the cornea to the pupil plane. Lens tilt with respect to the line of sight is then the difference of the angle alpha measured along the aligned PI and PIV and the lens tilt with respect to the aligned PI and PIV.

Lens decentration with respect to the line of sight is slightly more complex to derive. As shown in Fig. 5.10, point B is the center of the pupil; point O is the center of the lens; point E is the center of curvature of the cornea; line AF is the pupillary axis; line LN is the axis along which PI and PIV are aligned; line HK is the line of sight; distance MO is lens decentration with respect to the axis that PI and PIV are aligned; distance IO is the lens decentration with respect to the line of sight. $\angle LJH$ is angle alpha (α) measured by aligning PI and PIV; For the G-E eye model, RE=4.2 mm; ME=3.0 mm. To determine lens decentration with respect to the line of sight, it is convenient to use the construction on Fig. 5.10: a perpendicular line BR to line LN through point B; a line MP perpendicular to line IO through point M; a line MQ perpendicular to line HK through point M. Using the construction, the following relation is defined for lens decentration:

$$y_{\text{line of sight}} = y\cos\alpha + 1.2\sin\alpha - \rho\cos\alpha \qquad (5.1)$$

where ρ is the pupil decentration from aligned PI and PIV. α is positive to the temporal and to the inferior in the eye.

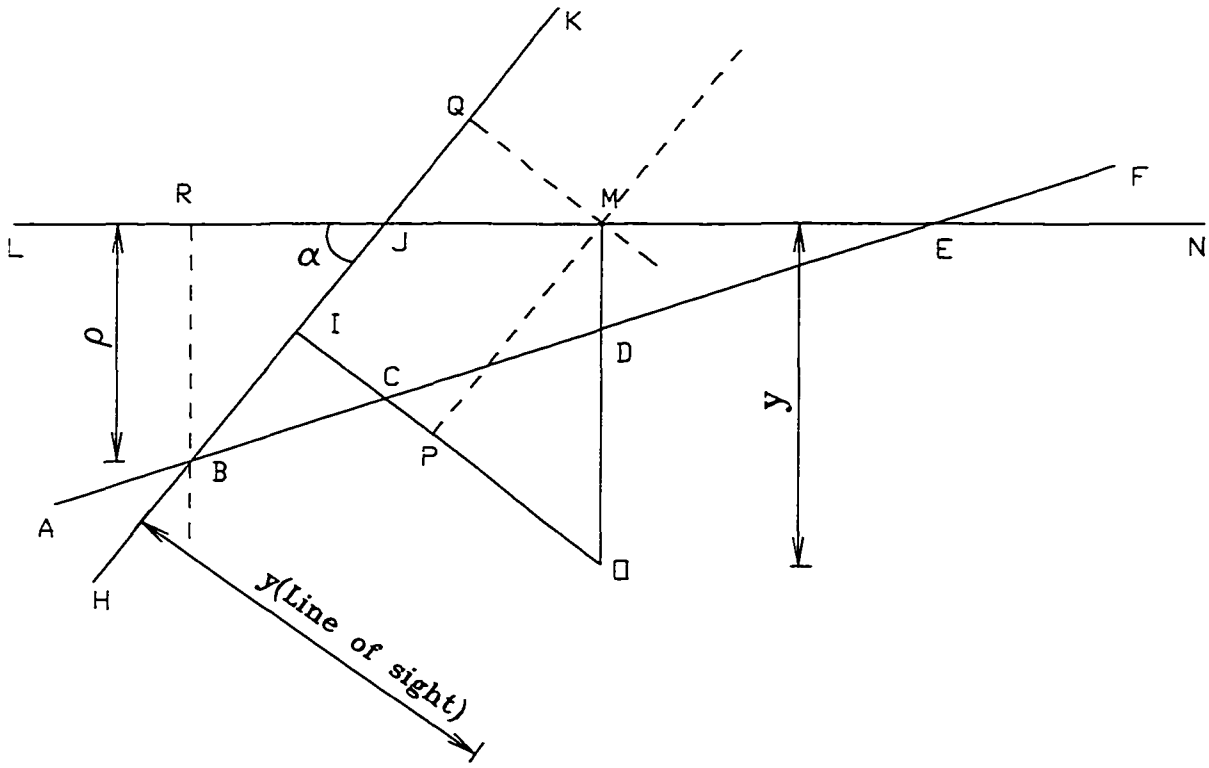


Fig. 5.10 Relationship between lens decentration with respect to the aligned PI&PIV and lens decentration with respect to the line of sight. B represents the center of the pupil; O represents the center of the lens; AF represents the pupillary axis; AN represents the axis along which PI and PIV can be aligned; HK represents the line of sight; MO represents the lens decentration with respect to the axis along which PI and PIV are aligned; IO represents the lens decentration with respect to the line of sight; ∠LJH is angle alpha (α) measured by aligning PI and PIV.

For lens tilt with respect to the line of sight ($\theta_{\text{line of sight}}$), the following relationship exists,

$$\theta_{line\ of\ sight} = \theta - \alpha \qquad (5.2)$$

where θ is lens tilt with respect to the aligned PI and PIV.

The results of the conversion are as shown in Table 5.4 and Fig. 5.11-5.12.

Table 5.4 The horizontal (H) and vertical (V) components of lens tilt and decentration with respect to the line of sight.

Subject	Tilt from line of sight (°)		Decentration from line of sight (mm)	
	H	V	H	V
AG	4.61	-2.48	0.17	0.20
LO	6.92	0.43	0.44	0.72
DC	6.01	0.89	0.21	0.38
SB	7.45	-0.98	0.17	0.05
MS	5.67	-2.79	0.14	0.50
PK	5.39	-1.78	0.24	0.03
JH	4.69	-0.45	0.12	0.48
KP	6.83	-4.39	-0.07	0.31
ME	5.48	-4.73	0.010	0.42
BN	8.47	-2.99	0.24	0.72
GD	5.10	-2.48	0.16	0.20
TP	7.11	-1.68	-0.04	0.05
DD	5.47	-3.54	0.48	0.19
DH	4.11	-1.65	0.41	0.33
GN	6.36	-4.65	0.30	0.23
DE	5.55	-2.99	0.24	0.26
NP	9.27	-3.57	-0.25	-0.05
MC	5.43	-4.55	0.02	0.32
HA	4.54	-1.78	0.02	0.11
AH	6.19	-5.13	0.14	0.19
LR	8.12	-3.94	-0.25	0.35
Mean	6.13	-2.63	0.14	0.29
STDV	1.37	1.70	0.20	0.21
	95% Confidence interval			
	0.63	0.77	0.09	0.09

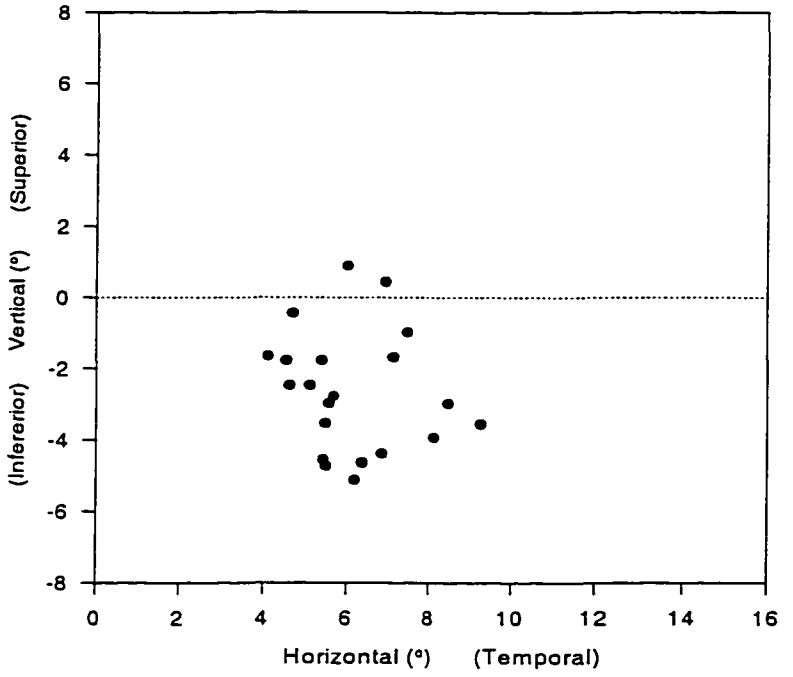


Fig. 5.11 Lens tilts with respect to the line of sight of the 21 eyes measured.

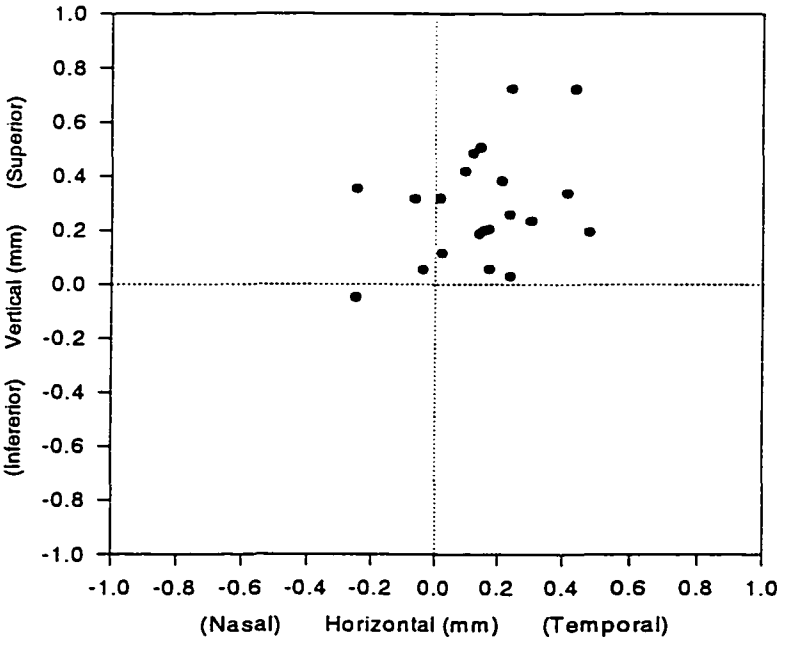


Fig. 5.12 Lens decentration with respect to the line of sight of the 21 eyes measured.

b) Lens tilt and decentration with respect to the pupillary axis

As shown in Fig. 5.13, point B is the center of the pupil; point O is the center of the lens; point E is the center of curvature of the cornea; line AF is the pupillary axis; line LN is the axis along which PI and PIV are aligned; distance MO is the lens decentration with respect to the axis along which PI and PIV are aligned. In order to determine the lens tilt and decentration with respect to the pupillary axis, draw a line OJ through point O perpendicular to line AF; draw a line BR perpendicular to line LN through B.

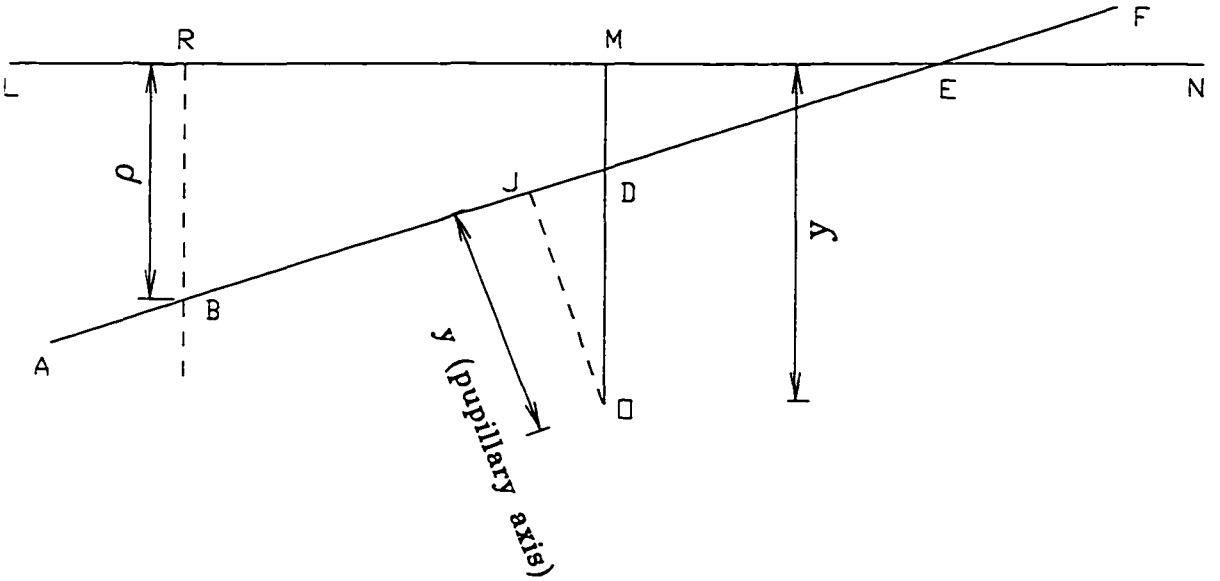


Fig. 5.13 Lens decentration with respect to the pupillary axis. O represents the center of the lens; E represents the center of curvature of the cornea; AF represents the pupillary axis; LN represents the axis along which PI and PIV are aligned; MO represents lens decentration with respect to the axis that PI and PIV are aligned; JO represents the lens decentration with respect to the pupillary axis.

Using this construction, one can find that lens decentration with respect to the pupillary axis is,

$$y_{\text{Pupillary axis}} = (y - 0.7 * \rho) * \cos(a\tan(\frac{\rho}{4.2})) \quad (5.3)$$

where ρ is the pupil decentration from the aligned PI and PIV and *4.2* is the distance from R to E in Fig. 5.13.

Also, for lens tilt, one has,

$$\theta_{\text{Pupillary axis}} = \theta - a\tan(\frac{\rho}{4.2}) \quad (5.4)$$

The results of conversion are shown in Table 5.5 and Fig. 5.14 - 5.15.

Table 5.5 Horizontal (H) and vertical (V) components of lens tilt and decentration of 21 subjects from the pupillary axis.

Subject	Tilt from pupillary axis (°)		Decentration from pupillary axis (mm)	
	H	V	H	V
AG	2.85	1.14	0.20	0.25
LO	9.75	10.07	0.37	0.59
DC	7.33	3.93	0.18	0.35
SB	5.98	-1.67	0.20	0.17
MS	5.33	3.36	0.15	0.47
PK	6.32	-1.37	0.21	0.11
JH	3.75	5.99	0.14	0.41
KP	4.35	-0.74	-0.02	0.35
ME	2.91	3.03	0.15	0.41
BN	10.02	7.16	0.20	0.62
GD	4.56	2.37	0.16	0.22
TP	1.50	0.58	0.08	0.16
DD	8.55	1.01	0.40	0.24
DH	7.56	4.11	0.33	0.30
GN	8.48	0.25	0.25	0.27
DE	6.37	1.17	0.21	0.28
NP	2.53	-3.47	-0.11	0.12
MC	1.80	1.97	0.09	0.34
HA	0.09	0.65	0.12	0.18
AH	4.16	-0.60	0.18	0.26
LR	1.97	1.18	-0.12	0.39
Mean	5.06	1.91	0.16	0.31
STDV	2.85	3.14	0.13	0.14
	95% Confidence interval			
	1.30	1.43	0.06	0.06

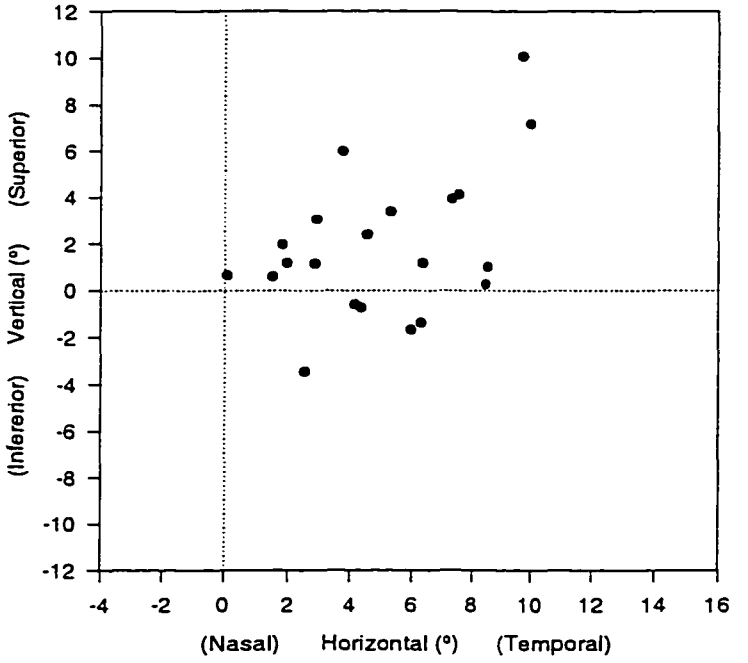


Fig. 5.14 Lens tilts with respect to the pupillary axis of the 21 eyes measured.

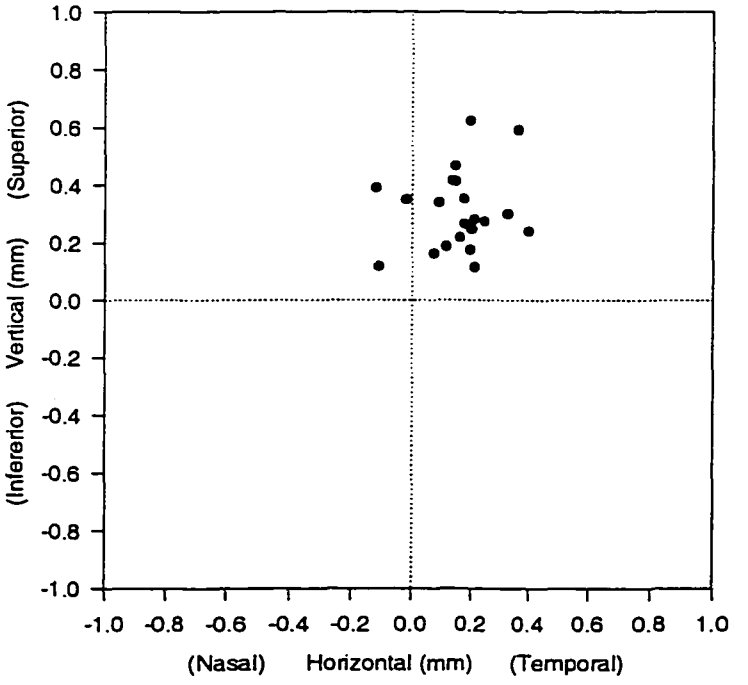


Fig. 5.15 Lens decentrations with respect to the pupillary axis of the 21 eyes measured.

5.6 Discussion

5.6.1 Precision and repeatability

a) Lens tilt and decentration

Results of repeatability test of lens tilt ad decentration measurement of subjects AR and JH are tabulated in Table 5.6.

Table 5.6 Horizontal (H) and vertical (V) components of lens tilt and decentration of subjects AR and JH measured two times, respectively.

	Tilt from the aligned PI&PIV (°)		Decentration from the aligned PI&PIV (mm)		Tilt from the coaxially sighted cornea reflex (°)		Decentration from the coaxially sighted cornea reflex (mm)	
	H	V	H	V	H	V	H	V
AR (1st)	0.90	-1.26	-0.05	0.08	6.39	-0.85	0.17	0.22
AR (2nd)	1.02	-1.39	-0.06	0.08	6.68	-0.53	0.30	0.25
AR-difference	**0.03**	**-0.03**	**-0.01**	**0**	**0.29**	**0.32**	**0.13**	**0.03**
JH(1st)	0.48	-0.93	-0.03	0.06	5.48	-1.64	0.13	0.10
JH (2nd)	0.77	-1.14	-0.05	0.07	5.43	-2.03	0.13	0.05
JH-difference	**0.29**	**-0.21**	**-0.02**	**0.01**	**0.05**	**-0.39**	**0**	**-0.05**

Values of lens tilt and decentration were calculated from displacements of PIII and PIV from PI. Errors of measurement were from two sources.

The first source of error is related to the experimenter's precision of aligning PI with the reference target on the video screen or aligning PI and PIV. This type of error could contribute to the variability in locating the reference axis and would account for some of the repeatability error. This error was more likely to occur in those sessions when the reference overlay was turned off in order to increase the visibility of the Purkinje images. During some sessions, a thin cross was drawn on the screen overlapping the position of the computer generated reference cross. Caution was used to view the video screen perpendicularly during the actual measurement to avoid parallax error. If PI was

not well aligned with the cross that was at the center of the screen represented by pixel point (256, 242), it would be apparent when the stored pictures were processed to measure the actual Purkinje image displacement and the result could always be discarded. The actual results showed that the PI alignment was always within pixel precision.

The other source of error is the actual Purkinje image displacement measurement after the experiments. It is directly related to the visibility of Purkinje images. PI and PIV were never a problem to view. PIII was always blurry. Therefore, all Purkinje image distances were measured three times. The center of PIII was defined by locating the centroid of the defocused image. Surprisingly, even for PIII, the distance measurements were highly repeatable at pixel level.

Because the actual measurement results were stored as pupil pictures with various Purkinje images, when PI and PIV were aligned, the picture should be independent of the system used to obtain the picture and the alignment. This was the case for the measurement along the aligned PI and PIV. For measurements along the CSCR, the error would present as itself as the error of defining a reference axis.

Therefore, the overall precision of measurement was at pixel level. Ignoring between subject variations of other ocular parameters in modeling, this error can be calculated by Eq. 2.17-2.18. One pixel of error in measuring the distance of Purkinje displacement would result in an angle measurement error of 0.23° and a decentration error of 0.03 mm (conservatively).

Actual measurements showed that the relative positions of the Purkinje images were highly consistent between different measurements.

Subject AR was measured twice right after the setup was constructed as an initial pilot run of the experiment. The two measurements for AR were taken on two consecutive days with natural pupil conditions. The maximum difference of lens tilt measured was 0.13°, which was about at the measurement precision level. The maximum difference of the decentration measured was 0.04 mm. Subject JH was measured again

about 10 months later. The maximum difference in the measured tilt was 0.29° and the maximum difference in decentration measured was 0.02 mm. Even with the long period of time between the two measurements of JH, the result was repeatable at the theoretical measurement precision level. This may imply the stability of the general optical structure of the eye for subject JH.

b) Pupil decentration

Results of the repeatability measurements of the pupil size and pupil decentration of subject JH are tabulated in Table 5.7.

Table 5.7 The differences of pupil size and pupil decentrations measured two times of subject JH. Pupil decentrations were measured both with the CSCR as the reference and the aligned PI and PIV as the reference. Pupil sizes were the averages of the pupil sizes measured using two different reference axes.

Measurement	Average pupil size (mm)	Pupil decentration from coaxially sighted cornea reflex (mm)		Pupil decentration from aligned PI and PIV (mm)	
		Horizontal	Vertical	Horizontal	Vertical
First time (Nov. 20,1995)	7.47	0.50	-0.43	-0.24	-0.51
Second time (Sept. 22, 1996)	9.11	0.21	-0.30	-0.06	-0.23
Difference	**1.64**	**0.29**	**-0.13**	**0.18**	**0.27**

The precision of measuring pupil decentration was mainly restricted by the resolution of the video system, which was one pixel or 0.032 mm in the horizontal meridian and 0.025 mm in the vertical meridian. The measurement of a line distance on the video screen would therefore be at a 2-pixel precision level, which would be 0.06 mm in the horizontal meridian and 0.05 mm in the vertical meridian. The test of the

repeatability of the measurement of pupil decentration was complicated by the true change of the decentration of the pupil when the pupil sizes were different for the two measurements. Table 5.7 shows the differences of pupil decentration measured for the two different times of subject JH. The difference was as large as 0.29 mm. However, there was also a substantial pupil size change which might bring in true pupil decentration change.

c) Angle Alpha

Results of the repeatability measurements of angle alpha of subjects AR and JH are tabulated in Table 5.8.

Table 5.8 Horizontal (H) and vertical (V) components of angle alpha values of the left eyes of subjects AR and JH measured two times by aligning PI & PIV and PI &PIII, respectively.

	Angle alpha (°) by PI & PIV		Angle alpha (°) by PI & PIII	
	H	V	H	V
AR (1st)	5.2	1.9	9.2	-6.4
AR (2nd)	5.1	1.9	9.7	-7.0
AR-difference	**-0.1**	**0**	**0.5**	**-0.6**
JH (1st)	4.21	-0.48	5.95	-2.91
JH (2nd)	4.25	-0.33	5.76	-2.79
JH-difference	**0.05**	**0.15**	**-0.19**	**0.12**

Error of angle alpha measurements could also be caused by various error sources. First, errors could come from the subject's fixation error. In most cases, this error would be less than 0.5°. Second, errors could arise from the measurement of the distance between the fixation point and the reference coordinates origin. In this study, the reference origin was located by a guiding laser beam at a precision level better than 1

mm. Distance measurement was also at a precision level better than 1 mm. Given a fixation distance of 2 m, a 1 mm distance would subtend an angle of 0.03 °, which is clearly not a concern. A third source would arise from the experimenter in aligning Purkinje images but these were also at pixel precision.

Measurements of angle alpha showed good consistency. During the two repeatability measurements of subject AR and JH, angle alpha data measured of AR by aligning PI and PIV showed a difference of 0.1° in the horizontal meridian and no difference in the vertical meridian. Angle alpha data measured of AR by aligning PI and PIII showed a difference of 0.5° in the horizontal meridian and 0.6° in the vertical meridian. Angle alpha data measured of JH by aligning PI and PIV showed no difference in the horizontal meridian and a difference of 0.15° in the vertical meridian. Angle alpha data measured of JH by aligning PI and PIII showed a difference of 0.2° in the horizontal meridian and 0.1° in the vertical meridian.

5.6.2 Comparison with other measurements

a) Lens tilt and decentration

There have been no reported systematic measurements of the crystalline lens tilt and decentration of the normal human eye *in vivo*. Tscherning was the first one known to examine the alignment of the three Purkinje images. His experiment has been extravagantly quoted without any further verification. Using an ophthalmophakometer, Tscherning accomplished the first angle alpha measurement. During his angle alpha measurement, he encountered the dilemma of being unable to align all the Purkinje images at the same time for some subjects. He attributed this situation to the misalignment of the crystalline lens and the cornea. Later there have been some reports on calculating the contribution of the tilt of the crystalline lens from the visual axis to the total astigmatism (Bennett and Rabbetts, 1984; Barnes et. al. 1987). In these reports,

angle alpha was basically used as the tilt of the crystalline lens from the visual axis or the line of sight.

The paucity of data on this topic was partially due to the difficulty in locating PIII in the normal eye and partially due to its insignificance in clinical applications. A related topic is the measurement of the tilt and decentration of intraocular lens (IOL) implants in pseudophakic eyes. There have been some measurements of post surgery intraocular lens tilt and decentration measurements utilizing a number of different technologies. Lakshminarayanan et. al. (1986) measured IOL tilt in cadaver eyes. Philips et. al. (1988) measured IOL tilt and decentration with a Purkinje image monitoring setup similar to the setup used in this research. The high reflection from the anterior surface of a IOL makes PIII equally bright as other Purkinje images.

The *in vivo* lens tilt and decentration data reported here are the first of its kind.

b) Pupil decentration

The deviation of the fovea from the optical axis of the eye is well known. But to which the pupil shall be centered is still not well answered although Bennett and Rabbetts (1984) have stated "typically, the pupil is thought to be decentered nasally from the optical axis by 0.25 mm". If the eye is to provide best image quality at the fovea, it is natural to imagine that the pupil would be decentered from the optical axis of the eye. The visual axis has been traditionally defined as the line joining the fixation point and the first nodal point of the eye. In the image space, this axis would be the line joining the second nodal point and the fovea. The two parts of this axis in object space and image space would be parallel to each other to define a visual line of direction. The imaginary nature of the nodal point results in the difficulty to experimentally define this axis. The easy substitute is the chief ray in object space. This chief ray has been called the line of sight. Even further, Bennett and Rabbetts (1984) attempt to justify that this chief ray should be called the visual axis instead in their classic textbook of visual optics. Therefore, the

pupil is usually used as a reference for measuring ocular optical characteristics. For instance, most aberration measurements use the geometrical center of the pupil as the reference for characterizing the aberration property of the eye (see Charman, 1991 for a review).

It should be mentioned that in the study of transverse chromatic aberration (TCA) of the eye and its effect on vision, the same topic was tackled from a different perspective. In the studies of TCA, the axis of zero TCA is defined as the achromatic axis and is used as a reference to measure pupil decentration (Thibos, et. al. 1990; Simonet and Campbell, 1990). Results of these studies show that the pupil is close to the achromatic axis and will certainly be away from the optical axis of the eye. Further, Rynders et. al. (1995) have reported a group mean of zero TCA and a group mean of no pupil decentration from the achromatic axis of a large population (170 eyes). In the studies of Thibos et. al. (1990) and Rynders et. al. (1995), the achromatic axis was claimed as the visual axis. If the Stiles-Crawford effect is also considered, the population average of the effective center of the pupil would not possibly be centered around the achromatic axis (Applegate and Lakshminarayanan, 1993; Gorrand and Delori, 1995).

The results in this study show that the average decentration of the pupil from the optical axis or the approximate optical axis of the eye is 0.3 mm to the nasal side of the optical axis and 0.3 mm to the inferior of the optical axis. The standard deviations for both the horizontal and vertical pupil decentration of the left eyes of the 21 subjects are 0.2 mm. With respect to the CSCR, the pupils were decentered to the temporal side with an average of 0.4 mm and to the inferior with an average of 0.2 mm. The standard deviation was 0.3 mm and 0.2 mm in the horizontal and vertical meridians, respectively. These results imply that for an average subject, the pupil is centered to somewhere in between the optical axis or the approximate optical axis of the eye and the CSCR.

In addition, Uozato et. al. (1983) reported an experimental setup for locating the visual axis in the eye. In their measurement, a system with a special aligned laser beam

combined with video cameras was used to locate the visual axis of the eye. Their preliminary results of 6 eyes gave an average pupil decentration of 0.33 mm to the temporal side of visual axis in the horizontal meridian. The vertical decentration is 0.087 mm to the superior. Given the experimental precision as claimed in their report, the result is clearly not consistent with the conclusion of Rydners et. al. (1995) that the pupil would tend to center at the visual axis of the eye, and this point needs to be clarified.

All these measurements tend to support the suggestion as stated in Chapter 4, that the coaxially sighted cornea reflex is fairly close to the traditionally defined visual axis or the nodal axis; and that the effective center of the pupil centers around the visual axis.

c) Angle Alpha

Subjects AR and DC also participated in the separate angle alpha measurement as described in Appendix I. Table 5.9 shows the comparison of the angle alphas for the left eyes of subject AR and DC measured by aligning PI ad PIV during the two different experiments. The differences of the values between the two different measurements for the two subjects are not large.

Table 5.9 Angle alphas of the left eyes of subjects AR and DC measured by aligning PI and PIV during two different measurements.

	Angle alpha (°) by PI & PIV	
	H	V
AR-Appendix I	5.4	1.5
AR-Chapter 5	5.2	1.9
AR-difference	**-0.2**	**0.4**
DC- Appendix I	4.3	-2.9
DC-Chapter 56	4.3	-2.3
DC-difference	**0**	**0.6**

As shown in Appendix I, the difference between Tscherning's classical results and the more recent results using PI and PIV shows that Tscherning's values tend to be larger in the horizontal meridian and pointing downward rather than scattered around zero value in the vertical meridian.

Now this difference can be well explained by the definition difference of angle alpha. Tscherning (1924) specifically stated in his angle alpha measurement that a compromised alignment of all three Purkinje images was used when all three Purkinje images could not be aligned at the same time. In more recent measurements of angle alphas (Effert et. al. 1992), PI and PIV were used to define the optical axis of the eye. Using PI and PIV to define and locate the optical axis of the eye greatly reduces the experimental difficulties in locating PIII, which makes experimentally locating the optical axis or approximate axis of the eye practical. The question is how much different would this optical axis defined by aligning PI and PIV be from the optical axis defined by roughly aligning all three Purkinje images in a compromised way as specified by Tscherning (1924). One way to resolve this issue is to examine the differences in angle alpha measured by aligning PI and PIV and by aligning PI and PIII, respectively. Except for one eye for which PIII was not visible in angle alpha measurement, the angle alphas of the left eyes of 20 subjects were measured both by aligning PI and PIV and by aligning PI and PIII. The data are as given in Table 5.3 and Fig.5.9. The differences between the two groups of angle alphas are obvious.

Theoretically, the misalignment of PIII from PI is more sensitive to lens tilt and decentration than the misalignment of PIV from PI. As shown in Eq. 2.17-2.18, a lens

decentration of 1 mm will induce a displacement of PIII from Purkinje I of 1.77 mm and a displacement of PIV from PI of 1.05 mm. A lens tilt of 10° will produce a 2.7 mm displacement of PIII from PI and a 0.6 mm displacement of PIV from PI. Therefore a compromised alignment of all three Purkinje images in the manner as specified by Tscherning would generate an approximate optical axis that is actually closer to an axis defined by PI and PIII.

5.6.3 The average values for the eyes measured

With the misalignment parameters measured in this study with respect to the aligned PI and PIV, the average parameters for the eyes measured in this study are listed in Table 5.10. They are also graphically illustrated as in Fig 5.16 and Fig. 5.17.

Table 5.10 Misalignment of ocular components in an average emmetropic human eye based on the 21 eyes measured with respect to the aligned PI and PIV. STDV is standard deviation; positive values represent the temporal or superior directions in the eye.

	Pupil decentration (mm)		Lens tilt (°)		Lens decentration (mm)		Angle Alpha by PI&PIV (°)	
	H	V	H	V	H	V	H	V
Mean	-0.31	-0.28	0.88	-1.91	-0.05	0.12	5.25	0.72
STDV	0.19	0.21	0.97	0.76	0.06	0.05	0.96	1.28

The averages and the standard deviations of lens tilt and decentration based on the 21 eyes measured with respect to the line of sight and the pupillary axis are given in Table 5.11.

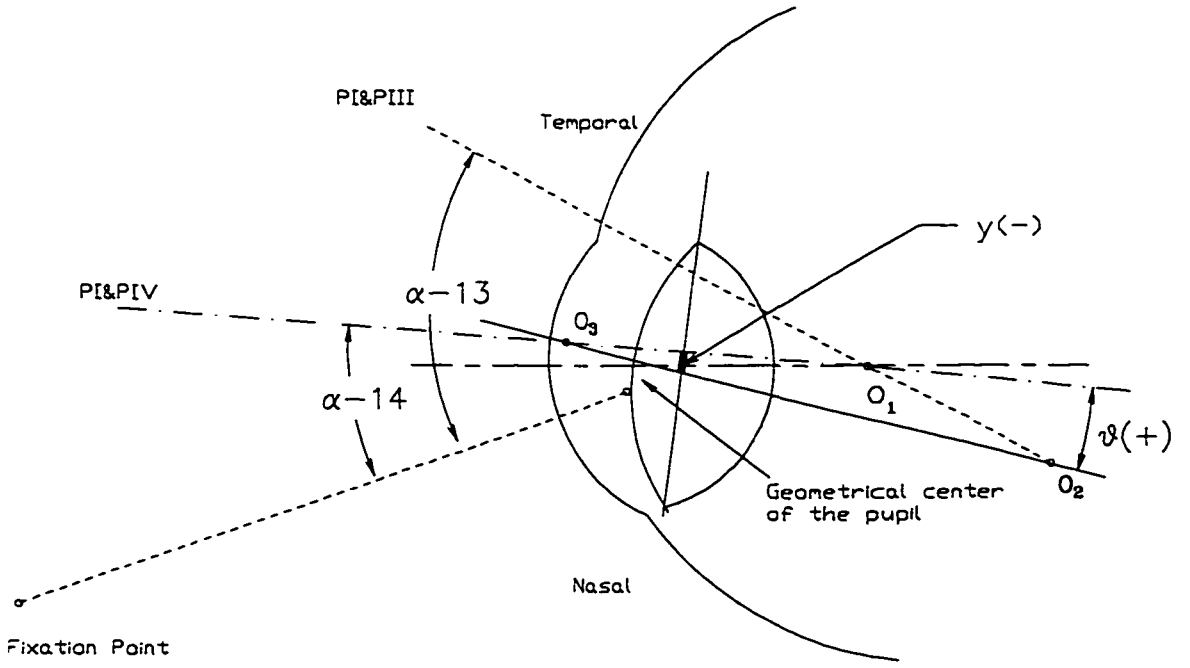


Fig. 5.16 Misalignment of ocular components in an average human eye in the horizontal meridian (an horizontal section of the eye). O_1, O_2 and O_3 represent the centers of curvature of the anterior surface of the cornea, posterior surface of the lens and anterior surface of the lens, respectively; y represents the amount of lens decentration; θ represents the amount of lens tilt; α-13 and α-14 represent the angle alphas measured by aligning PI and PIII and by aligning PI and PIV, respectively. The drawing is not to scale.

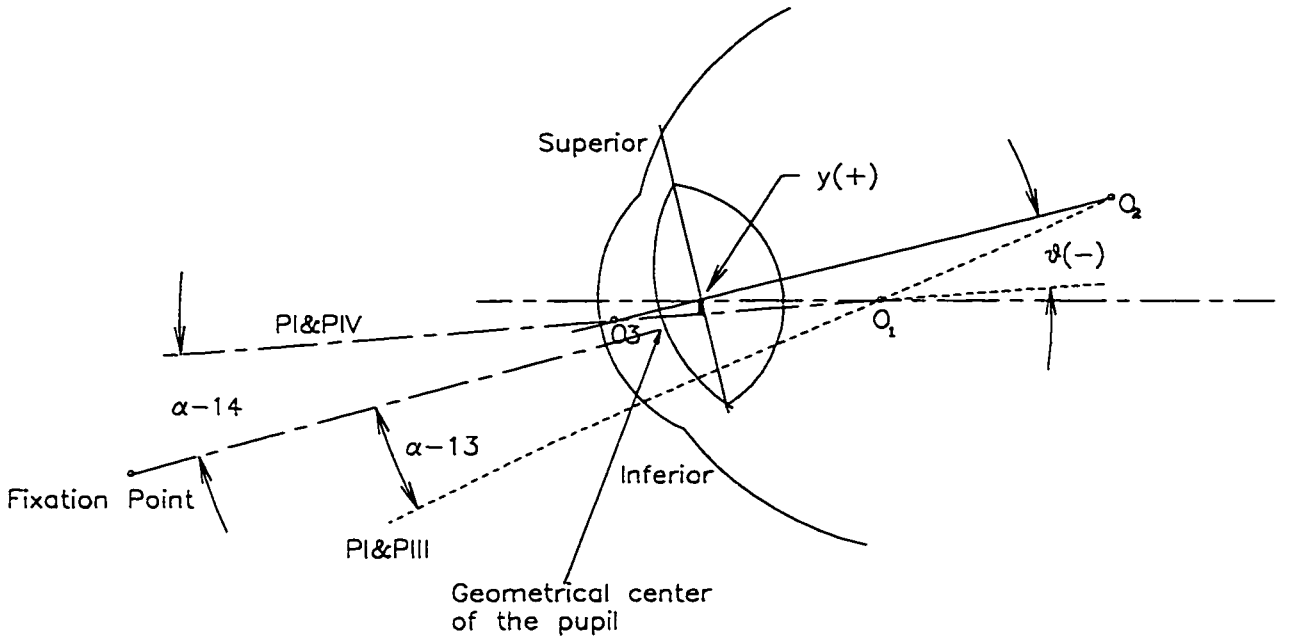


Fig. 5.17 Misalignment of ocular components in an average human eye in the vertical meridian (a vertical section of the eye). O_1, O_2 and O_3 represent the centers of curvature of the anterior surface of the cornea, posterior surface of the lens and anterior surface of the lens, respectively; y represents the amount of lens decentration; θ represents the amount of lens tilt; α-13 and α-14 represent the angle alphas measured by aligning PI and PIII and by aligning PI and PIV, respectively. The drawing is not to scale.

Table 5.11 The average lens tilt and decentration with respect to the line of sight and the pupillary axis, respectively.

	Tilt from line of sight (°)		Decentration from line of sight (mm)		Tilt from pupillary axis (°)		Decentration from pupillary axis (mm)	
	H	V	H	V	H	V	H	V
Average	*6.13*	*-2.63*	*0.14*	*0.29*	*5.06*	*1.91*	*0.16*	*0.31*
STDV	*1.37*	*1.70*	*0.20*	*0.21*	*2.85*	*3.14*	*0.13*	*0.14*

5.7 Conclusions

Various parameters of the misalignments of ocular components of the left eyes of 21 emmetropic subjects were measured in this study. The results of the measurements help to clear up many aspects of the general optical structure of the eye. Among these parameters measured are; crystalline lens tilt and decentration with respect to various reference axes, angle alphas and pupil centration with respect to other optical components.

This study,

a) supports previous findings that the human eye is a misaligned optical system;
b) shows a true optical axis generally does not exist in an emmetropic human eye; but an approximate optical axis can be defined by aligning PI and PIV;
c) shows the discrepancy between more recent angle alpha values measured and Tscherning's data is due to the difference in the definition of the optical axis of the eye;
d) confirms that the pupils of the majority of the eyes tend to decenter to the nasal side and inferior direction in the eye with respect to the approximate optical axis of the eye;
e) finds the majority of the crystalline lenses tilt to the temporal and forward direction with respect to their assumed aligned position with the cornea ;
f) finds the majority of the crystalline lenses decenter to the nasal and superior direction in the eye with respect to their assumed aligned position with the cornea.

Chapter 6

Ocular Monochromatic Aberrations and the Misalignment of Ocular Components

6.1 Introduction

In Chapter 4 and 5, both the overall wavefront aberration and the misalignments of various ocular components of the eye were systematically measured in one experimental session in the left eyes of 21 emmetropic subjects. These data can be used to verify whether the misalignments of ocular components in the eye significantly contribute to the asymmetrical component of the overall monochromatic aberration in the human eye.

In this Chapter, the possible correlation between the asymmetrical components of the overall wavefront aberration of the eyes and the misalignments of various ocular components are examined based on the data measured in Chapter 4 and Chapter 5.

6.2 Possible correlation between the asymmetrical component of the overall wavefront aberration and the misalignments of ocular components

Although a possible strong correlation between these misalignment factors and the overall monochromatic aberration of the eye is seemingly remote given the data obtained, there is still a clear distribution for each misalignment factor for the eyes measured. A closer examination would be to plot the misalignment parameters against the asymmetrical components of the overall monochromatic aberrations of the eyes measured.

6.2.1 Calculation of the asymmetrical components of wavefront aberrations measured

The Taylor polynomials obtained for each subject were used to calculate the asymmetrical components of the mean squared wavefront aberrations across a 6 mm

pupil (see Appendix XII). Mean squared wavefront aberration can be calculated by integrating the squared Taylor polynomials terms corresponding to specific aberration terms. For the asymmetrical component, all terms of an odd power should be used. The mean squared aberration of an eye is directly related to the pupil size and its relative

Table 6.1 Mean squared wavefront aberrations of the left eyes of 21 subjects and their symmetrical and asymmetrical components.

Subject	Overall aberration (μ^2)	Asymmetrical component (μ^2)	Symmetrical component (μ^2)
1. AG	3.79	0.83	2.96
2. LO	0.35	0.28	0.07
3. DC	0.40	0.35	0.05
4. SB	0.57	0.32	0.25
5. MS	1.57	1.20	0.36
6. PK	0.85	0.63	0.22
7. JH	1.18	0.25	0.94
8. KP	0.63	0.57	0.06
9. ME	0.43	0.36	0.07
10.BN	1.90	0.09	1.81
11.GD	1.90	0.05	1.86
12.TP	0.29	0.16	0.13
13.DD	0.39	0.21	0.17
14.DH	0.65	0.15	0.50
15.GN	0.38	0.19	0.18
16.DE	1.61	0.51	1.13
17.NP	0.77	0.29	0.50
18.MC	0.93	0.04	0.89
19.HA	0.50	0.42	0.07
20.AH	0.88	0.70	0.17
21.LR	0.44	0.11	0.34
Mean	0.97	0.37	0.61
STDV	0.82	0.29	0.77
	95% Confidence interval		
	0.38	0.13	0.35

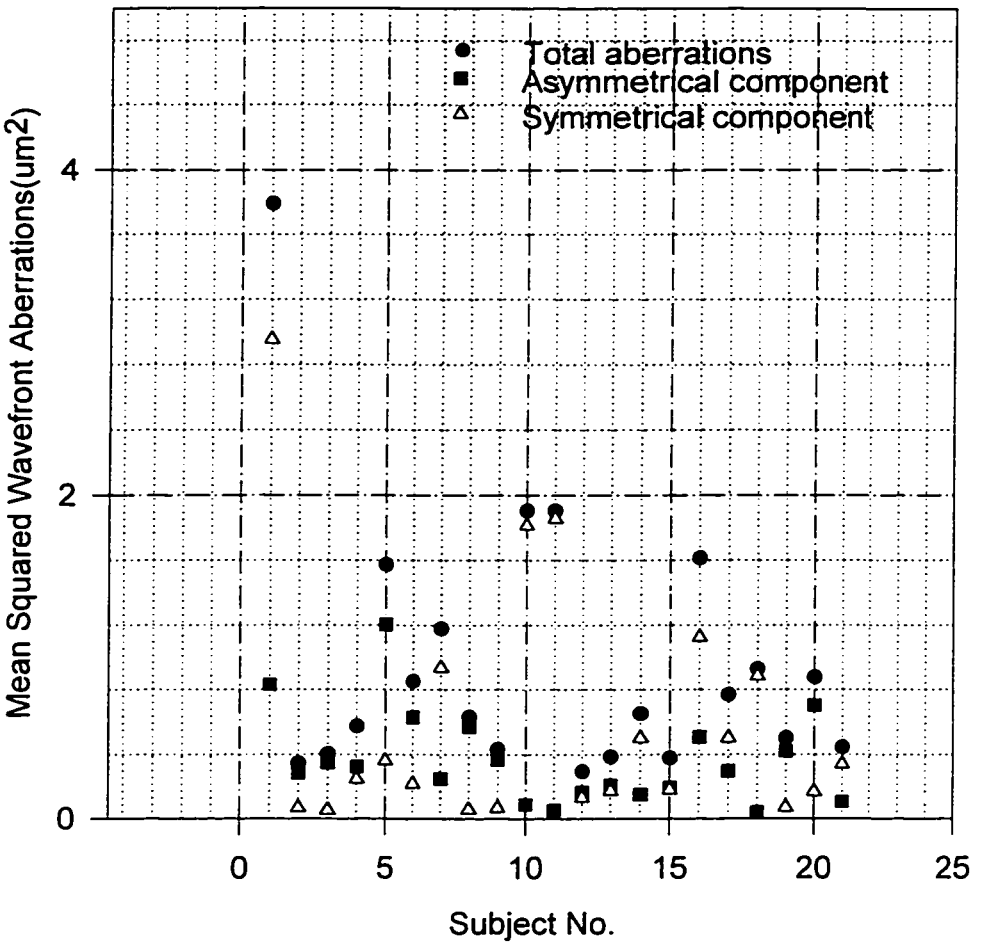


Fig. 6.1 Mean squared wavefront aberrations of the left eyes of 21 subjects and their symmetrical and asymmetrical components calculated assuming the pupil is centered around the coaxially sighted cornea reflex.

location. The most convenient way would be to integrate the squared aberration equation across the pupil plane with the center of the pupil as the origin of the coordinates provided the aberration equation is using the geometrical center of the pupil as the origin of the coordinates. The results for the 21 eyes measured with respect to the CSCR are tabulated in Table 6.1 for a pupil size of 6 mm.

Fig. 6.1 shows the plot of the results. It is clear that about half of the eyes measured have a dominant asymmetrical aberration.

For the purpose of comparison, the total wavefront aberration and its symmetrical and asymmetrical components were also calculated assuming the pupil is centered around the coaxially sighted cornea reflex. The results are given in Table 6.2.

Paired t-test showed that mean wavefront aberrations (overall symmetrical and asymmetrical components) were not significantly different with respect to the choice of reference axes (rejected at $P \leq .05$).

Table 6.2 Mean squared wavefront aberrations of the left eyes of 21 subjects and their symmetrical and asymmetrical components calculated assuming the pupil is centered around the coaxially sighted cornea reflex.

Subjects	Overall aberration (μ^2)	Asymmetrical component (μ^2)	Symmetrical component (μ^2)
1. AG	2.99	0.88	2.08
2. LO	0.23	0.18	0.05
3. DC	0.54	0.36	0.16
4. SB	0.55	0.32	0.24
5. MS	1.33	1.13	0.19
6. PK	0.77	0.55	0.21
7. JH	0.72	0.02	0.70
8. KP	0.95	0.76	0.19
9. ME	0.40	0.29	0.12
10.BN	2.45	0.58	1.83
11.GD	1.77	0.13	1.62
12.TP	0.22	0.03	0.19
13.DD	0.40	0.21	0.18
14.DH	0.74	0.07	0.67
15.GN	0.41	0.20	0.21
16.DE	1.24	0.21	1.03
17.NP	0.28	0.19	0.09
18.MC	0.66	0.04	0.61
19.HA	0.62	0.52	0.09
20.AH	0.100	0.80	0.19
21.LR	0.56	0.05	0.51
Mean	0.90	0.36	0.53
STDV	0.72	0.32	0.61
	95% Confidence interval		
	0.33	0.15	0.28

6.2.2 Correlation of angle alpha and the asymmetrical component of the mean squared wavefront aberration

The modulus of the 3-dimensional angle alphas measured by aligning PI and PIV of the left eyes of the 21 subjects were plotted against the asymmetrical components of the mean squared wavefront aberration calculated of each eye as shown in Fig. 6.2.

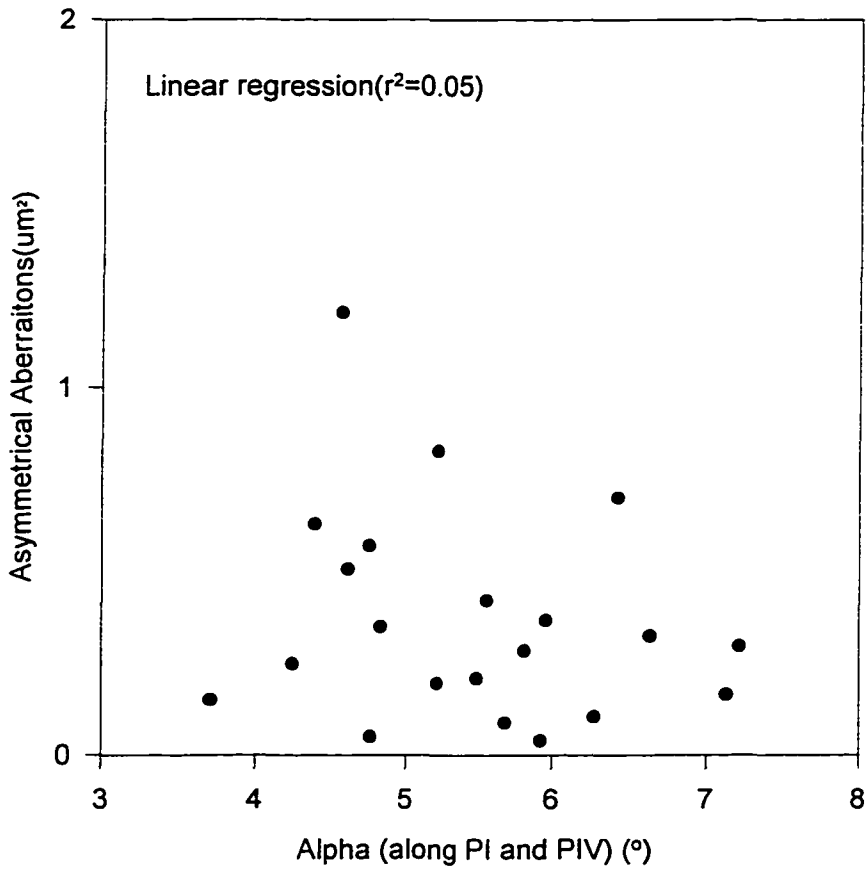


Fig. 6.2 Correlation between the mean squared asymmetrical components of wavefront aberrations and the angle alphas measured by aligning PI and PIV.

The r-squared value of the linear regression is 0.05, indicating there is no significant correlation between the two sets of data.

Angle alphas measured by aligning PI and PIII of the left eyes of the 21 subjects were also plotted against the asymmetrical components of the mean squared wavefront aberration calculated of each eye as shown in Fig. 6.3.

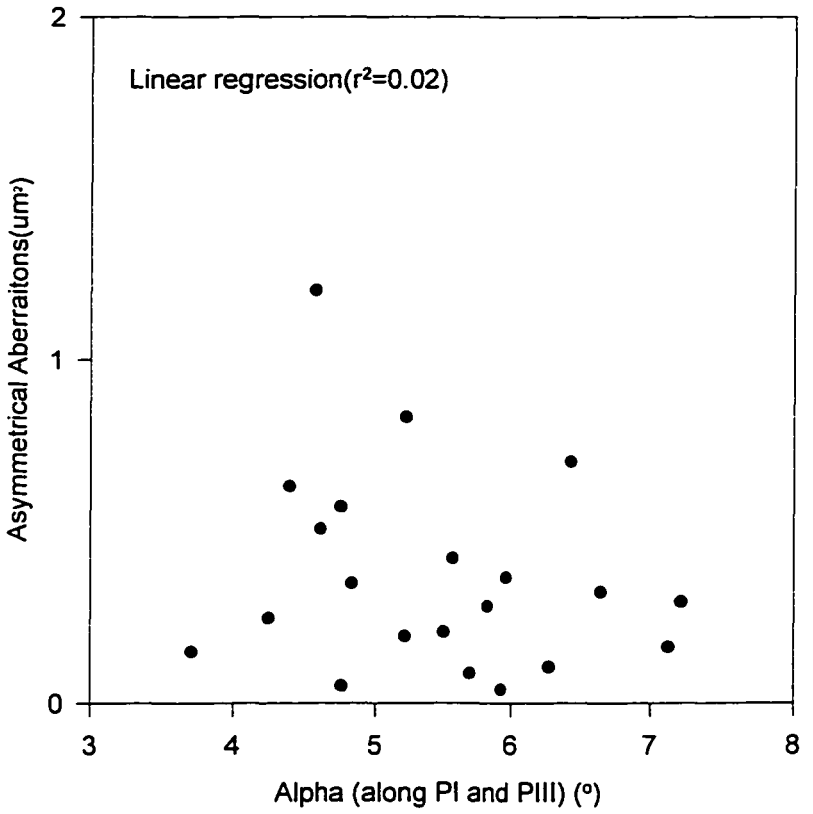


Fig. 6.3 Correlation between the mean squared asymmetrical components of wavefront aberrations and the angle alphas measured by aligning PI and PIV.

The r-squared value of the linear regression is 0.02. Again, there is no significant correlation between the two sets of data.

6.2.3 Correlation of lens tilt and decentration and the asymmetrical component of MS wavefront aberration

Lens tilt and decentration with respect to the aligned PI and PIV were calculated from misalignments of Purkinje images and then converted to lens tilt and decentration with respect to the line of sight as described in Chapter 5.

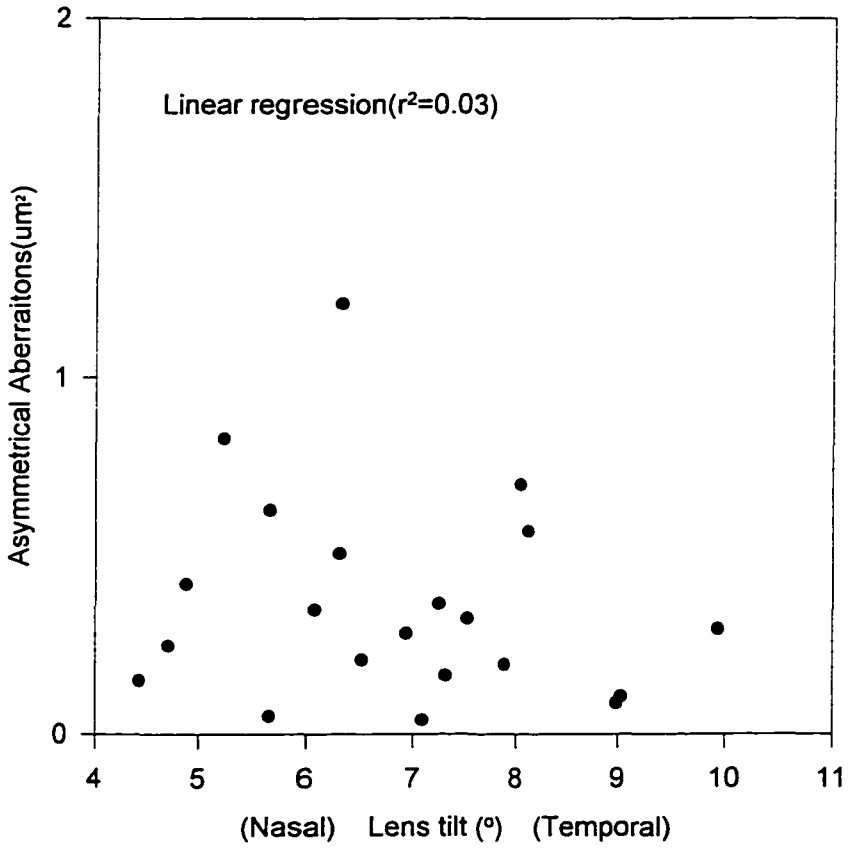


Fig. 6.4 Correlation of the asymmetrical component of the mean squared wavefront aberration of the left eyes of 21 subjects and lens tilt with respect to the line of sight.

The modules of the 2-dimensional data of the lens tilts with respect to the line of sight measured were plotted with the asymmetrical component of the overall wavefront aberrations as given in Fig.6.4. The r-squared value of linear regression is 0.03.

Lens decentrations with respect to the line of sight were also plotted with the asymmetrical components of the overall wavefront aberration as given in Fig. 6.5. The r-squared value of the linear regression is 0.01.

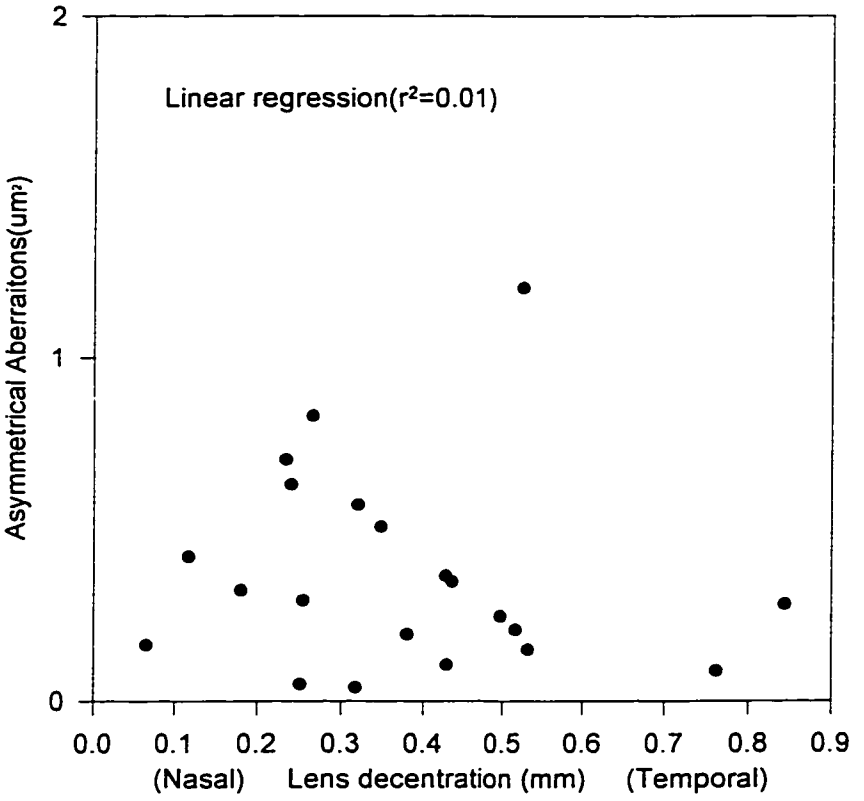


Fig. 6.5 Correlation of the asymmetrical component of the mean squared wavefront aberration of the left eyes of 21 subjects and lens decentration with respect to the line of sight.

6.2.4 Correlation of pupil decentration and the asymmetrical component of MS wavefront aberration

Pupil decentrations with respect to aligned PI and PIV were also obtained in Chapter 5. Aligned PI and PIV represent common optical axis of the anterior surface of the cornea and the back surface of the lens. It should be fairly close to the optical axis of the eye if an exact optical axis does not exist. Therefore the asymmetrical components of the overall wavefront aberrations of the 21 eyes measured can be plotted against pupil decentrations with respect to aligned PI and PIV. The plot is shown in Fig. 6.6.

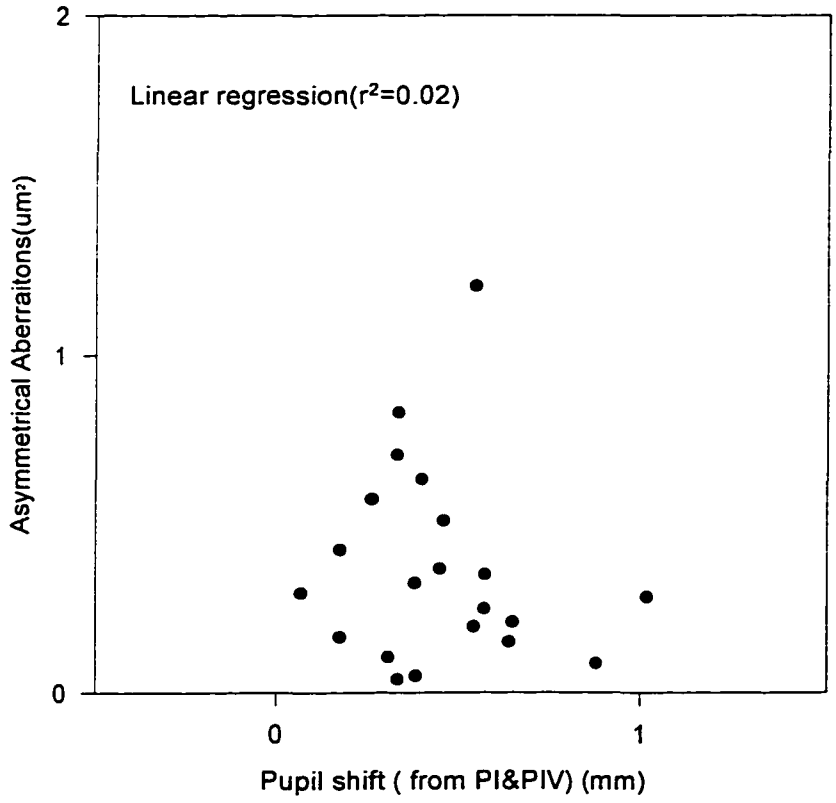


Fig. 6.6 Correlation of the asymmetrical component of the mean squared wavefront aberrations of the left eyes of the 21 subjects and pupil decentration with respect to the approximate optical axis of the eye.

6.2.5 Correlation of the misalignment of ocular components with the symmetrical component of MS wavefront aberration

No significant correlation of the misalignment parameters with the symmetrical component of the total wavefront aberration was found by similar analyses.

6.3 Conclusions

For the average human eye, the cornea, the pupil and the crystalline lens showed significant amount of misalignments with each other. There is no significant correlation of the misalignment factors measured in this study with the asymmetrical components of the overall wavefront aberration of the eyes measured at the same time. There is also no significant correlation of the misalignment factors with the symmetrical components of the overall wavefront aberration of the eyes.

This study has shown that the misalignment of ocular optical components does not contribute significantly to ocular asymmetrical monochromatic aberration in a young emmetropic population. This negative finding supports the suggestion that the cornea is possibly the predominant contributor to ocular asymmetrical monochromatic aberrations (Howland et. al. 1994).

Chapter 7

Conclusions and Future Directions

7.0 Introduction

In this thesis, the misalignment of ocular components and ocular monochromatic aberrations in the left eyes of 21 young adult emmetropes were investigated. No correlation was found between the misalignment of ocular components and the asymmetrical component of ocular wavefront aberration.

The lens continues to grow throughout life, hence the structure and position of the lens are likely to be different at different ages. The eyes of ametropes are likely to be significantly different in their optical structures. As a result, there may be differences in their general misalignment characteristics. Additionally, these structural differences may also produce significant differences in their wavefront aberrations. Therefore, the results of this study may not be representative of the general population. However, both the type and magnitudes of aberrations measured in this study are similar to those reported by Howland and Howland (1977) with a general adult subject group which included both emmetropes and ametropes.

7.1 Misalignment features in the human eyes

The general misalignment features in the 21 eyes were systematically examined.

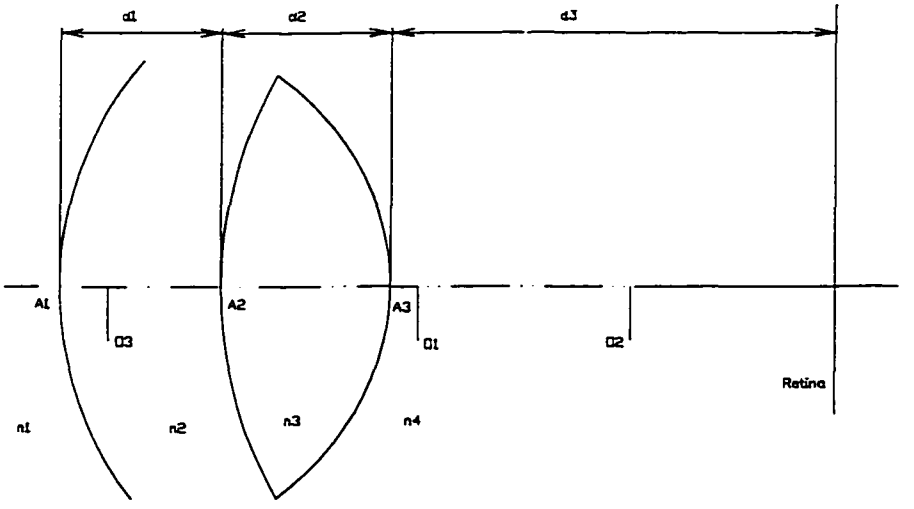


Fig 7.1a The relaxed G-E eye model with its parameters.

A method of calculating crystalline lens tilt and decentration from Purkinje image misalignments was developed. A general trend of misalignment in eye measured was found despite the large between subject variation.

This study was based on the G-E eye model as described by Fig.7.1a and Table 7.1. A new misaligned schematic eye model can be established based on the measured misalignment parameters.

Fig. 7.1b and Fig. 7.1c show the horizontal and the vertical sections of the new misaligned eye model, respectively. The misalignment parameters in Fig. 7.1b and Fig. 7.1c are given in Table 7.1.

Table 7.1 Parameters of the G-E schematic eye and the misalignment parameters of the misaligned G-E model eye. Positive values represent the temporal or superior directions in the eye.

G-E Parameter		Misalignment Parameter (mm)		
n1	1	*pdc**	H	-0.31
n2	1.3333		V	-0.28
n3	1.4160	θ	H	0.88
n4	1.3333		V	-1.91
d1	3.6 mm	*y*	H	-0.05
d2	3.6 mm		V	0.12
d3	16.69 mm	α_{14}	H	5.25
r1(A1O1)	7.8 mm		V	0.72
r2(A2O2)	10.0 mm	α_{13}	H	6.21
r3(A3O3)	-6.0 mm		V	-2.59

*Note: * represents pupil decentration from PI&PIV.*

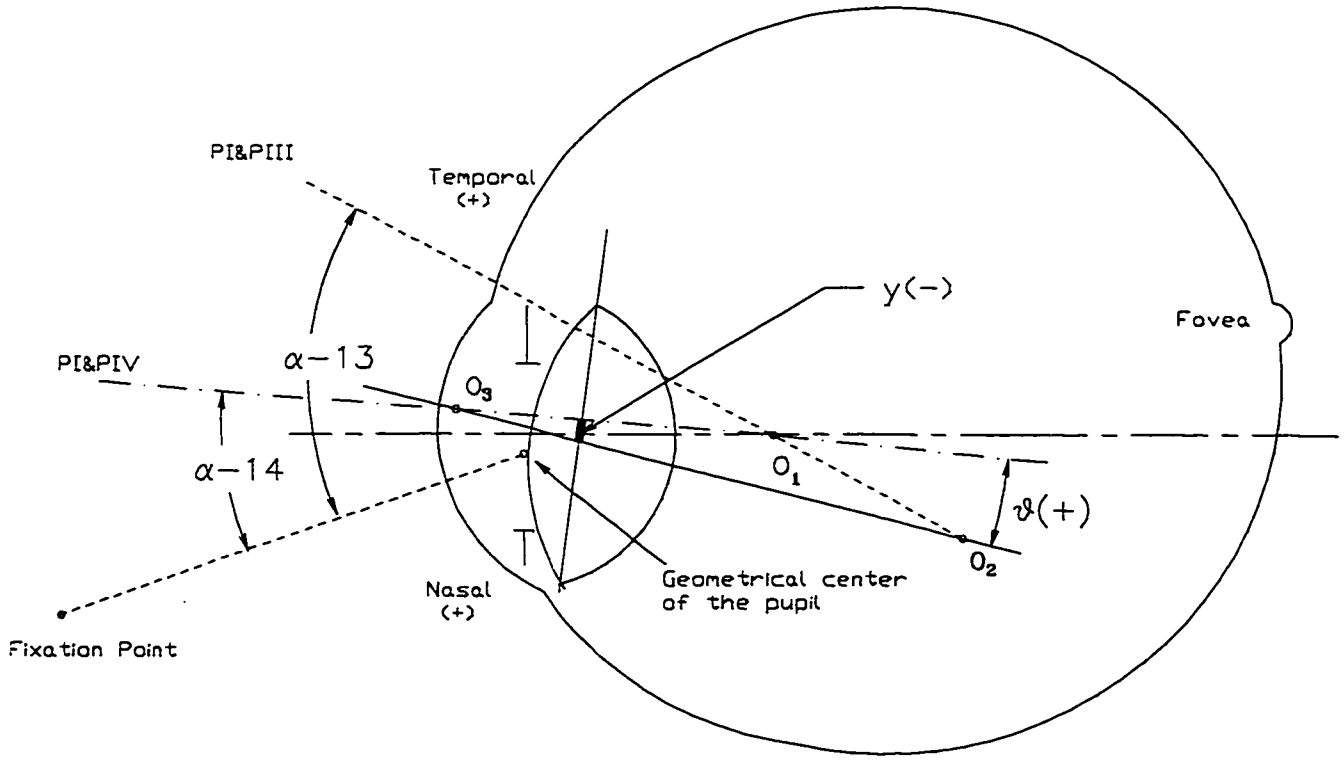


Fig. 7.1b The horizontal section of the misaligned G-E eye model. O_1, O_2 and O_3 represents the centers of curvature of the anterior surface of the cornea, posterior surface of the lens and anterior surface of the lens, respectively; y represents the amount of lens decentration; θ represents the amount of lens tilt; α-13 and α-14 represent the angle alphas measured by aligning PI and PIII and by aligning PI and PIV, respectively. The drawing is not to scale.

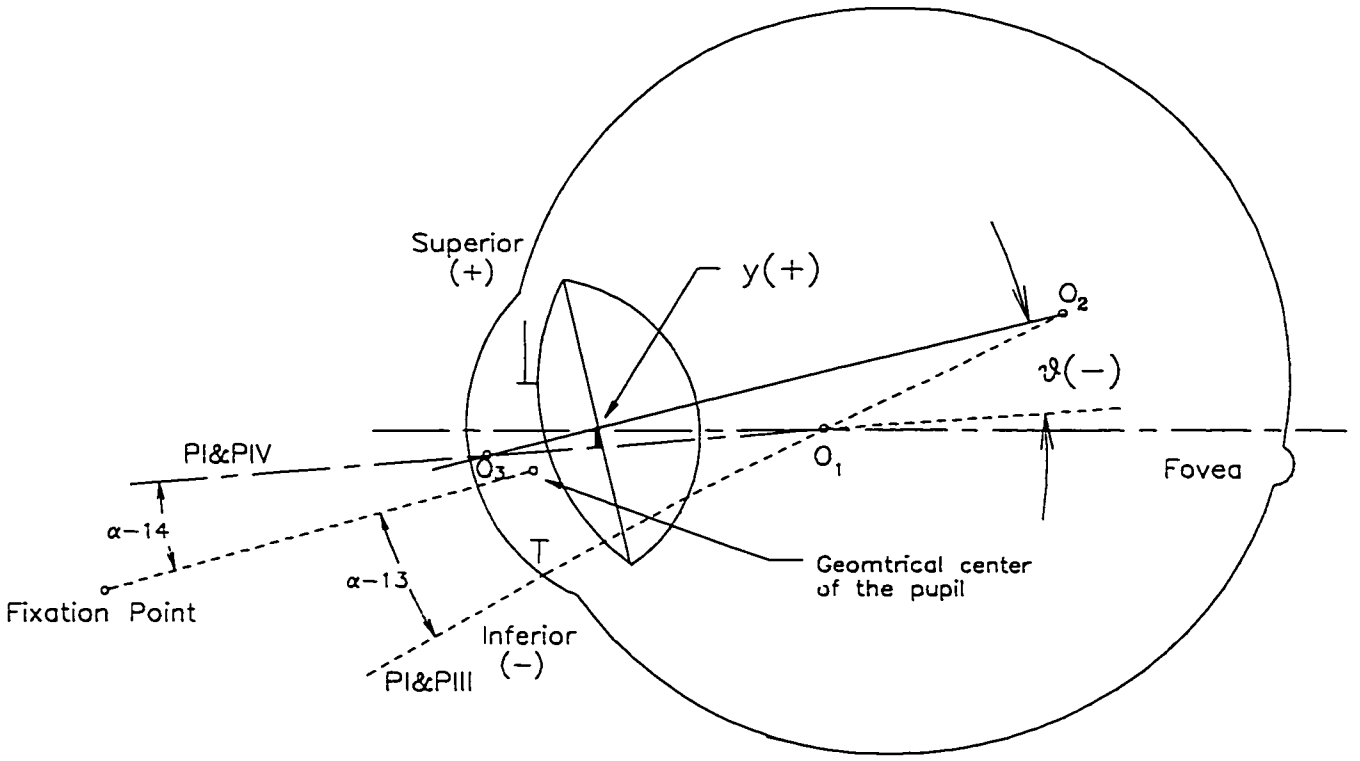


Fig. 7.1c The Vertical section of the misaligned G-E eye model. O_1, O_2 and O_3 represents the centers of curvature of the anterior surface of the cornea, posterior surface of the lens and anterior surface of the lens, respectively; y represents the amount of lens decentration; θ represents the amount of lens tilt; α-13 and α-14 represent the angle alphas measured by aligning PI and PIII and by aligning PI and PIV, respectively. The drawing is not to scale.

7.1.1 Angle alpha

Angle alphas were measured both by aligning PI and PIV, and by aligning PI and PIII, along with the measurement of other misalignment features of the 21 eyes. The results show that the difference between Tscherning's data and the more recent data is due to the difference in defining the optical axis.

The data presented in this thesis are both in the horizontal and vertical meridian while most recent measurements were only in the horizontal meridian. The results also show that a true optical axis usually does not exist in the eye. Strictly speaking, the theoretical definition of angle alpha loses its ground. Tscherning's technique of approximate alignment of all 3 Purkinje images in fact biases the reference axis towards a PI and PIII alignment.

7.1.2 Pupil centration

Considerable effort has been devoted to the study of pupil centration because of its important role in the optical system of the eye. Most of these studies dealt with pupil centration without considering other ocular optical components. In this study, the centration of the pupil with respect to other optical components in the eye was examined.

Results of pupil decentration measured with respect to the aligned PI and PIV (represents the approximate optical axis of the eye) in this thesis show that the geometrical center of the pupil is significantly deviated to the nasal side. The vertical deviation is not significantly different from zero. In the horizontal meridian, the

geometrical center of the pupil tends to be centered at between the approximate optical axis of the eye and the nodal axis or visual axis of the eye.

The CSCR was theoretically shown to be very close to the traditionally defined visual axis or the nodal axis in this thesis. Stiles-Crawford data suggest that the effective center of the pupil may be centered on the CSCR and also centered on the traditionally defined visual axis.

The immediate application of the result of this study is to provide guidance for the choice of a reference axis in current refractive surgical procedures.

Given the importance of pupil centration, it would be desirable to have Stiles-Crawford sensitivity functions on the same subjects to show the actual relationship between the Stiles-Crawford function and the various reference axes in the eye.

7.1.3 Crystalline lens tilt and decentration

Lens tilt and decentration was calculated based on theoretical modeling and the misalignment of the Purkinje images. With respect to the aligned PI and PIV, the data showed that, on the average, the lens tilted to the temporal side in the horizontal meridian and tilted forward in the vertical meridian. The lens also decentered to the nasal side in the horizontal meridian and to the superior in the vertical meridian.

With respect to the pupillary axis, the data showed that, on the average, the lens significantly tilted to the temporal side in the horizontal meridian and significantly tilted backward in the vertical meridian. The lens also decentered to the temporal side in the horizontal meridian and to the superior in the vertical meridian.

With respect to the line of sight, the data showed that, on the average, the lens significantly tilted to the temporal side in the horizontal meridian and tilted forward in the vertical meridian. The lens also decentered to the temporal side in the horizontal meridian and to the superior in the vertical meridian. The cause of this general trend of misalignment of the lens in the eye is unknown.

The technique and theory developed in this study can be used to study the centration of intraocular lens implant in pseudophakic eyes. It has been pointed out that IOL tilt and decentration can induce aniseikonia (Lakshminarayanan, 1994a; 1994b). This study is the first of its kind to show the systematic misalignment of the lens in the human eye. The data obtained can be used to accurately model the details of the optics of the eye. The data presented are also essential to understand the relationship between various reference axes in the eye, which is important both in research and in clinical applications.

Future studies of the dependence of the misalignment of the crystalline lens on age and refractive error can be useful to understand the ultimate cause and possible implication of these peculiar misalignment features in the human eye.

7.2 Wavefront aberration measurement

7.2.1 A semi-Maxwellian view wavefront aberration measurement system

A reliable, easy to use and precise two-dimensional semi-Maxwellian view ocular wavefront aberration measurement system was designed. The measurement system utilized human's hyperacuity to measure wavefront aberration as it was perceived by the subject. The measurement system could sample any number of sampling positions on the pupil

plane. The wavefront reconstruction method could use any form of polynomials to reconstruct the wavefront aberration based on measured ray aberration data. The wavefront reconstruction data processing method has been shown to be fast and reliable. For a uniform sampling scheme of 49 points on a 6 mm pupil, one measurement session took about 45 minutes.

The system could be used to measure the wavefront aberration of the eye under a variety of conditions, such as under natural pupil conditions.

Preliminary measurements of a small number of subjects using the geometrical center of the pupil as the reference axis have produced results consistent with other reported measurement results using different measurement methods.

7.2.2 Measuring wavefront aberration along the CSCR

Monochromatic ray aberrations of the left eyes of 21 emmetropic subjects were measured using the CSCR as the reference. This new reference axis provided a convenient and reliable measurement reference. 6^{th} order Taylor polynomials were used to reconstruct the wavefront aberrations of the 21 eyes measured. Precision and repeatability of the measurements were analyzed.

Relationships of the coefficients between using geometrical center of the pupil and using the CSCR as two different reference axes were derived, in order to calculate the overall wavefront aberrations across the actual pupil.

For the average of the 20 subjects measured, the total mean squared aberration is 0.25 μm^2; the asymmetrical component is 0.07 μm^2; the symmetrical component is 0.18 μm^2. The result proves that the average wavefront aberration of the subject group measured

is symmetrical in nature. A 4th order Taylor polynomial fit also produced a fit of a r-squared value of 0.996, which suggests there was predominantly primary aberrations in the average eye of the population sample.

Of the 21 eyes measured, the asymmetric components of the overall wavefront aberration do not show a group mean increase if the pupils are assumed to be centered at the CSCR. This substantiates the possibility that the effective center of the pupil may be centered with the CSCR, which is close to the visual axis of the eye. In other words, the optical quality of the optical zone of the eye surrounding the CSCR is as good as the optical quality of the zone surrounding the geometrical center of the pupil. Given the unsettled disputes in this area regarding the choice of a reference axis in the eye and its importance, this study may contribute to the final clarification of these issues.

Two measurement repeatability studies were also done. One used the geometrical center of the pupil as the reference while the other used the CSCR as the reference. The studies showed that the CSCR was a better reference axis. The aberration difference in repeated sessions for one subject using the CSCR as the reference was comparable to the difference between a 6^{th} and a 8^{th} order Taylor polynomial wavefront fit. The studies also confirmed that there can be true aberration changes between different measurement sessions for the same subject (Smirnov, 1961). But these changes are relatively small and the general aberration characteristics of the eye tend to remain the same.

7.3 Correlation between the misalignments of optical components and the asymmetrical component of wavefront aberration

Each misalignment factor measured was examined against the asymmetrical component of the wavefront aberration. The asymmetric components of the total

wavefront aberration were plotted against the modules of each misalignment factor. None of the plots showed significant correlation.

The group means of all the misalignment factors in the eyes measured showed significant deviations from zero. On the other hand, the group mean of the wavefront aberrations showed virtually symmetrical aberrations. A visual examination of these data may immediately disfavor the possibility of significant correlation.

On the other hand, the group mean of corneal topographic maps tends to be symmetrical. This is consistent with Howland et al's (1994) suggestion that the cornea may be the main contributor to the asymmetrical aberrations in the human eye.

With the possible development of more accurate corneal topographic measurement systems, more accurate measurement of corneal aberration may finally explain the cause of asymmetric monochromatic aberration in the human eye.

Appendix I

A Preliminary Measurement of Angle Alpha

A1.1 Introduction

The catoptric images-- the Purkinje images, the fixation point and some visible physiological features of the front section of the eye including the pupil are often used as references to define the optics of the eye. If the eye is a centered optical system, all the apexes of the optical surfaces of the eye, the geometrical center of the pupil and the fovea should align on one axis. This axis would be the optical axis of the eye by definition.

In reality, an axis to align all Purkinje images may not exist (Tscherning, 1924; Shipley and Rawlings, 1970). However, an axis to roughly align all the Purkinje images can be defined in all situations (Tscherning, 1924). The fixation point and the center of the pupil defines a visual line that forms an angle with the optical axis of the eye . This angle is named as angle alpha (Tscherning, 1924).

This special structure in the human eye had caused a great deal of chaos in precisely defining the optics of the eye (Martin, 1942). Many unique terms were coined to represent different aspects of this peculiar structure. Martin was accredited for recommending the use of a much smaller collection of such terms.

The direct phenomenon of the existence of the angle alpha is the fact that the fixation point does not lie on the axis along which all Purkinje images can roughly be aligned (Tscherning, 1924). In geometrical optics, this implies that the fovea is not on the optical axis. Dunne and Barns (1989) went on to argue whether angle alpha is caused by the crystalline lens tilt from the visual axis or by the rotation of the entire eye. By the crystalline lens tilt, they seemed to refer that the cornea is assumed to be centered around the visual axis but the lens is tilted away; by the rotation of the entire eye, they mean that both the cornea and the lens are tilted away from the visual axis, which is equivalent to saying that the visual axis is tilted away from the optical axis of the eye. Dunne and Barns concluded that corneal topographic data mostly support a decentered cornea from the visual axis. Consequently, they supported the theory that the rotation of the entire eye causes angle alpha.

Dunne and Barns essentially dealt with the problem using the visual axis as the reference axis. Given the fact that a rough optical axis of the eye nonetheless exists, it excluded the possibility that angle alpha is caused by lens tilt from the cornea. An average angle alpha value is around of 5°. If the lens is tilted away from the cornea by 5°, it would not be possible to define a rough optical axis of the eye. When Tscherning first stated his angle alpha measurement, he did express lens tilt with respect to the visual axis (Tscherning, 1924). In my opinion, Tscherning only used the visual axis as a reference axis. In other words, he did not mean that the cornea was centered with the visual axis and therefore the lens was titled away from the cornea .

Now that the optical structure that produces angle alpha is clear, what remains to be answered is the mechanism behind this peculiar optical structure of the eye. In other words, one can ask why the fovea has to be away from the optical axis of the eye.

The first speculation will naturally be that it is an imaging demand. Indeed, Jennings and Charman (1981) measured monochromatic image quality of the eye across the retina and found that deterioration of image quality was roughly symmetrical with the optical axis of the eye. In another word, the eye has the best image quality in the region of the retina where the optical axis intercepts the retina. However, this interesting measurement result has never been reconfirmed. The other interesting topic is oblique astigmatism. It has been suggested that if the optical axis rather than the visual axis is used as the reference, the measured peripheral astigmatism results tend to be more symmetrical (Lotmar and Lotmar, 1974). All these results imply that a deviated fovea position does not have an imaging advantage. Similar arguments can also be made for transverse chromatic aberration. This line of argument is, of course, comparing on-axis imaging with a centered optical system including a centered pupil with off-axis imaging. In reality, it is possible that the pupil may deviate from the optical axis of the eye to compensate off-axis aberrations. Controversially, Martin quoted Duke-Elder " Angle alpha has a teleological significance since it tends to correct chromatic aberration at the fovea"(Martin, 1942). But

if his conclusion was drawn from his experimental data, then it was highly possible that a decentered pupil tended to neutralize the transverse chromatic aberration at the fovea caused by angle alpha, not the other way around.

There has been another interesting factor to argue about the possible benefit of an angle alpha in the eye for imaging purpose. That is the existence of lens suture inside the crystalline lens (Kuszak et.al. 1984; Kuszak et.al. 1991; Bullock et. al. 1995). When the pupil is small, the lens suture could greatly degenerate image quality. Consequently, a fovea located slightly off the optical axis of the eye would use a clear part of the lens rather than the suture. This rather interesting point deserves to be confirmed.

Park was quoted by Martin (Martin, 1942) as suggesting the involvement of ciliary muscle on angle alpha. Given the direct interaction between the lens and the ciliary muscle, what Park suggested could be true but does not say much about the mechanism behind the existence of angle alpha.

Last but not the least, like many other peculiar features of the human body, angle alpha could simply be an artifact of evolution. Emsley once was quoted as saying " Angle alpha is probably an accompaniment of the gradual evolutionary movement of the eyes around(the word "round" was used in Martin's original quotation) towards the forward looking position" (Martin, 1942). To support the evolutionary theory, Martin (1942) also quoted Gibson's angle alpha data of animals. Gibson found that angle alpha becomes greater in proportion to the divergence between the eyes.

Actually, a 5° angle in each eye corresponds to a converging point of about the normal reading distance, which means when the extra-ocular muscles are relaxed, the eyes are fixating at the reading distance.

Angle alpha is an important parameter for defining and modeling the ocular optical system. Also the variation in the size of angle alpha may produce apparent strabismus. It is therefore of clinical significance (Martin, 1942; Effert et. al. 1992).

The first angle alpha measurement was carried out by Tscherning about a century ago using his ophthalmophakometer (Tscherning, 1924). Tscherning reported a value range of 4°-7° in the horizontal meridian with the visual axis to the nasal of the optical axis outside the eye and 2°-3° in the vertical meridian with the visual axis above the optical axis outside the eye.

Uozato et. al. (1983) reported a much smaller range of angle alphas measured during their measurement of the visual axis.

More recently, Effort et. al. (1992) reported angle alpha measurements by using a hand-held Purkinje images reflection pattern examination apparatus. Only PI and PIV were used to define the optical axis of the eye. The angle alphas of 60 adults that they reported were significantly lower than Tscherning's values.

These newer lower angle alpha values needs to be verified and explained . In this report, a computer-controlled CCD video camera system of high magnification was developed to measure the angle alphas using PI and PIV. The angle alpha values of both eyes of 11 subjects were measured. The measurements were done both for the horizontal component and for the vertical component of angle alpha.

A1.2 Apparatus and methods

Similar to Tscherning's measurement and as shown in Fig. A1.1 for the horizontal measurement, a CCD camera with a Nikon™ 105 cm focal length macro lens was mounted on an optical bench which could be moved transversely by a micrometer. A LED green source as the fixation target was mounted on the movable hand of a caliper which was perpendicularly mounted on the optical bench. The CCD camera system was controlled by an IBM™ 386 computer and connected to a JVC™ video monitor with a center mark. The camera system provided a picture of the eye in real time with a magnification of about 18 times on the video screen. Three optical fiber bundles mounted

on a mounting plate in the form of a unilateral triangle connected with a photoflash unit were also mounted on the optical bench with a supporting aluminum bar.

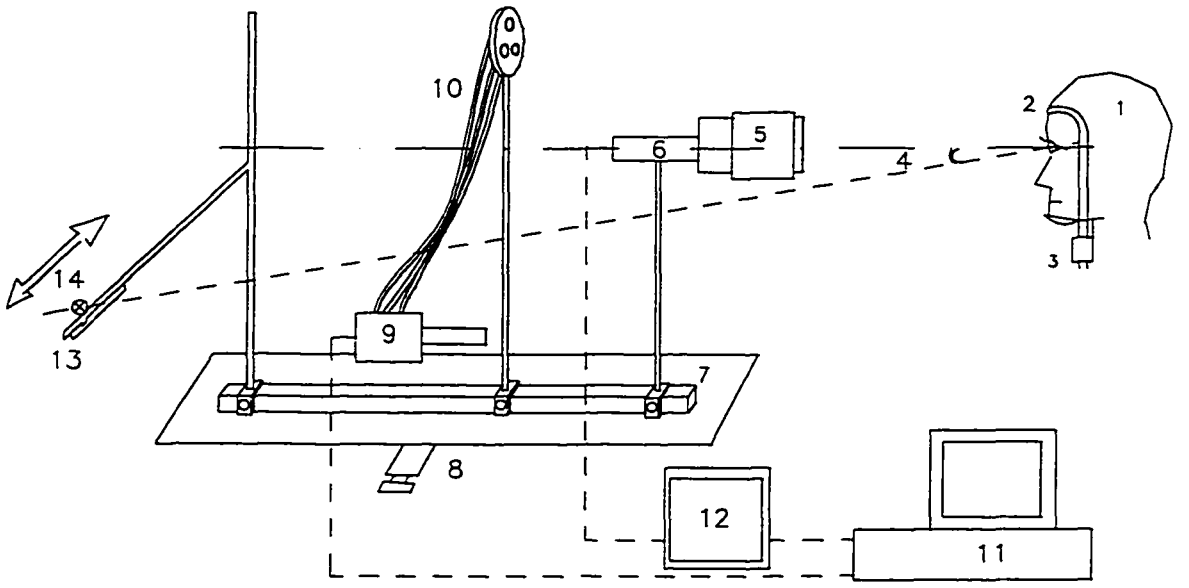


Fig. A1.1 A diagram of the setup for measuring the horizontal component of angle alpha. 1) Subject; 2) Headrest; 3) Chin rest height adjustment knob; 4) Corresponding horizontal component of angle alpha; 5) Macro lens; 6) CCD camera; 7) Optical bench; 8) Transversely movable table; 9) Photoflash gun; 10) Optical fiber bundles; 11) Computer; 12) Video screen; 13) Caliper; 14) Red light diode.

The center of the camera, the apex of the optical fiber bundle triangle and the supporting bar were all aligned with the axis of the optical bench. Supporting software could provide both image viewing in real time with continuous illumination and instant image grabbing by firing the photoflash gun. The grabbed picture could be saved for later processing. The subject was seated 40 cm in front of the camera supported by a chin rest and a head rest. A projection lamp was mounted on the desk to provide continuous illumination of the aluminum bar supporting the optical fiber triangle. The PI of the continuously illuminated aluminum bar provided a reference line to be aligned horizontally with the center mark on the CCD monitor screen. By adjusting the optical bench

transversely, the PI of the continuously illuminated aluminum bar was maintained at the center of the screen, which made the PI of the aluminum bar aligned with the optical bench, or the axis of the camera.

System alignment was crucial for the measurement.

1) Alignment of the camera with the optical bench

A point mark was made on a pole mounted on the optical bench. The point mark was made at the center of the optical bench or the axis of the optical bench by measurement using a caliper. The camera was moved along the optical bench and focused at the point mark from different positions on the bench. The orientation of the camera was then adjusted until the image of the point object always stayed at the center of the video screen when the focus of the camera was adjusted.

(2) Alignment of the PI of the aluminum bar with the axis of the camera system.

At the beginning of the experiment, the picture of the eye under test illuminated with the desk lamp was first roughly placed at the center of the screen by adjusting the position of the chin rest. The projection lamp was then turned on to illuminate the aluminum bar appropriately. A clear PI of the bar could be obtained on the screen by adjusting the camera distance. The PI of the bar had then always been kept aligned with the central mark of the screen by adjusting the optical bench transversely to track the moving eye .

The subject was required to fixate the LED target steadily. The axis of photography was fixed and pictures were taken for different positions of the fixation target. The experimenter adjusted the chin position and made sure that the PI was aligned with the center mark of the screen and then fired the photoflash unit to grab the picture of the Purkinje images of the optical fiber bundles. For each session, the proper location of the target where the PI and PIV were roughly aligned was first located by several trials without saving the pictures. Then the target was moved at about this position in steps of 3 mm for about 8 positions and had the pictures grabbed and saved. The

pictures were analyzed to decide the position of the target when the PI and PIV were best aligned. This position of the target was then used to calculate corresponding angle alpha.

For the vertical measurement, the light source and the fixation target mounting arm were rotated 90°. The PI of a horizontally mounted aluminum bar which was mounted at the same height as the optical fiber sources and illuminated by a desk lamp was adjusted by adjusting the chin rest to stay aligned with a center mark on the video screen. The alignment and procedure for the vertical component measurements were similar to that of the horizontal measurement.

Both the left and right eyes of 11 subjects, 4 males and 7 females aged from 23-43 years old were measured without any refractive corrections. The measurements were done both horizontally and vertically. To maintain good fixation, emmetropic or close to emmetropic subjects were chosen. Six subjects were perfect emmetropes. One subject was slightly hyperopic. Two subjects had one emmetropic eye and one myopic eye. One subject was about 2.5 D myopic with both eyes. However, her unaided vision was good enough to see the target.

To test the repeatability of the setup, subject AR's horizontal angles and subject LZ's vertical angles were measured for three more times. For each measurement, the setup was dismantled and rebuilt again.

My right eye was also measured. Although the eye was 3.8D myopic, it showed the clearest PIII. The misalignment of the Purkinje images are shown in the discussion to demonstrate the measurement error that could have possibly been induced by the fact that it was impossible to align all the Purkinje images at the same time for some subjects.

A1.3 Results

As an example, aligned pictures for the left eye of subject LZ horizontally and vertically are shown in Fig. A1.2 and Fig. A1.3, respectively.

As an example. aligned pictures for the left eye of subject LZ horizontally and vertically are shown in Fig. A1.2 and Fig. A1.3. respectively.

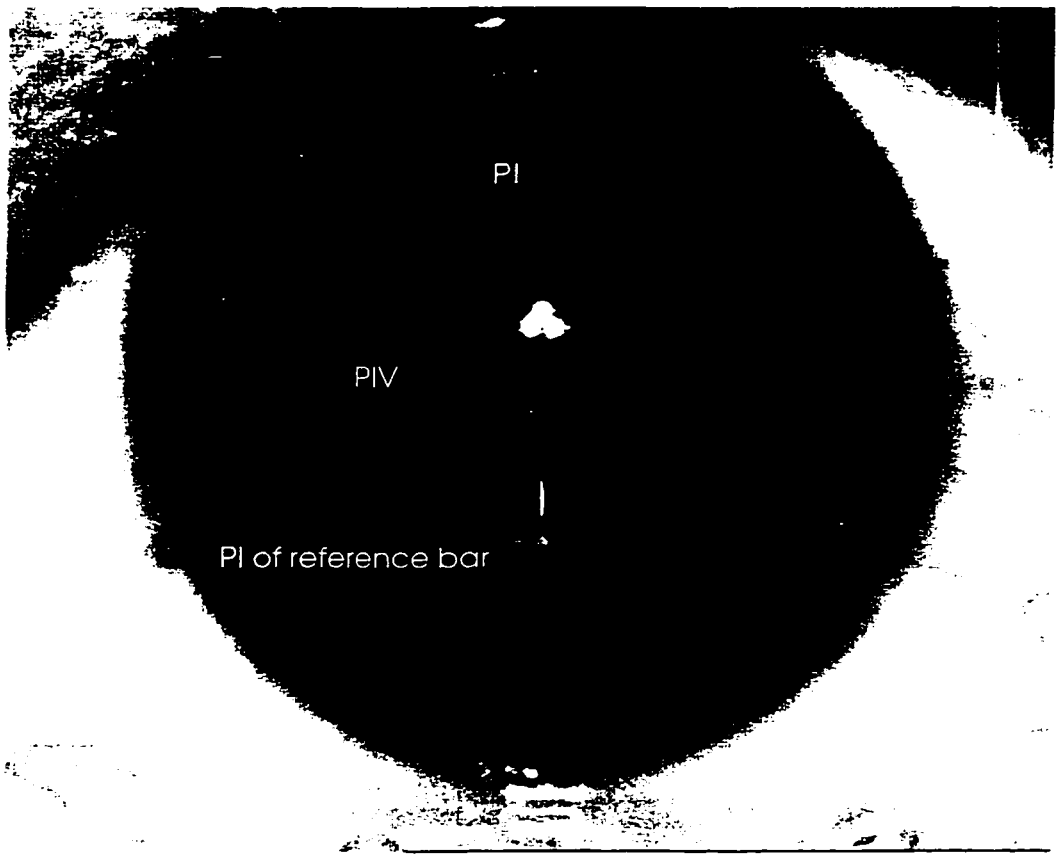


Fig. A1.2 Horizontally aligned Purkinje images of the left eyes of subject LZ. The light sources for forming these Purkinje images are three ends of three optical fiber cables transmitting light from a photographic photoflash unit. The three fiber optical cable ends are mounted in a form of a unilateral triangle. The brightest image which is erect is PI. The largest image which is also the foggiest is PIII. The smallest image which is upside down is PIV. The bright vertical line is the PI is the reference aluminum bar. The bright patch on the right of the Purkinje images is the PI of myself in a white shirt.

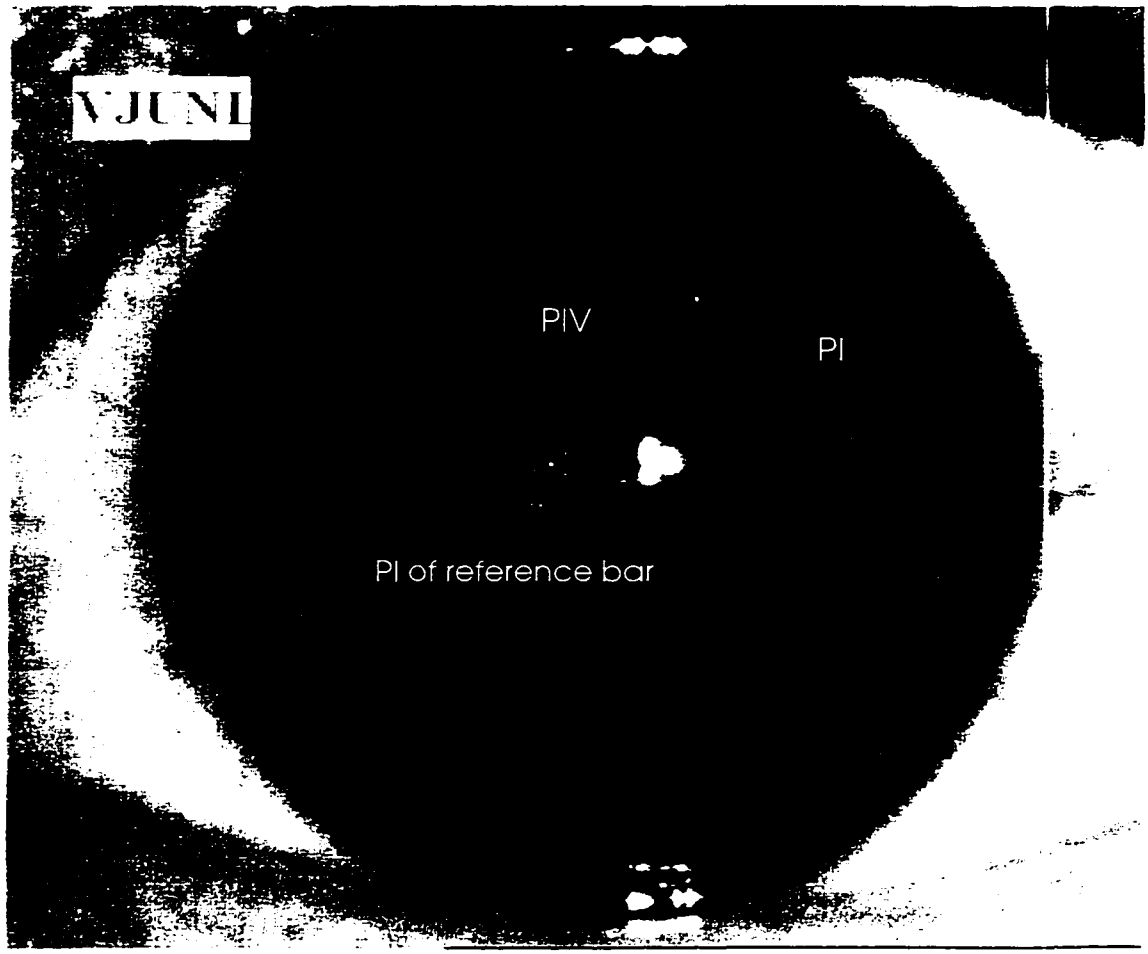


Fig. A1.3 Vertically aligned Purkinje images of the left eyes of subject LZ. Each item in the picture the vertical version of the corresponding items as in Fig. A1. 2.

The distance from the target to the eye and the distance from the target to the axis of the optical bench were recorded and used to calculate the angle alpha. The results are given in Table A1.1.

Table A1.1 Measured angle alpha values of 11 subjects. The prescriptions of the subjects are also given.

Subject No. (Initials)		Prescription	Angle alpha(°)			
			Horizontal	Vertical*	Total angle	Orientation (°)
1	R	NA	5.6	1.4	5.8	194.0
(AR)	L	NA	5.2	1.5	5.4	196.1
2	R	0/-1.25x180	4.6	0.5	4.6	186.2
(MSk)	L	+3.0/-2.0x180	4.8	1.1	4.9	192.9
3	R	NA	3.5	0.6	3.6	189.7
(AN)	L	NA	3.0	0.5	3.0	189.5
4	R	+1.00/-1.50x170	4.8	1.5	5.0	197.4
(BB)	L	+0.75/-1.25x005	3.7	2.4	4.4	213.0
5	R	-2.50/-0.50x010	4.0	-1.2	4.2	163.3
(LV)	L	-0.50/-0.50x170	4.6	-0.5	4.6	173.8
6	R	NA	4.9	1.7	5.2	199.1
(AB)	L	NA	5.5	1.1	5.6	191.3
7	R	NA	4.2	0.3	4.2	184.1
(LB)	L	NA	5.0	-0.2	5.0	177.7
8	R	-0.50/-0.75x90	5.2	-2.2	5.7	157.1
(DC)	L	-0.50/-0.75x90	4.3	-2.9	5.2	146.0
9	R	NA	5.8	-0.3	5.8	177.0
(JD)	L	NA	5.8	-1.9	6.1	161.9
10	R	NA	4.9	-0.5	4.9	174.2
(MSt)	L	NA	4.9	-0.4	4.9	175.4
11	R	-2.75/0	5.9	-0.4	5.9	176.1
(LZ)	L	-2.50/0	5.9	1.0	6.0	189.6
Mean	R		4.9	0.1	5.0	181.7
	L		4.8	0.1	5.0	182.5
Std.	R		0.7	1.2	0.8	13.4
	L		0.9	1.5	0.8	18.2

* Positive sign denotes the visual axis is to the nasal side horizontally and to the inferior vertically.

To demonstrate the general distribution of angle alpha among the 11 subjects, the total angle value and its orientation in a polar coordinate system were calculated and tabulated in Table A1.1. A scatter plot of the results is given in Fig. A1.4.

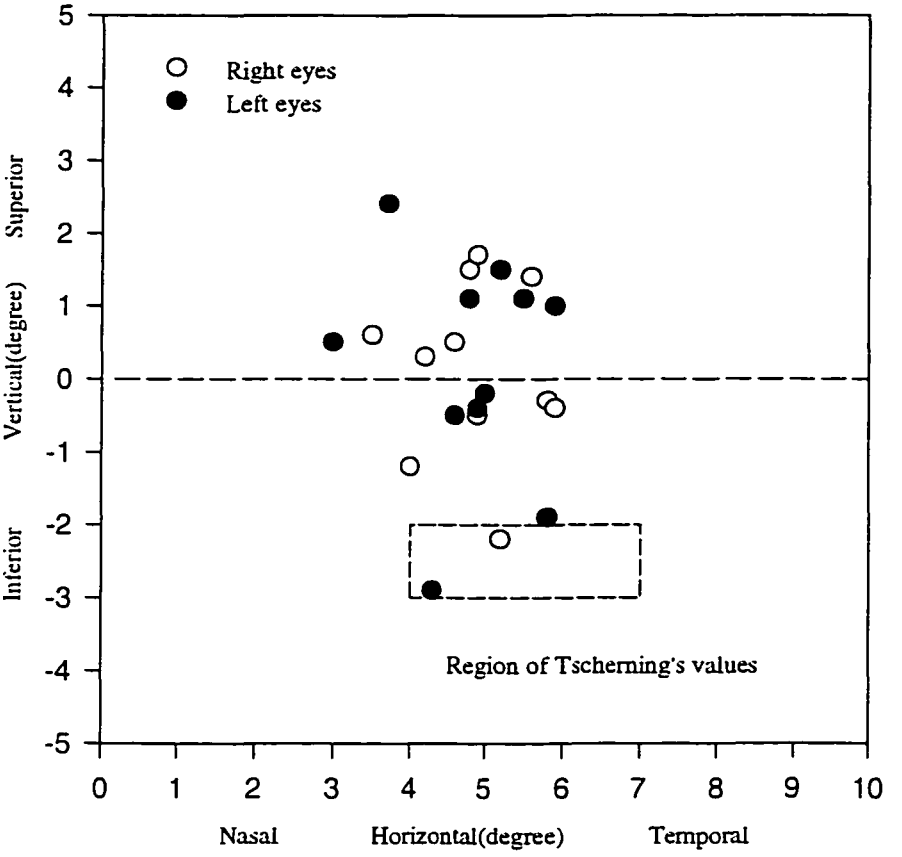


Fig. A1.4 Scatter plot of the measured angle alphas of 11 subjects. Each measured value is represented by a circle. Open circles represent values of the right eyes while the filled circles represent values of the left eyes. The box drawn with broken line is the value range as reported by Tscherning (1924).

Results of repeatability measurement are given in Tab.A1.2. It can be seen that for both subjects the repeatability was at about the 0.2° level, which was consistent with fixation errors.

The measured total angle alpha values of the right and left eye of each subject were plotted against each other as shown in Fig. A1.5 . A linear regression curve is also plotted. The r-squared value of the regression is 0.7.

Table A1.2 Results of repeatability measurements.

Measurement	AR(Horizontal) (°)		LZ(Vertical) (°)	
	R	L	R	L
1	5.6	5.2	-0.4	0.9
2	5.2	5.7	-0.3	1.0
3	5.5	5.3	-0.4	0.9
4	5.3	5.3	-0.6	1.0
Mean	5.4	5.4	-0.4	1.0
Standard deviation	0.2	0.2	0.1	0.1

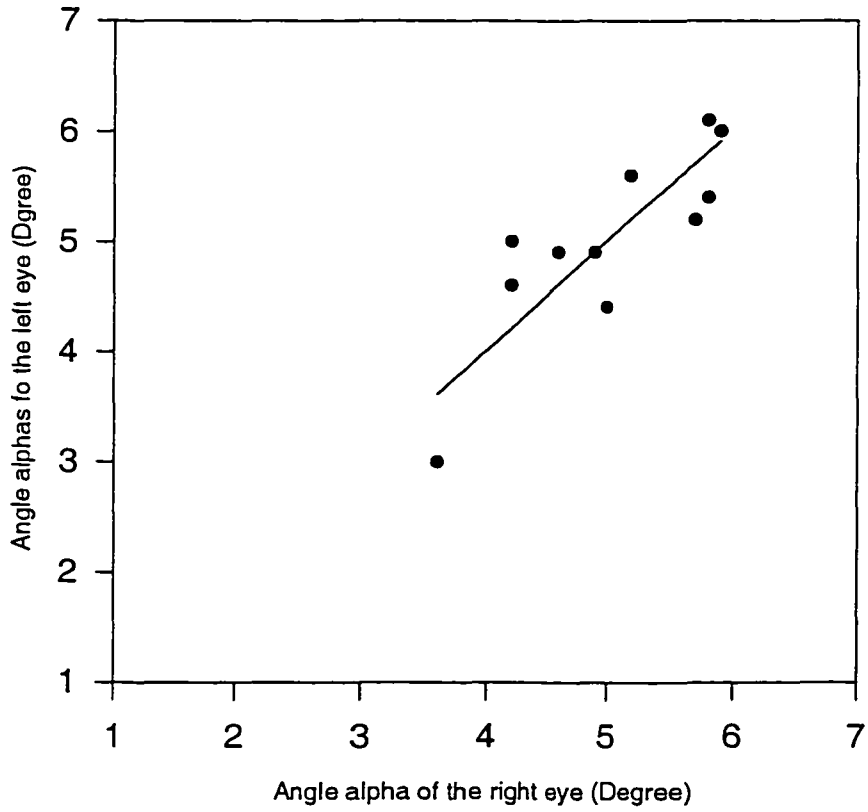


Fig. A1.5 The correlation between the angle alpha values of the right eye and the left eye of the 11 subjects measured. The solid line through the data is the linear regression line of the data.

A1.4 Discussion

Because the relative longer distance from the eye to the fixation target compared to the dimension of the pupil, the approximation in defining visual axis would produce negligible impact on the calculation of angle alpha.

There could also have been a small difference between the geometrical center of the entrance pupil and the optical axis which is expressed by the two aligned Purkinje images. The difference usually is very small (Shipley and Rawlings, 1970). This difference will also make no significant difference in calculating angle alpha due to the same reason as stated above.

The precision of the measurement depended on the system magnification. The system could easily resolve 0.03 mm in the positioning of the Purkinje images. This corresponds to a resolution of 0.1° in fixation angle. For the measurement of each meridian, the light source and the reference aluminum bar had to be displaced perpendicularly to the measured direction slightly from the axis of the camera, this could induce a small error due to possible asymmetry of the cornea shape of some of the subjects. However, this error was expected to be small due to the relative longer fixation distance. Repeatability of the measurements mainly depended on the repeatability of aligning the Purkinje images by the experimenter and the fixation error of the subject. The measured repeatability of 0.2° was actually better than the value expected.

The measured horizontal values range from 3.0° to 5.9°. The mean value for the tested right eyes is 4.9° with a standard deviation of 0.7° while the mean for the tested left eyes is 4.8° with a standard deviation of 0.9°. Effert et. al. (1992) recently reported an investigation of the relationship of angle alpha with age using a hand-held Purkinje Reflection Pattern Examination apparatus. For their children group of 59 subjects aged 1 years old, they reported an average value of 4.5° for the right eyes and 4.8° for the left

eyes with a standard deviation of 1.1° and 1.2°, respectively. For their adult group of 60 subjects, the average value is 3.7° for the right eyes and 3.9° for the left eyes. The values were larger than their adult group. In their measurement, the fixation distance was set at 30 cm. The fixation distance in this measurement was 130 cm. This may explain the significant differences between the two measurements. Interestingly, both measurements gave values smaller than Tscherning's historical results of 4°-7°. Tscherning reported using a fixation distance of 86 cm (Tscherning, 1924) which was not much different than the values used in this study.

The cause for the difference between Tscherning's measured values and those of the recent studies could be due to the fact that Tscherning used a rough alignment of PI , PIII and PIV while in this study and in Effert et. al.'s study (1992), only PI and PIV were used to define the optical axis of the eye. The factor that causes this difference in angle alpha deserves to be verified.

Actually, as shown in Fig. A1.6-Fig. A1.7, the value of angle alpha measured by aligning PI and PIV and by aligning PI and PIII were different for my right eye

The difference of angle alpha values measured by aligning each two of the three as shown was approximately 1°

The measured values of the two eyes of the same subject were about the same in this measurement with a few exceptions. Dependencies of angle alpha on age and refraction cannot be concluded from this data due to the relative small size of the sample of this measurement.

The measured vertical values range from -2.9° to 2.4° which is different from Tscherning's values of -2° to -3° (with the sign convention in this study) reported. However, Tscherning (1924) did mention that there were opposite results in his measurement. The group means were both 0.1° for the right eyes and the left eyes. The standard deviation is 1.2° for the right eye and 1.5° for the left eyes. The vertical mean value of the tested eyes is not significantly different from 0. From this data, it is obvious

that there is no specific trend for the vertical values as for the horizontal values. Again, the choice of considering aligning PI and PIV in this study could be a reason for the difference. Also, a population difference is not impossible.

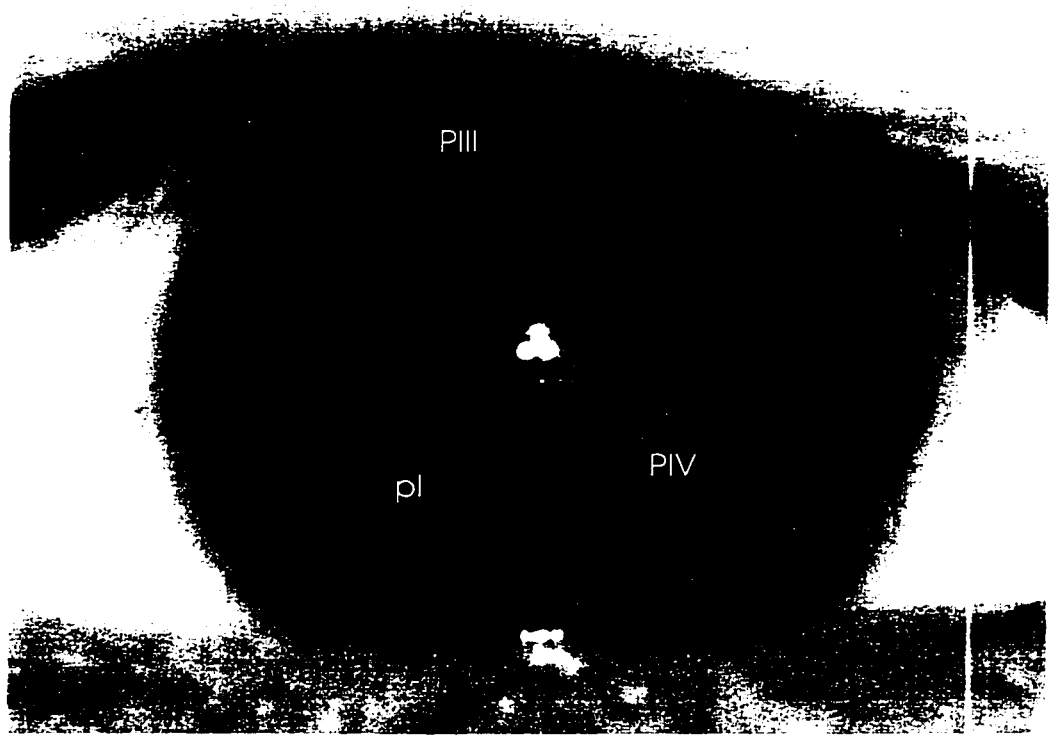


Fig. A1.6 A situation when PI, III and IV could not be aligned at the same time. PI and PIII were aligned while PIV was displaced from PI and PIII.

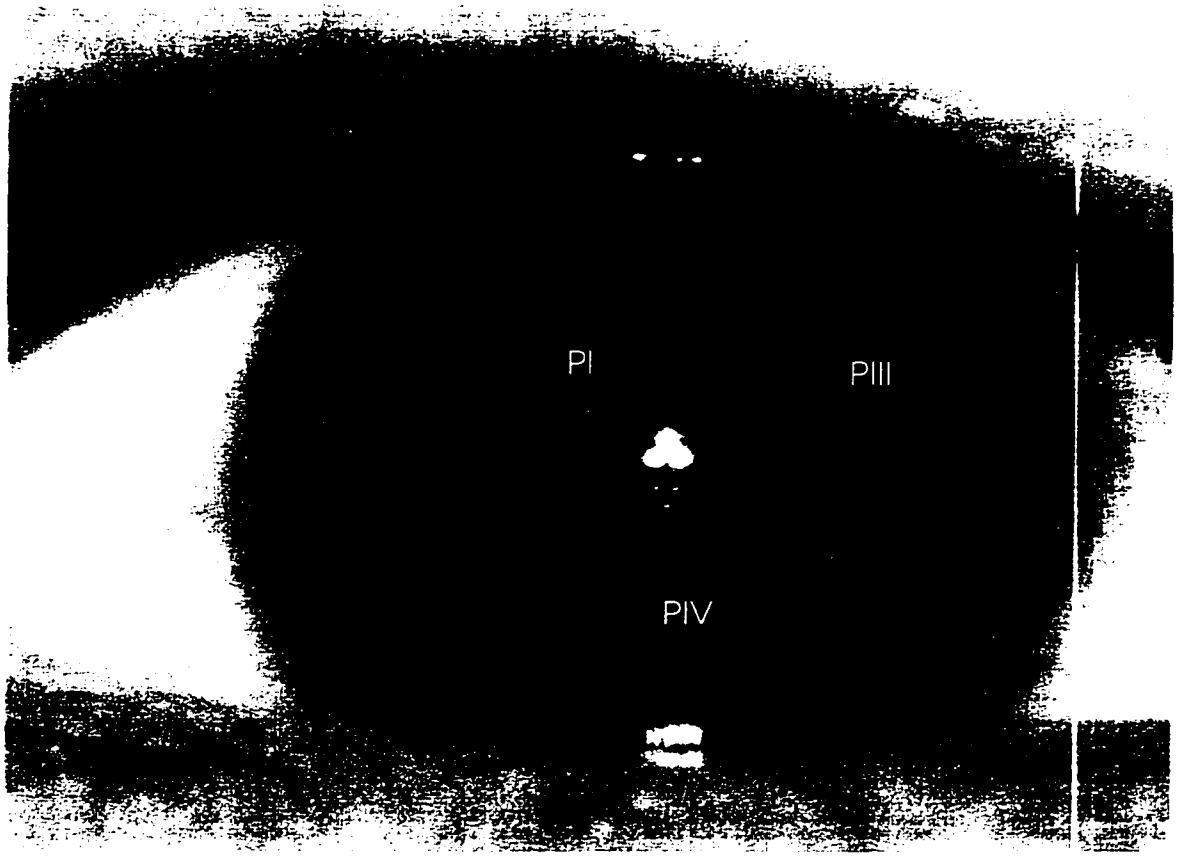


Fig. A1.7 A situation when PI, III and IV could not be aligned at the same time. PI and PIV were aligned while PIII was displaced from PI and PIII.

A1.6 Conclusions

An angle alpha measurement system was built. Angle alphas of the left and right eyes of 11 subjects were measured. The measured values are significantly smaller than the values reported by Tscherning. The measured mean value for the tested right eyes is 4.9° with a standard deviation of 0.7° while the mean for the tested left eyes is 4.8° with a standard deviation of 0.9°. The measured mean vertical values are not significantly

different from zero at a 99% significance level, which is different with the values reported by Tscherning. The difference caused by the choice of the optical axis of eye in the measurement is suggested. Also, a correlation between the angle alphas of the right eye and the left eye was found.

APPENDIX II

Calculation of the displacements of Purkinje images due to lens tilt (t) and decentration (y)

The program uses the G-E eye model to calculate the Purkinje image displacement with respect to the corneal optical axis as functions of lens tilt and decentration.

Set the numerical precision to 6 digits.

```
>Digits:=6:
```

Parameters setup (G-E schematic eye)

```
>r1:=7.8;
```

$$r1 := 7.8$$

```
>r2:=10.0;
```

$$r2 := 10.0$$

```
>r3:=6.0;
```

$$r3 := 6.0$$

```
>n1:=1.0;
```

$$n1 := 1.0$$

```
>n2:=1.333;
```

$$n2 := 1.333$$

```
>n3:=1.416;
```

$$n3 := 1.416$$

```
>d1:=3.6;
```

$$d1 := 3.6$$

```
>d2:=3.6;
```

$$d2 := 3.6$$

```
>d:=1.219;
```

$$d := 1.219$$

```
>x0:=d1+d;
```

$$x0 := 4.819$$

```
>
```

(Lens tilt t in terms of t0 in degrees)

```
>t:=t0*3.14/180;
```

$$t := .0174445\ t0$$

(Lens decentration is set to y0)

```
>y:=y0;
```

$$y := y0$$

Calculation of the equivalent mirror of the anterior surface of the lens.
(x coordinate of the apex of the equivalent mirror of the anterior surface of the lens)

```
>xma2:=r1/(n2*r1/(x0-d*cos(t))+(1-n2));
```

$$xma2 := 7.8 \frac{1}{10.3974 \frac{1}{4.819 - 1.219 \cos(.0174445\ t0)} - .333}$$

(x coordinate of the center of curvature of the equivalent mirror of the anterior surface of the lens)

```
>xmo2:=r1/(n2*r1/(x0+(r2-d)*cos(t))+(1-n2));
```

$$xmo2 := 7.8 \frac{1}{10.3974 \frac{1}{4.819 + 8.781 \cos(.0174445\ t0)} - .333}$$

(y coordinate of the apex of the equivalent mirror of the anterior surface of the lens)

```
>yma2:=(y+d*sin(t))/(x0-d*cos(t))*xma2*n2/n1;
```

$$yma2 := 10.3974 \frac{y0 + 1.219 \sin(.0174445\ t0)}{(4.819 - 1.219 \cos(.0174445\ t0))\left(10.3974 \frac{1}{4.819 - 1.219 \cos(.0174445\ t0)} - .333\right)}$$

(y coordinate of the apex of the equivalent mirror of the anterior surface of the lens)

```
>ymo2:=(y-(r2-d)*sin(t))/(x0+(r2-d)*cos(t))*xmo2*n2/n1;
```

$$ymo2 := 10.3974 \frac{y0 - 8.781 \sin(.0174445\ t0)}{(4.819 + 8.781 \cos(.0174445\ t0))\left(10.3974 \frac{1}{4.819 + 8.781 \cos(.0174445\ t0)} - .333\right)}$$

(The angle tilt of the equivalent mirror of the anterior surface of the lens with respect to the corneal optical axis. (The nasal side of the corneal optical axis in the object space is positive.)

```
>t2:=180/3.14*arctan((yma2-ymo2)/(xma2-xmo2));
```

$$t2 := 57.3248 \arctan\left(\left(10.3974 \frac{y0 + 1.219 \sin(.0174445\ t0)}{(4.819 - 1.219 \cos(.0174445\ t0))\left(10.3974 \frac{1}{4.819 - 1.219 \cos(.0174445\ t0)} - .333\right)} - 10.3974 \frac{y0 - 8.781 \sin(.0174445\ t0)}{(4.819 + 8.781 \cos(.0174445\ t0))\left(10.3974 \frac{1}{4.819 + 8.781 \cos(.0174445\ t0)} - .333\right)}\right) \Big/ \left(7.8 \frac{1}{10.3974 \frac{1}{4.819 - 1.219 \cos(.0174445\ t0)} - .333} - 7.8 \frac{1}{10.3974 \frac{1}{4.819 + 8.781 \cos(.0174445\ t0)} - .333}\right)\right)$$

(The radius of the equivalent mirror of the anterior surface of the lens)

```
>mr2:=sqrt((yma2-ymo2)^2+(xma2-xmo2)^2);
```

$$mr2 := \left(\left(10.3974 \right. \right.$$

$$\frac{y0 + 1.219 \sin(.0174445\ t0)}{(4.819 - 1.219 \cos(.0174445\ t0))\left(10.3974 \dfrac{1}{4.819 - 1.219 \cos(.0174445\ t0)} - .333 \right)} -$$

$$10.3974$$

$$\left. \frac{y0 - 8.781 \sin(.0174445\ t0)}{(4.819 + 8.781 \cos(.0174445\ t0))\left(10.3974 \dfrac{1}{4.819 + 8.781 \cos(.0174445\ t0)} - .333 \right)} \right)^2 + \left(\right.$$

$$7.8 \frac{1}{10.3974 \dfrac{1}{4.819 - 1.219 \cos(.0174445\ t0)} - .333}$$

$$\left. \left. - 7.8 \frac{1}{10.3974 \dfrac{1}{4.819 + 8.781 \cos(.0174445\ t0)} - .333} \right)^2 \right)^{1/2}$$

The distance between PI and PIV is:

*>p13:=-mr2*sin(-t2*3.14/180)+yma2;*

$$p13 := \left(\left(10.3974 \frac{y0 + 1.219 \sin(.0174445\ t0)}{\%1\ \%2} - 10.3974 \frac{y0 - 8.781 \sin(.0174445\ t0)}{\%3\ \%4} \right)^2 \right.$$

$$\left. + \left(7.8 \frac{1}{\%2} - 7.8 \frac{1}{\%4} \right)^2 \right)^{1/2} \sin\left(1.00000 \right.$$

$$\left. \arctan\left(\frac{10.3974 \dfrac{y0 + 1.219 \sin(.0174445\ t0)}{\%1\ \%2} - 10.3974 \dfrac{y0 - 8.781 \sin(.0174445\ t0)}{\%3\ \%4}}{7.8 \dfrac{1}{\%2} - 7.8 \dfrac{1}{\%4}} \right) \right)$$

$$+ 10.3974 \frac{y0 + 1.219 \sin(.0174445\ t0)}{\%1\ \%2}$$

$$\%1 := 4.819 - 1.219 \cos(.0174445\ t0)$$

$$\%2 := 10.3974 \frac{1}{\%1} - .333$$

$$\%3 := 4.819 + 8.781 \cos(.0174445\ t0)$$

$$\%4 := 10.3974 \frac{1}{\%3} - .333$$

The angle between the corneal optical axis and the direction to align Purkinje image I and III is,
(The nasal side in the object space is positive.)

```
>t13:=arctan(ymo2/(xmo2-r1));
```

$$t13 := \arctan\left(10.3974\,(y0 - 8.781\sin(.0174445\,t0))/\left((4.819 + 8.781\cos(.0174445\,t0))\left(10.3974\,\frac{1}{4.819 + 8.781\cos(.0174445\,t0)} - .333 \right)\left(7.8\,\frac{1}{10.3974\,\frac{1}{4.819 + 8.781\cos(.0174445\,t0)} - .333} - 7.8 \right) \right) \right)$$

Calcualtion of the equivalent mirror of the posterior surface of the lens
(x coordinate of the apex of the equivalent mirror of the posterior surface of the lens)

```
>xma3:=r1/(n2*r1/(x0-d*cos(t)+r2*n2*cos(t)/(n3*r2/d2+n2-n3))+1-n2);
```

$$xma3 := 7.8\,\frac{1}{10.3974\,\frac{1}{4.819 + 2\,24304\cos(.0174445\,t0)} - .333}$$

(x coordinate of the center of curvature of the equivalent mirror of the posterior surface of the lens)

```
>xmo3:=r1/(n2*r1/(x0-d*cos(t)+r2*n2*cos(t)/(n3*r2/(d2-r3)+n2-n3))+1-n2);
```

$$xmo3 := 7.8\,\frac{1}{10.3974\,\frac{1}{4.819 - 3.44698\cos(.0174445\,t0)} - .333}$$

(y coordinate of the apex of the equivalent mirror of the posterior surface of the lens)

```
>yma3:=(y+d*sin(t)-r2*n2*sin(t)/(n3*r2/d2+n2-n3))/(x0-d*cos(t)+r2*n2*cos(t)/(n3*r2/d2+n2-n3))*xma3*n2/n1;
```

$$yma3 := 10.3974\,\frac{y0 - 2.24304\sin(.0174445\,t0)}{(4.819 + 2.24304\cos(.0174445\,t0))\left(10.3974\,\frac{1}{4.819 + 2.24304\cos(.0174445\,t0)} - .333 \right)}$$

(y coordinates of the center of curvature of the equivalent mirror of the posterior surface of the lens)

```
>ymo3:=(y+d*sin(t)-r2*n2*sin(t)/(n3*r2/(d2-r3)+n2-n3))/(x0-d*cos(t)+r2*n2*cos(t)/(n3*r2/(d2-r3)+n2-n3))*xmo3*
>n2/n1;
```

$$ymo3 := 10.3974\,\frac{y0 + 3.44698\sin(.0174445\,t0)}{(4.819 - 3.44698\cos(.0174445\,t0))\left(10.3974\,\frac{1}{4.819 - 3.44698\cos(.0174445\,t0)} - .333 \right)}$$

(The angle tilt of the equivalent mirror of the posterior surface of the lens with respect to the corneal optical axis.
(The nasal side of the corneal optical axis in the object space is positive.)

```
>t4:=180/3.14*arctan((yma3-ymo3)/(xma3-xmo3));
```

$$t4 := 57.3248 \arctan\left(\left(\left(10.3974 \right.\right.\right.$$

$$\frac{y0 - 2.24304 \sin(.0174445\ t0)}{(4.819 + 2.24304 \cos(.0174445\ t0))\left(10.3974 \dfrac{1}{4.819 + 2.24304 \cos(.0174445\ t0)} - .333\right)}$$

$$- 10.3974$$

$$\left.\left.\left.\frac{y0 + 3.44698 \sin(.0174445\ t0)}{(4.819 - 3.44698 \cos(.0174445\ t0))\left(10.3974 \dfrac{1}{4.819 - 3.44698 \cos(.0174445\ t0)} - .333\right)}\right)\right)$$

$$\Bigg/\left(\left(7.8 \frac{1}{10.3974 \dfrac{1}{4.819 + 2.24304 \cos(.0174445\ t0)} - .333}\right.\right.$$

$$\left.\left.- 7.8 \frac{1}{10.3974 \dfrac{1}{4.819 - 3.44698 \cos(.0174445\ t0)} - .333}\right)\right)$$

(The radius of the equivalent mirror of the posterior surface of the lens)

```
>mr3:=sqrt((yma3-ymo3)^2+(xma3-xmo3)^2);
```

$$mr3 := \left(\left(\left(10.3974 \right.\right.\right.$$

$$\frac{y0 - 2.24304 \sin(.0174445\ t0)}{(4.819 + 2.24304 \cos(.0174445\ t0))\left(10.3974 \dfrac{1}{4.819 + 2.24304 \cos(.0174445\ t0)} - .333\right)}$$

$$- 10.3974$$

$$\left.\left.\left.\frac{y0 + 3.44698 \sin(.0174445\ t0)}{(4.819 - 3.44698 \cos(.0174445\ t0))\left(10.3974 \dfrac{1}{4.819 - 3.44698 \cos(.0174445\ t0)} - .333\right)}\right)\right)^2$$

$$+\left(\left(7.8 \frac{1}{10.3974 \dfrac{1}{4.819 + 2.24304 \cos(.0174445\ t0)} - .333}\right.\right.$$

$$\left.\left.\left.- 7.8 \frac{1}{10.3974 \dfrac{1}{4.819 - 3.44698 \cos(.0174445\ t0)} - .333}\right)^2\right)^{1/2}$$

The distance between PI and PIV is,

```
>p14:=mr3*sin(-t4*3.14/180)+yma3;
```

$$p14 := -\left(\left(10.3974 \frac{y0 - 2.24304 \sin(.0174445\ t0)}{\%1\ \%2} - 10.3974 \frac{y0 + 3.44698 \sin(.0174445\ t0)}{\%3\ \%4} \right)^2 + \left(7.8 \frac{1}{\%2} - 7.8 \frac{1}{\%4} \right)^2 \right)^{1/2} \sin\left(1.00000 \arctan\left(\frac{10.3974 \frac{y0 - 2.24304 \sin(.0174445\ t0)}{\%1\ \%2} - 10.3974 \frac{y0 + 3.44698 \sin(.0174445\ t0)}{\%3\ \%4}}{7.8 \frac{1}{\%2} - 7.8 \frac{1}{\%4}} \right) \right) + 10.3974 \frac{y0 - 2.24304 \sin(.0174445\ t0)}{\%1\ \%2}$$

$$\%1 := 4.819 + 2.24304 \cos(.0174445\ t0)$$

$$\%2 := 10.3974 \frac{1}{\%1} - .333$$

$$\%3 := 4.819 - 3.44698 \cos(.0174445\ t0)$$

$$\%4 := 10.3974 \frac{1}{\%3} - .333$$

The angle between the optical axis of the cornea and the direction to align Purkinje image I and IV is, (The nasal side in the object space is positive)

>t14:=tan(ymo3/(xmo3-r1));

$$t14 := \tan\left(\frac{\left(y0 + 1.219 \sin(.01744444445\ t0) - \frac{r2\ n2 \sin(.01744444445\ t0)}{\frac{n3\ r2}{d2 - r3} + n2 - n3} \right) r1\ n2}{\%2 \left(\frac{n2\ r1}{\%2} + 1 - n2 \right) n1 \left(\frac{r1}{\frac{n2\ r1}{\%2} + 1 - n2} - r1 \right)} \right)$$

$$\%1 := \cos(.01744444445\ t0)$$

$$\%2 := d1 + 1.219 - 1.219\ \%1 + \frac{r2\ n2\ \%1}{\frac{n3\ r2}{d2 - r3} + n2 - n3}$$

APPENDIX III

Verification of the wavefront fit program

---by generating transverse aberration data using the Maple V™ format with a known wavefront equation .

Here is the case of a mixture of primary spherical aberration with +-30 arcsecs nosie. By CCui, March 9, 1997. In the case without noise, the procedure is about identical except for the exclusion of the noise term in the ray aberration generation equation.

1) Read a sample experimental data file (agl1.dat) into array RAY for the actual standard samplin locations:

RAY := READPRN(agl1.dat);

Split the array into vectors to obtain the actual sampling location x and y coordinates.

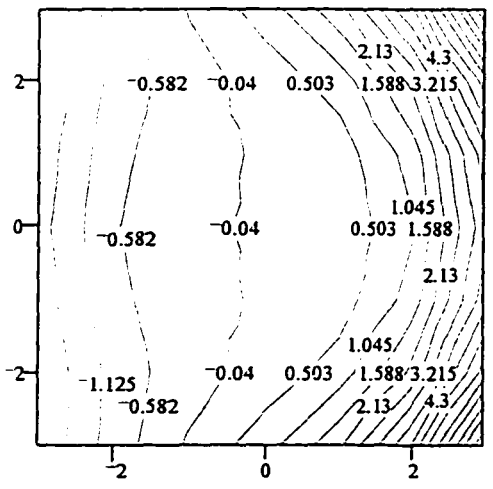
X_pos := RAY<1>	Y_pos := RAY<2>
0	3
-1.5	2.25
-0.75	2.25
0	2.25
0.75	2.25
1.5	2.25
-2.25	1.5
-1.5	1.5
-0.75	1.5
0	1.5
0.75	1.5
1.5	1.5
2.25	1.5
-2.25	0.75
-1.5	0.75
-0.75	0.75
0	0.75
0.75	0.75
1.5	0.75
2.25	0.75
-3	0
-2.25	0
-1.5	0
-0.75	0
0	0
0.75	0
1.5	0
2.25	0
3	0

-1.5	-0.75
-0.75	-0.75
0	-0.75
0.75	-0.75
1.5	-0.75
2.25	-0.75
-2.25	-1.5
1.5	-1.5
-0.75	-1.5
0	-1.5
0.75	-1.5
1.5	-1.5
2.25	-1.5
-1.5	-2.25
-0.75	-2.25
0	-2.25
0.75	-2.25
1.5	-2.25
0	-3

2) Creat a known wavefront equation
Typical primary spherical aberration in microns

$$ww := 0.1 \cdot (x^2 + y^2) \cdot x + 0.01 \cdot (x^2 + y^2)^2$$

Contour plot of the wavefront aberration:



ww

3) Calculate the corresponding transverse aberrations of the above wavefront aberration at the de experimental sampling locations.

'i' is the index of the sampling location from 0 to 48.

$i := 0..48$

'dwx' and 'dwy' are the x and y derivatives or the transverse aberration components of the wavefro aberration for the corresponding sampling locations (in mm).
To simulate experimental errors, a random noise generating term is added to the transverse ray aberration.

$$dwx_i = \frac{1.98 \cdot 3 \cdot X_pos_i^{\,2} - Y_pos_i^{\,2}}{10} \qquad k = 1980 \cdot \frac{1}{3600} \cdot \frac{1}{180} \cdot \pi$$

$$dwy_i = \frac{1.98 \cdot 2 \cdot X_pos_i \cdot Y_pos_i - 0.198 \cdot 2 \cdot (X_pos_i)^2 - (Y_pos_i)^2 \cdot 2 \cdot Y_pos_i}{10}$$

dwx =	dwy =
1.782	2.138
2.339	-0.033
1.337	0.334
1.002	0.902
1.337	1.671
2.339	2.64
3.453	-0.468
1.782	-0.356
0.78	-0.111
0.446	0.267
0.78	0.78
1.782	1.426
3.453	2.205
3.119	-0.334
1.448	-0.278
0.446	-0.156
0.111	0.033
0.446	0.29
1.448	0.613
3.119	1.002
5.346	0
3.007	0
1.337	0
0.334	0
0	0
0.334	0
1.337	0
3.007	0
5.346	0
3.119	0.334
1.448	0.278
0.446	0.156
0.111	-0.033
0.446	-0.29
1.448	-0.613
3.119	-1.002

3.453	0.468
1.782	0.356
0.78	0.111
0.446	-0.267
0.78	-0.78
1.782	-1.426
3.453	-2.205
2.339	0.033
1.337	-0.334
1.002	-0.902
1.337	-1.671
2.339	-2.64
1.782	-2.138

4) Generate the simulated data file for the wavefront reconstruction program

Column assignment:
0 - index; 1 - X_pos; 2 - Y_pos; 3 - dwx; 4-dwy.

$index_i := i$

$wtest^{<0>} := index \quad wtest^{<1>} := X_pos \quad wtest^{<2>} := Y_pos \quad wtest^{<3>} := dwx \quad wtest^{<4>} := dwy$

Write the simulated measurement data into file (wtest.prn) for the Maple V™ wavefront reconstruciton program.

WRITEPRN(wtestn) := wtest

APPENDIX IV

Wavefront Reconstruciton from Ray Aberration Data to a 6th order Taylor Polynomial

---

Set numerical precision to 10 digits after the decimal place.

```
> Digits:=10:
```

Inlude Maple linear algebra library.

```
> with(linalg):
```

Call read data matrix function.

```
> readlib(readdata):
```

Read in experimental data array.

```
> Mdat:=readdata(experimental_datafile,float,5):
```

Set the total number of terms of the Taylor polynomial.

```
> k:=27:
```

Split experimental data array into (r, s) sampling locations in mm and (p0,q0) tansverse ray aberrration in mm, respectively..

```
> r:=col(Mdat,2):
> s:=col(Mdat,3):
```

Convert transverse ray aberrations to arc secs and set up the sign convention to that of pupil locations(superior is "+", left is "+").

```
> p0:=col(-Mdat/1980,4):
> q0:=col(-Mdat/1980,5):
```

Stack the horizontal and vertical components of transverse ray aberration to form the transverse aberration vector "P". (Becasue the "stack" function only work for more than 2 columns, "p1" and "p2" are concatenated with "r" and "s" respectively
to form an array of 2 columns).

```
> p1:=concat(r,p0):
> q1:=concat(s,q0):
> pq:=stack(p1,q1):
> P:=col(-pq,2):
```

Set up terms of the Taylor polynomial up to the 27th term. "Z" refer to a Taylor polynomial term, the index is the index of the corresponding Taylor polynomial term.

```
> Z[1]:=(x,y)->x:
> Z[2]:=(x,y)->y:
> Z[3]:=(x,y)->x^2:
> Z[4]:=(x,y)->x*y:
> Z[5]:=(x,y)->y^2:
> Z[6]:=(x,y)->x^3:
> Z[7]:=(x,y)->x^2*y:
> Z[8]:=(x,y)->x*y^2:
> Z[9]:=(x,y)->y^3:
> Z[10]:=(x,y)->x^4:
> Z[11]:=(x,y)->x^3*y:
> Z[12]:=(x,y)->x^2*y^2:
> Z[13]:=(x,y)->x*y^3:
> Z[14]:=(x,y)->y^4:
> Z[15]:=(x,y)->x^5:
> Z[16]:=(x,y)->x^4*y:
> Z[17]:=(x,y)->x^3*y^2:
> Z[18]:=(x,y)->x^2*y^3:
> Z[19]:=(x,y)->x*y^4:
```

```
>    Z[20]:=(x,y)->y^5:
>    Z[21]:=(x,y)->x^6:
>    Z[22]:=(x,y)->x^5*y:
>    Z[23]:=(x,y)->x^4*y^2:
>    Z[24]:=(x,y)->x^3*y^3:
>    Z[25]:=(x,y)->x^2*y^4:
>    Z[26]:=(x,y)->x*y^5:
>    Z[27]:=(x,y)->y^6:
```

The following matrix operations are used to calculate the coefficient matrix of the equation(See theoretical part) to solve for the coefficents of the Taylor polynomial from partial derivatives of the Taylor polynomials terms at all pupil sample locations.

Calculate the partial derivative of each Taylor polynomial term in both the horizontal and vertical directions.

```
>    dzx:=map(D[1],Z):
>    dzy:=map(D[2],Z):
```

To reset the index for arrays to cope with Maple special internal index management bug.

```
>    m:='m':
>    n:='n':
```

Calculate the values of the partial derivative of each Taylor polynomial term at each pupil sampling location in both the horizontal and vertical directions.

```
>   for m to k  do
>      DXr[m]:=zip(dzx[m],r,s);
>      DYr[m]:=zip(dzy[m],r,s)
>   od:
```

Assemble the coefficients matrix by stacking(The first row is set first for the horizontal component and the vertical component, respectively. The first rows are then stacked with the above calculated derivtive values until the last Taylor polynomial term. The resulted horizontal and vertical matrix are then concatenated to form the coefficent matrix.

```
>   DX:=DXr[1]:
>   DY:=DYr[1]:
>    for n from 2 to k do
>       DX:=stack(DX,DXr[n]);
>       DY:=stack(DY,DYr[n])
>    od:
>    D:=concat(DX,DY):
```

Calculate the transpose of the coefficients matrix.

```
>    Dt:=transpose(D):
```

Multiply the coefficients matrix and its transpose .

```
>    DDt:=evalm(D&*Dt):
```

Calculate the inverse matrix of the above .

```
>    iDDt:=evalm(DDt^(-1)):
```

Solve for the coefficents of the Taylor polynomial.

```
>    A:=evalm(iDDt&*D&*P);
```

Wrtie the final Taylor polynomial.

```
>    W:=sort(1000*sum('A[i]*Z[i](x,y)','i'=1..k),[x,y],tdeg);
```

Print the resulted Taylor polynomial coefficient array.

```
>    Ca:=array(1..k):
>    for e from 1 to k do Ca[e]:=DDt[e,e] od:
>    print(Ca);
```

Plot the obtained wavefront surface.

```
> pp:=proc(u,v)  if u^2+v^2<=9 then RETURN(1000*sum('A[i]*Z[i](u,v)','i'=1..k)) else
```

```
> RETURN(0) fi end:
> plot3d(pp,-3..3,-3..3,grid=[70,70],orientation=[-135,0],labels=[x,y,w],color=white,title=Wav
> efront_Identifiation,style=contour,axes=framed);
```

The Followig calculations are to test the fit.

Calculate the transverse ray aberration from the obtained wavefront aberration equation.

```
>    DX_p0:=(x,y)->-sum('A[i]*dzx[i](x,y)','i'=1..k):
>    DY_p0:=(x,y)->-sum('A[i]*dzy[i](x,y)','i'=1..k):
>    DX_p:=zip(DX_p0,r,s):
>    DY_q:=zip(DY_p0,r,s):
>    DX_pq:=concat(DX_p,r):
>    DY_pq:=concat(DY_q,s):
>    D_pq0:=stack(DX_pq,DY_pq):
>    D_p:=col(D_pq0,1):
>    lm:=rowdim(D_pq0):
>    SP:=0:
>    SP2:=0:
>    SDP:=0:
>    SDP2:=0:
>    SPD:=0:
>    for l from 1 to lm do
>       SP:=SP+(-P[l]);
>       SP2:=SP2+(-P[l])*(-P[l]);
>       SDP:=SDP+D_p[l];
>       SDP2:=SDP2+D_p[l]*D_p[l];
>       SPD:=SPD+(-P[l])*D_p[l]
>    od:
>    l:='l':
```

Correlation coefficient:

```
>    cor_r:=(lm*SPD-SP*SDP)/(sqrt(lm*SP2-SP*SP)*sqrt(lm*SDP2-SDP*SDP));
```

R-squred value:

```
>    r_sqr:=cor_r^2;
```

Standard error of prediction:

```
>    STDP:=sqrt(lm*SDP2-SDP*SDP)/lm:
>    S_error_prd:=STDP*sqrt(1-r_sqr);
```

Standard deviation of mesurement:

```
>    stdvpq:=40/3600/180*3.14;
```

Standard error of each obtained Taylor coefficent:

```
>    stderr_ca:=evalf(map((x)->stdvpq/sqrt(x),Ca)):
```

95% confidence interval:

```
>    conl_95up:=zip((x,y)->x+1.96*y,A,stderr_ca):
>    conl_95lo:=zip((x,y)->x-1.96*y,A,stderr_ca):
>    confidence95:=concat(conl_95lo*1000,conl_95up*1000);
```

Appendix V

C programs written for the operation of the 2-dimensional semi-Maxwellian view wavefront aberration measurement system

Fig. A5.1 shows the general structure of the program used in the experiments described in this thesis. The menu and some other parts of the final program was contracted to an agent and finished according to my design. The rest of this appendix is a collection of these sources codes that I wrote.

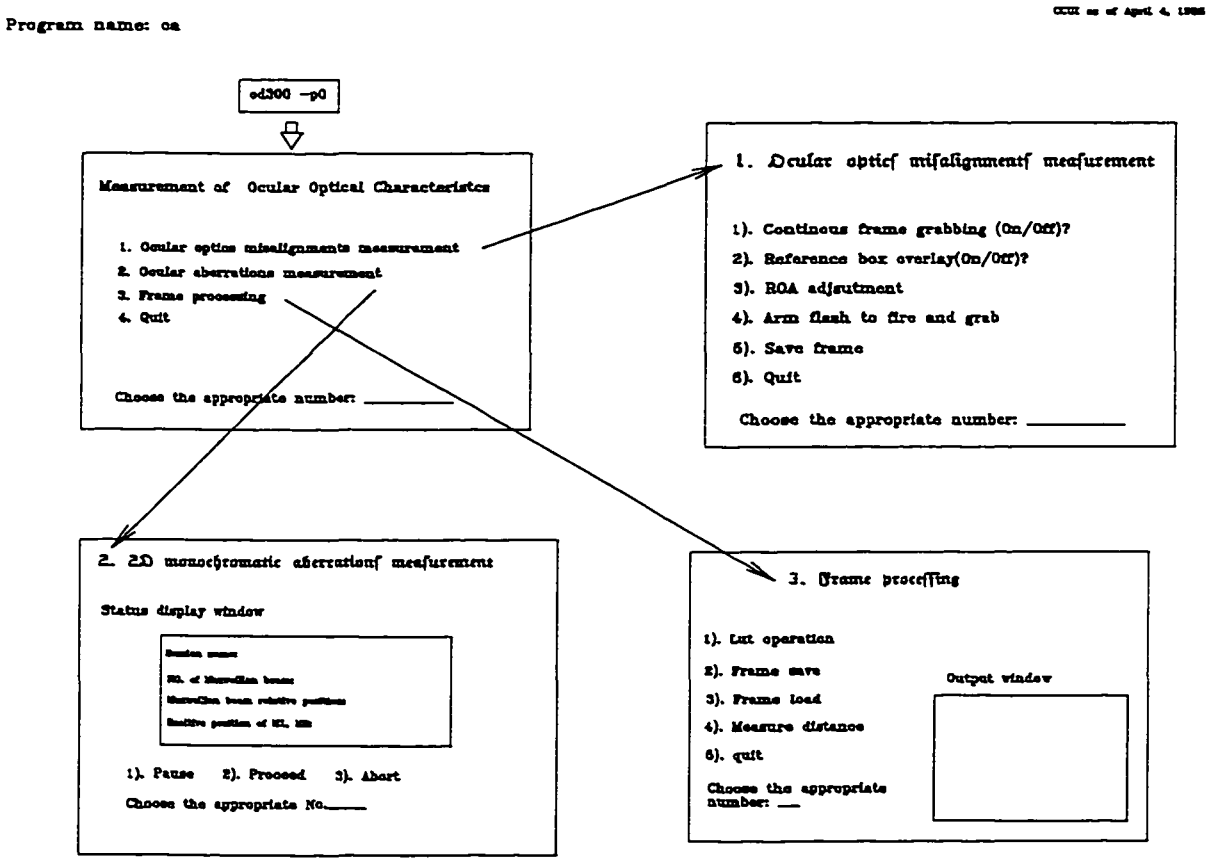


Fig. A5.1 General structure of the program used in this thesis. It consisted of three main parts- aberration measurement; misalignment measurement; frame image processing.

1. ca.c

—This module calls various compiled objects that control the CCD image system for synchronous grabbing, saving, loading, processing and photoflash light firing control. All the codes here were written and tested under Turbo C™ IDE.

```
/*****************************************************
main of "ca" written for cc by cc, March 21, 1995
program calls

        system od300 -p0
        void box_c
        void flash_cf
        int fbsave
        int fbload
        void cur_mef
        system od300 -k
*****************************************************/

#include <odx.h>
#include <opr.h>
#include <stdio.h>
#include <chrono.h>
#include <alloc.h>
static void progress( int y, int ylen)
  {
  int time;
  time = tick();
  printf("Time: %5d ms %3d%% complete\r", time, (int)(y * (long) 100 / ylen));
  }


int main ()
{
int nodx;
int sts_save, sts_load;
char name_save[10], name_load[10];


static char *msg_save[] =
    {
    "PWIN saved to %s",
    "Not enough memory",
    "Cannot create %s",
    "Not enough space to save %s correctly"
    };


static char *msg_load[] =
    {
    "PWIN loaded from %s",
    "Not enough memory",
    "Cannot open %s",
    "Error while reading %s",
```

```
    "Cannot decode this TIFF format"
    };

/** load od300 -p0 **/

system("od300 -p0");

/** check odx **/

nodx=odxbind();
if (nodx<1)
        {
        printf("Cannot Access any ODX Driver\n");
    }

fbgrab (-1); /*start continous grab */
printf("*****Press a key to stop grabbing..\n\n");
getch();
fbgrab(0);

while (opr_inq( FGON)); /*check if grab completed */

/** call box_c function to generate graphic layer **/


box_c();

printf("start continuos grab with box.\n");
fbgrab(-1);/*start continous grabbing*/
printf("press anykey to stop grabbing.\n");
getch();
fbgrab(0);
while(opr_inq(FGON));

/** call flash_cf **/

flash_cf();


/** call fbsave **/
  printf("Please enter name of file to save,\n");
  scanf("%s", &name_save);

  pwin( 0, 0, opr_inq( DWIN_XLEN), opr_inq( DWIN_YLEN));
  printf("press ESC to save full, or choose the right size by mouse and press ESC.\n");
  box( "Xlen: %4d Ylen: %4d Size: %4d Kbytes\r");
  printf("\n");
  init_tick();
  sts_save = fbsave( name_save, progress);
  printf("\n");
  printf( msg_save[sts_save], name_save);
  printf("\n");
  free_tick();

/** call fbload **/
```

```
    printf("To load image, please give name of image\n");
    scanf("%s",name_load);

    pwin( 0, 0, opr_inq( DWIN_XLEN), opr_inq( DWIN_YLEN));
    printf("press ESC to loaded to the full frame, or choose the right size by mouse and press
ESC.\n");
    box( "Xlen: %4d Ylen: %4d Size: %4d Kbytes\r");
    printf("\n");
    init_tick();
    sts_load = fbload( name_load, progress);
    printf("\n");
    printf( msg_load[sts_load], name_load);
    printf("\n");
    free_tick();

  /**call cur_mea**/

  cur_mef();

  system("od300 -k");
  exit (0);
```

2. box_save.c

--The source code of frame saving.

```
/*****************************************************
main of box_save written for cc by cc, March 7, 1995
program calls
        system od300 -p0
        void box_c
        system od300 -k
*****************************************************/

#include <odx.h>
#include <opr.h>
#include <stdio.h>
#include <chrono.h>
#include <alloc.h>
static void progress( int y, int ylen)
  {
  int time;
  time = tick();
  printf("Time: %5d ms %3d%% complete\r", time, (int)(y * (long) 100 / ylen));
}


int main ()
{
int nodx;
```

```
int sts_save, sts_load;
char name_save[10], name_load[10];


static char *msg_save[] =
    {
    "PWIN saved to %s",
    "Not enough memory",
    "Cannot create %s",
    "Not enough space to save %s correctly"
    };


static char *msg_load[] =
    {
    "PWIN loaded from %s",
    "Not enough memory",
    "Cannot open %s",
    "Error while reading %s",
    "Cannot decode this TIFF format"
    };

/** load od300 -p0 **/

system("od300 -p0");

/** check odx **/

nodx=odxbind();
if (nodx<1)
        {
        printf("Cannot Access any ODX Driver\n");
    }

fbgrab (-1); /*start continous grab */
printf("*****Press a key to stop grabbing..\n\n");
getch();
fbgrab(0);

while (opr_inq( FGON)); /*check if grab completed */

/** call box_c function to generate graphic layer **/


box_c();

printf("start continuos grab with box.\n");
fbgrab(-1);/*start continous grabbing*/
printf("press anykey to stop grabbing.\n");
getch();
fbgrab(0);
while(opr_inq(FGON));

/** call flash_cf **/
```

```
flash_cf();

/** call fbsave **/
  printf("Please enter name of file to save,\n");
  scanf("%s", &name_save);

  pwin( 0, 0, opr_inq( DWIN_XLEN), opr_inq( DWIN_YLEN));
  printf("press ESC to save full, or choose the right size by mouse and press ESC.\n");
  box( "Xlen: %4d Ylen: %4d Size: %4d Kbytes\r");
  printf("\n");
  init_tick();
  sts_save = fbsave( name_save, progress);
  printf("\n");
  printf( msg_save[sts_save], name_save);
  printf("\n");
  free_tick();

/** call fbload **/

  printf("To load image, please give name of image\n");
  scanf("%s",name_load);

  pwin( 0, 0, opr_inq( DWIN_XLEN), opr_inq( DWIN_YLEN));
  printf("press ESC to loaded to the full frame, or choose the right size by mouse and press
   ESC.\n");
  box( "Xlen: %4d Ylen: %4d Size: %4d Kbytes\r");
  printf("\n");
  init_tick();
  sts_load = fbload( name_load, progress);
  printf("\n");
  printf( msg_load[sts_load], name_load);
  printf("\n");
  free_tick();

system("od300 -k");
exit (0);
```

3. cur_mef.c

--The source code of image distance measurement.

```
/******************
program by cc for cc to initiate a distance measure routine
march 21, 1995.
get two pints and measure the distance between them.
**********************/
#include <odx.h>
#include <opr.h>
#include <stdio.h>
#include <math.h>

int x, y, grl;
```

```
void cur_mef()
{
extern int x;
extern int y;
int i;
int x1, x2, y1, y2;

x=0;
y=0;

printf("To measure a distance, locate the first point by mouse, if done press 'ESC'\n");
for (i=0;i<2;i++)
{
curs("[x:%4d, y:%4d]\r");

        rmwpix(0,0);

        if(i == 0)
                {
                x1 = x;
                y1 = y;
                sound(400);
                delay(300);
                sound(400);
                nosound();
         printf("locate the second point,  press'ESC'\n");

                }
        else
                {
                x2 = x;
                y2 = y;
                }
};
/*
distance = sqrt(pow((x2-x1),2) + pow((y2-y1),2));
*/
sound(600);
delay(300);
sound(900);
delay(600);
nosound();
printf("the distance is, x:%4d, y:%4d\n", x2-x1, y2-y1);
```

3. box_c.c

--The source code of the reference box generation in video memory of the frame grabbing board.

```
/*****************************************************
```

```
main of box_C written for cc by cc, March 1, 1995
program calls
        system od300 -p0
        void box_c
        system od300 -k
**************************************************/

#include <odx.h>
#include <opr.h>
#include <stdio.h>
extern void box_c();

int main ()
{
int nodx;

/** load od300 -p0 **/

system("od300 -p0");

/** check odx **/

nodx=odxbind();
if (nodx<1)
        {
        printf("Cannot Access any ODX Driver\n");
        return (1);
        }
fbgrab (-1); /*start continous grab */
printf("*****Press a key to stop grabbing..\n\n");
getch();
fbgrab(0);

while (opr_inq( FGON)); /*check if grab completed */

/** call box_c function to generate graphic layer **/

box_c();

fbgrab (-1);

printf("and now, press any key to stop grabbing and end program.\n\n");

getch();
fbgrab(0);

while (opr_inq( FGON));

system("od300 -k");

return 0;
```

4. c_track.c

--The source code of an algorithm and routine for identifying the pupil edge out of a video frame.

```
/******************
Image processing to track the pupil.
For cc by cc as of April 17, 1995.

Add all thresholds control, apr. 19, 1995 by cc.
Fixed a nasty bug and put up a nice menu. april 19, nite, 1995 by cc.
Added the eye blinking compensation function. april 20, 1995 by cc.
******************/


#include <odx.h>
#include <opr.h>
#include <stdio.h>
#include <math.h>
#include <mem.h>
#include <stdlib.h>
int x,y,grl;
main()
{
int i,j;
int k0, k[9];
extern int x,y;
int xc,yc, x0, y0,x0_reset,y0_reset;
int BUFSIZE;
long l;
int THRESHOLD[8];
int grey_medi, grey_level, grey_3, temp_3;
int key;
int counter;
char buf[256];
double pos_x1,pos_x2,pos_y1,pos_y2,center_x,center_y,pos_y;
double square, diameter,diameter_temp;
double cali_x,cali_y;

system("cls");
window(1,1,80,6);
clrscr();
gotoxy(5,2);
cprintf("****************************************");
gotoxy(5,3);
cprintf("PupTrak is working for you from now...");
gotoxy(5,4);
cprintf("Copyright 1995 CCUI. Free for friends to use only.");
gotoxy(5,5);
cprintf("****************************************\n");
sound(500);
delay(400);
sound(900);
delay(400);
```

```
sound(1500);
delay(800);
sound(500);
delay(300);
nosound();


system("od300 -p0");
if (odxbind()<1) exit(1);
window(1,6,80,9);
clrscr();

opr_set(PFB,0);
opr_set(DFB,0);
opr_set(AFB,0);
roa(250,0);

fbgrab(-1);
window(1,7,80,7);
gotoxy(1,7);
cprintf("_____");
window(1,8,80,8);
clrscr();
gotoxy(1,8);
cprintf("Press any key to stop grabbing after camera adjustment...");

window(1,9,80,9);
clrscr();
gotoxy(1,9);
cprintf("Use mouse to locate rough center of pupil, ");
window(1,10,80,10);
clrscr();
gotoxy(1,10);
cprintf("Press'Esc' to start tracking.");
window(1,11,80,11);
clrscr();
gotoxy(1,11);
cprintf("Use NumLoc(On+Off-) and number pad to control");
window(1,12,80,12);
clrscr();
gotoxy(1,12);
cprintf("individual tracking dot to get the nasty edge... Press 'q' to quit");
window(1,13,80,13);
clrscr();
gotoxy(1,13);
cprintf("_____");
getch();
fbgrab(0);

window(1,8,80,8);
clrscr();

window(1,16,80,17);

curs("[x:%4d,y:%4d], grey level %4d\r");
```

```
window(1,16,80,17);
clrscr();

window(1,9,80,10);
clrscr();
window(1,7,80,7);
clrscr();
window(1,9,80,9);
gotoxy(1,9);
cprintf("_____");

cali_x=3.00/102;
cali_y=3.00/127;

k0=60;
x0=x;
y0=y;
x0_reset=x;
y0_reset=y;
counter=0;
diameter_temp =0;
BUFSIZE = 256;


for (j=1;j<9;j++) k[j]=k0;

for(;;)
        {
        fbgrab(1);
        while(opr_inq(FGON));

        sound(1000);
        delay(10);
        nosound();

        if(kbhit())
                {
                key =getch();
                if( key == 0x71)
                {
                window(1,1,80,25);
                clrscr();
                cprintf("Thank you for using CCUI product. Any comment, send to R220.\n");
                break;
                  }
                if(key < 0x40)
                switch (key)
                                {
                                case 0x31:k[6]++;break;
                                case 0x32:k[7]++;break;
                                case 0x33:k[8]++;break;
                                case 0x34:k[5]++;break;
                                case 0x36:k[1]++;break;
                                case 0x37:k[4]++;break;
                                case 0x38:k[3]++;break;
```

```
                                        case 0x39:k[2]++;break;
                                        }
                        if(key >0x40)
                                {
                                        switch (key)
                                        {
                                        case 0x4f:k[6]--;break;
                                        case 0x50:k[7]--;break;
                                        case 0x51:k[8]--;break;
                                        case 0x46:k[5]--;break;
                                        case 0x4d:k[1]--;break;
                                        case 0x47:k[4]--;break;
                                        case 0x48:k[3]--;break;
                                        case 0x49:k[2]--;break;
                                        }
                                }
                        }

                for (j=1;j<9;j++)
                        {
                        amov(x0,y0);
                        rdline(buf,j,BUFSIZE);
                        grey_medi =0;
                        grey_level = 0;
                        temp_3 = 0;
                        grey_3 =0;

                        for(i=0;i<BUFSIZE;i++)
                        grey_medi += (int) buf[i];

                        grey_medi=grey_medi/BUFSIZE;
                        diameter = 0;
                        if(k[j]<1) k[j] = 1;
                        THRESHOLD[j] = grey_medi*10/k[j];

                        for (i=0;i<BUFSIZE; i++)
                                {
                                grey_level =(int) buf[i];
                                grey_3= (int) buf[i-2]+ (int) buf[i+2] + (int) buf[i-1]+(int) buf[i]+(int)
buf[i+1];
                                if(i<5) temp_3 =grey_3;

                                if ( abs(grey_3-temp_3)> THRESHOLD[j])
                                        {
                                        xc=x0;
                                        yc=y0;
                                        l =i;  /* ???????? */
                                        switch(j)
                                                {
                                                case 1: xc+=i;break;
                                                case 2:
                                                        xc+=l;
                                                        yc-=l;
                                                        break;
                                                case 3:yc-=i;break;
```

```
                                        case 4: xc-=l;
                                                yc-=l;
                                                break;
                                        case 5:xc-=i; break;
                                        case 6: xc-=l;
                                                yc+=l;
                                                break;
                                        case 7: yc+=i;break;
                                        case 8:   xc+=l;
                                                yc+=l;
                                                break;
                                        }
                                amov(xc,yc);
                                wtpix(255,0);
                                if( j==1)
                                {
                                pos_x2=(double)xc;
                                pos_y=(double)yc;
                                }
                                if(j==5) pos_x1=(double)xc;
                                if (j==3 )pos_y1=(double)yc;
                                if(j==7) pos_y2=(double)yc;
                                break;
                                }
                        temp_3 = grey_3;
                        }

                }

                center_x=(pos_x2+pos_x1)/2;
                center_y=(pos_y2+pos_y1)/2;
                square = (pos_x2-center_x)*(pos_x2-center_x)+(pos_y-center_y)*(pos_y-
center_y);
                diameter=2*sqrt(square);

                window(10,20, 50,20);
        clrscr();
                gotoxy(5,20);
                cprintf("Pupil center:[%.2f,%.2f]mm", (center_x-256.0)*cali_x,(center_y-
242.0)*cali_y);
                window(10,21,80,21);
                clrscr();
                gotoxy(5,21);
                cprintf("Diameter:[%.2f]mm",diameter*cali_x);

                x0=(int) center_x;
                y0=(int) center_y;

                if(abs(diameter-diameter_temp)>10)
                {
                x0=x0_reset;
                y0=y0_reset;
                }

                counter++;
```

```
                if (counter>20)
                {
                counter=0;
                x0_reset=x0;
                y0_reset=y0;
                }
                diameter_temp=diameter;

        }
system("od300 -k");
window(1,2,80,4);
clrscr();
}
```

5. c_whl_fr.c

--The source code of pupil tracking in real time.

```
/*****************
image processing to monitor eye movement.
for cc by cc as of April 17, 1995.
*****************/


#include <odx.h>
#include <opr.h>
#include <stdio.h>
#include <math.h>
#include <mem.h>
#include <stdlib.h>

main()
{
int i,j;
int grey_level, temp_grey;
char buf[512];

system("od300 -p0");
if (odxbind()<1) exit(1);
opr_set(PFB,0);
opr_set(DFB,0);
opr_set(AFB,0);
roa(70,15);
fbgrab(-1);
printf("press any key to stop grabbing.\n");
getch();
fbgrab(0);
for(;;)
        {
        fbgrab(1);
        while(opr_inq(FGON));
        sound(500);
        delay(50);
```

```
        sound(700);
        delay(100);
        nosound();
        for (j=0;j<484;j++)
                {
                amov(0,j);
                rdline(buf,1,512);
                temp_grey =0;

                for (i=0;i<512;i++)
                        {
                        grey_level =(int) buf[i];

                        if (abs(grey_level-temp_grey) > 10)
                                {
                                amov(i,j);
                                wtpix(255,0);
                                }
                        temp_grey = grey_level;
                        }
                }
}
system("od300 -k");

}
```

6. flash_c

--Source code of photoflash firing and synchronous frame grabbing routine.

```
/*********************
program for cc by on March 8, 1995
to fire the flash gun and grab a picture.
proj.
flash_c.prj(flash_c,tickl.obj,odxcalll.obj)
**********************/

#include <stdio.h>
#include <dos.h>
#include <odx.h>
#include <opr.h>
#include "key.h"

void flash_cf()
{
int base, outval;
char yn;
int video_offset, video_range;

for(;;){

base = 0x378;
outval = 1;
```

```
                /*** adjust offset and range ***/

                printf("current offset=%d, range=%d\n", opr_inq(ROA_OFFSET),
opr_inq(ROA_RANGE));
                printf("new offset=?");
                scanf("%d", &video_offset);
                printf("new range=?");
                scanf("%d", &video_range);
                roa(video_range, video_offset);


                printf("start continous grab. to flash and grab, press the triger\n");
                fbgrab(-1);
                outportb(base,1);
                while(!bioskey(1)&& (inportb(0x379))&8);

                /** check blank period **/
                while(opr_inq(ACQSTATUS) & 8);

                /**fire falsh gun and grab frame **/
                outportb( base, outval+2); /*(0x378,3)*/
                fbgrab(1);

                /** check grabbed frame **/
                printf("if picture acceptable press y key to proceed, press n to repeat.\n");
                scanf("%s", &yn);
                if (yn == 'y')
                break;
           }

        }
```

7. port.c

--Source code for the power control of pupil illumination and the optical shutter.

```
/*****
open 300 watts source for cc by cc, april 26,1995.
*******/
#include <stdio.h>
#include <dos.h>
void light_on()
{
int ctrl_in, ctrl_out;
ctrl_in=inportb(0x37a);
ctrl_out=ctrl_in & 0x1;
outportb(0x37a,ctrl_out);
}

/*****
turn off 300 watts source for cc by cc, april 26,1995.
*******/
```

```
#include <stdio.h>
#include <dos.h>
void light_off()
```

8. Program flow chart of the aberration measurement

–The source codes mostly come with the motion control system from the manufacturer. Fig. A5.2 is the flow chart of the aberration measurement routine.

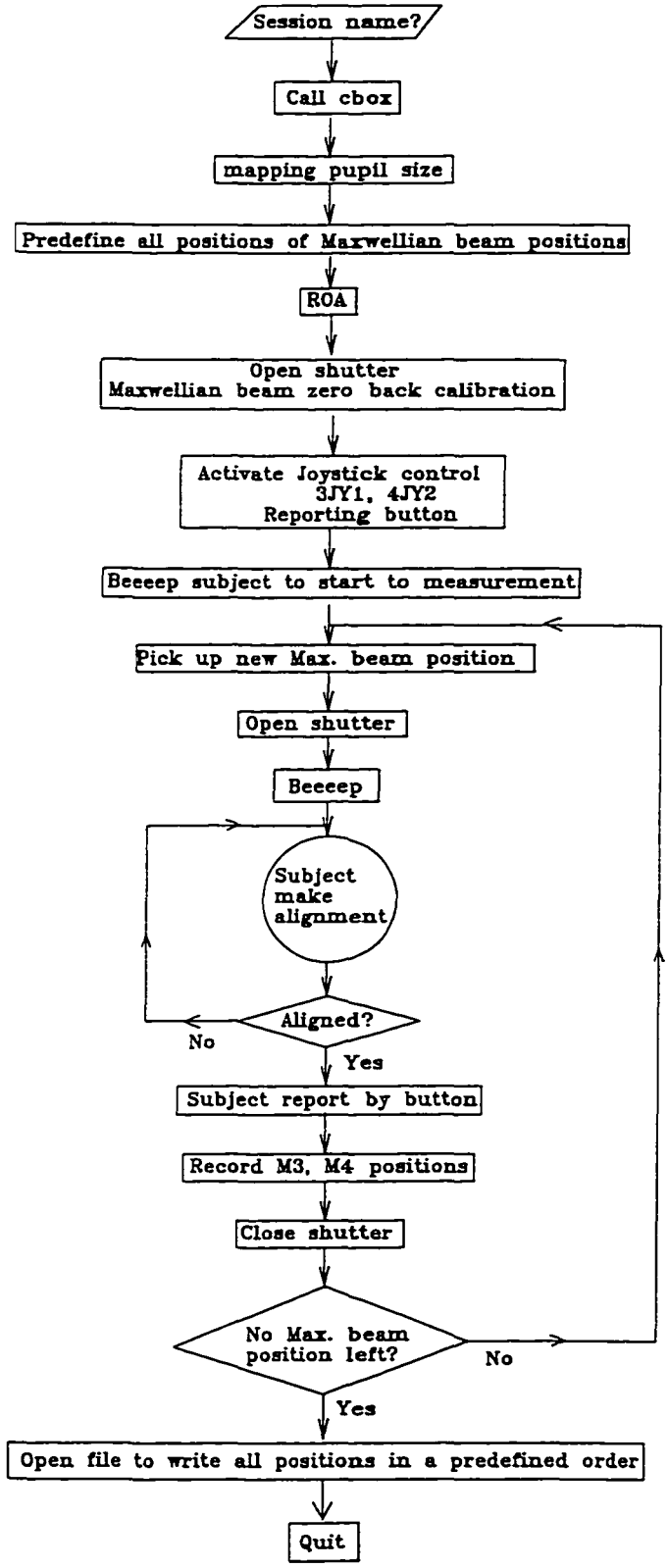


Fig. A5.2 Flow chart of the aberration measurement routine.

Appendix VI

Alignment of the Wavefront Aberration Measurement system

The proper alignment of the system described in Chapter 3 was crucial. When the system was aligned, it had the optical axes of the Maxwellian view channel, the normal view channel and the camera system all coincided. The following procedures describe the alignment of each part of the measurement system as given in Chapter 3.

A6.1 Basic preparation

i) The geometrical centers of all the optical components were marked with an water-based erasable marker either by geometrical measurements or by aligning the reflective images of the optical surfaces.

ii) The positions of all the optical components on the optical table as shown in the system layout diagram were marked. The optical axes of all the optical components were set at a height of 170 mm. Two standard alignment conic pins made with a M6 male thread at the bottom and a sharp conic tip on the top were used to align the optical system. These conic pins were also set at a height of 170 mm.

iii) The light source (PS) was replaced with a Class IIb He-Ne laser tube. By using the alignment conic pins, the laser beam was adjusted by the alignment screws of the laser tube to be parallel to the optical table surface. The laser beam always maintained a beam height of 170 mm. The conic pins were then moved along the specific column of mounting holes. Adjustment of the laser tube was done via the horizontal alignment screw of the laser mount to keep the laser beam intercepting the tips of both pins.

A6.2 Alignment of the Maxwellian view channel

i) The two conic pins were lined up with a row of mounting holes with an appropriate distance between them. Beam splitter BS1 was placed centering around this row of mounting holes and the column of mounting holes where the center of the

Maxwellian view pinhole was adjusted. The beam splitter was rotated and tilted until the beam just intercepted the tips of both pins.

ii) The Maxwellian view pinhole (PH) and the related motorized stages (MS12, MS34) were mounted at positions as shown in the system diagram. The pinhole position was adjusted until the laser beam intercepted the pinhole at the center.

iii) Mirror (M1) was set up at its corresponding position and adjusted until the laser beam intercepted the geometrical center of the mirror. The two conic pins were mounted along the column of mounting holes along which the Maxwellian view lens was to be mounted, one pin was mounted nearer to mirror (M1) and the other was mounted further away from mirror M1. The mirror was adjusted until the laser beam intercepted the tips of both conic pins.

iv) Mirror (M2) was set up as in ii). The mirror position was adjusted so that the laser beam intercepted the geometrical center of the mirror. The two conic pins were mounted along the column of mounting holes along which the center of the camera beam splitter was to be set, one pin was mounted nearer to mirror (M1) and the other was mounted further away. The mirror was adjusted until the laser beam intercepted the tips of both conic pins.

v) The Maxwellian view lens (L4) was set up and adjusted at its designated position so that the laser beam still intercepted the tips of both conic pins..

vi) The Maxwellian view target was set up and adjusted at its designated position so that the laser beam intercepted the target by its center when motorized stage M34 was preset at the middle of its travel range.

A6.3 Alignment of the normal view channel

i) Mirror (M4) was set up and the two conic pins was set up along which lens (L1) was to be mounted. The position of the mirror was adjusted until the reflected beam touched the tips of both alignment conic pins.

ii) The collimating lens (L1) was set up and adjusted until the laser beam intercepted the tips of both conic pins.

iii) Mirror (M5) was set up and the two pins were mounted along the row of mounting holes by which mirror (M5) and mirror (M6) were to be mounted. The positioning of the mirror (M5) was adjusted until the beam intercepted the tips of both conic pins.

iv) Mirror (M6) was set up and the two pins were mounted along the column of mounting holes along which mirror (M3) was to be mounted. The position of the mirror was adjusted until the beam intercepted the tips of both conic pins.

v) Mirror (M3) was set up at its designated position and the two pins were mounted at the column of mounting holes along which the camera beam splitter (BS2) was to be mounted. The position of the mirror was adjusted until the laser beam intercepted the mirror at its center and the beam also intercepted the tips of both conic pins.

vi) Lens (L2) and (L3) were set up as shown in the system diagram and the laser beam reflected by mirror (M3) was kept intercepting the tips of both conic pins after the lens was mounted. The neutral density wedge was positioned at the common focal plane of lens (L2) and (L3).

vii) The normal view target was set up so that the distance from mirror (M3) to the normal view target is the same as the distance of the Maxwellian view target from the mirror (M3). The target was positioned so that the laser beam intercepted the target by its center.

A6.4 Alignment of the camera mount

i) The center mark of the center of rotation of the camera mount was illuminated properly by a special projection lamp.

ii) The camera was set at its shortest focusing distance (31 cm), corresponding screws of the camera mount were adjusted to have the center mark of the rotations of the camera mount at a clear focus and positioned at the center of the screen (256, 242).

iii) The camera was then slid back and the defocused image of the center mark was examined. If the defocused image was not at the center of the screen, screws of the camera mount were adjusted to bring it to superimpose at the center of the screen. Then the camera was set to focus at the center mark of rotations to make sure that the focused image of the center of rotation stayed at the center of the screen. If not, the last two steps were repeated until the image of the center of rotation was always at the center of the screen.

A6.5 Alignment of the camera beam splitter (BS2)

i) The camera beam splitter (BS2) was set up and adjusted until the alignment laser beam intercepted the beam splitter at its geometrical center. The reflective coated surface of the beam splitter was set to face the subject.

ii) The two alignment conic pins were placed along the row of mounting holes going through the position of the beam splitter.

iii) The beam splitter position was adjusted so that the reflected laser beam intercepted the tips of both conic pins.

A6.6 Alignment of the camera beam splitter (BS2) and the camera mount

After camera beam splitter (BS2) was aligned, the camera stand needed to be aligned with beam splitter (BS2).

i) The position of the camera mount was adjusted until the reflected laser beam intercepted the center mark of rotation of the camera mount. The mounting screws of the camera mount were then tightened. After this procedure, the center mark of the camera mount would be no longer at the center of the screen.

ii) The camera stand was slid transversely by the corresponding adjustment micrometer in order to position the center mark of the camera stand to the center of the screen. A screen was placed at the pupil plane of the subject, the laser beam passing through the beam splitter might also be at the center of the screen as shown in Fig. A6.1.

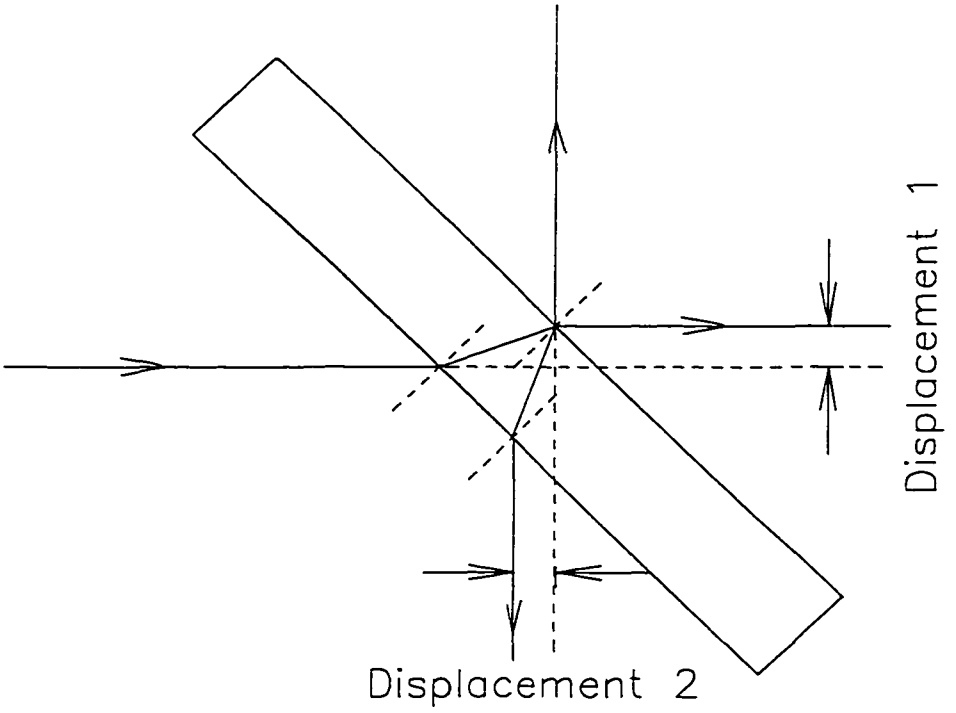


Fig. A6.1 A diagram of beam shift through the beam splitter. The right side the beam splitter was half coated. The Incoming ray was split into two channels and resulted in displacement 1 and 2 in the two channels, respectively. Displacement 1 is equal to displacement 2.

The screen was moved back and forth and the defocused laser spot on the screen would always stay at the center of the screen if the system was well aligned. If not, it most possibly meant that the camera had moved on the camera stand. Finer adjustment of the camera mounting screws were therefore needed to keep the defocused laser spot at the center of the video screen.

iii) The interference filter was removed and the projection light source (PS) was set to a higher output (close to full output). An image of the Maxwellian view pinhole was formed clearly when a white screen was used to receive the image. The camera mount was slid via the micrometer toward the pupil plane until a focused image of the image of the Maxwellian view pinhole was obtained on the video screen.

vi) A customized model eye (see Appendix VII) was placed at the designated eye position. The model eye was moved until the camera captured a clear picture of the pupil of the model eye. By this time, if the arm of the camera stand was rotated, the pupil of the model eye usually was no longer centered at the video screen because the camera might not point at the reflected image of the center of the pupil as intended. The camera stand then needed to be slid parallel to the pupil plane of the subject back and forth, by the corresponding micrometer while keeping the camera focused at the pupil plane of the model eye, until the pupil always stayed at the center of the video screen horizontally when the arm of the camera mount was rotated. Similarly, the camera stand was also moved up and down by the corresponding adjustment knob to keep the pupil of the model eye stay at the center of the video screen vertically when the arm of the camera mount was tilted up and down.

v) The camera mount position was recorded to be the "0" position.

Appendix VII

A Model Eye

To assist the alignment and adjustment of the aberration system and also to test the theoretical models for measuring lens tilt and decentration, a model was built by Mr. Robin Jones of the machine shop according to my specification.

AVII.1 Construction

The cornea of the model was a hard contact lens (Polycon II). The lens is a biconvex lens. Related parameters are given in Table A7.1.

Table A7.1. Parameters of the model eye used in this thesis.

	Refractive Index	Diameter (mm)	Apex thickness (mm)	Power (Diopters)
Cornea	1.48	9.50	0.15	-0.25
Lens	1.52	10.00	4.80	100

The globe of the model eye was made of a steel cylinder. The lens was mounted on a metal arm that could be rotated horizontally. The amount of rotation was precisely controlled by a micrometer. The drawing is given in Fig. A7.1

AVII.1 Calculation of related parameters

In the calculation of the lens tilt and decentration, a single cornea surface was assumed. Therefore, the equivalent radius of curvature of a single surface can be calculated.

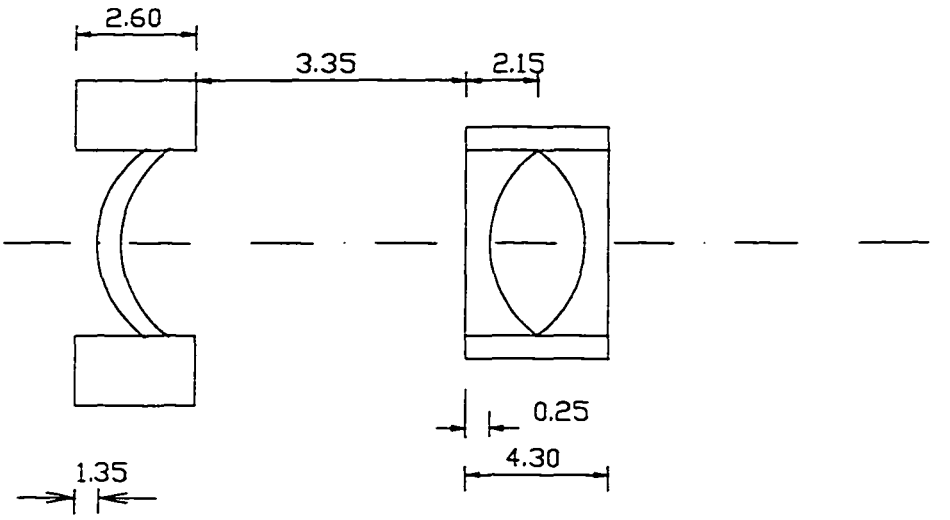


Fig. A7.1 The model eye and its dimensions. The cornea is a rigid contact lens; the lens is a biconvex lens; the contact lens is embedded in the wall of a steel cup; the lens is held by a lens holder via a rigid arm which can be rotated to generate rotation of the lens.

Assume the power of the front surface of the lens is *F1* and the power of the back surface of the contact lens is *F2*, one have,

$$F1 = \frac{n - 1}{r_1} \qquad \text{(AVII.1)}$$

and

$$F2 = \frac{1 - n}{r_2}. \qquad \text{(AVII.2)}$$

where n is the refractive index of the cornea; $r1$ and $r2$ are the radii of the curvature of the two surfaces, respectively.

Because the total power of the eye (F) can be calculated by,

$$F = F1 + F2 - \frac{d}{n} F1F2 \qquad \text{(AVII.3)}$$

The radius of the equivalent single surface was then calculated to be 8.08 mm.

Similar to the calculations related to the cornea, the radius of the bi-convex lens was also calculated. The calculated radii of curvature is to be 8.808 mm.

AVII.3 Parameters of the model eye for lens tilt and calculation

The parameters that will be used in the calculation of lens tilt and decentration is given in Table A7.2

Table A7.2 Parameters of the model eye for the calculation of lens tilt and decentration.

Parameters	Values
d1	4.7mm
d2	3.55mm
d	1.9mm
r1	8.0mm
r2	9.47mm
n1	1
n2	1.333
n3	1.5187

Appendix VIII

Errors Induced by Lens Aberrations

-examined by raytracing through the Maxwellian view lens

To examine the measurement errors that can possibly be induced by the aberrations of the Maxwellian view doublet lens, raytracing via CODE V™ was done. In this appendix, both the direct input and output forms from CODE V™ were included.

A8.1 Calculation of the aberration induced by the achromatic lens when the Maxwellian view pinhole is off-axis(at 5mm).

A8.1.1 The achromatic lens data

LEN1 Lens Data CODE V
Doublet

Surf	Type	Radius	Thickness	Glass/GL1	RMD	Aperture	Dec
OBJ		INFINITY	2000.0000000				
STO		528.52000	12.5000000	BK7_SCHOTT	REFR	50.0594	
2		-456.43000	9.0000000	SF12_SCHOTT	REFR	49.9591	
3		-2083.30000	1987.7305093s			49.9110	
IMG		INFINITY	0.0000000			4.9942	

Effective focal length	1000.3616	Entrance pupil diameter	100.0000
Back focal length	988.5216	Entrance pupil distance	0.0000
Front focal length	-998.4844	Exit pupil diameter	100.1880
F/number	10.0036	Exit pupil distance	-13.7206
Semi-field angle	0.1432	Paraxial image height	4.9942
Image distance	1987.7305	Paraxial image distance	1987.7305
Overall length	21.5000	Lens in mm. - Ref. wavelength	555.0
Reduction ratio	0.9988	Total track	4009.2305
Finite F/number	19.9832	Object distance	2000.0000

Fields/Wavelengths

Field input type: 2 1. Field angle 2. Object height 3.Image height
Number of fields: 2
Y-Object height 0.0 5.0000
X-Object height 0.0 0.0
Number of wavelengths: 1 Reference wavelength number: 1
Wavelengths 555.000
Weights 1
Coating defining wavelength 555.00

A8.1.2 For the principal ray of the Maxwellian view,

a) **<u>When the Maxwellian view pinhole is on axis,</u>**

Single Ray Data

Surface output range: From 0 to 4 Position: ALL Wavelength no. 1
X Y
Actual coordinates on surface 3 0.00000 0.00000

Relative field coordinates OR Field number
X Y
1

Surf	X	Y	Z	TANX	TANY	LENGTH	ET
OBJ	0.00000	0.00000	0.00000	0.00000	0.00000		
STO	0.00000	0.00000	0.00000	0.00000	0.00000	0.00000	
2	0.00000	0.00000	0.00000	0.00000	0.00000	12.50000	
3	0.00000	0.00000	0.00000	0.00000	0.00000	9.00000	
IMG	0.00000	0.00000	0.00000	0.00000	0.00000	1987.73051	
	OPD =	0.000	Waves				

b) **When the Maxwellian view pinhole is 5mm off-axis,**

Single Ray Data

Surface output range: From 0 to 4 Position: ALL Wavelength no. 1

X Y

Actual coordinates on surface 3 0.00000 0.00000

Relative field coordinates OR Field number

X Y

2

Surf	X	Y	Z	TANX	TANY	LENGTH	ET
OBJ	0.00000	5.00000	0.00000	0.00000	-0.00248		
STO	0.00000	0.03441	0.00000	0.00000	-0.00166	0.00000	
2	0.00000	0.01369	0.00000	0.00000	-0.00152	12.50002	
3	0.00000	0.00000	0.00000	0.00000	-0.00251	9.00001	
IMG	0.00000	-4.99424	0.00000	0.00000	-0.00251	1987.73678	
	OPD =	0.000	Waves				

Theoretically, the image position should be at -5.00000 with an tany=-5/2000=0.0025. The induced aberration by the achromatic lens for the position is 0.006mm or an angle difference of -0.0025-(-0.00251)=0.00001 or 2 arc secs.

A8.1.3 For the ray determines the position of the shadow of the target when the alignment is completed

a) When the Maxwellian view pinhole is on axis.

Single Ray Data

Surface output range: From 0 to 4 Position: ALL Wavelength no. 1

X Y

Actual coordinates on surface 3 0.00000 10.00000

Relative field coordinates OR Field number

X Y

1

Surf	X	Y	Z	TANX	TANY	LENGTH	ET
OBJ	0.00000	0.00000	0.00000	0.00000	0.00502		
STO	0.00000	10.04960	0.09555	0.00000	-0.00318	0.09555	
2	0.00000	10.01047	-0.10979	0.00000	-0.00115	12.29472	
3	0.00000	10.00000	-0.02400	0.00000	-0.00503	9.08579	
IMG	0.00000	-0.00250	0.00000	0.00000	-0.00503	1987.77968	
	OPD =	0.006	Waves				

Single Ray Data

Surface output range: From 0 to 4 Position: ALL Wavelength no. 1

X Y

Actual coordinates on surface 3 0.00000 10.00000

Relative field coordinates OR Field number

X Y

2

Surf	X	Y	Z	TANX	TANY	LENGTH	ET
OBJ	0.00000	5.00000	0.00000	0.00000	0.00254		
STO	0.00000	10.08379	0.09620	0.00000	-0.00484	0.09620	
2	0.00000	10.02429	-0.11009	0.00000	-0.00267	12.29385	
3	0.00000	10.00000	-0.02400	0.00000	-0.00754	9.08612	
IMG	0.00000	-4.99564	0.00000	0.00000	-0.00754	1987.81107	
	OPD =	0.003	Waves				

Theoretically, the image position should be at -5.00000 with an tany=(-5-10)/2000=-0.0075. The induced aberration by the achromatic lens for the position is 0.004mm 006mm or an angle difference of -0.0075-(-0.00754)=0.00004 or 9 arc secs.

A8.2 Calculation of the aberrated rays that pass by each of the four Maxwellian view target tips.

Assuming the target is at the center of the lens and the normal view mirror is 1cmx1cm square, the coordinates of the tips are (0,5.0), (5.0,0), (0,-5.0) and (-5.0,0) respectively. The ray positions can be calculated by CODE V™ as follows,

a) **For (0,5.0),**

LEN1 Lens Data CODE V
Doublet

Surf	Type	Radius	Thickness	Glass/GL1	RMD	Aperture	Dec
OBJ		INFINITY	2000.0000000				
STO		528.52000	12.5000000	BK7_SCHOTT	REFR	50.0594	
2		-456.43000	9.0000000	SF12_SCHOTT	REFR	49.9591	
3		-2083.30000	1987.7305093s			49.9110	
IMG		INFINITY	0.0000000			4.9942	

Single Ray Data

Surface output range: From 0 to 4 Position: ALL Wavelength no. 1

	X	Y
Actual coordinates on surface 3	0.00000	5.00000

Relative field coordinates OR Field number

X	Y	
		2

Surf	X	Y	Z	TANX	TANY	LENGTH	ET
OBJ	0.00000	5.00000	0.00000	0.00000	0.00003		
STO	0.00000	5.05935	0.02422	0.00000	-0.00325	0.02422	
2	0.00000	5.01892	-0.02759	0.00000	-0.00210	12.44825	
3	0.00000	5.00000	-0.00600	0.00000	-0.00503	9.02161	
IMG	0.00000	-4.99433	0.00000	0.00000	-0.00503	1987.76163	
	OPD =	0.000	Waves				

The aberration induced by the lens is a distance difference of 0.006mm in y and an angle difference of 6 arc secs in the y direction.

b) **For (0,-5.0)**

Single Ray Data

Surface output range: From 0 to 4 Position: ALL Wavelength no. 1

	X	Y
Actual coordinates on surface 3	0.00000	-5.0000

Relative field coordinates X	Y	OR	Field number
			2

WL 1 SINGLE RAY DATA

Surf	X	Y	Z	TANX	TANY	LENGTH	ET
OBJ	0.00000	5.00000	0.00000	0.00000	-0.00500		
STO	0.00000	-4.99065	0.02356	0.00000	-0.00007	0.02356	
2	0.00000	-4.99147	-0.02729	0.00000	-0.00095	12.44914	
3	0.00000	-5.00000	-0.00600	0.00000	0.00000	9.02130	
IMG	0.00000	-4.99348	0.00000	0.00000	0.00000	1987.73651	
	OPD =	0.001	Waves				

The aberration induced by the lens is a distance difference of 0.007mm in y and an angle difference of 0 arc secs in the y direction.

b) **For (5.0, 0)**

Single Ray Data

Surface output range: From 0 to 4 Position: ALL Wavelength no. 1

X Y

Actual coordinates on surface 3 5.00000 0.00000

Relative field coordinates OR Field number

X Y

2

Surf	X	Y	Z	TANX	TANY	LENGTH	ET
OBJ	0.00000	5.00000	0.00000	0.00251	-0.00248		
STO	5.02500	0.03436	0.02389	-0.00159	-0.00166	0.02389	
2	5.00520	0.01372	-0.02744	-0.00058	-0.00152	12.44870	
3	5.00000	0.00000	-0.00600	-0.00252	-0.00251	9.02146	
IMG	-0.00037	-4.99413	0.00000	-0.00252	-0.00251	1987.74907	
	OPD =	0.000	Waves				

The aberration induced by the lens is a distance difference of 0.0004mm in x, 0.006 in y, an angle difference of 4 arc secs in x and 2 arc secs in y.

d) **For (-5.0, 0)**

Single Ray Data

Surface output range: From 0 to 4 Position: ALL Wavelength no. 1

X Y

Actual coordinates on surface 3 -5.0000 0.00000

Relative field coordinates OR Field number

X Y

2

Surf	X	Y	Z	TANX	TANY	LENGTH	ET
OBJ	0.00000	5.00000	0.00000	-0.00251	-0.00248		
STO	-5.02500	0.03436	0.02389	0.00159	-0.00166	0.02389	
2	-5.00520	0.01372	-0.02744	0.00058	-0.00152	12.44870	
3	-5.00000	0.00000	-0.00600	0.00252	-0.00251	9.02146	
IMG	0.00037	-4.99413	0.00000	0.00252	-0.00251	1987.74907	
	OPD =	0.000	Waves				

UP/DOWN arrows - Scroll | B - Bypass

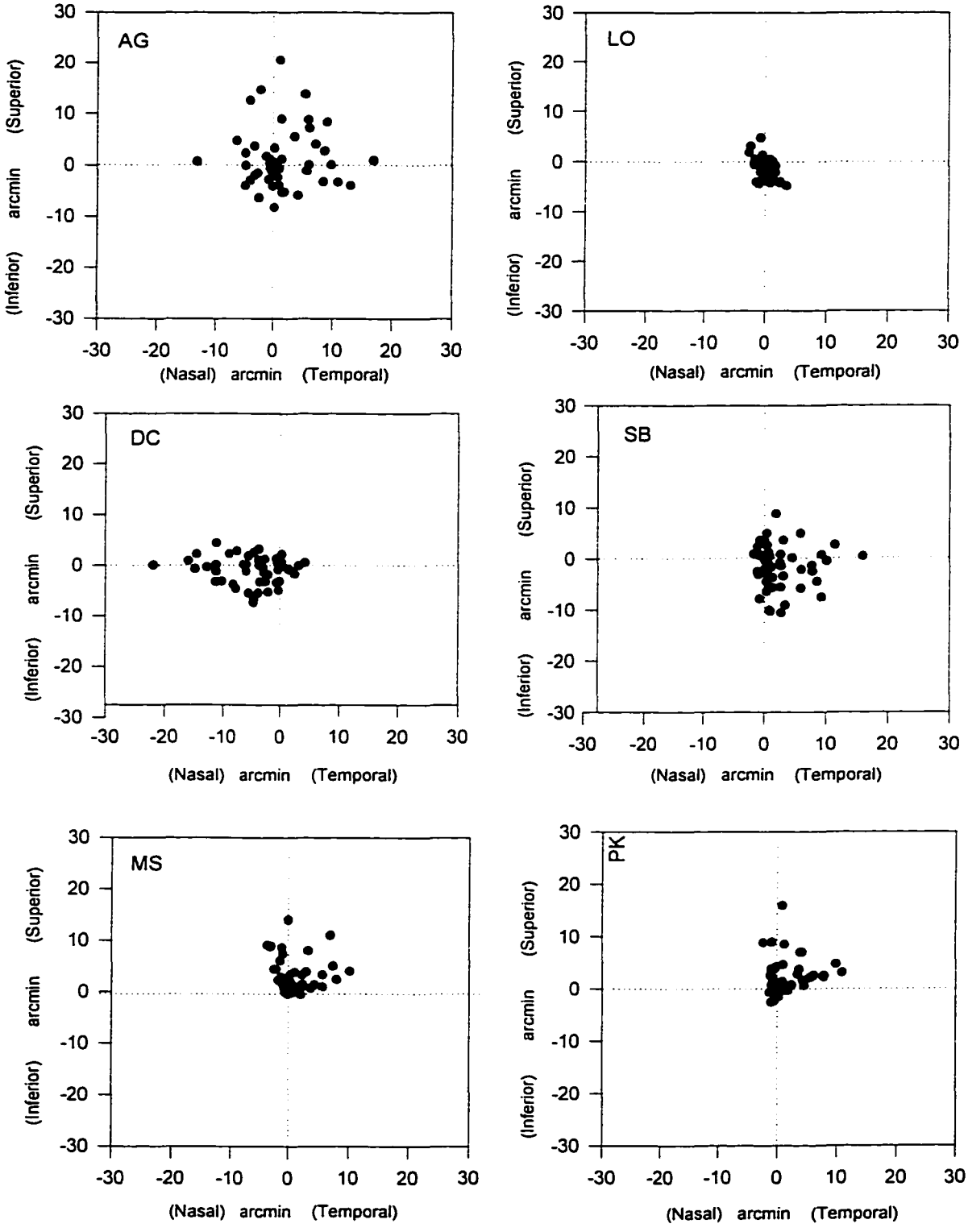
The aberration induced by the lens is a distance difference of 0.0004 in x and 0.006mm in y, an angle difference of 4 arc secs in x and 2 arc secs in y.

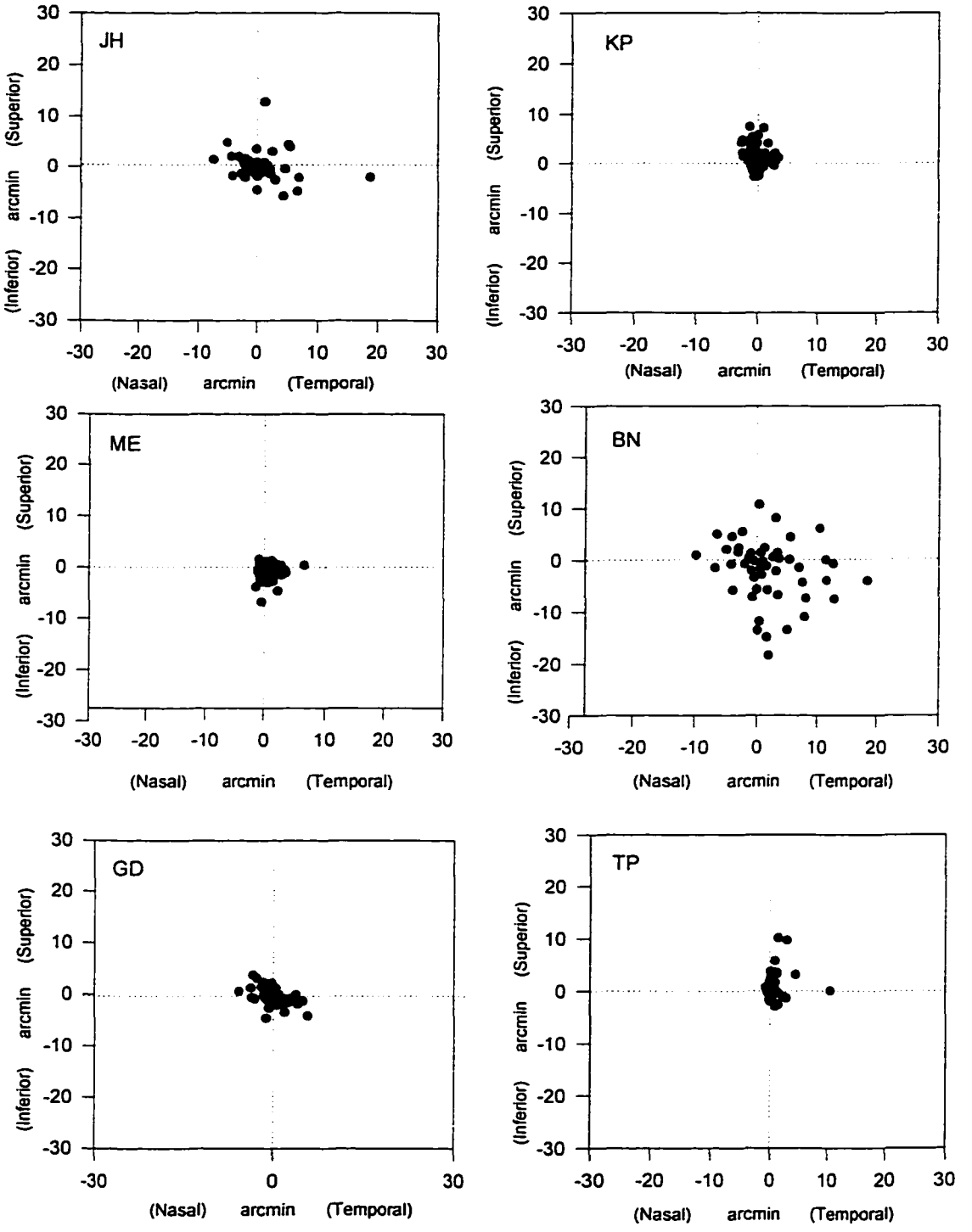
Appendix VIIII

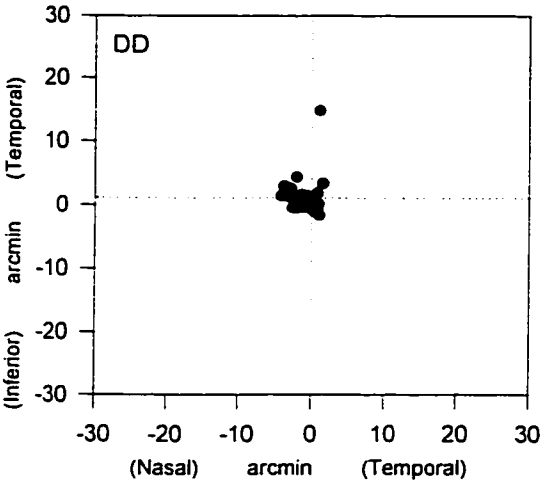
Diagrams of the left eyes of the 21 subjects measured as described in Chapter 4.

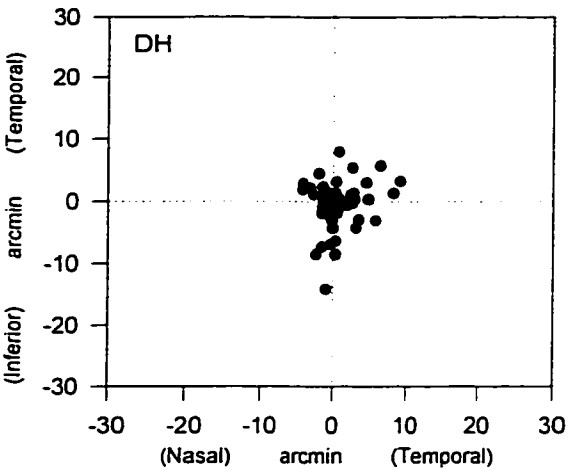
The raw measured data were converted to angle values in arc mins using the same sign convention as that of the pupil coordinate system. Individual eyes are plotted to show the general blur shape. Positive signs denote the temporal side in the horizontal meridian and the superior in the vertical meridian, respectively.

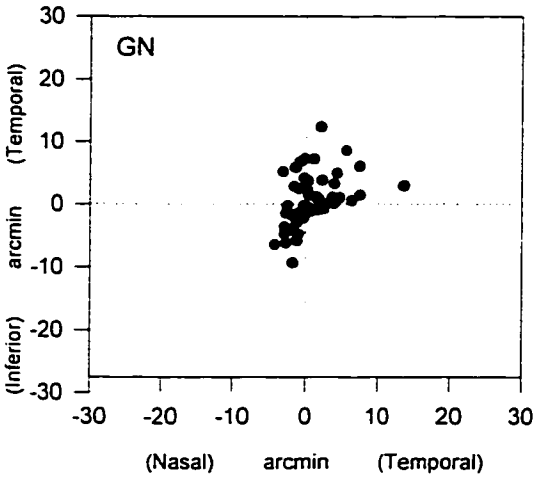
Fig. A9.1 Measured diagrams of the left eyes of 21 subjects (identified by the initials); the sign convention is the same as that of the pupil coordinate system—positive denotes the temporal side of the eye in the horizontal meridian and the superior side of the eye in the vertical meridian, respectively; the scale is in arc mins in both meridians; the ray aberration of each sampling location used is represented by a filled circle on the plots; the general distribution of these circles on each plot therefore reflects the aberration of each eye measured.

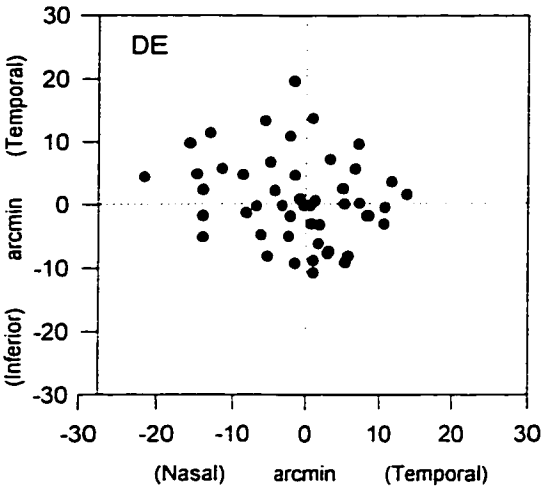

AG
LO
DC
SB
MS
PK
(Superior)
arcmin
(Inferior)
(Nasal) arcmin (Temporal)
30
20
10
0
-10
-20
-30

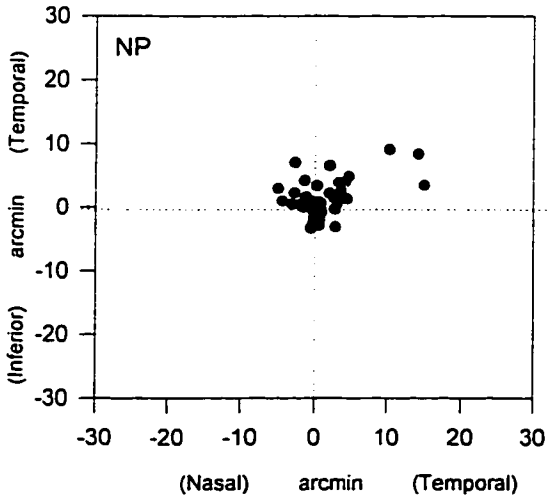

JH
KP
ME
BN
GD
TP
30
20
10
0
-10
-20
-30
(Superior)
arcmin
(Inferior)
(Nasal) arcmin (Temporal)

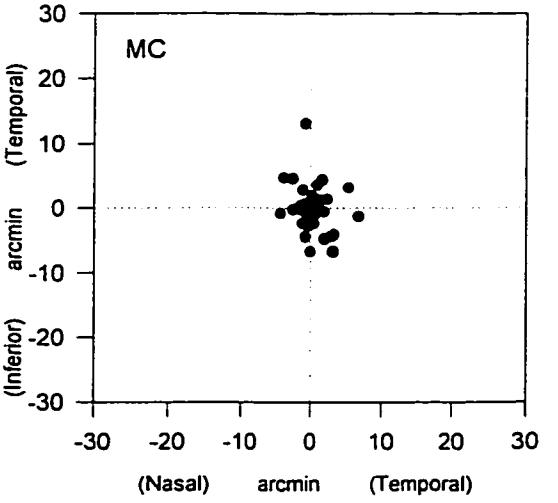

DD
30
20
10
0
-10
-20
-30
(Inferior) arcmin (Temporal)
-30 -20 -10 0 10 20 30
(Nasal) arcmin (Temporal)

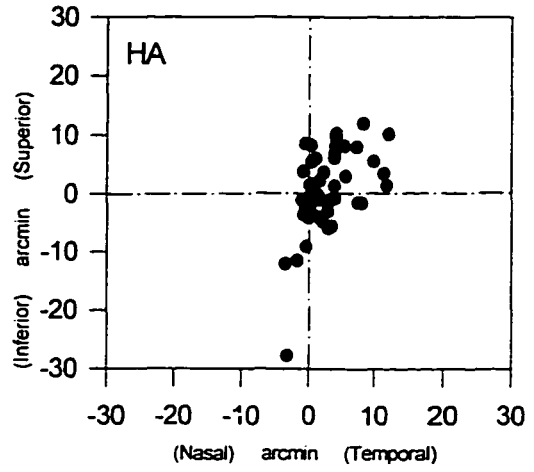

DH
30
20
10
0
-10
-20
-30
(Inferior) arcmin (Temporal)
-30 -20 -10 0 10 20 30
(Nasal) arcmin (Temporal)

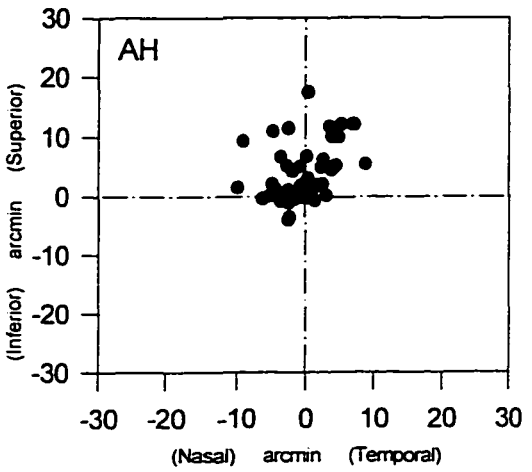

GN
30
20
10
0
-10
-20
-30
(Inferior) arcmin (Temporal)
-30 -20 -10 0 10 20 30
(Nasal) arcmin (Temporal)

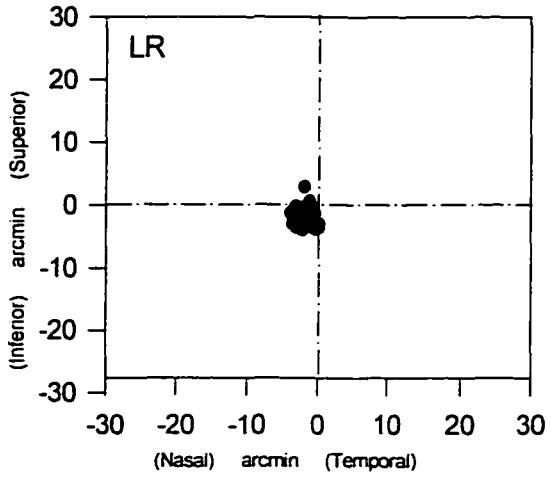

DE
30
20
10
0
-10
-20
-30
(Inferior) arcmin (Temporal)
-30 -20 -10 0 10 20 30
(Nasal) arcmin (Temporal)

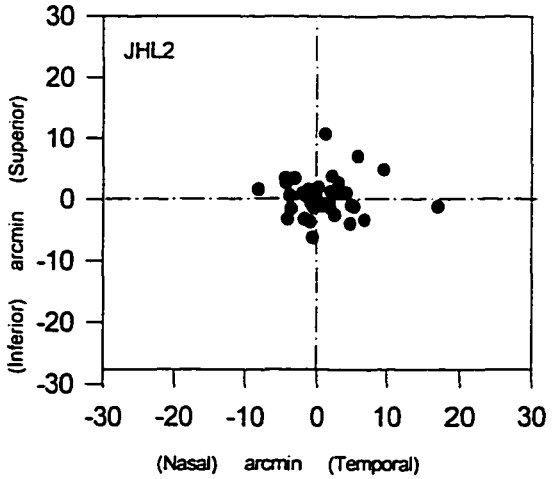

NP
30
20
10
0
-10
-20
-30
(Inferior) arcmin (Temporal)
-30 -20 -10 0 10 20 30
(Nasal) arcmin (Temporal)

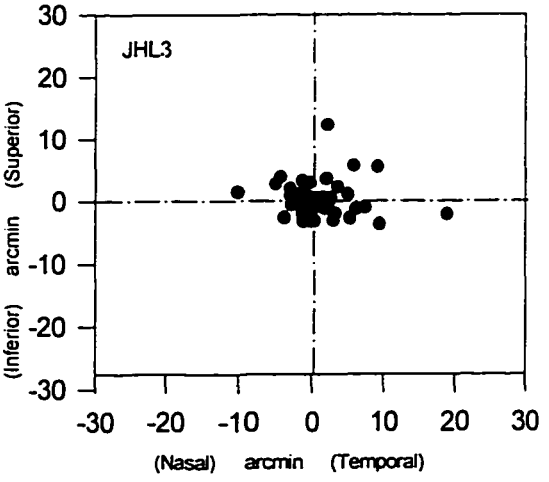

MC
30
20
10
0
-10
-20
-30
(Inferior) arcmin (Temporal)
-30 -20 -10 0 10 20 30
(Nasal) arcmin (Temporal)


HA
30
20
10
0
-10
-20
-30
(Inferior) arcmin (Superior)
-30 -20 -10 0 10 20 30
(Nasal) arcmin (Temporal)


AH
30
20
10
0
-10
-20
-30
(Inferior) arcmin (Superior)
-30 -20 -10 0 10 20 30
(Nasal) arcmin (Temporal)


LR
30
20
10
0
-10
-20
-30
(Inferior) arcmin (Superior)
-30 -20 -10 0 10 20 30
(Nasal) arcmin (Temporal)


JHL2
30
20
10
0
-10
-20
-30
(Inferior) arcmin (Superior)
-30 -20 -10 0 10 20 30
(Nasal) arcmin (Temporal)


JHL3
30
20
10
0
-10
-20
-30
(Inferior) arcmin (Superior)
-30 -20 -10 0 10 20 30
(Nasal) arcmin (Temporal)

Appendix X

Wavefront Reconstruciton from Ray Aberraiton Data to a 6th order Zernike Polynomial

---

Set numerical precision to 10 digits after the decimal place.

```
> Digits:=10:
```

Inlude Maple linear algebra library.

```
> with(linalg):
```

Call read data matrix function.

```
> readlib(readdata):
```

Read in the experimental data array.

```
> Mdat:=readdata(experimental_datafile,float,5):
```

Set the total number of terms of the Zernike polynomial.

```
> k:=27:
```

Split experimental data array to (r, s) sampling locations in mm and (p0,q0) tansverse ray aberrration in mm, respectively.

```
> r:=col(Mdat,2):
> s:=col(Mdat,3):
```

Convert transverse ray aberrations to arc secs and convert the sign convention to that of pupil locations(superior is "+", left is "+").

```
> p0:=col(-Mdat/1980,4):
> q0:=col(-Mdat/1980,5):
```

Stack the horizontal and vertical components of transverse ray aberration to form the transverse aberration vector "P". (Becasue the "stack" function only work for more than 2 columns, "p1" and "p2" are concatenated with "r" and "s" respectively to form arrays of 2 columns).

```
> p1:=concat(r,p0):
> q1:=concat(s,q0):
> pq:=stack(p1,q1):
> P:=col(-pq,2):
```

Setup terms of Zernike polynomials up to the 27th term. "Z" refers to a Zernike polynomial term, the index is the index of the corresponding Zernike polynomial term.

The following matrix operations are used to calculate the coefficient matrix of the equation(See theoretical part) to solve for the coefficents of Zernike polynomials from partial derivatives of Zernike polynomials terms at all the pupil sample locations.

Calculate the partial derivative of each Zernike polynomial term in both the horizontal and vertical directions.

```
> nr:=3.0:
> Z[1]:=(x,y)->2*x/nr:
> Z[2]:=(x,y)->2*y/nr:
> Z[3]:=(x,y)->3^(0.5)*(2*(x^2+y^2)/nr^2-1):
> Z[4]:=(x,y)->2*6^(0.5)*x*y/nr^2:
> Z[5]:=(x,y)->6^(0.5)*(x^2-y^2)/nr^2:
> Z[6]:=(x,y)->8^(0.5)*y/nr*(3*(x^2+y^2)/nr^2-2):
> Z[7]:=(x,y)->8^(0.5)*x/nr*(3*(x^2+y^2)/nr^2-2):
> Z[8]:=(x,y)->8^(0.5)*y/nr*(3*x^2-y^2)/nr^2:
> Z[9]:=(x,y)->8^(0.5)*x/nr*(x^2-3*y^2)/nr^2:
> Z[10]:=(x,y)->5^(0.5)*(6*(x^2+y^2)^2/nr^4-6*(x^2+y^2)/nr^2+1):
> Z[11]:=(x,y)->10^(0.5)*(2*(x^2+y^2)/nr^2-3)*(x^2-y^2)/nr^2:
> Z[12]:=(x,y)->10^(0.5)*x*y/nr^2*(4*(x^2+y^2)/nr^2-3):
> Z[13]:=(x,y)->10^(0.5)*((x^2+y^2)^2-8*x^2*y^2)/nr^4:
```

```
> Z[14]:=(x,y)->4*10^(0.5)*x*y*(x^2-y^2)/nr^4:
> Z[15]:=(x,y)->12^(0.5)*x/nr*(10*(x^2+y^2)^2/nr^4-12*(x^2+y^2)/nr^2+3):
> Z[16]:=(x,y)->12^(0.5)*y/nr*(10*(x^2+y^2)^2/nr^4-12*(x^2+y^2)/nr^2+3):
> Z[17]:=(x,y)->12^(0.5)*x/nr*(5*(x^2+y^2)/nr^2-4)*(4*x^2/nr^2-3):
> Z[18]:=(x,y)-> 12^(0.5)*y/nr*(5*(x^2+y^2)/nr^2-4)*(3-4*y^2/nr^2):
> Z[19]:=(x,y)->12^(0.5)*x/nr*(16*x^4-20*x^2*(x^2+y^2)+5*(x^2+y^2)^2)/nr^4:
> Z[20]:=(x,y)->12^(0.5)*y/nr*(16*x^4-12*x^2*(x^2+y^2)+(x^2+y^2)^2)/nr^4:
> Z[21]:=(x,y)->7^(0.5)*(20*(x^2+y^2)^3/nr^6-30*(x^2+y^2)^2/nr^4+12*(x^2+y^2)/nr^2-1):
> Z[22]:=(x,y)->2*14^(0.5)*x*y/nr^2*(15*(x^2+y^2)^2/nr^4-2*(x^2+y^2)/nr^2+6):
> Z[23]:=(x,y)->14^(0.5)*(15*(x^2+y^2)^2/nr^4-2*(x^2+y^2)/nr^2+6)*(x^2-y^2)/nr^2:
> Z[24]:=(x,y)->4*14^(0.5)*x*y/nr^2*(6*(x^2+y^2)/nr^2-5)*(x^2-y^2)/nr^2:
> Z[25]:=(x,y)->14^(0.5)*(6*(x^2+y^2)/nr^2-5)*((x^2+y^2)^2-8*x^2*y^2)/nr^4:
> Z[26]:=(x,y)->2*14^(0.5)*x*y/nr^2*(-16*x^2*y^2+3*(x^2+y^2)^2)/nr^4:
> Z[27]:=(x,y)->14^(0.5)*(32*x^6-48*x^4*(x^2+y^2)+18*x^2*(x^2+y^2)^2-(x^2+y^2)^3)/nr^6:
>    dzx:=map(D[1],Z):
>    dzy:=map(D[2],Z):
```

To reset the index for arrays to cope with Maple internal index management bug.

```
>    m:='m':
>    n:='n':
```

Calculate the values of the partial derivative of each Zernike polynomial term at each pupil sampling locations in both the horizontal and vertical directions.

```
>   for m to k  do
>      DXr[m]:=zip(dzx[m],r,s);
>      DYr[m]:=zip(dzy[m],r,s)
>   od:
```

Assemble the coefficients matrix by stacking(The first row is set first for the horizontal and vertical component, respectively. The first rows are then stacked with the above calculated values till the last Zernike polynomial term. The resulted horizontal and vertical matrix are then concatenated to form the coefficent matrix.

```
>   DX:=DXr[1]:
>   DY:=DYr[1]:
>    for n from 2 to k do
>       DX:=stack(DX,DXr[n]);
>       DY:=stack(DY,DYr[n])
>    od:
>    D:=concat(DX,DY):
```

Calculate the transpose of the coefficients matrix.

```
>    Dt:=transpose(D):
```

Multiply the coefficients matrix and its transpose .

```
>    DDt:=evalm(D&*Dt):
```

Calculate the inverse matrix of the above .

```
>    iDDt:=evalm(DDt^(-1)):
```

Solve for the coefficents of the Zernike polynomial.

```
>    A:=evalm(iDDt&*D&*P);
> save A, zdh:
```

Wrtie the final Zernike polynomial.

```
>    W:=sort(1000*sum('A[i]*Z[i](x,y)','i'=1..k),[x,y],tdeg);
```

Print the resulted Zernike polynomial coefficient array.

```
>    Ca:=array(1..k):
>    for e from 1 to k do Ca[e]:=DDt[e,e] od:
>    print(Ca);
```

Plot the obtained wavefront surface.

```
> pp:=proc(u,v)  if u^2+v^2<=9 then RETURN(1000*sum('A[i]*Z[i](u,v)','i'=1..k)) else
> RETURN(0) fi end:
> plot3d(pp,-3..3,-3..3,grid=[70,70],contours=[-5.5,-4.4,-3.85,-3.3,-2.75,-2.2,-1.65,-1.1,-0.55,
> 0,0.55,1.1,1.65,2.2,2.75,3.3,3.85,4.4,4.95,5.5,6.05,6.60,7.15,7.70,8.25,8.80],orientation=
> [-135,0],labels=[x,y,w],color=white,title=MeasurementIdentification,style=contour,axes=fr
> amed);

>
```

The Followig calculations are to test the fit.

Calculate the transverse ray aberration from the obtained wavefront aberration equation.

```
>    DX_p0:=(x,y)->-sum('A[i]*dzx[i](x,y)','i'=1..k):
>    DY_p0:=(x,y)->-sum('A[i]*dzy[i](x,y)','i'=1..k):
>    DX_p:=zip(DX_p0,r,s):
>    DY_q:=zip(DY_p0,r,s):
>    DX_pq:=concat(DX_p,r):
>    DY_pq:=concat(DY_q,s):
>    D_pq0:=stack(DX_pq,DY_pq):
>    D_p:=col(D_pq0,1):
>    lm:=rowdim(D_pq0):
>    SP:=0:
>    SP2:=0:
>    SDP:=0:
>    SDP2:=0:
>    SPD:=0:
>    for l from 1 to lm do
>       SP:=SP+(-P[l]);
>       SP2:=SP2+(-P[l])*(-P[l]);
>       SDP:=SDP+D_p[l];
>       SDP2:=SDP2+D_p[l]*D_p[l];
>       SPD:=SPD+(-P[l])*D_p[l]
>    od:
>    l:='l':
```

Correlation coefficient:

```
>    cor_r:=(lm*SPD-SP*SDP)/(sqrt(lm*SP2-SP*SP)*sqrt(lm*SDP2-SDP*SDP));
```

R-squred value:

```
>    r_sqr:=cor_r^2;
```

Standard error of prediction:

```
>    STDP:=sqrt(lm*SDP2-SDP*SDP)/lm:
>    S_error_prd:=STDP*sqrt(1-r_sqr);
```

Standard deviation of mesurement:

```
>    stdvpq:=40/3600/180*3.14;
```

Standard error of each obtained Taylor coefficents:

```
>    stderr_ca:=evalf(map((x)->stdvpq/sqrt(x),Ca)):
```

95% confidence interval:

```
>    conl_95up:=zip((x,y)->x+1.96*y,A,stderr_ca):
>    conl_95lo:=zip((x,y)->x-1.96*y,A,stderr_ca):
>    confidence95:=concat(conl_95lo*1000,conl_95up*1000);
```

Appendix XI

The Use of a Telecentric Stop

Because PIII is not formed at the same image plane as PI and PIV, PIII will be defocused when the camera is focused at the pupil plane. The relative position of PIII will not be at the same position due to defocus. An effective solution is to construct a telecentric stop at the secondary focal plane of the camera lens as shown in Fig. A11.1 (Smith, 1990; Philips, 1988).

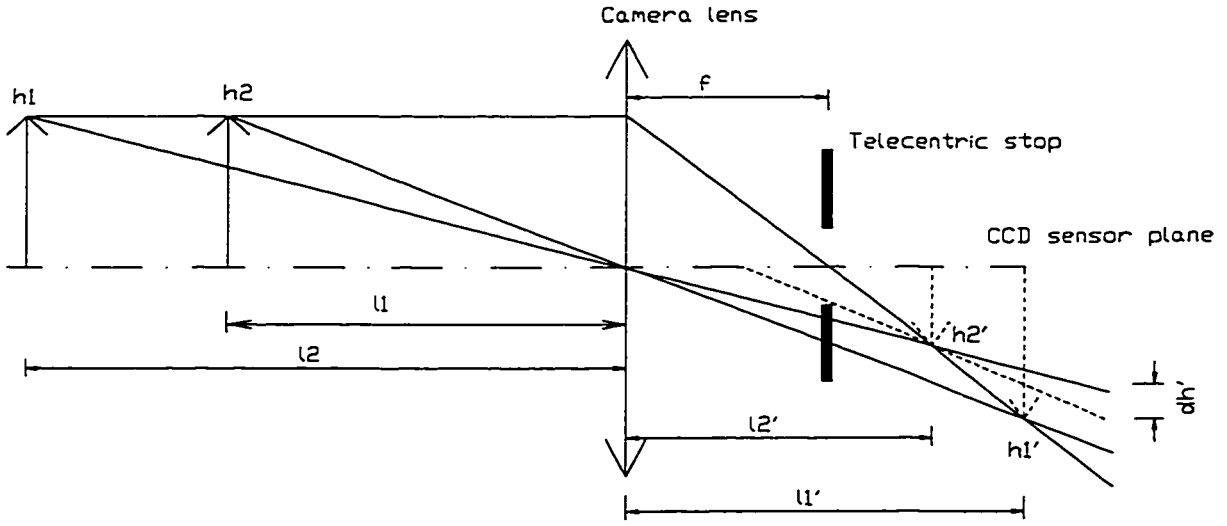


Fig. A11.1 A telecentric stop inside a camera lens set. The telecentric stop only allows rays from the object parallel to the optical axis of the camera lens pass through to the CCD, therefore objects of the same heights will always have the same image height regardless of where they are viewed.

Object *h1* and *h2* are of the same heights but are at different distances from the lens system. When the camera lens system is focused at object *h1*, the image *h2'* of object *h2* will be defocused at the imaging receiving plane. If the telecentric stop is ideally small, the image height of *h1* at the detector plane should be of the same size as the image height of *h1*. If the telecentric stop is not ideally small, there will be a difference of *dh'*. The theoretical limit of the size of the telecentric stop can therefore be determined by the tolerance of *dh'* which is determined by the resolution of the camera system.

The maximum diameter(*D*) of the telecentric stop can be derived from Fig. AXI.1 as,

$$D = 4 * \text{resolution of camera system} * \frac{l1 - f}{l2 - l1} \qquad \text{(AXI.1)}$$

Appendix XII

QuickBasic™ Programs for the Calculation of Mean Squared Wavefront Aberrations

A12.1 Extraction of polynomial (any order) coefficients from the special Maple output format for one measurement

```
DIM dum$, dum0$, dum1$
DIM i, j, k, l, m
DIM rr(100) AS SINGLE
DIM dumfile AS STRING
    CLS
    PRINT "Enter maple coef file name."
    INPUT dumfile
    OPEN dumfile FOR INPUT AS #3

    dum$ = ""
    DO
        LINE INPUT #3, dum1$
        dum$ = dum$ + dum1$
    LOOP UNTIL EOF(3)
    CLOSE #3
    PRINT
    PRINT "Enter number of polynomial terms."
    INPUT m
    PRINT
    PRINT "Enter sorted coef file to save."
    INPUT dumfile

    'open "sorted coefficients output file"
    OPEN dumfile FOR OUTPUT AS #4
    FOR i = 1 TO m
        dum0$ = "(" + RIGHT$(STR$(i), LEN(STR$(i)) - 1) + ")="
        j = INSTR(dum$, dum0$)
        dum1$ = RIGHT$(dum$, LEN(dum$) - j)
        k = INSTR(dum1$, ",")
        rr(i) = VAL(MID$(dum$, j + LEN(dum0$), k + j))
        PRINT #4, rr(i)
    NEXT i
    CLOSE #4
    PRINT : PRINT "Sort complete. Saved as "; dumfile
END
```

AXII.2 Extraction of polynomial (6th order) coefficients from special Maple output format for 21 measurements

```
DIM dum$, dum0$, dum1$
DIM i, j, k, l
DIM rr(27) AS SINGLE
FOR l = 1 TO 21

    OPEN "sub" + RIGHT$(STR$(l), LEN(STR$(l)) - 1) FOR INPUT AS #3
    CLS
    dum$ = ""
    DO
        LINE INPUT #3, dum1$
        dum$ = dum$ + dum1$
    LOOP UNTIL EOF(3)
    CLOSE #3
     OPEN "Sub" + RIGHT$(STR$(l), LEN(STR$(l)) - 1) + ".dat" FOR OUTPUT AS #4
    FOR i = 1 TO 27
```

```
        dum0$ = "(" + RIGHT$(STR$(i), LEN(STR$(i)) - 1) + ")="
        j = INSTR(dum$, dum0$)
        dum1$ = RIGHT$(dum$, LEN(dum$) - j)
        k = INSTR(dum1$, ",")
        rr(i) = VAL(MID$(dum$, j + LEN(dum0$), k + j))
        PRINT #4, rr(i)
    NEXT i
    CLOSE #4
NEXT l
END
```

A12.3 Calculation of mean squared wavefront aberrations from fitted Taylor polynomials. The program was set to calculate the symmetrical component of the total wavefront aberration. The total mean squared wavefront aberration and the asymmetrical component can be calculated by a minor modification of the program

```
DECLARE FUNCTION wav! (x AS SINGLE, y AS SINGLE)
DIM i, j, l
DIM x0 AS SINGLE
DIM y0 AS SINGLE
DIM SHARED A(27) AS SINGLE
DIM p AS SINGLE
DIM d AS SINGLE
DIM sumw AS SINGLE
DIM sumw0 AS SINGLE
p = 3
d = .01
CLS
'OPEN "rs_sphr1.dat" FOR OUTPUT AS #4

FOR l = 1 TO '21
    OPEN "sub" + RIGHT$(STR$(l), LEN(STR$(l)) - 1) + ".dat" FOR INPUT AS #1
    FOR i = 1 TO 27
        INPUT #1, A(i)
    NEXT i
    CLOSE #1
    sumw = 0
    sumw0 = 0
    FOR y0 = -p TO p STEP d
        FOR x0 = -SQR(p ^ 2 - y0 ^ 2) TO SQR(p ^ 2 - y0 ^ 2) STEP d
            sumw = sumw + (1000 * wav(x0, y0)) ^ 2 * d * d
            sumw0 = sumw0 + 1 * d * d
        NEXT x0
    NEXT y0
    sumw = sumw / sumw0

    PRINT #4, sumw
NEXT l
CLOSE #4

FUNCTION wav (x AS SINGLE, y AS SINGLE)
'All components
'wav = A(6) * x ^ 3 + A(7) * x ^ 2 * y + A(8) * x * y ^ 2 + A(9) * y ^ 3 + A(10) * x ^ 4 + A(11) * x ^ 3 * y + A(12) * x
^ 2 * y ^ 2 + A(13) * x * y ^ 3 + A(14) * y ^ 4 + A(15) * x ^ 5 + A(16) * x ^ 4 * y + A(17) * x ^ 3 * y ^ 2 + A(18) * x ^
2 * y ^ _
```

```
 3 + A(19) * x * y ^ 4 + A(20) * y ^ 5 + A(21) * x ^ 6 + A(22) * x ^ 5 * y + A(23) * x ^ 4 * y ^ 2 + A(24) * x ^ 3 * y ^ 3
+ A(25) * x ^ 2 * y ^ 4 + A(26) * x * y ^ 5 + A(27) * y ^ 6
'Asymmetrical component
'wav = A(6) * x ^ 3 + A(7) * x ^ 2 * y + A(8) * x * y ^ 2 + A(9) * y ^ 3 + A(15) * x ^ 5 + A(16) * x ^ 4 * y + A(17) * x
^ 3 * y ^ 2 + A(18) * x ^ 2 * y ^ 3 + A(19) * x * y ^ 4 + A(20) * y ^ 5
'Symmetricl component
wav = A(10) * x ^ 4 + A(11) * x ^ 3 * y + A(12) * x ^ 2 * y ^ 2 + A(13) * x * y ^ 3 + A(14) * y ^ 4 + A(21) * x ^ 6 +
A(22) * x ^ 5 * y + A(23) * x ^ 4 * y ^ 2 + A(24) * x ^ 3 * y ^ 3 + A(25) * x ^ 2 * y ^ 4 + A(26) * x * y ^ 5 + A(27) * y
^ 6
END FUNCTION
```

A12.4 Calculation of mean squared wavefront aberrations from fitted Taylor polynomials after pupil shift. The program was set to calculate the symmetrical component of the total wavefront aberration. The total mean squared wavefront aberration and the asymmetrical component can be calculated by a minor modification of the program.

```
DECLARE FUNCTION wav! (x AS SINGLE, y AS SINGLE)
DIM i, j, l
DIM x0 AS SINGLE
DIM y0 AS SINGLE
DIM A(27) AS SINGLE
DIM SHARED b(27) AS SINGLE
DIM p AS SINGLE
DIM d AS SINGLE
DIM sumw AS SINGLE
DIM sumw0 AS SINGLE
DIM DX(21) AS SINGLE
DIM dy(21) AS SINGLE

OPEN "ps_x.txt" FOR INPUT AS #2   'Load horizontal pupil shift data
FOR i = 1 TO 21
    INPUT #2, DX(i)
NEXT i
DX(1) = .403
CLOSE #2

OPEN "ps_y.txt" FOR INPUT AS #3   'Load vertical pupil shift data
FOR i = 1 TO 21
    INPUT #3, dy(i)
NEXT i
dy(1) = -.195
CLOSE #3

CLS
'---Calculate reference shifted coefficients.
FOR l = 1 TO 21
    'Load coefficients of the Taylor polynomial of each subject.
    OPEN "sub" + RIGHT$(STR$(l), LEN(STR$(l)) - 1) + ".dat" FOR INPUT AS #1
    FOR i = 1 TO 27
        INPUT #1, A(i)
    NEXT i
    CLOSE #1
    'Calculate the shift transformed new Taylor coefficients.

    b(0) = A(16) * DX(l) ^ 4 * dy(l) + A(15) * DX(l) ^ 5 + A(26) * DX(l) * dy(l) ^ 5 + A(20) * dy(l) ^ 5 + A(21) *
DX(l) ^ 6 + A(27) * dy(l) ^ 6 + A(19) * DX(l) * dy(l) ^ 4 + A(7) * DX(l) ^ 2 * dy(l) + A(8) * DX(l) * dy(l) ^ 2 + A(11)
* DX(l) ^ _
```

```
3 * dy(l) + A(18) * DX(l) ^ 2 * dy(l) ^ 3 + A(13) * DX(l) * dy(l) ^ 3 + A(12) * DX(l) ^ 2 * dy(l) ^ 2 + A(24) * DX(l) ^
3 * dy(l) ^ 3 + A(22) * DX(l) ^ 5 * dy(l) + A(17) * DX(l) ^ 3 * dy(l) ^ 2 + A(25) * DX(l) ^ 2 * dy(l) ^ 4 + A(23) *
DX(l) ^ 4 *
dy(l) ^ 2 + A(4) * DX(l) * dy(l) + A(1) * DX(l) + A(2) * dy(l) + A(3) * DX(l) ^ 2 + A(5) * dy(l) ^ 2 + A(6) * DX(l) ^ 3
+ A(9) * dy(l) ^ 3 + A(10) * DX(l) ^ 4 + A(14) * dy(l) ^ 4
    b(1) = 3 * A(6) * DX(l) ^ 2 + A(26) * dy(l) ^ 5 + 3 * A(24) * DX(l) ^ 2 * dy(l) ^ 3 + 2 * A(25) * DX(l) * dy(l) ^ 4
+ A(13) * dy(l) ^ 3 + 2 * A(3) * DX(l) + 5 * A(15) * DX(l) ^ 4 + 4 * A(16) * DX(l) ^ 3 * dy(l) + 3 * A(11) * DX(l) ^ 2
* dy(l _
) + 2 * A(18) * DX(l) * dy(l) ^ 3 + A(4) * dy(l) + 5 * A(22) * DX(l) ^ 4 * dy(l) + 6 * A(21) * DX(l) ^ 5 + A(8) * dy(l) ^
2 + 4 * A(10) * DX(l) ^ 3 + 2 * A(7) * DX(l) * dy(l) + A(19) * dy(l) ^ 4 + A(1) + 3 * A(17) * DX(l) ^ 2 * dy(l) ^ 2 + 2
* A(12) _
 * DX(l) * dy(l) ^ 2 + 4 * A(23) * DX(l) ^ 3 * dy(l) ^ 2
    b(2) = 5 * A(26) * DX(l) * dy(l) ^ 4 + 2 * A(12) * DX(l) ^ 2 * dy(l) + A(16) * DX(l) ^ 4 + 4 * A(14) * dy(l) ^ 3 +
4 * A(19) * DX(l) * dy(l) ^ 3 + A(2) + 3 * A(13) * DX(l) * dy(l) ^ 2 + 2 * A(17) * DX(l) ^ 3 * dy(l) + 5 * A(20) * dy(l)
^ 4 + _
 A(22) * DX(l) ^ 5 + 3 * A(18) * DX(l) ^ 2 * dy(l) ^ 2 + 2 * A(5) * dy(l) + A(11) * DX(l) ^ 3 + A(4) * DX(l) + 6 *
A(27) * dy(l) ^ 5 + 3 * A(24) * DX(l) ^ 3 * dy(l) ^ 2 + 3 * A(9) * dy(l) ^ 2 + 4 * A(25) * DX(l) ^ 2 * dy(l) ^ 3 + A(7) *
DX(l) ^ 2 + _
2 * A(23) * DX(l) ^ 4 * dy(l) + 2 * A(8) * DX(l) * dy(l)
    b(3) = 3 * A(11) * DX(l) * dy(l) + 15 * A(21) * DX(l) ^ 4 + A(3) + 6 * A(10) * DX(l) ^ 2 + 10 * A(22) * DX(l) ^
3 * dy(l) + 3 * A(17) * DX(l) * dy(l) ^ 2 + 3 * A(6) * DX(l) + A(7) * dy(l) + A(25) * dy(l) ^ 4 + 3 * A(24) * DX(l) *
dy(l) ^ 3 + _
 10 * A(15) * DX(l) ^ 3 + A(12) * dy(l) ^ 2 + A(18) * dy(l) ^ 3 + 6 * A(23) * DX(l) ^ 2 * dy(l) ^ 2 + 6 * A(16) * DX(l)
^ 2 * dy(l)
    b(4) = 6 * A(18) * DX(l) * dy(l) ^ 2 + 8 * A(25) * DX(l) * dy(l) ^ 3 + 5 * A(22) * DX(l) ^ 4 + 2 * A(8) * dy(l) + 3
* A(13) * dy(l) ^ 2 + 8 * A(23) * DX(l) ^ 3 * dy(l) + 2 * A(7) * DX(l) + 3 * A(11) * DX(l) ^ 2 + 6 * A(17) * DX(l) ^ 2
* dy(l _
) + 4 * A(12) * DX(l) * dy(l) + 5 * A(26) * dy(l) ^ 4 + A(4) + 9 * A(24) * DX(l) ^ 2 * dy(l) ^ 2 + 4 * A(16) * DX(l) ^ 3
+ 4 * A(19) * dy(l) ^ 3
    b(5) = 6 * A(25) * DX(l) ^ 2 * dy(l) ^ 2 + 3 * A(24) * DX(l) ^ 3 * dy(l) + 3 * A(18) * DX(l) ^ 2 * dy(l) + 3 * A(9)
* dy(l) + 10 * A(20) * dy(l) ^ 3 + A(5) + 10 * A(26) * DX(l) * dy(l) ^ 3 + 6 * A(19) * DX(l) * dy(l) ^ 2 + A(23) *
DX(l) ^ 4 _
+ A(12) * DX(l) ^ 2 + 6 * A(14) * dy(l) ^ 2 + 15 * A(27) * dy(l) ^ 4 + A(8) * DX(l) + 3 * A(13) * DX(l) * dy(l) +
A(17) * DX(l) ^ 3
    b(6) = 10 * A(22) * DX(l) ^ 2 * dy(l) + 20 * A(21) * DX(l) ^ 3 + 4 * A(16) * DX(l) * dy(l) + A(11) * dy(l) + A(6)
+ 4 * A(23) * DX(l) * dy(l) ^ 2 + 4 * A(10) * DX(l) + A(24) * dy(l) ^ 3 + 10 * A(15) * DX(l) ^ 2 + A(17) * dy(l) ^ 2
    b(7) = 2 * A(12) * dy(l) + 3 * A(11) * DX(l) + 3 * A(18) * dy(l) ^ 2 + A(7) + 12 * A(23) * DX(l) ^ 2 * dy(l) + 6 *
A(16) * DX(l) ^ 2 + 10 * A(22) * DX(l) ^ 3 + 6 * A(17) * DX(l) * dy(l) + 4 * A(25) * dy(l) ^ 3 + 9 * A(24) * DX(l) *
dy(l) ^ 2
    b(8) = 3 * A(13) * dy(l) + 9 * A(24) * DX(l) ^ 2 * dy(l) + 2 * A(12) * DX(l) + 10 * A(26) * dy(l) ^ 3 + A(8) + 3 *
A(17) * DX(l) ^ 2 + 6 * A(19) * dy(l) ^ 2 + 6 * A(18) * DX(l) * dy(l) + 4 * A(23) * DX(l) ^ 3 + 12 * A(25) * DX(l) *
dy(l) ^ 2
    b(9) = 10 * A(20) * dy(l) ^ 2 + 4 * A(25) * DX(l) ^ 2 * dy(l) + 20 * A(27) * dy(l) ^ 3 + 4 * A(19) * DX(l) * dy(l)
+ 10 * A(26) * DX(l) * dy(l) ^ 2 + A(18) * DX(l) ^ 2 + A(9) + A(24) * DX(l) ^ 3 + A(13) * DX(l) + 4 * A(14) * dy(l)
    b(10) = A(16) * dy(l) + A(10) + 5 * A(15) * DX(l) + 5 * A(22) * DX(l) * dy(l) + 15 * A(21) * DX(l) ^ 2 + A(23)
* dy(l) ^ 2
    b(11) = 8 * A(23) * DX(l) * dy(l) + A(11) + 10 * A(22) * DX(l) ^ 2 + 4 * A(16) * DX(l) + 3 * A(24) * dy(l) ^ 2 +
2 * A(17) * dy(l)
    b(12) = 9 * A(24) * DX(l) * dy(l) + 6 * A(25) * dy(l) ^ 2 + 3 * A(18) * dy(l) + 3 * A(17) * DX(l) + A(12) + 6 *
A(23) * DX(l) ^ 2
    b(13) = 3 * A(24) * DX(l) ^ 2 + 4 * A(19) * dy(l) + 8 * A(25) * DX(l) * dy(l) + A(13) + 2 * A(18) * DX(l) + 10 *
A(26) * dy(l) ^ 2
    b(14) = 5 * A(26) * DX(l) * dy(l) + 5 * A(20) * dy(l) + A(19) * DX(l) + A(25) * DX(l) ^ 2 + A(14) + 15 * A(27)
* dy(l) ^ 2
    b(15) = A(15) + 6 * A(21) * DX(l) + A(22) * dy(l)
    b(16) = 2 * A(23) * dy(l) + A(16) + 5 * A(22) * DX(l)
    b(17) = A(17) + 3 * A(24) * dy(l) + 4 * A(23) * DX(l)
    b(18) = 4 * A(25) * dy(l) + A(18) + 3 * A(24) * DX(l)
    b(19) = 2 * A(25) * DX(l) + 5 * A(26) * dy(l) + A(19)
    b(20) = A(20) + A(26) * DX(l) + 6 * A(27) * dy(l)
    b(21) = A(21)
```

```
    b(22) = A(22)
    b(23) = A(23)
    b(24) = A(24)
    b(25) = A(25)
    b(26) = A(26)
    b(27) = A(27)

NEXT I

FUNCTION wav (x AS SINGLE, y AS SINGLE) 'Function of wavefront aberration

'Total aberrations
'wav = b(6) * x ^ 3 + b(7) * x ^ 2 * y + b(8) * x * y ^ 2 + b(9) * y ^ 3 + b(10) * x ^ 4 + b(11) * x ^ 3 * y + b(12) * x ^ 2
* y ^ 2 + b(13) * x * y ^ 3 + b(14) * y ^ 4 + b(15) * x ^ 5 + b(16) * x ^ 4 * y + b(17) * x ^ 3 * y ^ 2 + b(18) * x ^ 2 * y ^
_
3 + b(19) * x * y ^ 4 + b(20) * y ^ 5 + b(21) * x ^ 6 + b(22) * x ^ 5 * y + b(23) * x ^ 4 * y ^ 2 + b(24) * x ^ 3 * y ^ 3 +
b(25) * x ^ 2 * y ^ 4 + b(26) * x * y ^ 5 + b(27) * y ^ 6

'Asymmetrical component
'wav = B(6) * x ^ 3 + B(7) * x ^ 2 * y + B(8) * x * y ^ 2 + B(9) * y ^ 3 + B(15) * x ^ 5 + B(16) * x ^ 4 * y + B(17) * x ^
3 * y ^ 2 + B(18) * x ^ 2 * y ^ 3 + B(19) * x * y ^ 4 + B(20) * y ^ 5

'symmetrical component
wav = B(10) * x ^ 4 + B(11) * x ^ 3 * y + B(12) * x ^ 2 * y ^ 2 + B(13) * x * y ^ 3 + B(14) * y ^ 4 + B(21) * x ^ 6 +
B(22) * x ^ 5 * y + B(23) * x ^ 4 * y ^ 2 + B(24) * x ^ 3 * y ^ 3 + B(25) * x ^ 2 * y ^ 4 + B(26) * x * y ^ 5 + B(27) * y
^ 6

END FUNCTION
```

A12.5 Generating seeds for the sorting of symbolic Taylor terms from Maple transformation output after a reference shift

```
DIM DEG(27) AS STRING
DIM dumdeg  AS STRING
DIM a AS STRING
DIM b AS STRING
DIM co(27) AS INTEGER
I = 0
'--Generate terms Talyor polynomials as sorting seeds
FOR n = 1 TO 6
  FOR i = 0 TO n
    I = I + 1
    IF n - i = 0 THEN
     a = ""
    ELSEIF n - i = 1 THEN
     a = "u"
    ELSE
     a = "u^" + RIGHT$(STR$(n - i), 1)
    END IF
    IF i = 0 THEN
     b = ""
    ELSEIF i = 1 THEN
     b = "v"
    ELSE
     b = "v^" + RIGHT$(STR$(i), 1)
    END IF
```

```
      IF a = "" THEN
       DEG(l) = b
      ELSEIF b = "" THEN
       DEG(l) = a
      ELSE
       DEG(l) = a + "*" + b
      END IF
      PRINT l, DEG(l)
   NEXT i
NEXT n
DEG(0) = "1"
'---Number each term to each Taylor term
OPEN "LUCDEG0.TXT" FOR INPUT AS #3
l = -1
DO
l = l + 1

INPUT #3, dumdeg
FOR i = 0 TO 27
IF dumdeg = DEG(i) THEN co(l) = i: PRINT l, dumdeg, co(l)
NEXT i
LOOP UNTIL EOF(3)
CLOSE #3

'---save the Taylor term number (0..27) of each term in the maple output.
OPEN "deg207.txt" FOR OUTPUT AS #3
FOR i = 0 TO 27
PRINT #3, co(i)
NEXT i
CLOSE #3
```

A12.6 Sorting of the output of the symbolic Maple transformation after a reference shift

```
DIM A, l, b AS INTEGER
DIM DUM AS STRING
DIM DUM0 AS STRING
DIM duml  AS STRING
DIM cof(27) AS STRING
DIM CO(27) AS INTEGER
'---Reads in the order of the Taylor terms as generated by A12.5
OPEN "deg207.txt" FOR INPUT AS #3
FOR I = 0 TO 27
INPUT #3, CO(I)
PRINT CO(I)
NEXT I
CLOSE #3
'---sort terms according to the order read in as above.
OPEN "coef_sht.TXT" FOR INPUT AS #3
A = 0
l = 0
DUM0 = ""
DO
LINE INPUT #3, DUM
DUM0 = DUM0 + DUM
LOOP UNTIL EOF(3)

duml = DUM0
DO
```

```
      b = INSTR(dum1, ",")
      IF b = 0 THEN
        cof(CO(I)) = dum1
        b = LEN(dum1)
      END IF
      cof(CO(I)) = LEFT$(dum1, b - 1)
      PRINT I, CO(I); "==="; cof(CO(I))
      dum1 = RIGHT$(dum1, LEN(dum1) - b)
      I = I + 1
LOOP UNTIL dum1 = ""
CLOSE #3
'---Output sorted Taylor coefficients(0..27)
OPEN "srtco_xy.txt" FOR OUTPUT AS #3
FOR I = 0 TO 27
   PRINT #3, cof(I)
   PRINT I, "=", cof(I)
NEXT I
CLOSE #3
```

Bibliography

American Conference of Governmental Industrial Hygienists (ACGIH) (1995) *Threshold Limit Values for Chemical Substance and Physical Agents and Biological Exposure Indices*. ACGIH Press.

Ames, A. and Proctor, C.A. (1921) Dioptrics of the eye. *J. Opt. Soc. Am.* **11** 22-84.

ANSI (1993) *American National Standard for the Safe Use of Lasers ANSI Z136.1-1993*, Orlando, Florida, Laser Institute of America.

Applegate, R.A. and Howland, H. C. (1995) Noninvasive measurement of corneal topography. *IEEE Engineering in Medicine and Biology* **42** 30-42.

Applegate, R.A. and Lakshminarayanan, V. (1993) Parametric representation of Stiles-Crawford functions: Normal variation of peak location and directionality. *J. Opt. Soc. Am. A* **10**, 1611-1623.

Artal, P., Marcos, S., Navarro, R., and Williams, D.R. (1995) Odd aberrations and double-pass measurements of retinal image quality. *J. Opt. Soc. Am. A.* **12**, 195-201.

Atchison, D.A., Collins, M.J., Wildsoet, C.F., Christensen, J., and Waterworth, M.D. (1995) Measurement of monochromatic ocular aberrations of human eyes as a function of accommodation by the Howland aberroscope technique. *Vision Res.* **35**, 313-323.

Barnes, D.A., Dunne, M.C.M., and Clement, R.A. (1987) A schematic eye model for the effects of translation and rotation of ocular components on peripheral astigmatism. *Ophthal. Physiol. Opt.* **7**, 153-158.

Bedford, R. E. and Wysecki, G. (1957) Axial chromatic aberration of the human eye. *J. Opt. Soc. Am.* **64**, 1724-5.

Bennet, A. G. and Rabbetts, R. B. (1984) Clinical Visual Optics. Toronto, Butterworth.

Berny, F. and Slansky, S. (1969) Wavefront Determination resulting from Foucault Test applied to the Human Eye and Visual Instruments. In: *Optical Instruments and Techniques*, 375-385. Edited by Home Dickon, J. London, Oriel Press.

Bing, L. and Campbell, M.C.W. (1994) The change of monochromatic aberrations with lens tilt and pupil decentration in a four aspherical surface model eye. *Invest. Ophthalmol Vis Sci. Suppl.* **35**, 1803.

Bradley, A. (1992) Perceptual manifestations of imperfect optics in the human eye: Attempts to correct for ocular chromatic aberration. *Optom. Vis. Sci.* **69**, 515-521.

Brown, N. (1973) The change in shape and internal form of the lens of the eye on accommodation. *Exp. Eye Res.* **15**, 441-459.

Bullock, B., Glasser, A., and Campbell, M.C.W. (1995) Does lens suture position influence optimal visual axis tilt *in vivo*. *Invest. Ophthalmol Vis Sci. Suppl.* **36**, S937

Campbell, M.C., Harrison, E.M., and Simonet, P. (1990) Psychophysical measurement of the blur on the retina due to optical aberration of the eye. *Vision Res.*. 30, 1587-1602

Charman, W.N., Jennings, J.A.M., and Whitefoot, H. (1978) The refraction of the eye in relation to spherical aberration and pupil size. *Br. J. Physiol. Opt.* **32**, 78-93.

Charman, W.N. (1983) The retina image in the human eye. In: *Progress in Retinal Research*, 1-50. Edited by Osborne, N. and Chader, G. Oxford, Pergamon.

Charman, W.N. (1991) Optics of the Human Eye. In: *Visual Optics and Instrumentation*, 1-14. Boca Raton, CRC Press Inc.

Charman, W.N. and Jennings, J.A.M. (1976) Objective measurements of the longitudinal chromatic aberration of the human eye. *Vision Res.* **16**, 999-1005.

Colliac, J. H., Shammas, H. J., and Bart D. J. (1994) Photorefractive keratectomy for the correction of myopia and astigmatism. *Am. J. Opthal.* **117**, 369-80.

Cubalchini, R. (1979) Modal wave-front estimation from phase derivative measurements. *J. Opt. Soc. Am.* **69**, 972-977.

Cui, C., Campbell, M.C.W., Charman, W.N., and Voisin, L. (1993) Reducing aberration at the fovea by defocus. *Ophthalmic and Visual Optics Technical Digest* **3**, 164-167.

Dingeldein, S.A. and Klyce, S. (1989) The topography of normal corneas. *Arch. Ophthalmol.* **107**, 512-518.

Dunne, M.C.M. and Barnes, D.A. (1989) Modeling angle alpha. *Ophthal. Physiol. Opt.* **9**, 338-339.

Edmund, C. (1987) Corneal apex in keratoconic patients. *Am. J. Optom. Physiol. Opt.* **64**, 905-908.

Dunes, M. C. M., Misson, G. P., White, E. K., and Barnes D. A. (1993) Peripheral astigmatic asymmetry and angle alpha. *Opthal. Physiol. Opt.* **13**, 303-5.

Effert, R., Barry, J.C., Kaupp, A., and Kleine, M. (1992) New methods for the assessment of eye deviations in strabismus. *Chibret International Journal of Ophthalmology* **9**, 49-60.

EL Hage, S. and Berny, F. (1973) Contribution of the crystalline lens to the spherical aberration of the eye. *J. Opt. Soc. Am.* **63**, 205-211.

Emsley, H.H. (1952) *Visual Optics*, London, Hatton.

Enoch, J. M. and Lakshminarayanan, V. (1991) Retinal fiber optics. In: *Vision and visual dysfunction*, edited by J. Cronly-Dillon. Boca Raton: CRC Press, 280-309.

Freeman, M.H. (1990) *Optics*, 10th Ed., Toronto, Butterworths.

Gorrand, J. and Delori, F. (1995) A reflectometric technique for assessing photoreceptor alignment. *Vision Res.* **35**, 999-1010.

Guillon, J.P. (1982) Tear film photography and contact lens wear. *J. Br. Contact Lens Ass.* **5**, 84-86.

Hitzenberger, C., Baumgartner, A., Drexler, W., and Fercher, A. (1994) Interferometric measurement of corneal thickness with micrometer precision. *Am. J. Opthal.* **118**, 468-476.

Howarth, P.A. and Bradley, A. (1986) The longitudinal chromatic aberration of the human eye, and its correction. *Vision Res.* **26**, 361-366.

Howland, H.C., Glasser, A., and Applegate, R.A. (1992) Polynomial approximation of corneal surfaces and corneal curvature topography. *Ophthalmic and Visual Optics Technical Digest (OSA, Washington, D. C.)* **3**, 34-37.

Howland, H.C. and Buettner, J., and Applegate, R. A. (1994) Computation of the shape of normal corneas and their monochromatic aberrations from videokeratometric

measurement. ***Technical digest series of the Ophthalmic and visual optics meeting of OSA***. (OSA, Washington DC) **2**, 54-57.

Howland, H.C. and Howland, B. (1977) A subjective method for the measurement of monochromatic aberrations of the eye. *J. Opt. Soc. Am.* **11**, 1508-1518.

Ivanoff, A. (1956) About the spherical aberration of the eye. *J. Opt. Soc. Am.* **46**, 901-904.

Jacobs, P.M., Cheng, H., and Price, N.C. (1983) Pseudophakodonesis and corneal endothelial contact:Direct observations by high-speed cinematography. *Br. J. Ophthalmol.* **67**, 650-654.

Janisse, M.P. (1973) *Pupillary Dynamics and Behavior*. New York, Plenum.

Jenkins, T.C.A. (1963) Aberrations of the eye and their effects on vision: Part I. *Br. J. Physiol. Opt.* **20**, 59-91.

Jennings, J. A. M. and Charman, W. N. (1981) Off-axis image quality in the human eye. *Vis. Res.* **21**, 445-455.

Josephson, J.E. (1983) Appearance of the pre-ocular tear film lipid layer. *Am. J. Optom. Physiol. Opt.* **60**, 883-887.

Kiely, P.M., Smith, G., and Cerney, L.G. (1982) The mean shape of the human cornea. *Opt. Acta* **29**, 1027-1040.

Koomen, M., Tousey, R., and Scolnik, R. (1949) The spherical aberration of the human eye. *J. Opt. Soc. Am.* **39**, 370-376.

Kuszak, J.R., Bertram, B.A., Macsai, M.S., and Rae, J.L. (1984) Sutures of the crystalline lens: a review. *Scanning Microsc.* **III**, 1369

Kuszak, J.R., Sivak, J.G., and Weerheim, J.A. (1991) Lens optical quality is a direct function of lens sutural architecture. *Invest. Ophthalmol. &Vis. Sci.* **32**, 2119-2129.

Lakshminarayanan, V., Enoch, J.M., Raasch, T., Crawford, B., and Nygaard, R.W. (1986) Refractive changes induced by intraocular lens tilt and longitudinal displacement. *Arch. Ophthalmol.* **104**, 90-92.

Lakshminarayanan, V., Lang, A., Bailey, J.E. and Enoch, J.M. (1994a) Aniseikonia in bilateral pseudophakia. *Ophthalmic and Visual Optics Technical Digest* **4**, 192-195.

Lakshminarayanan, A., Bailey, J.E. and Enoch, J.M. (1994b) Aniseikonia in intraocular (IOL) implants: an optical analysis. *Eur. J. Implant Ref. Surg.* **6**, 22-29.

Liang, J. (1991) A New Method to Precisely Measure the Wave Aberrations of the Human Eye with a Hartmann-Shack-Wavefront-Sensor. *Ph.D. dissertation.* University of Heidelberg.

Liang, J., Grimm, B., Goelz, S., and Bille, J.F. (1994) Objective measurement of wave aberrations of the human eye with use of a Hartmann-Shack wave-front sensor. *J. Opt. Soc. Am. A* **11**, 1949-1957.

Lotmar, W. and Lotmar, T. (1974) Peripheral astigmatism in the human eye: experimental data and theoretical model prediction. *J. Opt. Soc. Am.* **64**, 510-3.

Mandell, R.B. and Helen, R.S. (1969) Position and curvature of the corneal apex. *Am. J. Optom. Arch. Am. Acad. Optom.* **46**, 25-29.

Marcos, S., Artal, P., and Green, D.G. (1994) The effect of decentered small pupils on ocular modulation transfer and contrast sensitivity. *Invest. Ophthalmol. &Vis. Sci.* **35**, 1258

Martin, F.E. (1942) The importance and measurement of angle alpha. *Br. J. Physiol. Opt.* **3**, 27-45.

Martola, E.L. and Baum, J.L. (1968) Central and peripheral corneal thickness-a clinical study. *Arch. Ophthalmol.* **79**, 28-30.

Millodot, M. and Sivak, J. (1979) Contribution of the cornea and lens to the spherical aberration of the eye. *Vision Res.* **19**, 685-687.

Nakao, S., Mine, K., Nishioka, K., and Kamiya, S. (1969) The distribution of refractive indices in the human crystalline lens. *Jap. J. Clin. Opthalmol.* **23**, 41-44.

Pande, M. and Hillman, J.S. (1993) Optical zone centration in keratorefractive surgery. *Ophthalmology* **100**, 1230-1237.

Parker, J.A. (1972) Aspherical optics of the human lens. *Can. J. Ophthalmol.* **7**, 168-175.

Philips, P. H., Rosskothen, H. D., Perez-Emmanuelli, J., and Koester, C. (1988) Measurement of intraocular lens decentration and tilt in vivo. *J. Cataract. Refract. Surg.* **14**, 129-34.

Rimmer, M.P. (1974) Method for evaluating lateral shearing interferograms. *Appl. Opt.* **13**, 623-629.

Roorda, A. (1996) Double pass reflections in the human eyes. *Ph. D. Dissertation.* University of Waterloo, Ontario, Canada.

Roorda, A. and Campbell, M.C.W. (1994) The relationship between double and single pass image quality in the human eye. *Invest. Ophthalmol. & Vis. Sci. Suppl.* **35**, 1258.

Royston, J.M., Dunne, M.C.M., and Barnes, D.A. (1990) Measurement of posterior corneal surface toricity. *Optom. Vis. Sci.* **67**, 757-763.

Ruben, P. L. (1963) Aberrations arising from decentration and tilts. *J. Opt. Soc. Am.* **54**, 45-51.

Rynders, M. C., Navarro, R., and Losada, M. A. (1996) Off-axis longitudinal chromatic aberrations in the human eye. *Vision Science and its Applications, Technical Digest.* (Washington DC, OSA). **1**, 238-241.

Shipley, T. and Rawlings, S.C. (1970) The nonius horopter-II. An experimental report. *Vision Res.* **10**, 1263-1299.

Simonet, P. and Campbell, M.C.W. (1990) The optical transverse chromatic aberration on the fovea of the human eye. *Vision Res.* **30**, 187-206.

Simpson, G.C. (1953) Ocualr halos and coronas. *Br. J. Ophthal.* **37**, 450-486.

Sivak, J.G. (1982) The contribution of the crystalline lens to chromatic and spherical aberrations of the eye. *Can. J. Optom* **44**, 89-91.

Smirnov, M.S. (1961) Measurement of the wave aberration of the human eye. *Biofizika* **6**, 687-703.

Smith, W.J. (1990) *Modern Optical Engineering*, 2nd Ed., New York, McGraw Hill, Inc.

Southwell, W.H. (1980) Wave-front estimation from wave-front slope measurements. *J. Opt. Soc. Am.* **70**, 998-1006.

Stine, G.H. (1930) Variations in refraction of the visual and extravisual pupillary zones. *Am. J. Opthal.* **13**, 101-112.

Thibos, L.N., Bradley, A., Still, D.L., Zhang, X., and Howarth, P.A. (1990) Theory and measurement of ocular chromatic aberration. *Vision Res.* **30**, 33-49.

Thibos, L.N., Bradley, A., and Zhang, X. (1991) Effect of ocular chromatic aberration on monocular visual performance. *Optom. Vis. Sci.* **68**, 599-607.

Tomlinson, A. and Schwartz, C. (1979) The position of the corneal apex in the normal eye. *Am J. Optom. Physio. Opt.* **56**, 236-40.

Tscherning, M. (1924) *Physiologic Optics*, 4th Ed., Philadelphia, Keystone Publishing Co.

Uozato, H., Makino, M., Saishin, M., and Nakao, S. (1983) Measurement of visual axis using a laser beam. *Advances in diagnostic visual optics*, Spring series in optical science. **41**, 22-29.

Uozato, H. and Guyton, D.L. (1987) Centering Corneal Surgical Procedures. *Am. J. Opthal.* **103**, 264-275.

van Meeteren, A. and Dunnewold, C., J (1983) Image quality of the human eye for eccentric entrance pupils. *Vision Res.* **23**, 573-579.

Wald, G. and Griffin, D. R. (1947) The change of the refractive power of the human eye in dim and bright light. *J. Opt. Soc. Am.* **37**, 321-36.

Walsh, G., Charman, W.N., and Howland, H.C. (1984) Objective technique for the determination of monochromatic aberrations of the human eye. *J. Opt. Soc. Am. A* **1**, 987-992.

Walsh, G. (1988) The effect of mydriasis on pupillary centration of the human eye. *Ophthal. Physiol. Opt.* **8**, 178-182.

Walsh, G. and Charman, W.N. (1988) The effect of pupil centration and diameter on ocular performance. *Vision Res.* **28**, 659-665.

Walsh, G. and Charman, W.N. (1992) Variation in ocular accommodation and phase transfer functions with grating orientation. *Ophthal. Physiol. Opt.* **12**, 365-369.

Warnicki, J.W., Rehkopf, P.G., Arffa, R.C., and Stuart, J.C. (1992) Corneal topography using a projected grid. In: *Corneal Topography: Measuring and Modifying the Cornea*, 25-32. Edited by Schanzlin, D.J. and Robin, J.R. New York, Springer-Verlag.

Webb, R.H., Penney, M., and Thompson, K.P. (1992) Measurement of ocular local wavefront distortion with a spatially resolved refractometer. *Appl. Opt.* **31**, 3678-3686.

Welford, W.T. (1991) *Aberrations of Optical Systems*, New York, Adam Hilger.

Westheimer, G. (1966) The Maxwellian view. *Vision Res.* **6**, 669-682.

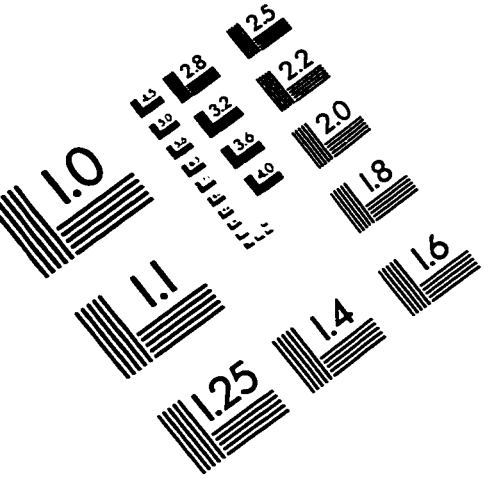
Westheimer, G. and Mckee, S.P. (1976) Spatial configuration for Visual Hyperacuity. *Vision Res.* **17**, 941-947.

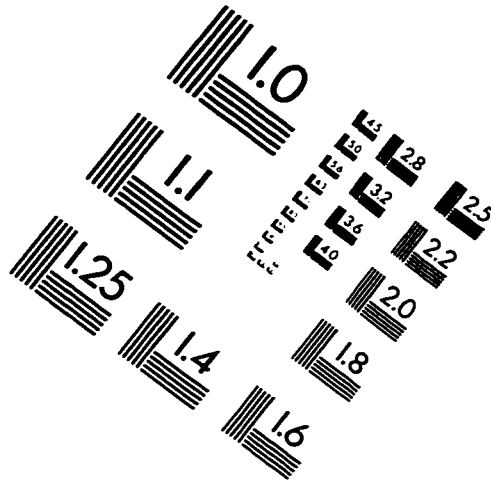
Wilson, M.A., Campbell, M.C.W., and Simonet, P. (1992) Change of pupil centration with change of illumination and pupil size. *Optom. Vis. Sci.* **69**, 129-136.

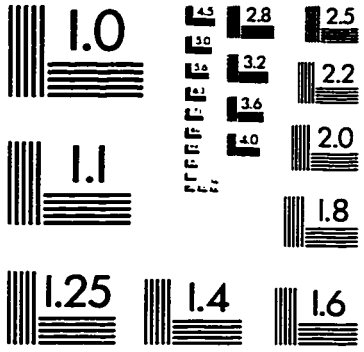
Witte, R.S. (1989) *Statistics*, 3rd Ed., Toronto, Holt, Rinehart and Winston.

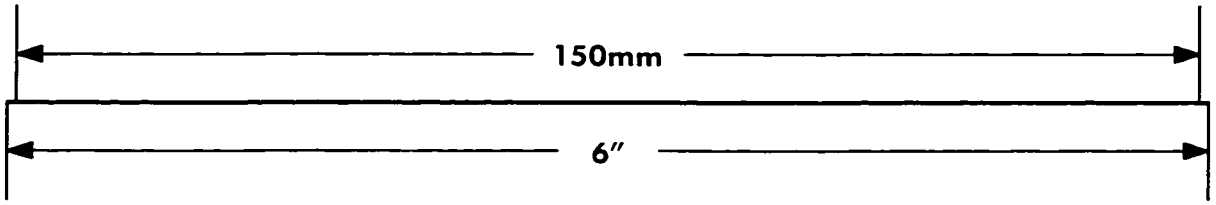
Ye, M., Bradley, A., Thibos, L.N., and Zhang, X. (1992) The effect of pupil size on chromostereopsis and chromatic diplopia: Interaction between the Stiles-Crawford effect and chromatic aberrations. *Vision Res.* **32**, 2121-2128.

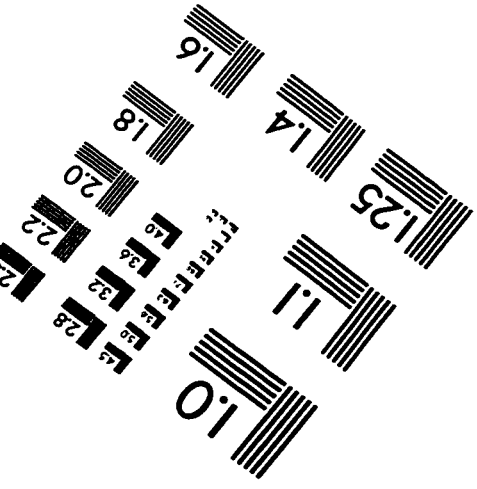
IMAGE EVALUATION
TEST TARGET (QA-3)

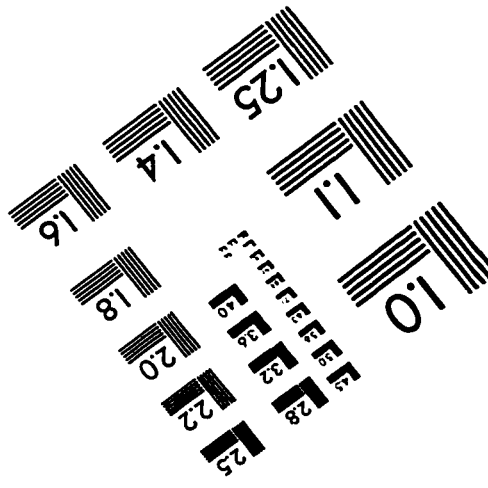












APPLIED IMAGE, Inc
1653 East Main Street
Rochester, NY 14609 USA
Phone: 716/482-0300
Fax: 716/288-5989

© 1993, Applied Image, Inc., All Rights Reserved